Ultrafast spin dynamics and transport in magnetic metallic heterostructures

Quentin Remy

UNIVERSITÉ DE LORRAINE

École doctorale C2MP

Ultrafast spin dynamics and transport in magnetic metallic heterostructures

THÈSE

présentée et soutenue publiquement le 9 Septembre 2021

pour l'obtention du

Doctorat de l'Université de Lorraine

(en Physique)

par

Quentin Remy

Composition du jury

Rapporteurs :	Chiara Ciccarelli	Cambridge University
	Bert Koopmans	TU Eindhoven
Examinateurs :	Sangeeta Sharma	Max-Born Institute - Berlin
	Jeffrey Bokor	University of California - Berkeley
	André Thiaville	Université Paris Saclay
Invité :	Christophe Chatelain	Université de Lorraine
Directeurs de thèse :	Stéphane Mangin	Université de Lorraine
	Gregory Malinowski	Université de Lorraine

Institut Jean-Lamour - UMR 7198 - Université de Lorraine

Département de Physique de la Matière et des Matériaux

Nanomagnétisme et Electronique de spin

INSTITUT JEAN LAMOUR

Mis en page avec la classe thesul.

Résumé

Le contrôle de l'aimantation, et donc du spin, aux échelles de temps ultra courtes, est un sujet d'importance fondamentale pour l'élaboration de systèmes qui peuvent stocker de l'information beaucoup plus rapidement. La possibilité d'écrire de l'information avec des pulses laser femtoseconde sur des métaux magnétiques tels que GdFeCo ou MnRuGa en quelques picosecondes fut une étape conséquente pour pouvoir réaliser ce progrès technologique. Cependant, le renversement de l'aimantation observé dans ces matériaux après les avoir irradiés avec un unique pulse laser, appelé retournement tout optique indépendent de l'hélicité (AO-HIS pour *All Optical Helicity Independent Switching* en anglais), est toujours limité à une petite catégorie de matériaux ferrimagnétiques et sa description physique n'est toujours pas entièrement comprise.

Dans cette thèse, nous étudions l'AO-HIS dans des films minces composés d'une ou deux couches d'alliages de GdFeCo de différentes compositions. Nous montrons que ces couches génèrent des courants de spin qui peuvent modifier l'AO-HIS de ces matériaux. En particulier, nous montrons qu'il est possible d'utiliser ces courants de spin pour renverser l'aimantation des différentes multicouches ferromagnétiques, avec un seul pulse laser femtoseconde, qui ne subiraient qu'une désaimantation et ne se retourneraient donc pas autrement. En changeant la composition de l'alliage de GdFeCo et la température de Curie du matériau ferromagnétique, nous pouvons modifier l'énergie nécessaire pour engendrer le renversement magnétique de la multicouche ferromagnétique avec un pulse de lumière. De plus, nous montrons que l'AO-HIS de l'alliage de GdFeCo n'est en réalité pas nécessaire ainsi que l'illumination directe de la couche ferromagnétique par la lumière laser. Il est donc possible de retourner l'aimantation d'un matériau ferromagnétique en utilisant uniquement des courants ultra courts de chaleur et de spin qui sont créés par la désaimantation ultra rapide partielle de l'alliage de GdFeCo et transportés jusqu'à la couche ferromagnétique via une couche de cuivre. Ces expériences sont comprises grâce à un modèle de transport semi classique dans un système contenant des électrons, des phonons et des spins quantiques et qui est basé sur l'échange de moment cinétique entre des spins localisés et itinérants.

Enfin, nous avons mesuré la dynamique du renversement de l'aimantation de ce système ferromagnétique. Nous montrons que ce retournement se passe en moins d'une picoseconde, ce qui est le retournement d'aimantation le plus rapide jamais observé. Nous montrons que le courant de spin provenant de l'alliage de GdFeCo à un pouvoir réfrigérant sur l'aimantation, déjà

visible en moins d'une picoseconde, et qui peut augmenter l'aimantation transitoire du système jusqu'à trente pourcents. Ces résultats sont également compris dans le cadre de notre modèle de transport de chaleur et de moment cinétique.

Mots-clés: Aimantation, Hors équilibre, Courants de spin, Pulses laser femtoseconde.

Abstract

The control of magnetization, and thus spin, at the shortest timescale, is a fundamental subject for the development of faster data storage devices. The capability to encode information with femtosecond laser pulses on magnetic metals such as GdFeCo or MnRuGa within a few picoseconds was a significant step towards the realization of such a technology. However, the reversal of magnetization observed in these materials upon a single laser pulse irradiation, called All Optical Helicity Independent Switching (AO-HIS), is still limited to a small class of ferrimagnetic materials and its physical mechanism is not completely understood.

In this work, we study AO-HIS in magnetic thin films composed of a single or two GdFeCo layers with different alloy compositions. We show that these layers generate spin currents that can affect the AO-HIS of these materials. In particular, we can use such spin currents to reverse the magnetization of various ferromagnetic multilayers, with a single femtosecond laser pulse, which would otherwise only demagnetize and never switch. Playing with the GdFeCo alloy concentration and the ferromagnetic multilayer Curie temperature, we can tune the energy required to observe single shot reversal of the ferromagnet. In addition, we show that neither AO-HIS of the GdFeCo layer is actually required nor direct light illumination of the ferromagnetic multilayer. It is then possible to reverse the magnetization of ferromagnets using only ultrashort heat and spin currents which are generated by the partial ultrafast demagnetization of GdFeCo and transported via a thick metallic copper spacer. These experimental results were successfully understood using semiclassical transport equations for electrons, phonons and quantum spins based on exchange of angular momentum between localized and itinerant spins.

Finally, we were able to measure the dynamics of the ferromagnetic multilayer magnetization reversal which is shown to happen in less than a picosecond, being the fastest magnetization reversal ever observed. The action of the external spin current is shown to have an ultrafast cooling effect on the spin which is visible at the sub-picosecond timescale and which can enhance the transient magnetization by up to thirty percent. These results are also understood using our model of heat and angular momentum transport.

Keywords: Magnetization, Non-equilibrium, Spin currents, Femtosecond laser pulses.

Acknowledgments

This part concludes my work of the last three years which would not have been possible without the sustained support of many people.

First and foremost, I would like to thank my Ph.D. supervisor Stéphane Mangin greatly. First for introducing me to the field of magnetism and spintronics as a teacher during my graduate studies and for his continuing guidance as I was pursuing my masters. Second, for giving me the opportunity to work on what I present in this thesis and letting me understand and study all the aspects that I found interesting. Finally, for his still continuing guidance as I start my post doctoral career.

Secondly, I would like to thank my co-supervisor Grégory Malinowski. I greatly appreciated working with you, for all the discussions we had and your availability, your many explanations about all the topics involved in my Ph.D. subject (experimental and theoretical), as well as your constructive feedbacks, commentaries and suggestions on my work. I hope we can still work together in the future.

Then I would like to thank Bert Koopmans for his great involvement in my work, through the "following committee", for inviting me to his laboratory in Eindhoven and the ongoing collaboration with Maarten Beens, for the several very interesting discussions we could have on many occasions and also for carefully reading my manuscript. Naturally, I am also thankful to Maarten Beens for his help in understanding many theoretical aspects of ultrafast magnetization dynamics and transport, theoretical predictions presented in Chapter 7 of this thesis and his kind welcome when I went to Eindhoven.

I thank Chiara Ciccarelli for carefully reading my manuscript, the discussions we already had (including during my Ph.D. defense) and for allowing me to continue working on this very interesting subject by expanding its complexity and the methods used to understand it.

I am also grateful to the remaining members of my Ph.D. jury for reading my manuscript and all the discussions/questions I could have during my Ph.D. defense. I am especially grateful to Christophe Chatelain for the long discussions we had on the second chapter of this thesis.

I thank my collaborators from Tohoku University Hideo Ohno, Shunsuke Fukami and especially Junta Igarashi and Satoshi Iihama for the close collaboration we had and the numerous interactions we have had in person or online. Special thanks also go to Junta Igarashi for his greatly appreciated welcome during my stay in Sendai and at the very end of my Ph.D. in P's house.

My work also could not have been possible without the great work of other members of the Nanomagnetism and Spintronics team at Institut Jean Lamour. I thank Jean-Loïs (more

below) and Michel Hehn for sample growth (there were a lot of samples, much more than what is presented in this work), Jon Gorchon for many explanations and great ideas in general (I owe the idea presented in Chapter 9, among others, to a discussion we had at the beginning of my Ph.D.) as well as many informal interactions of various kinds, Philippe Scheid also for many profound discussions about Physics and for giving me the opportunity to help him on his review project, Julius Hohlfeld for being the passionate physicist that I needed as an office mate to discuss everything that can be labeled as Physics, in the deepest possible way, and for his priceless help and dedication regarding the TR-MOKE microscopy experiments (the final hope when I was scared we could not do it) performed in Chapter 8 of this thesis, together with the also important help of Maxime Vergès and Yann Le Guen. I also would like to thank the Nanomagnetism and Spintronics team in general (also those without special thanks below) for the general great atmosphere inside the team, in formal and less formal contexts. In addition, all of this could not have been possible without the great efforts of the administrative staff at Institut Jean Lamour which I also thank a lot.

Other people that are not from the Nanomagnetism and Spintronics team helped me in my work, including Thomas Easwarakhanthan for ellipsometry measurements, Valery Gridnev for online exchanges regarding his theory of AO-HIS, as well as my interns Marie-Laure Chavazas, Romain Billet and Alexy Bertrand for their great work on several simulation aspects under my supervision.

I can hardly envision how one could survive a Ph.D. without too much pain, especially during a pandemic, without the support of friends. Among my friends, whether they are from France, Canada or Institut Jean Lamour, I especially thank Christophe[1], Nicolas, Gaëtan, Magalie, Aloïs, Charlotte, Julien, Moéa, Alexis, Jan-Erik, Anji, Thomas, Moose, Emma, Mike, Curtis, Riya, Shirley, Thomas, Alex, Insung, Jeanie, Hank, Jean-Loïs[2], Maxime[3], Boris, Anna, Maryam, Kosseila, Elodie, Gauthier, Charles, Alberto, Kaushal, Junta, Valentin, Gabrielle, Sandrine, Claudia, Philippe, Pierre, Thibaud and Sébastien, for the various kinds of support that you gave me during these three years. I thank you deeply for it.

1) I would like to give extra special thanks to Christophe for always having supported me during this Ph.D. but also all along my studies, for always giving me comforting thoughts and helping me taking difficult decisions, no matter what the subject is and also for always believing in me when I think I am not capable (and it turns out you are always right, just like for pretty much everything else). For all of this and also for bearing me, I can't thank you enough.

2) My ultimate comrade since the very beginning of this hell of an adventure, Jean-Loïs, I can't imagine how bad all of this would have been without your company. I will miss our synergy

and common understanding regarding a wide range of subjects from humor to emotions, passing by science, whether it was on two different couches, a balcony on a third floor or around a round table, under the rain, on a 19th of May. Hopefully, this is just the beginning of better days.

3) My last office mate Maxime, always here to cheer me up and continue our jokes with Jean-Loïs. I really appreciated your unlimited sympathy and your gift to remember pretty much everything. Too bad quantum tunneling is so much enhanced when we are together, say, less than 200 meters apart. But thanks to this we really had good banters with Jean-Loïs. Thanks bro!

Lastly, none of this, even before I started my studies, would have been possible without the strong support of my family: I thank very very much my parents and Anaïs (coucou soeurette :D), my grand parents, all of my uncles, aunts and cousins, Fabienne and also obviously Dedette. I also thank very much those of you who could attend my defense, even though it was a week day and a bit far. Thanks again for always believing in me, I love you all very much.

Enfin, rien de cela n'aurait pu être possible, même avant que je commence mes études, sans le précieux soutien de ma famille: je remercie très vivement mes parents et Anaïs (coucou encore ;p), mes grands parents, tous mes oncles, tantes et cousins, Fabienne et aussi évidemment Dedette. Je remercie aussi ceux qui ont pu faire le trajet pour venir assister à ma soutenance même si le lieu et la date n'étaient pas forcément très pratiques. Merci encore de toujours croire en moi, je vous aime très fort.

"Rockets flying to the glowing sun..."

Contents

List of Figures

List of Tables

Chapter 1

Introduction

Progress in physics is often achieved by reaching new extremes: studying bigger and smaller spatial scales, shorter or longer times scales, higher energies, stronger interactions, higher or lower temperatures and pressures, etc. This ultimately resulted in the technological developments and all their consequences that we know today as well as a still increasing knowledge in all of science. Progress also often requires to go faster, mostly faster computation and communication. In this context, it is crucial to understand the fastest processes of what supports information. One promising such support, whether regarding traditional hard drives or the much-publicized quantum computers[1], is the spin that certain physical systems can carry.

It is then fundamental to study the dynamics of spin, and more generally angular momentum, in such condensed matter, low energy, systems. It was first attempted to understand the dynamics of magnetization, the quantity that is related to the angular momentum of particles that have an electric charge, in an external magnetic field such as what notoriously happens when one puts a compass in Earth's magnetic field. This was first done by Landau and Lifshitz[2] and later by Gilbert which led to the so called Landau-Lifchitz-Gilbert (LLG) equation[3]. This equation rigorously takes into account the effect of an external magnetic field on a magnetic moment but the complex interactions that lead to the relaxation of the magnetization inside the condensed matter system are only treated phenomenologically and are still studied nowadays[4]. In order to store information using spins for classical computing, it is required to be able to switch those spins between two stable states. It was shown that reversing magnetization with an external magnetic field pulse cannot be done deterministically for pulse durations of 2.3 picoseconds or lower[5]. Therefore, speeding up computation and communication will require another type of interaction between spin and an external leverage. It was very recently discovered that such an external mean

could be either light in the form of ultrashort (picosecond down to the femtosecond/attosecond timescale) laser pulses or even ultrashort (picosecond) electron pulses. These two methods are now widely studied whether it concerns the fundamental questions this new physics raises or the possible applications for faster storage devices[6].

This thesis is organized as follow:

In Chapter 2, we shortly review some of the basic physical concepts that are involved for a complete understanding of the ultrafast dynamics of spins and which will serve as a thread for the remaining discussions of the thesis. This includes a discussion regarding conserved quantities (energy, angular momentum, etc.) and their transport equations, interactions between these quantities and their origin.

Chapter 3 covers in detail the experimental and theoretical study of magnetization dynamics in metals at the ultrashort (femtosecond to picosecond) timescale after an electromagnetic or electronic excitation. We start with non equilibrium light-matter interaction in normal metals followed by the traditional theory of magnetization dynamics in spintronics. Then we expose the combined physics of laser induced ultrafast magnetization dynamics by reviewing ultrafast demagnetization and spin injection as well as the two magnetization reversal processes known as All Optical Helicity Dependent Switching (AO-HDS) and All Optical Helicity Independent Switching (AO-HIS). Then we will focus on the ultrafast magnetization dynamics induced by ultrashort hot electron pulses before concluding this review section with a particular combination of ultrafast demagnetization and ultrashort spin current pulses.

Chapter 4 introduces the different experimental techniques that have been used in the work shown in this thesis. A short introduction is made regarding sample growth, especially to introduce the different thin film architectures. A second part is devoted to the description of our femtosecond laser setup as well as the ultrashort pulses characterization methods. Most of the magnetic (static or dynamic) characterization of the grown samples relied on the Magneto-Optic Kerr Effect (MOKE). This phenomenon will be reviewed as well as how it was concretely used. The traditional polar MOKE with a continuous wave (cw) laser was used to measure magnetic hysteresis loops of the magnetic samples. A MOKE microscope was used to monitor domain formation after laser irradiation or application of an external magnetic field. Time Resolved MOKE (TR-MOKE) was used to obtain the magnetization dynamics. We also discuss to what extent TR-MOKE is actually able to measure magnetization and not some other non equilibrium electronic properties that depend on the initial orientation of the sample's magnetization. Finally, we also present TR-MOKE microscopy which has been used for the results presented in the last chapter.

The physics studied in this work is not completely understood yet. *Ab initio* techniques require an enormous amount of computation resources* and do not necessarily provide a lot of insight about the physical mechanisms at play. Any other type of model inevitably lacks predictivity as it requires extra parameters that must be adjusted so as to reproduce experiments. In chapter 5, we detail such a parametric model which has the required ingredients to provide a qualitative understanding of the processes surveyed in the following chapters. First, we extend the well-known Transfer Matrix Method (TMM) used to calculate light absorption in multilayered structures in order to get the true time dependence of light absorption and take chromatic dispersion into account. Then a Two Temperature Model (2TM) in multilayered structures is introduced together with its numerical implementation. To introduce magnetization dynamics, we discuss Gridnev's model of AO-HIS which is used in chapter 6. Finally, we introduce the s-d model of Beens *et al.* and discuss why it is suitable and necessary for a qualitative understanding of the experiments presented in the next chapters.

Chapter 6 focuses on the long time behavior of GdFeCo and GdFeCo/Cu/GdFeCo structures after exposition to a sequence of femtosecond laser pulses. We show that a wide variety of behaviors can be observed. Most importantly, magnetic layers that do not exhibit AO-HIS in a structure by themselves can exhibit it when they are in a bilayer structure. This fact is explained in terms of an ultrafast spin current generated by the ultrafast demagnetization of GdFeCo. The role of magnetic interactions of dipolar origin or such as the Ruderman-Kittel-Kasuya-Yoshida (RKKY) coupling are discussed. The influence of capping layers and laser irradiation direction is also studied.

Chapter 7 concerns similar bilayer (spin valve) structures as in chapter 6 except that one of the layers is replaced by a ferromagnetic [Co/Pt] or [CoNi/Pt] multilayer. We study heterostructures with different such multilayers in order to get more insight on the physical process that leads to the magnetization reversal of that ferromagnetic layer after irradiation with a single laser pulse. We also change the alloy concentration and the laser pulse duration to control the amount of angular momentum that is transferred from GdFeCo to the [Co/Pt] multilayer. We show that it is even possible to achieve magnetization reversal of the ferromagnetic multilayer without observing the magnetization reversal of the ferrimagnet. Finally, we reproduce similar experiments for different copper thicknesses and GdFeCo concentrations. It is shown that a higher Gd concentration in the alloy helps the magnetization reversal of the [Co/Pt] multilayer and that the later

*The current state of the art real time-Time Dependent Density Functional Theory is used to model tens of atoms for up to a few hundreds of femtoseconds[7,8]. In order to model magnetization reversal of disordered systems such as GdFeCo introduced later, one would need to go to tens of picoseconds[9] and around a million of atoms to capture spatial inhomogeneities effects[10]

is observable for copper thicknesses up to at least 80 nanometers.

Chapter 8 tries to bring further comprehension to the physics of the magnetic structures of chapter 7 by looking at there magnetization dynamics with TR-MOKE microscopy. We show that we can retrieve the magnetization dynamics of both magnetic layers as a function of space and fluence. In particular, we observed a complete magnetization reversal of the ferromagnetic layer in less than a picosecond, which is the fastest magnetization reversal ever reported. Finally, we show that this magnetization dynamics is well reproduced by the s-d model of Beens *et al.* with a physically realistic spin accumulation source as would be created by GdFeCo.

Finally chapter 9 will conclude the work of this thesis and provide some perspectives.

Chapter 2

General Context

The purpose of this chapter is to lay down the physical basis this work, and the general field of ultrafast magnetization dynamics, is based upon. It is a low energy physics (without antiparticles) of electrodynamics for condensed matter systems but where quantum effects play a fundamental role. We start by discussing the conservation laws that come from the Dirac Lagrangian for electrons. The angular momentum and magnetic moment of the electron is then naturally introduced. We then also consider nuclei and review the low energy limit that is used in condensed matter physics. Next, we discuss the statistical approaches generally used to deal with the many body problem. Finally, magnetization is introduced in the context of the macroscopic Maxwell equations.

2.1 Classical conservation laws

Even though we are only interested in low energy physics, it is convenient to start with a more general approach that encodes all the symmetries required to describe the conservation laws of condensed matter systems interacting with the electromagnetic field. Those symmetries are space-time translations and Lorentz invariance together with a local U(1) gauge symmetry. For a massive fermionic field with spin 1/2, this leads to the following Lagrangian density[11–13]:

$$\mathscr{L} = \overline{\psi}\left(i\hbar c\gamma^{\mu}\partial_{\mu} - qc\gamma^{\mu}A_{\mu} - mc^{2}\right)\psi - \frac{1}{4\mu_{0}}F_{\mu\nu}F^{\mu\nu} \tag{2.1}$$

Where ψ is the fermionic complex bispinor field representing electrons, γ^{μ} are the gamma matrices*, $\overline{\psi} = \psi^{\dagger}\gamma^{0}$ is the Dirac conjugate of ψ, $F_{\mu\nu} = \partial_{\mu}A_{\nu} - \partial_{\nu}A_{\mu}$ where A_{μ} is the (real)

*Spinor indices are omitted as is customary but one should be aware that bispinor fields have four components

electromagnetic four-vector potential, $\mu = 0$, 1, 2 or 3, and any occurence to the time coordinate $\mu = 0$ is multiplied by the velocity of light (e.g. $\partial_0 = \frac{1}{c}\partial_t$). Space-time variable dependency of the fields has been omitted, the Einstein summation convention with Minkowski metric $g_{\mu\nu}$ (with $g_{00} = 1$) is used and $\partial_\mu = (\partial_0, \boldsymbol{\nabla})$. m and $q = -|e|$ are the mass and the electric charge of the electron respectively. From this Lagrangian density, one can obtain the equation of motion for both electron and electromagnetic fields:

$$\left(i\hbar c\gamma^\mu \partial_\mu - mc^2\right)\psi = qc\gamma^\mu A_\mu \psi \tag{2.2}$$

$$\Box A^\mu = \mu_0 cq\bar{\psi}\gamma^\mu\psi \tag{2.3}$$

Equation 2.2 is the Dirac equation for an electron coupled to the electromagnetic field A_μ. Equation 2.3 is Maxwell's equations where we chose Lorenz gauge. Compared to the standard electrodynamics result, equation 2.3 contains spin angular momentum in its source term as will be shown below*. These equations are only valid if one assumes that the Least Action Principle (LAP) is satisfied. When this is the case, the resulting theory is said to be a theory of classical fields i.e. wave mechanics. It is still a quantum theory (leading for instance to uncertainty relations) but is fundamentally only capable of describing a single electron interacting with an electromagnetic field. Considering many electrons requires second quantization of the fields and the LAP is no longer satisfied[12–15]. We stick to classical fields in this section. For what is considered in this thesis, it is always sufficient to consider the electromagnetic field as classical.

The symmetries mentioned above are encoded in the Lagrangian density. This signifies that the action, the space-time integral of the Lagrangian density, is invariant under transformations of the fields associated with these symmetries[14]. Based on the LAP, Noether's theorem[12,14] then states that there exists a conserved quantity for each **global** symmetry of the action. This leads to four different quantities that are the building blocks of any quantity that can be measured in condensed matter physics. Those quantities are the energy, the momentum, the angular momentum and the charge of the system. Space-time symmetries (i.e. space-time translation and Lorentz invariance) lead to the following conservation laws:

$$\partial_\mu T^{\mu\nu} = 0 \tag{2.4}$$

and gamma matrices are four by four matrices. In particular, gamma matrices do not commute with fermionic fields but they do with electromagnetic fields.

*One may retrieve the standard form of Maxwell's equations by defining $(\phi/c, -A^x, -A^y, -A^z) \equiv A_\mu$, the magnetic induction $\mathbf{B} = \boldsymbol{\nabla} \times \mathbf{A}$ and the electric field $\mathbf{E} = -\boldsymbol{\nabla}\phi - \partial_t \mathbf{A}$.

Where $T^{\mu\nu}$ is Belinfante's energy-momentum tensor which is symmetric contrary to the canonical energy momentum tensor given by translation invariance only[14]. This immediately leads to another conservation law:

$$\partial_\mu M^{\mu\nu\eta} = 0 \tag{2.5}$$

Where $M^{\mu\nu\eta} = x^\nu T^{\mu\eta} - x^\eta T^{\mu\nu}$. An explicit expression of these tensors can be obtained from the Lagrangian density[11,14,16]:

$$T^{\mu\nu} = \frac{1}{\mu_0}\left(-F^{\mu\alpha}F^{\nu}{}_{\alpha} + \frac{1}{4}g^{\mu\nu}F_{\alpha\beta}F^{\alpha\beta}\right) + \frac{i\hbar c}{4}\bar{\psi}\left[\gamma^\mu D^\nu + \gamma^\nu D^\mu - \overleftarrow{D}^\nu\gamma^\mu - \overleftarrow{D}^\mu\gamma^\nu\right]\psi \tag{2.6}$$

Where $D^\mu = (\partial^\mu + iqA^\mu/\hbar)$, $\overleftarrow{D}^\mu = (\overleftarrow{\partial}^\mu - iqA^\mu/\hbar)$ and the left arrow indicates that the partial derivatives act on the Dirac conjugated fermionic field on the left. The local U(1) symmetry implies a global U(1) symmetry which leads to the following conservation law:

$$\partial_\mu J^\mu = 0 \tag{2.7}$$

Where $J^\mu = cq\bar{\psi}\gamma^\mu\psi$ is the charge four-current density. Taking the spatial integral of (2.4), (2.5) and (2.7) shows that the following quantities are conserved in time:

$$E \equiv \int T^{00}\mathrm{d}x^3 = \int\left[\frac{1}{2}\left(\varepsilon_0\mathbf{E}^2 + \frac{\mathbf{B}^2}{\mu_0}\right) + \psi^\dagger\left(i\hbar\partial_t - q\phi\right)\psi\right]\mathrm{d}x^3 \tag{2.8a}$$

$$p^i \equiv \int\frac{T^{0i}}{c}\mathrm{d}x^3 = \int\left[\frac{S^i}{c^2} + \frac{1}{2}\left(\psi^\dagger\left(-i\hbar\partial_i - qA^i\right)\psi - \psi^\dagger\left(-i\hbar\overleftarrow{\partial}_i + qA^i\right)\psi\right)\right]\mathrm{d}x^3 \tag{2.8b}$$

$$j^i \equiv \frac{\varepsilon_{ijk}}{2c}\int\left(x^jT^{0k} - x^kT^{0j}\right)\mathrm{d}x^3 = \mathbf{j}_{\mathrm{EM}} + \mathbf{j}_{\mathrm{e}} \tag{2.8c}$$

$$Q \equiv \int\frac{J^0}{c}\mathrm{d}x^3 = \int q\left|\psi\right|^2\mathrm{d}x^3 \tag{2.8d}$$

Where latin letters* can take values $1, 2$ and 3, $\mathbf{S} = (\mathbf{E}\times\mathbf{B})/\mu_0$ is Poynting's vector and ε_{ijk} is the totally antisymmetric tensor with $\varepsilon_{123} = 1$ which is used to transform the spatial part of the time independent and antisymmetric tensor $M^{\mu\nu} = \int\left(x^\mu T^{0\nu} - x^\nu T^{0\mu}\right)\mathrm{d}x^3$ into a spatial pseudo-vector†. One then recognizes the energy E, momentum p_i, angular momentum j_i and

*Whether latin letters are subscripts or superscripts does not matter in these expressions as they would in any non covariant equation.

†The time components of $M^{\mu\nu}$ are time independent but they explicitly depend on the time coordinate, thus they do not commute with the Hamiltonian as quantum operators[14]. They are associated with the conservation of the velocity of the center of mass.

charge Q of the system. $\mathbf{j}_{\text{EM}}$* and $\mathbf{j}_{\text{e}}$ are given by[18]:

$$\mathbf{j}_{\text{EM}} = \frac{1}{\mu_0 c^2}\int \mathbf{r}\times\left(E^i\boldsymbol{\nabla}A^i\right)\mathrm{d}x^3 + \frac{1}{\mu_0 c^2}\int \mathbf{E}\times\mathbf{A}\mathrm{d}x^3 \tag{2.9a}$$

$$\mathbf{j}_{\text{e}} = \frac{1}{2}\int \mathbf{r}\times\left(\psi^\dagger(-i\hbar\boldsymbol{\nabla}-q\mathbf{A})\psi - \psi^\dagger(-i\hbar\overleftarrow{\boldsymbol{\nabla}}+q\mathbf{A})\psi\right)\mathrm{d}x^3 + \frac{\hbar}{2}\int\psi^\dagger\overline{\boldsymbol{\sigma}}\psi\mathrm{d}x^3 \tag{2.9b}$$

Where $\mathbf{r}$ is the position vector and $\overline{\boldsymbol{\sigma}} = \boldsymbol{\sigma}\otimes\mathbf{I}_2$ is the four by four version of the Pauli matrices vector. One important conclusion can be drawn from equation (2.6) regarding the energy, momentum and angular momentum of the system. In the cases of a free electromagnetic field or non interacting electrons, equation (2.6) reduces to its first or second term respectively. Then, one can unambiguously define the energy, momentum and angular momentum of the electromagnetic field and the electrons. However, this is generally not true (because of the fact that D^μ depends on A^μ) and the only quantities that are conserved and that can thus be reasonably defined are the energy, momentum and angular momentum of the total system. Any attempt to separate, say, momentum from light and matter, would be devoted of any physical sense†. This is a well-known problem for energy conservation[20]. An electron being charged, it always generates an electromagnetic field. This field will in turn interact with the electron. If the total energy of the system is not considered, such as what is done in Poynting's theorem (conservation of energy of the electromagnetic field in the presence of charges, as derived from Maxwell equations only), divergences arise and one must artificially remove the electric field generated by electrons[20]. Still, we define the "angular momentum" of light as $\mathbf{j}_{\text{EM}}$ and the "angular momentum" of an electron as $\mathbf{j}_{\text{e}}$. The first term in each equation is the orbital angular momentum while the second term is the spin angular momentum, being independent on the choice of spatial origin. The electronic spin term arises from a term in T^{0i} which vanishes when it is integrated over all space, thus not appearing in the expression of p^i. Angular momentum is a flux of energy that rotates just as momentum is a flux of energy that goes in a straight line[18] as can be seen from equation (2.8). Thus, one can get angular momentum and momentum dynamics from the equations that govern energy dynamics, which is what is usually done. Analogously, magnetic moment is associated with a flux of charge that rotates. By definition (because this is what

*Note that the expression for $\mathbf{j}_{\text{EM}}$ is identical to the expression for the pseudo-angular momentum of phonons[17], which makes sense because both phonons and photons are vector fields and pseudo-angular momentum and angular momentum are identical in vacuum. Pseudo-angular momentum is introduced below.

†This is at the heart of the Abraham-Minkowski controversy at macroscopic scales. We will be confronted with a similar issue in chapter 5 but the Abraham-Minkowski controversy is beyond the scope of this thesis. The interested reader can find more information in reference 19.

couples with the magnetic field in the Hamiltonian) the magnetic moment $\mathbf{m}$ is given by:

$$\mathbf{m} = \frac{1}{2}\int (\mathbf{x} \times \mathbf{J}) \mathrm{d}x^3 \tag{2.10}$$

In order to progress, one decomposes the charge four-current density J^μ using the Gordon identity[18]. Because charge is the coupling between light and matter, one should use the Gordon identity in the presence of an electromagnetic field. We obtain for the spatial part:

$$\begin{aligned}\mathbf{J} = &\frac{q}{2m}\left(\overline{\psi}(-i\hbar\boldsymbol{\nabla} - q\mathbf{A})\psi - \overline{\psi}(-i\hbar\overleftarrow{\boldsymbol{\nabla}} + q\mathbf{A})\psi\right) \\ &+ \boldsymbol{\nabla} \times \left(\frac{q\hbar}{2m}\psi^\dagger\gamma^0\overline{\boldsymbol{\sigma}}\psi\right) + \frac{\partial}{\partial t}\left(\frac{-iq\hbar}{2mc}\psi^\dagger\boldsymbol{\gamma}\psi\right)\end{aligned} \tag{2.11}$$

Where $\boldsymbol{\gamma}$ is the vector formed by the spatial γ matrices. All three terms contribute to the magnetic moment. The first term is the charge current density in the presence of a vector potential, the second term is a magnetic dipole or spin current density and the last term is an electric dipole or polarization current density. Thus the first term of equation (2.11) produces orbital magnetic moment while the second one produces spin magnetic moment. The third term is negligible in the non-relativistic limit[18]. One then obtains:

$$\mathbf{m} = \frac{q}{4m}\int \mathbf{x} \times \left(\overline{\psi}(-i\hbar\boldsymbol{\nabla} - q\mathbf{A})\psi - \overline{\psi}(-i\hbar\overleftarrow{\boldsymbol{\nabla}} + q\mathbf{A})\psi\right)\mathrm{d}x^3 + \frac{q\hbar}{2m}\int \psi^\dagger\gamma^0\overline{\boldsymbol{\sigma}}\psi\mathrm{d}x^3 \tag{2.12}$$

Thus we obtain the well known relation*:

$$\hat{\mathbf{m}} = \frac{q}{2m}\hat{\mathbf{l}} + \frac{q}{m}\gamma^0\hat{\mathbf{s}} \tag{2.13}$$

Where an operator $\hat{o}$ associated with a quantity o is here defined as $o = \int \psi^\dagger\hat{o}\psi\mathrm{d}x^3$, $\mathbf{l}$ is the orbital part of $\mathbf{j}_\mathrm{e}$ while $\mathbf{s}$ is the spin part. This equation is valid for the specific separation of angular momentum between light and matter that we chose above but is always true for an isolated electron. Because the spin angular momentum does not depend on the frame of reference, it is conserved separately for free electrons and then the orbital angular momentum is also conserved separately†. Thus in this case, magnetic moment is also conserved. In the general interacting case, only the total angular momentum of the system is conserved and thus magnetic moment is not always conserved. Indeed, an electron can for instance exchange spin angular momentum with a magnetic field pulse. The electromagnetic field gains this angular momentum but no magnetic

*It is important to note that for electrons $q = -|e|$ where e is the electric charge, thus magnetic moment and angular momentum have opposite directions.

†A free electron actually has zero orbital angular momentum because it has a linear motion. In condensed matter, orbital angular momentum is not zero but it is not conserved in general because of, for instance, spin-orbit coupling.

moment because it has no charge. In the absence of an electromagnetic field, the expectation value of the electronic angular momentum and magnetic moment operators are proportional to each other via Landé's g-factor[21]. The γ^0 factor will change the sign of the antiparticle part of the fermionic field which is negligible at low energies.

The conservation laws are often written as[14]:

$$\left[\hat{H}, \hat{H}\right] = 0 \tag{2.14a}$$

$$\left[\hat{H}, \hat{p}^i\right] = 0 \tag{2.14b}$$

$$\left[\hat{H}, \hat{j}^i\right] = 0 \tag{2.14c}$$

$$\left[\hat{H}, \hat{Q}\right] = 0 \tag{2.14d}$$

Where $\hat{H}$ is the Hamiltonian of the system i.e. the quantum operator associated with the energy E and all the other quantities are the quantum operators associated with the other corresponding conserved quantities. The triviality of equation (2.14a) resides in the fact that $\exp(-i\hat{H}t/\hbar)$ is the time translation operator. This statement is equivalent to the general form of Schrödinger equation $i\hbar\dot{\phi} = \hat{H}\phi$ for a state ϕ in Schrödinger's picture. In order to take into account decoherence and dissipations in a system due to interactions with another large external system, one can generalize Schrödinger equation and describe the system with a density matrix $\hat{\rho}$ and the time evolution of the system is provided by Von Neumann equation[22]:

$$i\hbar\frac{\partial\hat{\rho}}{\partial t} = \left[\hat{H}, \hat{\rho}(t)\right] \tag{2.15}$$

We note that this equation is the most general equation describing the evolution of any system. The density matrix and the Hamiltonian must correspond to the complete universe in principle, meaning the system of interest plus all its surrounding, for light and matter in general. Using this equation plus the fact that the expectation value of any measurable quantity (such as the conserved ones above) described by a quantum operator $\hat{O}$ in Schrödinger's picture is $\mathrm{Tr}(\hat{\rho}(t)\hat{O})/\mathrm{Tr}(\hat{\rho}(t))$, one can obtain the (exact) quantum equivalent of equations (2.4), (2.5) and (2.7). These kind of equations are known as quantum kinetic equations while (2.4), (2.5) and (2.7) are classical. Direct second quantization of the fields allows to retrieve similar quantum kinetic equations from (2.4), (2.5) and (2.7) except that the formulation with a density matrix (which also requires second quantification) allows us to include mixed states in the mathematical formalism. In practice however, equation (2.15) is impossible to solve and one must resort to approximations.

2.2 Low energy limit

To proceed further, we first simplify the Hamiltonian. The theory presented so far is valid for high energies, which is not required in the context of this work[23]. In the low energy regime, particle number is conserved, meaning that the antiparticle part of the fermionic fields ψ is negligible[11,24,25]. Then, a Foldy-Wouthuysen transformation may be performed on the electronic part $i\hbar\partial_t - q\phi^*$ of the Hamiltonian to achieve this simplification[23,25–28]. In Coulomb gauge[11,29], the total Hamiltonian then takes the form:

$$\begin{aligned}\hat{H} = &\sum_i \frac{(\mathbf{p}_i - q\mathbf{A}(\mathbf{r}_i))^2}{2m} + \frac{1}{2}\sum_{i\neq j}\frac{q^2}{r_{ij}} - \sum_i \frac{q}{|q|}\frac{g\mu_B}{\hbar}\mathbf{s}_i\cdot\mathbf{B}(\mathbf{r}_i) + V \\ &- \sum_i \frac{q}{4m^2c^2}\mathbf{s}_i\cdot[\mathbf{E}(\mathbf{r}_i)\times(\mathbf{p}_i - q\mathbf{A}(\mathbf{r}_i)) - (\mathbf{p}_i - q\mathbf{A}(\mathbf{r}_i))\times\mathbf{E}(\mathbf{r}_i)] \\ &+ \int \frac{1}{2}\left(\varepsilon_0(\partial_t\mathbf{A})^2 + \frac{\mathbf{B}^2}{\mu_0}\right)\mathrm{d}x^3\end{aligned} \tag{2.16}$$

Where we included several electrons with position vectors $\mathbf{r}_i$ and momentum $\mathbf{p}_i = -i\hbar\boldsymbol{\nabla}_i$, $r_{ij} = |\mathbf{r}_i - \mathbf{r}_j|$ and $\mu_B = |e|\hbar/(2m)$ is Bohr magneton. The magnetic moment of the electron in the low energy approximation is now $-\mu_B(\mathbf{l}_i + g\mathbf{s}_i)/\hbar$ with $\mathbf{l}_i$ the usual orbital angular momentum operator, $\mathbf{s}_i = \hbar\boldsymbol{\sigma}_i/2$ the spin angular momentum operator and we take $g = 2$. This Hamiltonian is an operator that acts on many body electronic states that are now represented as spinors instead of bispinors. Second quantization is performed in a standard way[29,30] by defining single particle field operators as $\psi(\mathbf{r}) = \sum_\lambda c_\lambda\phi_\lambda(\mathbf{r})$ where c_λ are annihilation operators satisfying fermionic or bosonic commutation relations and $\phi_\lambda(\mathbf{r})$ are wave functions that form a complete basis indexed by λ. Single particle operators require a single field operator ($\int \psi(\mathbf{r}_i)^\dagger\hat{O}_1\psi(\mathbf{r}_i)\mathrm{d}\mathbf{r}_i$) while two particle operators need two field operators ($\int \psi(\mathbf{r}_i)^\dagger\psi(\mathbf{r}_j)^\dagger\hat{O}_2\psi(\mathbf{r}_j)\psi(\mathbf{r}_i)\mathrm{d}\mathbf{r}_i\mathrm{d}\mathbf{r}_j$). The integration in the last term of (2.16) remains because the electromagnetic field is not quantized. The first term is the usual kinetic energy in the presence of an electromagnetic field. In the case of a uniform external magnetic field, it gives the coupling between the magnetic field and orbital angular momentum as well as the diamagnetic energy. The second term is the Coulombian interaction that comes from the $(\boldsymbol{\nabla}\phi)^2$ term when expanding $\mathbf{E}^2 = (-\boldsymbol{\nabla}\phi - \partial_t\mathbf{A})^2$. The cross term disappears because of Coulomb gauge. Because the electric potential ϕ has been integrated out,

*The electronic Hamiltonian is $i\hbar\partial_t - q\phi$ and not $i\hbar\partial_t$, where the differentiation acts only on matter fields. The Coulomb interaction comes from the electromagnetic part upon use of the equation of motion (2.3). The other equation of motion (2.2) is used to transform $i\hbar\partial_t - q\phi$ which thus does not contain the electrostatic potential term. However, this does not affect the Foldy-Wouthuysen transformation procedure.

the Coulombian interaction depends on two particles while the original Dirac Hamiltonian only contains interactions with a single electron*. The third term is the Zeeman energy describing the coupling between any magnetic field with spin angular momentum. The fifth term is the spin-orbit coupling. We included the most general form such that the Hamiltonian is still hermitian[23,26–28], as it should. Note that $\mathbf{p}$ does not commute with the electric field such that both terms in the second line are indeed different. In particular, the second term of the spin-orbit coupling term includes a $\boldsymbol{\nabla} \times \mathbf{E}$ term where the differentiation only acts on the electric field and not on the wave function. We neglect other relativistic corrections. The last term is the energy of the electromagnetic field if it was free. When we write $\mathbf{E}$, $\mathbf{B}$ and $\mathbf{A}$, we always mean the total fields due to external radiation (transverse) and fields generated by matter (one may thus include uniform external fields). What has been discussed so far does not include nuclei. In condensed matter physics, nuclei are modeled as wave functions for bound states which carry mass, charge and spin. Here the effect of nuclei is included in the forth term V which includes kinetic energy of the nuclei, all possible Coulombian interactions between nuclei and electrons as well as any other possible interaction due to magnetic and electric multipoles nuclei may have.

The most important terms are Coulombian interactions which are responsible for many body effects[21,29,31–34]. It leads for instance to the exchange interaction between localized spins[21], spin dependent or independent electron-phonon coupling[31,35], electron-magnon coupling[29] as well as many other interactions involving various quasi-particles or collective modes. These interaction terms often rely themselves on approximations based on, for instance, the fact that nuclei masses are large compared to the electron mass (Born-Oppenheimer approximation) or that core electrons together with the nucleus may be considered as a bound state that has a localized spin, charge and mass. Another important many body effect in magnetism is the magnetic dipole interactions (between electrons, nuclei or atoms depending on the approximations) which comes into play when one intregrates out the magnetic field generated by magnetic dipoles[21,36]. We will come back to the role of these interactions in ultrafast magnetization dynamics in the next chapter.

We note however that the standard treatment in which these interactions appear relies on a Foldy-Wouthuysen transformation for time independent electromagnetic fields such as the one generated by a nucleus at rest. It is however possible to perform a Foldy-Wouthuysen transformation for time dependent electromagnetic fields[23,28] which significantly increases the complexity of the problem.

*This is why this term contains four creation/annihilation operators in second quantization while there are only two fields ψ in equation (2.8a).

Once one deals with low energy condensed matter systems with nuclei, and thus with a lattice of nuclei, there is another important concept that has been very recently highlighted. This is the concept of pseudo-conserved quantities, especially the already well-known pseudo-momentum and much more interesting in the discussions of this work, pseudo-angular momentum[17]. Conserved quantities result from a global invariance of the action (which can sometimes be translated into an invariance of the Lagrangian) or more concretely an invariance of the total system in all of time and space under a certain symmetry as explained above. Pseudo-conserved quantities on the other hand result from an invariance of the Lagrangian, that describes a part of the total system, under a field transformation. In the context of this work, the fields under considerations are usually phonons and magnons fields because of the presence of a lattice of charges and spins. The Lagrangian describing these fields is then invariant under certain translations and rotations of both those fields* but the Lagrangian of the total system is not in general. This is because the lattice itself is not affected by those transformations. The resulting pseudo-momentum and pseudo-angular momentum of phonons and magnons are not conserved but they are still the quantities that are mostly used in condensed matter physics. The reason for this is because one usually applies periodic boundary conditions, which prevents any non trivial rotation or translation of the lattice. These boundary conditions make physical sense because the studied samples in experiments are fixed to a sample holder. This means however that one should consider the sample holder, and everything connected to it, in order to take conservation of momentum and angular momentum into account[17]. Considering this much bigger system would considerably increase the complexity of the problem and cannot be solved. In this thesis, pseudo-conserved quantities are referred to as their corresponding conserved quantities to simplify discussions where this concept is not relevant.

2.3 Semiclassical and alternative approaches

The framework mentioned so far is still too complicated to be solved. The two main problems are (i) the fact that even an isolated system implies solving a many body problem but (ii) on top of this one needs to consider correlations with an external environment.

This may be treated using *ab initio* techniques such as Density Functional Theory (DFT) for ground state calculations or real time Time Dependent Density Functional Theory (rt-TDDFT)

*The case of rotation invariance in lattices is mostly useful in cases where the material can be considered as isotropic or when one focuses only on long wavelength excitations.

more generally. As already mentioned, the computational cost does not allow to model systems on long time and spatial scales even though some serious progress have been made in this direction[37]. A simple and common framework to study large systems on a long timescale is the semiclassical approach. Here, one uses the postulate of random phases where the density matrix $\hat{\rho}$ is assumed to be diagonal[38,39]. This can be justified from quantum field theory[40]. This postulate introduces decoherence which eventually leads to the H-theorem and so the second principle of thermodynamics[40,41]. The resulting conservation laws contain distribution functions that describe correctly fermions and bosons at equilibrium and interactions are considered as quantum transitions rates. The latter are often computed using Fermi's golden rule which neglects memory effects (Markov approximation) and assumes conservation of energy (secular approximation), which contradicts the time-energy uncertainty relation. A major drawback of this approach is that the conservation laws* are only valid close to equilibrium, when the distribution functions are close enough to Fermi-Dirac or Bose-Einstein distributions for fermions and bosons respectively. This approach is used in this thesis and some more details will be provided in chapters 3 and 5.

The semiclassical approximations can however be relaxed to consider more quantum effects and non-equilibrium conditions[15,42,43]. No matter which approximation is used, one still wants to solve a many body problem meaning that the computation of any correlation function (including any expectation value or response function such as a conductivity) involves the computation of correlation functions of higher order, a problem known as the Bogoliubov–Born–Green–Kirkwood–Yvon hierarchy[38]. The problem is made even harder in the study of non-equilibrium induced by pulsed stimuli because even more correlations need to be considered in order to take into account permanent interactions on top of transient ones[29,44]. In the restricted context of Keldysh formalism[42,44], this can be seen from the fluctuation dissipation theorem, only valid in thermal equilibrium, which provides an equation relating fluctuations (related to the distribution function of the semiclassical theory[15]) to dissipations (related to retarded and advanced Green's functions). Out of equilibrium this relation is no longer true and one needs a more general relation instead in order to obtain a closed system of equations.

Finally, we note that there is another class of models that are commonly used in magnetism. Those are thermodynamic models based on the minimization of energy† or more commonly minimization of free energy when temperature is fixed. In all models considered in ultrafast magnetization dynamics, the system is always assumed to be in thermal equilibrium before it

*Or more generally Boltzmann's equation from which the conservation laws can be obtained[38].

†Minimization of energy **at constant entropy** is obtained from conservation of energy when the second principle of thermodynamics is verified.

interacts with any external stimuli and thus its energy is minimized. Which approximation should be used to find a model that: (i) contains all the required ingredients to describe a physical situation and (ii) is solvable, is the main challenge of the current study of ultrafast magnetism.

2.4 Macroscopic Maxwell equations and magnetization

Magnetization appears in the context of condensed matter physics when one tries to derive Maxwell's equations for a macroscopic material system. They are obtained from a careful averaging procedure[45]. They read:

$$\boldsymbol{\nabla}\cdot\mathbf{D} = \rho_f \tag{2.17a}$$

$$\boldsymbol{\nabla}\cdot\mathbf{B} = 0 \tag{2.17b}$$

$$\boldsymbol{\nabla}\times\mathbf{E} = -\partial_t\mathbf{B} \tag{2.17c}$$

$$\boldsymbol{\nabla}\times\mathbf{H} = \mathbf{J}_f + \partial_t\mathbf{D} \tag{2.17d}$$

$$\mathbf{D} = \varepsilon_0\mathbf{E} + \mathbf{P} \tag{2.17e}$$

$$\mathbf{H} = \mathbf{B}/\mu_0 - \mathbf{M} \tag{2.17f}$$

These equations are only valid for a macroscopic medium at rest and all fields are understood to be macroscopic fields resulting from the averaging of the microscopic ones satisfying equation (2.3). The last two equations define $\mathbf{D}$ and $\mathbf{H}$ and equations (2.17b) and (2.17c) are identical to two of the microscopic Maxwell's equations. Here, ρ_f and $\mathbf{J}_f$ are the charge and current densities generated by free charges*. $\mathbf{P}$ and $\mathbf{M}$ are the polarization and magnetization which arise from electric and magnetic dipoles† generated by bound charges, respectively. Higher multipole moments contribute to the electric displacement field $\mathbf{D}$ and magnetic field $\mathbf{H}$ but they are usually neglected. The total current density in the framework of equation (2.17) is given by:

$$\mathbf{J} = \mathbf{J}_f + \boldsymbol{\nabla}\times\mathbf{M} + \partial_t\mathbf{P} \tag{2.18}$$

*The right hand side of equation (2.17a) should also contain the charge density coming from the total charge of free bound states such as ions or charged impurities[45]. The same is true for $\mathbf{J}_f$. The individual charges of the constituents of those bound states are considered to define $\mathbf{D}$ and $\mathbf{H}$.

†The derivation presented by Jackson[45] does not include spin but it can be directly generalized by using the current density from equation (2.11), without the electric dipole term, instead of the standard charge current density $\mathbf{J} = \frac{q}{2m}(\overline{\psi}(-i\hbar\boldsymbol{\nabla} - q\mathbf{A})\psi - \overline{\psi}(-i\hbar\overleftarrow{\boldsymbol{\nabla}} + q\mathbf{A})\psi)$.

This current density should be introduced in the definition (2.10) to obtain the magnetic moment. As explained by Landau and Lifshitz[46], magnetization can be understood as magnetic moment per unit volume $\mathbf{m} = \int \mathbf{M} \mathrm{d}x^3$ only if $\mathbf{J} = \boldsymbol{\nabla} \times \mathbf{M}$. Free charges having linear motion, the latter equality is verified if the $\partial_t \mathbf{P}$ term can be neglected*. Landau and Lifshitz[46] show this is no longer the case when the considered electromagnetic fields have optical wavelengths or lower. In this case, one should set the magnetic permeability $\boldsymbol{\mu}$ defined by $\mathbf{B}(\mathbf{x}, \omega) = \boldsymbol{\mu}(\omega)\mathbf{H}(\mathbf{x}, \omega)$† to μ_0. This means that at sufficiently high electromagnetic energies, the charges contributing to $\mathbf{M}$ (at low energies) cannot be considered as bound charges anymore and magnetization is then ill-defined. Thus $\mathbf{B}$ and $\mu_0\mathbf{H}$ are essentially the same quantity. The same remarks hold for the electric counterpart of the electromagnetic field except that the electric permittivity $\boldsymbol{\varepsilon}$ defined by $\mathbf{D}(\mathbf{x}, \omega) = \boldsymbol{\varepsilon}(\omega)\mathbf{E}(\mathbf{x}, \omega)$ is equal to ε_0 when electromagnetic wavelengths are much smaller than atomic dimensions. Thus, for light with optical wavelengths, it is sufficient to know the electric permittivity of the medium to calculate how light will propagate inside this medium. This is the approach used in section 5.1.

One should be aware that this approach is mostly suited to calculate the dynamics of electromagnetic fields in a medium. It is generally not possible to rigorously infer the behavior of matter under the influence of an electromagnetic field in this framework. Also, in the field of ultrafast magnetization dynamics, the quantity of interest is the magnetic moment per unit volume, which includes the magnetic moment of free charges. However, it is still referred to as magnetization.

2.5 Conclusion

In this introductory chapter, we showed how the general conservation laws of condensed matter physics naturally emerge from symmetries encoded in a Lagrangian. In particular, using Belinfante's tensor which includes Lorentz invariance on top of space-time translations (which only leads to the standard stress-energy tensor) we show how spin angular momentum of the

*When considering spin, the spin current term in equation 2.11 will be contained in $\mathbf{J}_f$ and also needs to be negligible. It is usually not included/discussed in classical electrodynamics. However, this spin current has the form $\boldsymbol{\nabla} \times \mathbf{f}$ so one may redefine magnetization as $\mathbf{M} := \mathbf{M} + \mathbf{f}$ and keep the same equations. In the low energy limit, $\mathbf{f} = (q\hbar)/(2m)\psi^\dagger \boldsymbol{\sigma} \psi$ and so the newly defined magnetization contains magnetization due to bound states (whenever this qualification makes sense) as well as free charges.

†This formula does not consider any potential spatial dispersion. Also, we assumed time homogeneity $\mu(t, t') = \mu(t - t')$ and took the Fourier transform with respect to time.

electron appears in the theory. Going to the low energy regime permits to retrieve the usual Hamiltonian of solid state physics which should also contain the energy of the electromagnetic field in order to satisfy energy conservation in the most general case. General methods to find approximate solutions to the many body and out of equilibrium problem that we are interested in were introduced. Finally, because the main quantity of interest, in this thesis and the related experiments, is magnetization, we introduced it from the framework of the macroscopic Maxwell's equations. We reviewed, in particular, the condition under which magnetization can be seen as the density of magnetic moment.

Chapter 3

State of the Art

The previous chapter laid the ground to understand the different approaches used to understand the main topic of this work: ultrafast magnetization dynamics. Ultrafast processes are always generated using ultrashort stimuli and the most common one is an ultrashort laser pulse. Thus, we first start this chapter by reviewing some basic material regarding the response of metals to ultrashort laser pulses. In particular, this will introduce the 2TM which is the simplest model required to understand non equilibrium processes induced by a laser pulse. Then, we move on to the study of magnetic materials. First we review the basic theories of magnetism, various means to trigger magnetization motion and provide a general point of view of transport equations when it includes spin. The next section focuses on the laser pulse induced ultrafast demagnetization and the conservation of angular momentum in such processes. Finally, we discuss the various ways one can completely reverse magnetization using laser pulses. This last part includes AO-HDS, AO-HIS as well as more exotic means.

3.1 Laser induced out of equilibrium dynamics in metals

In metals, optical electromagnetic radiation mostly interacts with electrons. Thus, it is possible that a sufficiently short electromagnetic pulse may transfer its energy to the electronic system before much of that energy is transferred to the lattice. As a consequence, the temperature reached by the electrons might be significantly higher than the lattice or phonon temperature. The relaxation between electrons and phonons was first considered by Kaganov *et al.*[47] and the 2TM in the case of laser pulse excitations was first used by Anisimov *et al.*[48]. The idea of such a

model is essentially based on the time component of equation (2.4), i.e. conservation of energy, where one separates the energy of electrons and phonons, and assuming that the laser pulse only acts as an energy source term:

$$\frac{\partial u_\mathrm{e}}{\partial t} + \boldsymbol{\nabla} \cdot \mathbf{J}_\mathrm{e} = \left(\frac{\partial u_\mathrm{e}}{\partial t}\right)_{\text{e-p}} + \left(\frac{\partial u_\mathrm{e}}{\partial t}\right)_{\text{e-photon}} \tag{3.1a}$$

$$\frac{\partial u_\mathrm{p}}{\partial t} + \boldsymbol{\nabla} \cdot \mathbf{J}_\mathrm{p} = -\left(\frac{\partial u_\mathrm{e}}{\partial t}\right)_{\text{e-p}} \tag{3.1b}$$

Where u refers to energy density, $\mathbf{J}$ refers to a heat current density and "e" and "p" refer to electrons and phonons respectively. Note that summing both equations and neglecting the electromagnetic source term, one retrieves conservation of the total energy $E = E_\mathrm{e} + E_\mathrm{p}$. At this stage, equations (3.1) are still rather general, even considering quantum effects, but they are not valid too far from equilibrium, being equivalent to what one obtains from Boltzmann equation[38,49,50] if it is not coupled to other equations for other correlation functions[15,29,42–44]. In principle, these equations (3.1) are also coupled to the other conservation equations and thus one performs various approximations to end up with only two equations. This leads to several variants of the 2TM[49] which can for instance take into account deviations from Fourier's law. The traditional approximations, used later in this work are the following:

- The electronic bath is assumed to be at equilibrium at all times due to the efficiency of electron-electron scattering and can then be described by a temperature T_e satisfying $\dfrac{\partial u_\mathrm{e}}{\partial T_\mathrm{e}} = C_\mathrm{e}$ where C_e is the electronic heat capacity and Sommerfeld's model[51] is assumed to be correct, meaning that $C_\mathrm{e} = \gamma T_\mathrm{e}$.

- Similarly, phonons are assumed to always be at equilibrium and described by a temperature T_p satisfying $\dfrac{\partial u_\mathrm{p}}{\partial T_\mathrm{p}} = C_\mathrm{p}$ where C_p is the phonon heat capacity.

- The heat current density for electrons is evaluated using a generalized Fourier's law[50] $\mathbf{J}_\mathrm{e} = -\kappa_\mathrm{e}\dfrac{T_\mathrm{e}}{T_\mathrm{p}}\boldsymbol{\nabla} T_\mathrm{e}$ where κ_e is the electronic heat conductivity measured at equilibrium (when $T_\mathrm{e} = T_\mathrm{p}$).

- Phonons heat conductivity is given by Fourier's law $\mathbf{J}_\mathrm{p} = -\kappa_\mathrm{p}\boldsymbol{\nabla} T_\mathrm{p}$ where κ_p is the phononic heat conductivity.

- The electron-phonon scattering term is evaluated using Fermi's Golden rule[52], or more precisely application of Markov and the secular approximations (i.e. neglecting memory

effects and having conservation of energy; see references 22, 39 for more details) in either an equation of motion[53], a density matrix[39] or Green's function[29] technique for the electron-phonon interaction in metals. In the case where temperatures are larger than Debye's temperature, this term takes the form $-g_{\text{e-p}}(T_{\text{e}}-T_{\text{p}})$ where $g_{\text{e-p}}$ is the electron-phonon coupling constant which is assumed to be constant.

- One often studies thin film samples, thus equation (3.1) is usually solved in one dimension.

- The electromagnetic source term is usually assumed to be a simple gaussian function in time such that its amplitude corresponds to a certain energy density and its full width at half maximum corresponds to the pulse duration. On top of this, one can multiply this function by an absorption profile in order to consider spatial dependence of the source term. This absorption profile is calculated using the Transfer Matrix Method (TMM)[54] for multilayer structures. This method of calculating the source term is also based on several approximations. These will be discussed and relaxed in chapter 5.

The temperature dependence of the electron-phonon coupling and electronic heat capacities and conductivities have also been computed form *ab initio* calculations[55]. Similar calculations have also been carried out for magnetic materials[56]. Equation (3.1) contains, in principle, the energy of non thermal electrons that have directly interacted with the external electromagnetic field[57]. One cannot define a temperature for such electrons but they will exchange energy with the "thermal" electrons that have not been excited by the external field, and with phonons. It is possible to extend the 2TM to consider these non-thermal electrons by including a non-thermal distribution of electrons and considering the electron-electron interaction in simplified models[58–61]. Also, it has been realized that the phonon bath may not be at equilibrium before tens of picoseconds. It is then possible to further improve the 2TM by including temperature for several phonon subsystems each having a different wavelength and possibly belonging to different branches[62,63]. However, the 2TM still proved to be in very good agreement with time dependent reflectivity measurements in noble metals[64,65] and it can still provide qualitative insights for other materials. Nevertheless, we note that the 2TM may drastically overestimate (in terms of speed and temperature change) the electron temperature dynamics in metals such as Co and Fe[63]. The phonon temperature given by the 2TM, however, is in very good agreement with the average of the various phonon temperatures.

Finally, one notes that the assumptions above include a diffusive transport of heat. At the sub-picosecond timescale and in thin films however, the theory of diffusion is no longer correct because durations and distances may be shorter than the relaxation time and mean free path

respectively. Thus, at very short timescale, particles may move without colliding with other particles and the transport is said to be ballistic. One can easily incorporate ballistic transport of electrons in the 2TM in thin films by modifying the penetration depth of the electromagnetic source term[65,66]. This method is no longer realizable in multilayer structures because the absorption profile is not simply given as a Beer-Lambert law. At longer timescales, the transport will progressively become diffusive. In between, the transport is said to be superdiffusive[67]. These notions of transport apply to any conserved quantity but the corresponding characteristic scales may differ.

3.2 Standard magnetization dynamics

Before tackling magnetization dynamics, we briefly review the main theories that can explain the formation of magnetic order. In general, magnetic order appears due to the Coulomb interaction between electrons and may thus be accurately predicted with *ab initio* techniques. One can however provide more details about the origin of magnetism by considering simpler problems. First, we note that the existence of **any response of a material to an external magnetic field at a macroscopic scale** is a purely quantum effect as shown by Bohr-van Leeuwen theorem[21]. From a microscopic point of view, quantum mechanics is involved in **magnetic ordering** because of the many body nature of the problem. Because electrons are indistinguishable from one another, the total wave function of the system must be antisymmetric with respect to interchange of two particles for fermions (and symmetric for bosons). This leads on the one hand to the Pauli exclusion principle for fermions and to the existence of exchange integrals on the other hand. Those two facts will lead to spin dependent effects, even though Coulomb interaction does not depend on spin, and eventually to spontaneous magnetization at a given temperature if the material satisfies other conditions such as a suitable band structure or sufficiently high exchange integrals.

Exchange integrals are important to understand magnetism in materials where spin angular momentum* mostly comes from localized orbitals such as rare-earth atoms. In this case, the

*The contribution of orbital angular momentum to magnetization is sometimes negligible as it is quenched by the so called crystal-field[68] (see also reference 69). This is what is assumed in most of the works mentioned in this thesis and thus we shall use $\hat{\mathbf{m}} = -\frac{\mu_B}{\hbar} g\hat{\mathbf{s}}$ with $g = 2$ and where $\mu_B = \frac{e\hbar}{2m}$ is Bohr magneton. Orbital angular momentum plays an important role in the magnetization dynamics of materials containing rare earth elements such as terbium.

relevant part of the Hamiltonian to describe magnetism is the Heisenberg Hamiltonian[21]:

$$\begin{aligned}\hat{H} = -\sum_{i\neq j} J_{ij}\mathbf{S}_i \cdot \mathbf{S}_j &= -\sum_{i\neq j} J_{ij}\left(S_i^x S_j^x + S_i^y S_j^y + S_i^z S_j^z\right) \\ &= -\sum_{i\neq j} J_{ij}\left[\frac{1}{2}\left(S_i^+ S_j^- + S_i^- S_j^+\right) + S_i^z S_j^z\right]\end{aligned} \tag{3.2}$$

Where J_{ij} are the exchange integrals[21,70*], $\mathbf{S}_i$ is the spin operator, representing atomic spin, at lattice site i verifying the usual angular momentum commutation relations and $S_i^{\pm} = S_i^x \pm iS_i^y$. One can obtain this Hamiltonian for localized single particle wave functions having a spin of one half and extend it to any value S of spin thanks to Wigner-Eckart theorem. This Hamiltonian can be used to model ferromagnetism (one spin lattice or several spin sublattices with the same direction), antiferromagnetism (two equivalent spin sublattices with opposite direction) and ferrimagnetism (two different spin sublattices with opposite direction) depending on the values of the individual J_{ij}. Considering spins greater than one half is a simplification in the sense that one does not have to consider all the individual electrons that contribute to this localized spin in the Hamiltonian. However, because angular momentum commutation relations are different from fermionic or bosonic commutation relations, the usual techniques of second quantization cannot be applied. One usually resorts to the Holstein-Primakoff transformation which is at the basis of the theory of spin waves[21]:

$$S_i^z = \hbar(S - a_i^\dagger a_i) \tag{3.3a}$$

$$S_i^+ = \hbar\sqrt{2S - a_i^\dagger a_i}\, a_i \tag{3.3b}$$

$$S_i^- = \hbar a_i^\dagger \sqrt{2S - a_i^\dagger a_i} \tag{3.3c}$$

Where a_i is a bosonic annihilation operator. However, this transformation is usually performed together with a Taylor expansion of the square root which is valid either for very small deviation of spins (suitable at small temperatures) or for large values of spins. The Dyson-Maléev transformation avoids this issue but the resulting Hamiltonian is no longer hermitian[21]. A transformation that avoids all these issues is the Schwinger bosons transformation[71]:

$$S_i^z = \frac{\hbar}{2}(a_i^\dagger a_i - b_i^\dagger b_i) \tag{3.4a}$$

$$S_i^+ = \hbar\, a_i^\dagger b_i \tag{3.4b}$$

*Or numbers that depend on these exchange integrals in certain models such as Heitler-London model.

$$S_i^- = \hbar\, b_i^\dagger a_i \tag{3.4c}$$

$$2S = a_i^\dagger a_i + b_i^\dagger b_i \tag{3.4d}$$

Where a_i and b_i are two bosonic annihilation operators. They may be seen as operators that control the number of electrons with spin projection $+1/2$ (for a_i) and $-1/2$ (for b_i) on site i. The number operators $a_i^\dagger a_i$ and $b_i^\dagger b_i$ provide the number of electrons with spin $+1/2$ and $-1/2$ respectively. The sum of this two numbers should of course be equal to $2S$. This transformation is very close to the natural form of the exchange interaction between two spins with $S = 1/2$[21,29] which is still of the form (3.2) with:

$$S_i^z = \frac{\hbar}{2}\, c_{is}^\dagger \sigma_{ss'}^z c_{is'} = \frac{\hbar}{2}(c_{i\uparrow}^\dagger c_{i\uparrow} - c_{i\downarrow}^\dagger c_{i\downarrow}) \tag{3.5a}$$

$$S_i^+ = \frac{\hbar}{2}\, c_{is}^\dagger \sigma_{ss'}^+ c_{is'} = \hbar\, c_{i\uparrow}^\dagger c_{i\downarrow} \tag{3.5b}$$

$$S_i^- = \frac{\hbar}{2}\, c_{is}^\dagger \sigma_{ss'}^- c_{is'} = \hbar\, c_{i\downarrow}^\dagger c_{i\uparrow} \tag{3.5c}$$

Where c_{is} is the usual fermionic annihilation operator for an electron at site i and spin projection s. We defined $\sigma^\pm = \sigma^x \pm i\sigma^y$. Even though the Hamiltonian provided by equation (3.2) is a great simplification, it is still not exactly solvable. There are two important type of approximation that can be performed to this model. First is the molecular field approximation, or Weiss model[21]. In this framework, one neglects all fluctuations of the spin operators i.e. $\Delta S^\nu = \sqrt{\langle (S^\nu - \langle S^\nu \rangle)^2 \rangle} = 0$ where ν can be z, $+$ or $-$. For instance for ferromagnets, the Hamiltonian takes the form (up to a certain temperature dependent c-number)[21*]:

$$\hat{H} = -2J \langle S^z \rangle \sum_i S_i^z \tag{3.6}$$

Where one assumes that all lattice sites are equivalent i.e. $\langle S^z \rangle = \langle S_i^z \rangle$ and $J \equiv J_i \equiv \sum_i J_{ij}$ and the average is understood to be the quantum thermal average at a temperature T given by $\langle \hat{O} \rangle = \mathrm{Tr}(\hat{\rho}\hat{O})/\mathrm{Tr}(\hat{\rho})$. The canonical ensemble density matrix is given by its element $\rho_{mn} = \delta_{mn} e^{-\beta E_n}$ with $\beta = 1/(k_B T)$ and E_n is the eigenvalue of $\hat{H}$ in a quantum level n[38]. This Hamiltonian describes a system of spins in an effective magnetic (molecular) field of magnitude $B_m = 2J\hbar \langle S^z \rangle / (g\mu_B)$ and the corresponding magnetization is given by the solution of the following self-consistent equation:

$$M(T) = -ng\frac{\mu_B}{\hbar} \langle S^z \rangle = M(T=0) \mathrm{B}_S \left(\beta g \mu_B S B_m\right) \tag{3.7}$$

*One sometimes writes the Hamiltonian $\hat{H} = \Delta \sum_i S_i^z$ where Δ is the exchange splitting (with the dimension of an energy) and $S_i^z := S_i^z/\hbar$

And $M(T=0) = -ng\mu_B S$ is the magnetization at zero Kelvin, n is the number density and B_S is Brillouin function*. The magnetization vanishes at the Curie temperature $T_c = 2\hbar^2 JS(S+1)/(3k_B)$. Because this model neglects fluctuations, the only way energy (and thus magnetization) can be modified is by individually changing the spin projection ("flipping" a spin) of each atomic spin. Fluctuations actually allow excitations of much lower energies that are therefore important at low temperature. These excitations, known as spin waves, can be seen as a quantum superposition of states where a single atom has a spin flipped, for all atoms of the lattice and with a certain phase difference between each state†. The method known as Tyablikov decoupling allows one to consider spin waves on top of spin flips and thus is suitable for a description of ferromagnetism at low temperatures ($T \sim 0$ Kelvin) as well as high temperature (around T_c and above)[21,72]. In this approximation, the system magnetization is given by:

$$M(T) = -ng\mu_B \frac{(S-n(T))(1+n(T))^{2S+1} + (1+S+n(T))n(T)^{2S+1}}{(1+n(T))^{2S+1} - n(T)^{2S+1}} \tag{3.8a}$$

$$n(T) = \frac{1}{N}\sum_{\mathbf{k}} \frac{1}{e^{\beta E(\mathbf{k})} - 1} \tag{3.8b}$$

$$E(\mathbf{k}) = 2\hbar \langle S^z \rangle (J - J(\mathbf{k})) \tag{3.8c}$$

Where $J(\mathbf{k}) = (1/N)\sum_{i\neq j} J_{ij} \exp(i\mathbf{k}\cdot(\mathbf{r}_i - \mathbf{r}_j))$, $n(T)$ is the number of excited spin waves at temperature T and $E(\mathbf{k})$ is the energy of spin waves with wavevector $\mathbf{k}$. The Heisenberg Hamiltonian can also be used to model exchange interaction between conduction electrons and localized spins (such as impurities or rare-earth spins)[21,29,70]. These models are known as sp-d[73], s-d[29,70] or s-f[21] models, dependending on the bands the electrons that carry the different spins belong to. In the case of a single conduction band, the Hamiltonian is‡:

$$\hat{H} = -J\sum_i \mathbf{s}_i \cdot \mathbf{S}_i \tag{3.9}$$

Where $\mathbf{s}_i$ is the conduction electron spin operator given by equation (3.5). Contrary to the Heisenberg Hamiltonian, the exchange of angular momentum is local (i.e. it happens on a lattice site and not between different lattice sites) even though the origin of these two Hamiltonians

*$\mathrm{B}_S(x) = \frac{2S+1}{2S}\coth\left(\frac{2S+1}{2S}x\right) - \frac{1}{2S}\coth\left(\frac{x}{2S}\right)$.

†For instance, a single magnon state with wave vector $\mathbf{k}$, the quantum of spin waves, is $|\mathbf{k}\rangle = \frac{1}{\hbar\sqrt{2SN}}\sum_i e^{-i\mathbf{k}\cdot\mathbf{r}_i} S_i^- |0\rangle$ where N is the number of lattice sites, $\mathbf{r}_i$ is the position vector of lattice site i and $|0\rangle$ is the state with all spins parallel. $e^{-i\mathbf{k}\cdot\mathbf{r}_i}$ is the phase factor at site i and $S_i^- |0\rangle$ is the state where the spin projection number at site i is reduced by one unit.

‡This form of the Hamiltonian is actually based on the assumption that the exchange integrals in wave vector space can be approximated by $J_{i\mathbf{k}\mathbf{k}'} \simeq J\exp(i(\mathbf{k}-\mathbf{k}')\cdot\mathbf{r}_i)/N$[70].

is fundamentally the same i.e. the presence of exchange integrals due to Coulomb interaction. This model can be used to model interactions between electrons and magnons in the system of localized spins. These type of models are still sometimes crude approximations of the complete Hamiltonian because they consider that the localized electrons belong to a band which is well below the Fermi level or in general in a band that is completely separated from the "local" spin band (i.e. no hybridization is allowed)[70]. Those electrons are then fully polarized* and usually described by an Heisenberg Hamiltonian. This is of course not realistic for magnetic materials such as transition metals. The Hamiltonian (3.9) predicts an indirect exchange between different localized spins $\mathbf{S}_i$ known as Ruderman-Kittel-Kasuya-Yoshida (RKKY) coupling[21]. A localized spin can indeed transfer some angular momentum to conduction electrons which can then transfer it back to another localized spin. It is then an effect of second order in the interaction and can be calculated using time independent perturbation theory at the second order. It is then shown that the computed energy corrections are identical to the ones one would obtain from a first order perturbation theory starting from an Heisenberg Hamiltonian if the exchange parameter is given by†:

$$J_{ij}^{\mathrm{RKKY}} = \frac{J^2 k_F^6}{\varepsilon_F} \frac{\hbar^2}{(2\pi)^3 n^2} F(2k_F R_{ij}) \tag{3.10}$$

Where k_F and ε_F are the Fermi wave vector and energy respectively, n is the localized spin density, R_{ij} is the distance between localized spins i and j and the function F is given by $F(x) = (\sin(x) - x\cos(x))/x^4$. This interaction has then the remarkable property that it changes sign as the distance between localized spins vary.

In the case of transition metals, where the electrons that contribute to magnetism are less localized, typically of d character (hybridized with sp bands), one usually use another approximation which is Hubbard model. The general form of this model is derived from the following Hamiltonian that considers only on-site Coulomb interaction for electrons on a static lattice[21,29]:

$$\hat{H} = \sum_{ij;\mu\nu;s} T_{ij\mu\nu} c_{i\mu s}^{\dagger} c_{j\nu s} + \frac{1}{2} \sum_{i;\mu\nu\mu'\nu';ss'} U_{\mu\nu\mu'\nu'} c_{i\mu s}^{\dagger} c_{i\nu s'}^{\dagger} c_{i\nu' s'} c_{i\mu' s} \tag{3.11}$$

Where $T_{ij\mu\nu}$ are the hopping matrix elements and $U_{\mu\nu\mu'\nu'}$ are the coulombian matrix elements for electrons on different orbitals μ, ν, μ' and ν'. The standard Hubbard model only keeps the largest of these matrix elements $U_{\mu\nu\mu\nu}$ which corresponds to the standard coulombian repulsion. Interestingly, the exchange integral $U_{\mu\nu\nu\mu}$ is usually neglected and is not required for magnetic

*The spin quantum number S of this electronic band is fixed but not the projection m_S.

†This specific form the RKKY coupling is only true at zero Kelvin and for parabolic electronic dispersion relations[21].

ordering. In many cases, one also focuses on the single s band:

$$\hat{H} = \sum_{ij;s} T_{ij} c_{is}^{\dagger} c_{js} + \frac{U}{2} \sum_{i;s} n_{is} n_{i\bar{s}} \tag{3.12}$$

Where $\bar{s}$ denotes the spin projection opposite to s and $n_{is} = c_{is}^{\dagger} c_{is}$. This Hamiltonian cannot be solved exactly in general and thus one resorts to approximations similarly to what is done with Heisenberg model. First one can make a mean field approximation, known as Stoner model, which neglects fluctuations in the number operators n_{is}. In wave vector space, this takes the form (up to a temperature dependent c-number)[21]:

$$\hat{H} = \sum_{\mathbf{k};s} (E(\mathbf{k}) + U\bar{n}_{\bar{s}}) c_{\mathbf{k}s}^{\dagger} c_{\mathbf{k}s} \tag{3.13}$$

Where $\bar{n}_s$ is the average number of electron with spin projection s on a lattice site and $E(\mathbf{k})$ is the energy of the tight-binding part of the Hubbard Hamiltonian. Similarly to Weiss model, magnetism in Stoner model is due to an effective field of magnitude $U\bar{n}_{\bar{s}}/\mu_B$ that splits both bands of up and down spin. The exchange splitting is $\Delta = U(n_{\uparrow} - n_{\downarrow}) = Um$ where m is the electronic polarization related to magnetization by $M = -\mu_B m$. Noting that both m and the electronic density $\bar{n}$ depend on the exchange splitting, one realizes that the electronic polarization is given by the following self consistent equation:

$$m(T, \bar{n}) = \sinh\left(\frac{\beta U m}{2}\right) \int_{-\infty}^{\infty} \frac{D(E)}{\cosh\left(\beta\left(E + \frac{1}{2}U\bar{n} - \mu\right)\right) + \cosh\left(\frac{1}{2}\beta U m\right)} \mathrm{d}E \tag{3.14}$$

Where μ is the system chemical potential and D is the function giving the density of state in the absence of exchange splitting. The simplest approximation beyond the mean field approximation, which then considers fluctuations of the wave vector dependent electronic polarization $m(q) = \sum_{\mathbf{k}} c_{\mathbf{k}+\mathbf{q}\uparrow}^{\dagger} c_{\mathbf{k}\uparrow} - c_{\mathbf{k}+\mathbf{q}\downarrow}^{\dagger} c_{\mathbf{k}\downarrow}$ is the random phase approximation (RPA)[29,74]. One then looks at the spin susceptibility $\chi_s(q, \omega)$, which is roughly speaking a certain correlation function $\langle m(q,t) m(-q,0) \rangle$ and takes the well-known form:

$$\chi_s(q, \omega) = \frac{\chi_0(q, \omega; \Delta)}{1 - U\chi_0(q, \omega; \Delta)} \tag{3.15}$$

Where $\chi_0(q, \omega; \Delta)$ is the Pauli spin susceptibility. For certain values of the Pauli spin susceptibility, the spin susceptibility may diverge. The specific value of frequency and wave vector where this happens gives the allowed magnetic excitations of the system. Ferromagnetism exists when the infinite wavelength $q = 0, \omega = 0$ mode exists. In this case, one finds that the spin susceptibility diverges if the equality of Stoner criterion $D(E_F)U \geq 1$ is verified, where E_F

is the Fermi level. The divergence for $q \neq 0, \omega \neq 0$ give the excitations which can be divided into two general categories at sufficiently high wavelength, when the dispersion relations of both kinds are well separated. First, one has Stoner excitations, already considered by Stoner model, corresponding to a spin flip of an electron, possibly accompanied with a change of its wave vector. Second, one has what are also usually called magnons[74] and which are modes that are characterized by a gapless dispersion relation for an Hamiltonian without anisotropy. Those are the excitations which are neglected by Stoner model. Because they have a gapless dispersion relation, they usually have a much lower energy than Stoner excitations (at least for excitations with a small wave vector) and therefore may be preferred excitations*. This is similar to what one has in Heisenberg model. In fact, in the case of a perfectly half filled band, one can show that the Hubbard model is equivalent to a Heisenberg model[76]. Going beyond the RPA allows to consider electron-magnon coupling[74]. We note that in transition metals, magnetic order vanishes mostly due to excitation of magnons. Indeed, Stoner model predicts critical temperatures, Stoner temperatures, that are much higher than what is experimentally observed[56].

Both Heisenberg and Hubbard models are based on the Coulomb interaction i.e. a purely electric effect between electrons. As explained in section 2.2, one also has magnetic effects. Those include[21]:

- The Zeeman interaction: interaction between magnetic dipoles $\mathbf{m}_i$ and a magnetic induction $\mathbf{B}$: $\hat{H}_Z = -\sum_i \mathbf{m}_i \cdot \mathbf{B}(\mathbf{r}_i)$.
- The magnetic dipolar interaction $\hat{H}_D = \frac{\mu_0}{8\pi} \sum_{i \neq j} \frac{\mathbf{m}_i \cdot \mathbf{m}_j - 3(\mathbf{m}_i \cdot \mathbf{e}_{ij})(\mathbf{m}_j \cdot \mathbf{e}_{ij})}{|\mathbf{r}_{ij}|^3}$ with $\mathbf{r}_{ij} = \mathbf{r}_i - \mathbf{r}_j$ and $\mathbf{e}_{ij}$ is the unit vector with the same direction as $\mathbf{r}_{ij}$. This term may also include contact terms when the particles carrying the magnetic moment are overlapping. The usual lattice constants render the magnetic dipolar energy too small to explain the measured Curie temperatures. However it has significant effects on a macroscopic scale due to its long range. It is responsible for shape anisotropy (demagnetizing field), stray fields and contributes to the formation of a gap in the dispersion relation of magnons together with other sources of anisotropy[32]. This latter point is fundamental since it means that the ground state of magnetic materials at 0 Kelvin is actually not the state with all perfectly aligned magnetic moments[21].

*Investigation of the spin susceptibility shows that magnons are here correlated electron-hole (interacting) pairs with opposite spins. They are also collective excitations, as in Heisenberg model, which can be seen as a superposition of spin flips. Stoner excitations are uncorrelated electron-hole pairs with opposite spin. See also reference 75 for a more detailed discussion about spin wave excitations in itinerant ferromagnetism and the relation between Stoner excitations and magnons.

- The spin-orbit coupling $\hat{H}_{SO} = \lambda_{SO} \sum_i \mathbf{S}_i \cdot \mathbf{L}_i$ which is responsible for many effects such as crystalline anisotropy, spin relaxation to the lattice and interfacial effects such as Rashba and Edelstein effects. We note however that the given form of the provided spin-orbit interaction is not the most general as it neglects, in its derivation, interaction between the spin of an electron and the orbital angular momentum of another electron.

- There are also several other interactions that exist due to the existence of multipoles of higher orders, especially with nuclei and not only electrons themselves. However those interactions are always neglected in the works mentioned in this thesis.

- The lattice is usually assumed to be rigid in the models presented above as lattice vibrations are not necessary to explain the rise of magnetic order. However, many terms in the equations above depend on lattice positions, such as for instance exchange integrals. Including lattice vibrations can give rise to magnon-phonon interaction[77,78] or spin dependent electron-phonon interaction[35]. It is also often included as magnetoelastic coupling in continuous media models[46].

Crystalline anisotropy, Zeeman and demagnetizing energies can be included in a Weiss model in order to model magnetic hysteresis loops and magnetization versus temperature curves more accurately[79]. Another famous model that includes these contributions, based on energy minimization is the macrospin Stoner–Wohlfarth model[80]. It is valid at 0 Kelvin but can be extended to non-zero temperatures[81]. More realistic calculations can be made by considering individual atomic spins and all the interactions mentioned above (except nuclear interactions according to our knowledge) in micromagnetic simulations[82].

Now let us focus on magnetization dynamics. The most general way to obtain magnetization/magnetic moment dynamics is to calculate $\langle \hat{\mathbf{m}} \rangle (t) = \mathrm{Tr}(\hat{\rho}(t)\hat{\mathbf{m}})/\mathrm{Tr}\left(\hat{\rho}(t)\right)$ with the use of equation (2.15) for a given Hamiltonian that represents the system of interest. This can provide the full transient out of equilibrium dynamics but this is usually too difficult to do as already discussed above. Not too far from equilibrium, when Boltzmann equation is still approximately correct, magnetic moment dynamics is obtained from angular momentum dynamics given by equation (2.5) for the spatial part of $M^{\mu\nu}$:

$$\partial_t j^i + \partial_j J^{ij}_{\mathbf{j}} = 0 \tag{3.16}$$

One then notes that the angular momentum current density $\mathbf{J}_{\mathbf{j}}$ is here a (non symmetric) tensor. This is analog to the stress tensor (which is symmetric) for the momentum continuity equation.

In the low energy case when one only considers electronic spin angular momentum, one has[83]:

$$\partial_t s^i + \partial_j J_s^{ij} \neq 0 \tag{3.17a}$$

$$s^i = \psi^\dagger \sigma^i \psi \tag{3.17b}$$

$$J_s^{ij} = \mathrm{Im}\left(\psi^\dagger \frac{\hbar}{m} \sigma^i \partial_j \psi\right) \tag{3.17c}$$

Where ψ are spinors that depend on space and time and which are to be second quantized. The inequality sign in equation (3.17a) comes from the fact that spin angular momentum is not conserved, only the total angular momentum is. This is fundamental and it is one of the main objective of this chapter to discuss how spin angular momentum can be lost (meaning transformed into another form of angular momentum). The simplest way is magnetic moment dynamics generated by an external (or effective) classical magnetic field (induction). In this case the Hamiltonian is $\hat{H} = (g\mu_B/\hbar)\, \mathbf{S}\cdot\mathbf{B} = \gamma \mathbf{S}\cdot\mathbf{B} = -\mathbf{m}\cdot\mathbf{B}$ where $\gamma > 0$ is the gyromagnetic ratio, and direct application of equation (2.15) gives*:

$$\frac{\mathrm{d}\mathbf{M}}{\mathrm{d}t} = -\gamma \mathbf{M} \times \mathbf{B} \tag{3.18}$$

Where we now consider magnetization $\mathbf{M}$ as usual. This is valid for a single spin or for coherent rotation of several spins. It is remarkable that equation (3.18) is exact including for any time dependence of the magnetic induction. However this Hamiltonian is describing an isolated system so it conserves energy (the Hamiltonian of the total system obviously commutes with the Zeeman Hamiltonian) even though angular momentum is not conserved (the spin operator does not commute with the Zeeman Hamiltonian). This prevents the magnetic moment from aligning its direction with the magnetic field, which is probably the most well known experimental fact of magnetism. In models such as Stoner-Wohlfart, even though one does not generally focus on dynamics, this alignment is always verified because the model is based on minimization of energy and not its conservation. To include this effect, one needs to consider that the spin degree of freedom (one does not consider orbital angular momentum here) is coupled to an external environment which will lead to dissipations. Introducing these dissipations phenomenologically, it is shown that equation (3.18) becomes LLG equation[2–4]:

$$\frac{\mathrm{d}\mathbf{M}}{\mathrm{d}t} = -\gamma \mathbf{M} \times \left(\mathbf{H}_{\text{eff}} - \frac{\alpha}{\gamma M}\left(\frac{\mathrm{d}\mathbf{M}}{\mathrm{d}t} + \tau \frac{\mathrm{d}^2\mathbf{M}}{\mathrm{d}t^2}\right)\right) \tag{3.19}$$

*Using the cyclic invariance of the trace and the angular momentum commutation relations, one gets: $\frac{\mathrm{d}\langle m^i\rangle}{\mathrm{d}t} = \frac{\mathrm{d}}{\mathrm{d}t}\mathrm{Tr}(\hat{\rho}(t)m^i) = \mathrm{Tr}(\frac{i}{\hbar}[\gamma\mathbf{S}\cdot\mathbf{B}, \hat{\rho}(t)]\gamma S^i) = \frac{i\gamma^2}{\hbar} B^j \mathrm{Tr}(\hat{\rho}(t)[S^i, S^j]) = -\gamma^2 \varepsilon_{ijk} B^j \mathrm{Tr}(\hat{\rho}(t) S^k) = \gamma(\mathbf{B}\times\mathbf{m})_i$

Where $ng\gamma\mathbf{H}_{\text{eff}} = -\delta\hat{H}/\delta\mathbf{S}$ is an effective magnetic field* which can contain terms due to magnetic effects introduced above depending on the terms included in the Hamiltonian $\hat{H}$, α is Gilbert damping and τ is the angular momentum relaxation time. The last term of equation (3.19) is an inertial term that causes nutation of the dynamics on top of the usual precession and relaxation. It has been theoretically predicted and recently observed[4]. The relaxation time is believed to be around the picosecond timescale and may thus become important for ultrafast magnetization dynamics, but this has not been studied yet. It is fundamental to realize that dissipation is actually always present[27], even in, say, an isolated magnetic atom, because of the coupling of spin with $\boldsymbol{\nabla} \times \mathbf{E} = -\partial_t \mathbf{B} = -\mu_0(1 + \chi_s^{-1})\partial_t \mathbf{M}$†. This leads to intrinsic Gilbert damping[27].

The LLG equation is also only valid for a single (classical i.e. which can point in any direction) spin or macrospins because the amplitude of the magnetization remains the same. There are various ways to consider changes of the magnetization amplitude. The main reason for a diminution of the amplitude is a disorder in the atomic magnetic moment directions, generally because of temperature. The amplitude of the atomic magnetic moment does not change much with temperature but this change may be obtained from *ab initio* calculations. In order to consider temperature fluctuations of the atomic magnetic moment direction, one can resort to atomistic spin simulations[85]. The idea is to obtain Langevin dynamics by coupling the system to a thermal bath and taking the classical limit[15]. This is conveniently done in the framework of path integrals because fluctuations can then be seen as deviations from the equations of motions (obtained from the LAP which neglects those deviations). In this case, the partition function Z becomes[15‡]:

$$Z = \int \mathbf{D}[\boldsymbol{\xi}] e^{-\frac{1}{4\eta T}\int \boldsymbol{\xi}^2(t')\mathrm{d}t'} \int \mathbf{D}[\mathrm{M}]\delta\left(\partial_t \mathbf{M} - \mathbf{A}(\mathbf{M}) - \mathbf{B}(\mathbf{M})\boldsymbol{\xi}\right) \tag{3.20}$$

Where T is the thermal bath temperature, η is a certain constant that characterizes the coupling with the thermal bath, M and the fluctuation field $\boldsymbol{\xi}$ are functions of time and atomic site, $\mathbf{A}$ is a vector and $\mathbf{B}$ is a tensor in atomic site space. The expression of the latter two quantities are given in reference 85 for LLG equation. The inner path integration shows that, among all the possible

*One usually writes it $\mathbf{H}$ and call it magnetic field but it actually is magnetic induction if $[\gamma] = (\mathrm{Ts})^{-1}$ as in for instance references 4, 84.

†We note however a flaw in the derivation of reference 27 as the performed Foldy-Wouthuysen transformation is for time independent electromagnetic fields.

‡The partition function is $Z = \mathrm{Tr}(U_{\mathcal{C}}\hat{\rho}(-\infty))/\mathrm{Tr}(\hat{\rho}(-\infty))$ where $\mathcal{C}$ is the integration contour which is $-\infty \to \infty \to -\infty$ in Keldysh formalism. Inserting an observable at an instant t in this time contour, by separating the evolution operator $U_{\mathcal{C}}$ into two evolution operators, gives the expectation value of that observable at t. The partial derivative with respect to time must be performed in Ito regularization scheme in order to have $Z = 1$.

trajectories for $\mathbf{M}$, only those that satisfy the Langevin equations $\partial_t \mathbf{M} = \mathbf{A}(\mathbf{M}) + \mathbf{B}(\mathbf{M})\boldsymbol{\xi}(t)$ actually happen. The latter equation is basically equivalent to equation (3.19) if one adds the stochastic field $\boldsymbol{\xi}(t)$ to the effective field $\mathbf{H}_{\text{eff}}$. The stochastic field is fully characterized by the partition function. What the partition function says is that the actual dynamics is an average of solutions of the Langevin equations with a weight $e^{-\frac{1}{4\eta T}\int \boldsymbol{\xi}^2(t)\mathrm{d}t}$ for all possible noises. It is also equivalent to say that the stochastic field is fully characterized by its first and second statistical moments:

$$\langle \xi_i(t) \rangle = \int \mathbf{D}[\boldsymbol{\xi}] \xi_i(t) e^{-\frac{1}{4\eta T}\int \boldsymbol{\xi}^2(t')\mathrm{d}t'} = 0 \tag{3.21a}$$

$$\langle \xi_i(t)\xi_j(t') \rangle = \int \mathbf{D}[\boldsymbol{\xi}] \xi_i(t)\xi_j(t') e^{-\frac{1}{4\eta T}\int \boldsymbol{\xi}^2(t')\mathrm{d}t'} = 2\eta T \delta_{ij}\delta(t-t') \tag{3.21b}$$

For atomic sites i and j. The resulting stochastic LLG is strictly speaking only valid at equilibrium (locally) because it satisfies the fluctuation dissipation theorem[15]. This comes from the fact that the bath the magnetic system is coupled to is itself assumed to be at equilibrium. One can supplement this model with a model for the thermal bath temperature dynamics but it is still only rigorously valid for equilibrium because the thermal bath are at equilibrium by definition. It is also possible to add more thermal baths*.

The stochastic LLG requires to consider each atomic magnetic moment of the system. However, the partition function (3.20) contains all the information required to calculate the average magnetization of the system:

$$\langle \mathbf{M} \rangle (t) = \int \mathbf{D}[\boldsymbol{\xi}] e^{-\frac{1}{4\eta T}\int \boldsymbol{\xi}^2(t')\mathrm{d}t'} \int \mathbf{D}[\mathbf{M}] \mathbf{M}(t) \delta \left(\partial_t \mathbf{M} - \mathbf{A}(\mathbf{M}) - \mathbf{B}(\mathbf{M})\boldsymbol{\xi} \right) \tag{3.22}$$

Then, one may then just integrate over the magnetization paths in (3.20) that lead to a certain magnetization vector $\mathbf{M}$ at a time t to obtain the distribution function $f(\mathbf{M}, t)$ such that $\langle \mathbf{M} \rangle (t) = \int \mathbf{M} f(\mathbf{M}, t) \mathrm{d}\mathbf{M}$. One can then show that such distribution function obeys the Fokker–Planck equation[15] which may be seen as the classical analog of equation (2.15). This procedure leads to the Landau-Lifshitz-Bloch (LLB) equation[84,87]:

$$\frac{\mathrm{d}\mathbf{M}}{\mathrm{d}t} = -\gamma \mathbf{M} \times \mathbf{H}_{\text{eff}} + \alpha_{\parallel} \frac{(\mathbf{M} \cdot \mathbf{H}_{\text{eff}})\mathbf{M}}{M^2} - \alpha_{\perp} \frac{\mathbf{M} \times (\mathbf{M} \times \mathbf{H}_{\text{eff}})}{M^2} \tag{3.23}$$

This equation includes longitudinal as well as transverse relaxation parametrized by the susceptibilities $\alpha_{\parallel}$ and $\alpha_{\perp}$. This model depends on several parameters that we will not discuss[84]. One may obtain these parameters from the stochastic LLG, and the parameters in the Hamiltonian

*If a system has several temperatures, it is not strictly speaking at equilibrium but in the stochastic LLG, each spin is at equilibrium with the thermal bath even though the complete spin system may not be at equilibrium itself[86].

of the stochastic LLG may be obtained from *ab initio* calculation, thus performing a complete multiscale calculation of the magnetization dynamics[88,89]. An older equation that also includes longitudinal and transverse relaxation is the Bloch equation[90]:

$$\frac{\mathrm{d}M_x}{\mathrm{d}t} = -\gamma(\mathbf{M}\times\mathbf{B})_x - \frac{M_x}{T_2} \tag{3.24a}$$

$$\frac{\mathrm{d}M_y}{\mathrm{d}t} = -\gamma(\mathbf{M}\times\mathbf{B})_y - \frac{M_y}{T_2} \tag{3.24b}$$

$$\frac{\mathrm{d}M_z}{\mathrm{d}t} = -\gamma(\mathbf{M}\times\mathbf{B})_z - \frac{M_z - M_z^0}{T_1} \tag{3.24c}$$

Where T_1 and T_2 are relaxation times that characterize relaxations and M_z^0 is the equilibrium magnetization.

If one starts from the full quantum equation (2.15) (without going to the classical limit) instead of using the Fokker-Planck equation, the quantum LLB (qLLB) equation is obtained[84,91]. It is also "quantum" in the sense that it considers finite spin values (while classical approaches are equivalent to an infinite spin value) contrary to LLG, the stochastic version of LLG and LLB. The difference only arises in terms not proportional to $\mathbf{M}\times\mathbf{H}$ such that equation (3.18) is quantum, as shown by the derivation, but still identical to the classical case. This equation also uses Markov and the secular approximation and so is not valid too far from equilibrium*. We also note the existence of a different equation, the self-consistent Bloch equation, that has similarities with the LLB equation in references 94 and 95.

3.3 Ultrafast demagnetization and spin transport

From a fundamental point of view, ultrafast magnetization dynamics differs from the previously presented theories of magnetization dynamics (apart from qLLB) in that it is dynamics for a system that is possibly strongly out of equilibrium[96]. This is has been observed experimentally using time resolved MOKE[97], Second-Harmonic Generation (SHG)[98,99], two-photon photoemission[100] and later X-ray Magnetic Circular Dichroism (XMCD)[101]. Magnetization was shown to rapidly quench to reach its minimum value (which can be 0[99]) in a few hundreds of femtoseconds for experiments with sufficient time resolution. Hohlfeld *et al.*[98] probed the response of a bulk polycrystalline ferromagnetic nickel sample, after irradiation with a 150 fs

*We note that performing these two approximations does not make the non-diagonal elements of the density matrix vanish as in a semiclassical approach[22,39]. However in some models shown below, one only considers diagonal elements and the equation they obey does not depend on the non-diagonal ones[73,92,93].

laser pulse with a wavelength of 800 nm, using SHG. This technique allows them to obtain the electronic temperature T_e from ΔI^+ and the normalized magnetization $\mathbf{M}$ from ΔI^- where $\Delta I^{\pm}(t) = (I^{\pm}(t) - I_0^{\pm}(t))/I_0^{\pm}(t)$ is the relative change of $I^{\pm}$ compared to the signal $I_0^{\pm}$ at negative pump-probe delay. $I^{\pm}$ is obtained from the sum or difference of the SHG signal. The fundamental requirement to safely correlate $\Delta I^{\pm}$ to T_e or $\mathbf{M}$ is that the electrons are thermalized. For delays greater than 0.3ps, figure 3.1 (a) shows that the obtained temperatures and magnetizations agree really well with the Weiss model, thus proving that the electronic system is at equilibrium for these delays. Figure 3.1 (b) shows the same result but for only three fluences and also for pump-probe delays smaller than 0.3ps. One can then see a strong deviation from Weiss model at this timescale, thus showing that the electron system is no longer at equilibrium. This agrees with the previously mentioned work by Fann *et al.*[57] in paramagnetic gold and shows that ultrafast demagnetization is indeed accompanied with non equilibrium dynamics. Although it was already well understood that a non equilibrium state could exist at the picosecond timescale due to different temperatures for electrons and phonons[47,48] and that electrons could become non thermalized at the subpicosecond timescale[57], it was still expected that magnetic moment or spin would react very slowly (around the nanosecond timescale) to such stimuli[102]. The results of Beaurepaire *et al.*[97] were thus very unexpected. Similar results of observation of non-equilibrium of magnetization were already obtained in 1991 by Vaterlaus *et al.* for gadolinium using two-photon photoemission[103]. However, they found that the spin relaxation time was 100$\pm$80ps. This is much higher than the spin relaxation time in nickel but still lower than the predicted value for nickel around two nanoseconds. These results for gadolinium were later confirmed, with greater accuracy[104,105]. Wietstruk *et al.* found a spin relaxation time of 40$\pm$10ps in agreement with Vaterlaus *et al.*. However, Wietstruk *et al.* observed that the demagnetization proceeded in two steps. In a first step, they found that the magnetization was reduced by 30$\%$ in a characteristic time of 0.76ps while it was further reduced of 25$\%$ in a characteristic time of 40ps. This two step ultrafast demagnetization was actually already observed in nickel in the experiments of Scholl *et al.*[100], suggesting at the time a reconciliation for the disagreement between the results of Vaterlaus*et al.* and those of Beaurepaire *et al.* and Hohlfeld *et al.*. Interestingly, Wietstruk *et al.* also studied the ultrafast demagnetization of terbium and found a similar spin relaxation time of 0.74ps for the first step of the demagnetization while the second one was happening much faster than for gadolinium with a characteristic time of 8ps. This shows that, even though ultrafast demagnetization might indeed be a very general phenomenon resulting from the generation of an out of equilibrium state of the magnetic material, the details of the process of ultrafast demagnetization depend strongly on the material. The difference

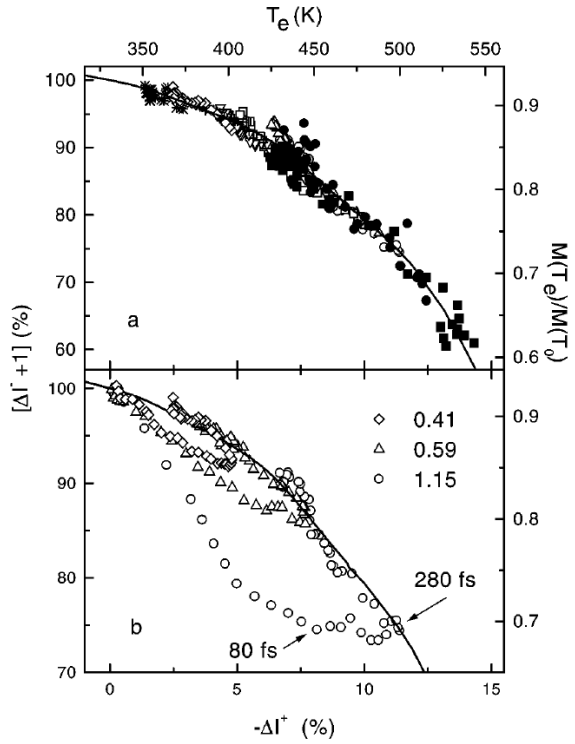

Figure 3.1: Relative SHG signal $\Delta I^{\pm}$ where $I^{\pm}$ is the sum or difference of the SHG signal obtained for opposite magnetization direction of the polished polycrystalline bulk nickel sample. The sum of the signal is used to obtain the electronic temperature T_e while the difference is related to the magnetization $\mathbf{M}$. Figure (a) is obtained for various fluences but at a pump-probe delay greater than 0.3ps when the electrons are thermalized. Figure (b) gives the results at three different fluences, calibrated by $1 \simeq 6\text{mJ/cm}^2$, but for all pump-probe delays. In both figures, the solid line is obtained from a Weiss model expansion around the Curie temperature. Figure taken from reference 98.

between gadolinium and terbium, apart from an additional 5d electron in gadolinium, is the filling of the 4f shell which has seven electrons in gadolinium and nine electrons in terbium. This leads to a slightly smaller spin angular momentum for terbium but more significantly, a zero orbital angular momentum for gadolinium while it has a value of three in terbium. This means that there cannot be any exchange of angular momentum between the spin and orbital part of the angular momentum in gadolinium because the spin-orbit coupling term of the Hamiltonian will be zero at each instant*. The spin angular momentum - orbital angular momentum - lattice angular momentum channel is believed to be the fundamental cause of the different ultrafast de-

*Provided that there is no build up of orbital angular momentum because gadolinium would not be in its ground state, following Hund's rules, anymore. However we note that this change should be accompanied with a change of angular momentum which might then come from the lattice.

magnetization dynamics in gadolinium and terbium even though the details and interpretation of the observed dynamics also strongly depends on the experiment itself[105,106]. The fact that the demagnetization can happen in one or two steps also depends on the material properties, but the general reasons why a second step may exist can already been understood from qualitative arguments and just focusing on the electron-phonon and magnetization (spin) relaxation time[107]. The first reason, which is the main cause for this second step in rare-earth metals, is that the spin relaxation time may be longer than the electron-phonon relaxation time. Then, when the electrons are still very hot, the induced demagnetization can be very fast, while once the electrons and phonons are at equilibrium, the electron temperature is much lower, slowing down the demagnetization, but still high enough such that the magnetization itself is not at equilibrium with the electron-phonon system. The second reason is critical slowdown of magnetization as it gets closer to zero[86,107]. This may happen in transition metals if one increases the laser fluence such that almost a complete demagnetization occurs. The reason for this slowdown may be understood from the point of view of conservation and transfer of angular momentum. In an Hamiltonian, transfer of angular momentum happens because of terms of the form $J\mathbf{S}\cdot\mathbf{j}$ where $\mathbf{S}$ is the angular momentum that will generate the observed magnetization, $\mathbf{j}$ is another source of angular momentum which is not usually measured (for instance because it is quickly dissipated or because it is a magnetic field) and J the coupling (assumed here to be constant in time and with temperature). If the contribution of $\mathbf{S}$ is small, then the transfer will be small because less interaction events will happen and thus the dynamics is slowed down. This is seen in equation (3.18) with $\mathbf{j}=\mathbf{B}$, when $\mathbf{M}$ is small, so is its derivative with respect to time. This is also the case with the LLG equation* and is also a feature of LLB[84] as well as all the other models of transfer of angular momentum introduced below. Interestingly, it is a feature of the self-consistent Bloch equation[95] but not the original Bloch equation (3.24) because when M_z is small, M_z^0 remains the same in the Bloch equation while this term depends on the instantaneous magnetization in the self consistent version.

In order to discuss the origin of ultrafast demagnetization, we go back to the general equations of angular momentum conservation (2.5) or (3.17a). What those equations say is that a local loss of angular momentum, say spin angular momentum, is due to a local transfer of angular momentum to another reservoir or to a transport of this angular momentum to another location (transport which is influenced by interactions due to separate equations in general). We will first focus on the local transfer of angular momentum and pursue with the transport of angu-

*This is best seen in the Landau-Lifshitz form of LLG[3]. Damping can be seen as a case where $\mathbf{j}=\mathrm{d}\mathbf{M}/\mathrm{d}t$ as can be seen in reference 27.

lar momentum afterwards. We note that, according to section 3.2, the loss of magnetic moment can manifest itself into two different magnetic excitations: either a spin flip (the fact that a localized spin changes its spin projection sharply as in a Weiss model, or a Stoner excitation in itinerant ferromagnetism models such as Stoner model), or a magnon (or a mixture of spin flips and magnons). These modes can be excited due to a local interaction and they can then propagate, which transports angular momentum, if they have a non zero wave vector. In terms of band structures, these two types of excitations lead to two different kinds of modification. Spin flips lead to a reduction of the exchange splitting while magnons lead to band mirroring[108]. A reduction of exchange splitting happens because Stoner excitations imply that majority electrons will start populating minority bands thus leading to energy shifts of the bands in order to keep a constant chemical potential for spin up and spin down electrons. Band mirroring is the fact that electron with ,say, a spin up, will become a superposition of electronic wavefunctions with spin up and down because of the creation of a magnon*. The density of state of spin up electrons is then mirrored, possibly with a smaller amplitude, on the spin down density of state and vice versa. Both effects are illustrated in figure 3.2.

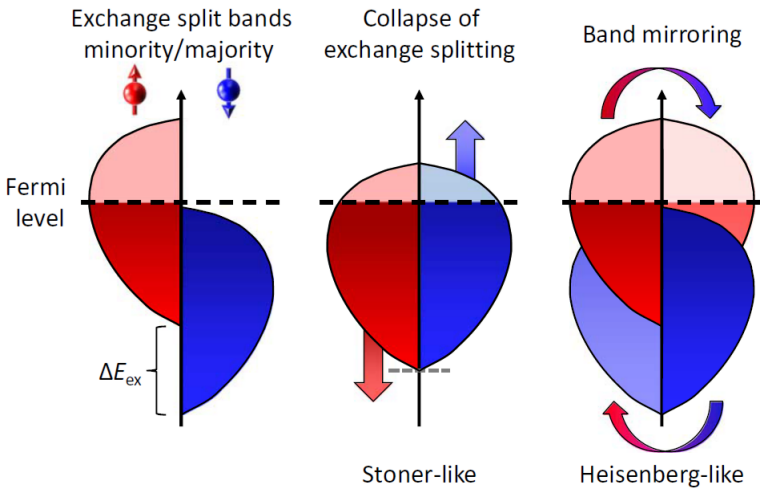

Figure 3.2: Illustration of the reduction of exchange splitting and band mirroring as explained in the text. ΔE_{ex} is the exchange splitting. Figure taken from reference 108.

Local transfer of angular momentum

The conservation of angular momentum in ultrafast demagnetization dynamics has already

*This fact is usually explained by the fact that one can obtain an effective Heisenberg Hamiltonian that reproduces magnetic properties obtained from *ab initio* calculations[109,110]. Then a magnon can be seen as a coherent rotation of atomic spins i.e. change of spin projection.

been discussed several times by Fähnle and his coworkers[111–114]. Here we will review the different local mechanisms of transfer of angular momentum following the discussion of reference 113 and we refer to the references cited in this paper for the numerous studies that have been done before 2013. From equation (2.8c), one may argue that the total angular momentum of any system that is considered here is made up of the spin and orbital angular momentum of the electromagnetic field and electrons plus the orbital angular momentum of the static lattice and spin angular momentum of phonons[17]. Provided that the laws governing the system are truly invariant under rotation, meaning that the action describing the system is invariant under rotation, angular momentum should be conserved. However as noted by Fähnle *et al.*[112] and Streib[17], samples are fixed to sample holders meaning that one would need to consider the sample holder and everything connected to it in order to keep rotation invariance. Fähnle *et al.* argued that the resulting non conservation of angular momentum may be neglected because the transfer of angular momentum to the lattice might happen in a timescale of hundreds of picosecond. However, this argument has now been refuted since the observation of the ultrafast Einstein-de Haas effect[115] where a transfer of 80% of the angular momentum lost during the ultrafast demagnetization of an iron thin film was observed to be transferred to the lattice within a characteristic time of 200fs. However, using periodic boundary conditions, and thus pseudo-angular momentum instead of angular momentum as the quantity of interest, Streib claims that the angular momentum transferred to the lattice will be absorbed by the boundary conditions. Then one just has to consider the spin of phonons and it can be assumed that any angular momentum in the phonons will be transferred out of the sample very quickly[115*].

In this case, one needs to consider the following possible local interactions[113]:

- An interaction between the laser pulse electromagnetic field and the electrons could possibly transfer angular momentum to the system. However this effect was shown to be very small[113].

- An interaction between the sample and the vacuum electromagnetic field i.e. through emission of photons. It was shown that ultrafast demagnetization indeed leads to an emission of photons, as can be seen through the simple general relation $\boldsymbol{\nabla} \times \mathbf{E} = -\partial_t \mathbf{B} = -\mu_0(1+\chi_s^{-1})\partial_t \mathbf{M}$, which is experimentally observed as the emission of THz electromag-

*Similarly to pseudo-momentum, pseudo-angular momentum is conserved up to a certain "reciprocal angle" m such that $e^{im\phi}$ is the factor that a wavefunction of the system will acquire when the system is rotated by an angle ϕ that leaves the lattice invariant. In theories reported below where this concept has been useful, the lattice was always supposed to be a continuous isotropic medium. This simplifies the problem, because in this case pseudo-angular momentum is conserved.

netic waves. In general, this radiation can be due to a direct change of magnetization or indirectly because of a combination of the generation of a spin current and Inverse Spin Hall Effect (ISHE)[116]. However, the emitted THz pulse were always observed to be linearly polarized, thus not showing any transfer of angular momentum to the electromagnetic field. This linearly polarized electromagnetic radiation is a signature of a longitudinal change of magnetization. A precessional motion of magnetization can however lead to circularly polarized THz emission[117]. However, this does not prove that no angular momentum is transferred to the electromagnetic field because the observation of THz emission is performed in the far field. It is *a priori* possible that angular momentum may be dissipated in the near field. Fähnle *et al.* argue that this effect may be small[112].

- An interaction between electrons and phonons may lead to a transfer of angular momentum. This was first considered in metals by Elliott[118] and Yafet[119] hence the name Elliott-Yafet scattering. The reason why angular momentum may be transferred during such an interaction is twofold and always due to spin-orbit coupling. First, spin-orbit coupling is the cause of a spin dependent term in the Hamiltonian $\lambda_{SO} \sum_i \mathbf{S}_i \cdot \mathbf{L}_i$ which can lead to a transfer of angular momentum, as explained above, if there exist some spin and orbital angular momentum*. Second, the spin-orbit coupling term in the Hamiltonian does not commute with either $\mathbf{S}_i$ or $\mathbf{L}_i$ and thus the orbital and spin angular momentum quantum numbers are no longer good quantum numbers. This implies that $\mathbf{S}_i$ (and $\mathbf{L}_i$) is not diagonal in the basis that diagonalizes the Hamiltonian of the system and the eigenstates of this Hamiltonian, used to calculate transition rates, become a superposition of a wave function with spin up and another one with spin down. This spin mixing appears mathematically as another way to transfer angular momentum because spin diagonal terms in the Hamiltonian will then also lead to transfer of angular momentum. As explained in reference 35, there is actually no transfer of angular momentum due to spin diagonal terms in the Hamiltonian because this transfer is only due to spin-orbit coupling. However the combined effect of spin-orbit coupling with other (spin diagonal) interactions lead to additional transfer of angular momentum channels. For the sole case of electron-phonon interaction, it has been shown that it can indeed participate to the ultrafast demagnetization but cannot be the only interaction that needs to be considered because the predicted demagnetization amplitudes are smaller than the ones experimentally observed. As for the

*This explains why the orbital angular momentum remains zero in gadolinium in a GdFeCo alloy[120]. The orbital angular momentum of gadolinium is zero and so it will remain like this provided that it remains in its lower energy level as already mentioned.

other mechanisms that eventually lead to transfer of angular momentum to the lattice, the spin angular momentum is first transferred to the orbital angular momentum of electrons before being transferred to the spin of phonons. A theory that completely considers this transfer from orbital angular momentum to phonon spin angular momentum for crystals (due to electron-phonon coupling) is still missing according to our knowledge. In the case of anisotropic media or when the crystalline structure of the sample can be neglected, some serious improvements have been achieved[69,121–123]. For crystalline structures, we note the work of Fähnle *et al.*[124] which was not able to reproduce the observed transfer of angular momentum to the lattice and also the work of Chen and Wang[7]. In the latter work, the authors used a modified rt-TDDFT that takes nucleus motion into account. They were able to show transfer of angular momentum from the electronic degrees of freedom to the lattice. We note however that they do not have an exact conservation of angular momentum even after the laser pulse is no longer effective. This could be due to the fact, as the authors note, that there could be some (very small) transfer of angular momentum to the electromagnetic field*. As noted by Illg *et al.*[113], if the angular momentum is transferred to the lattice through orbital angular momentum, the latter quantity must be quenched in less than around 50 femtosecond, the time resolution of current experiments, because an increase of orbital angular momentum has never been observed (see the references in 109 as well as the work of Bergeard *et al.*[120] and Hennecke *et al.*[125]).

- As explained in the previous case, in the presence of spin-orbit coupling, even terms in the Hamiltonian that do not depend on spin can lead to a transfer of angular momentum to the lattice. Thus electron-electron scattering may participate and is believed to be one of the most important contributions. By electron-electron scattering, we mean the direct electron-electron interaction i.e. without exchange terms as in the work of reference 126.

- Another important contribution is the electron-magnon interaction. It also does not transfer angular momentum to the lattice without spin-orbit coupling as can be seen from the s-d model Hamiltonian for electron-magnon scattering $-J \sum_i \mathbf{s}_i \cdot \mathbf{S}_i$. It is also obvisous from the fact that the electron-magnon interaction is fundamentally a contribution of Coulomb interaction (which does not depend on spin). Haag *et al.*[127] performed such (*ab initio*) calculations and showed that even though it might contribute to the ultrafast demagnetiza-

*We also note that when the laser pulse is effective, the total angular momentum is also not conserved. We believe this is related to the same effect seen for energy in section 5.1, also already mentioned in chapter 2, where the only angular momentum that makes physical sense in the presence of an external source of electromagnetic radiation is the total angular momentum of the system with matter and the electromagnetic field.

tion process, it is not sufficient. However a combination of electron-phonon and electron-magnon interactions may agree with experiments. We also note the works based on the s-d model Hamiltonian of Manchon *et al.*[72] for thermalized magnons and Tveten *et al.*[128] for out of equilibrium magnons. One can also consider an electron-spin interaction as in the models of references 73 for semiconductors and 93 for metals. Those models rely on the same s-d Hamiltonian except that they neglect magnons in the spin system by using a mean field approximation.

- Electron interaction with defects or interfaces may lead to a transfer of angular momentum. Illg *et al.*[113] argue that these effects nearly do not affect ultrafast demagnetization. However this may not be the case when angular momentum is transported through an interface into another layer as for instance modeled in reference 128 but we will come back to this issue later when considering transport of angular momentum.

- Illg *et al.* also discuss the possible role of phonon-phonon interaction as a possible way to evacuate the angular momentum into the lattice as a global rotation, and thought at the time that this effect would be too small. Although as we now know, this effect is probably really important as discussed previously[115].

- Magnon-phonon interaction is another possible mechanism which has been discussed in various contexts[91,122,124]. However so far the role of this mechanism is not clear and Illg *et al.*[113] believe it is a small effect. As for the electron-magnon interaction, one could also consider spin-phonon scattering.

- There could be any other kind of higher order interaction coming for instance from the expansion in lattice displacement of the Hamiltonian, the Holstein-Primakoff transformation or more generally by considering more correlations. However because these effects imply more particles or quasi-particles, they are generally believed to be small. We note however that such considerations come from a perturbative point of view while non-perturbative effects may sometimes lead to significant contributions. In particular we note that this may be the case with all interactions involving magnons in the Heisenberg sense because the Holstein-Primakoff expansion is most likely a bad approximation for ultrafast demagnetization when atomic spins strongly deviate from a parallel alignment. Also, Mentink *et al.*[69] showed that considering non perturbative effects in the electron-phonon interaction leads to a transfer of angular momentum at the femtosecond timescale due to an external oscillating magnetic field while such effects are usually thought to be small.

- Up to here the discussion focused on materials made of a single element, mostly iron, cobalt and nickel. However, additional mechanism may exist in alloys and multilayers[129–133], especially Optical Intersite Spin Transfer (OISTR) where a laser impulsion may induce a spin flip of an electron by transporting it from one element to another. In FM/Pt multilayers and FMPt alloys (where FM can be iron, cobalt or nickel) the additional source of spin-orbit coupling from platinum together with OISTR leads to larger demagnetization amplitudes as well as slightly shorter demagnetization times[131].

When those interactions happen, they will cause the reduction of the average magnetization due to either a spin flip and/or a magnon as explained above. For instance Elliott-Yafet and electron-electron scattering events will reduce the magnetization because of a spin flip while an electron-magnon scattering event will create a magnon (together with a spin flip in such a way that some angular momentum is transferred to the lattice because of spin-orbit coupling). In order to investigate which interactions might effectively be dominant during ultrafast demagnetization, it is then natural to experimentally observe if magnetization is reduced because of magnon generation or Stoner excitations. Shokeen *et al.*[134] argued that ultrafast demagnetization is due to spin flips (plus some spin superdiffusion) while most of the other studies[108,116,135] claim magnons is the most important contribution. Especially, Turgut *et al.*[135] found that magnons account for two thirds of the observed demagnetization and are generated at shorter timescale (subpicosecond) than spin flips. Spin flips however last for several picoseconds which may be understood by the fact that the generated magnons are expected to have high energies[136] which may decay efficiently into Stoner excitations[75]. We note however that in those time resolved experiments, a restricted part of the Brillouin zone is probed such that other mechanisms may contribute at different wave vectors. Static photoemission experiments show that electron-magnon interaction is indeed an important mechanism for an element such as iron[137]. A direct consequence of the reduction of magnetization is a change of the band structure of the material. It has been shown that this change must be considered in order to reproduce the experimentally observed amplitudes[138]. Indeed, spin flips, for instance, lead to a reduction of exchange splitting which in turns lead to a difference of chemical potential for spin up and spin down electrons (i.e. a spin accumulation). This spin accumulation will tend to disappear which will also reduce the exchange splitting. This feedback effect[139,140] can enhance the demagnetization. However it has been shown that this effect alone is not sufficient for electron-phonon scattering[113] but including electron-magnon scattering[127] (and so magnons) may reproduce the experimentally observed demagnetization amplitudes. This is in agreement with the experimental fact that magnons are generated during ultrafast demagnetization. Then a simple reduction of exchange splitting due

to spin flip is not sufficient (although it most likely contributes to the demagnetization) but a band-mirroring effect, which can be reproduced by localized spin models[138], needs to be considered. The fact that the reduction of magnetization is mostly in the form of magnons has been theoretically predicted by Töws and Pastor[141] from exact resolution of the many body problem on a small system.

Most of the calculations performed in the works previously mentioned in this section are based on the Boltzmann equation (without transport) with Fermi's golden rule for transition rates. One may thus wonder if this simple approximation is sufficient[114]. Weng *et al.*[142] considered some[114] of the correlations that are neglected by Fermi's golden rule and observed that it only added some oscillations to the magnetization dynamics. However, it has been shown[7,141,143] that electronic correlations and memory effect can actually have a significant effect as well as initial spin correlations (disorder)[7]. Such spin disorder can only be properly taken into account in large systems (otherwise periodic boundary conditions maintain too much order) and thus requires specific techniques to be modeled. Most of the works also consider that the system is not too far from equilibrium, even though the particle or quasi-particle distribution functions are not assumed to be the thermal ones (see for instance references 61, 116, 128, 139, 144). Real time TDDFT calculations[7,8,143,145] can consider the full out of equilibrium problem with all correlations, in principle, but apart from reference 7 they neglect nuclei motion. This may cast some doubts on the validity of their results[69]. Secchi *et al.*[146–148] considered all the non equilibrium correlations analytically with a path integral technique but they also neglected nuclei motion. This theory is much more complex than the previously mentioned theories because of all the correlations that need to be considered and it has not been applied to compute ultrafast magnetization dynamics in metals according to our knowledge.

Before introducing spin transport, we highlight the fact that ultrafast magnetization dynamics for transition and rare-earth metals has been modeled using the stochastic LLG equation[86,106,149], relying on damping parameters, as well as the LLB equation[84,89] coupled with a 2TM. Those models however cannot bring insights concerning the microscopic mechanism of ultrafast demagnetization and are more suitable to study effects that may appear in systems of greater sizes that would require too much computation time for *ab initio* techniques. The quantum version of LLB[150] is similar to Boltzmann equation plus Fermi's golden rule techniques and can then also model ultrafast demagnetization. Molecular dynamics methods[151,152] can provide Langevin equations for the coupled system of spin, electrons and lattice. They are classical methods that can also reproduce ultrafast demagnetization dynamics provided that one uses the appropriate input parameters. One advantage of such techniques compared to the stochastic LLG equation

is that one does not need Gilbert damping and it already contains the dynamics of electrons and phonons.

Angular momentum transport

We now also consider the possibility of transport/non-local effects in ultrafast demagnetization. We will focus on collinear effects, meaning that the average of angular momentum (of electrons) has the same direction in all locations of the considered system. Non-collinear effects[153] lead to torques on the average angular momentum such as in spin transfer torque[154,155] which still exist at an ultrashort timescale[156,157]. We note that spin transfer torque also exists in collinear structure[158] because at finite temperature, atomic spins are never parallel to each other. As we will see, they also exist at an ultrashort timescale but will not appear as a torque in the formalism because we do not use a macrospin formulation (invalid at high temperatures) and consider the (average) magnetization.

Transport is characterized by the presence of non zero current densities which have the general form $\mathbf{J}(\mathbf{r}) = \mathrm{Im}(\psi^\dagger(\mathbf{r})O\psi(\mathbf{r}))$* for some single particle operator O which is a linear combination of operators of the form $A\partial_i$ with A an hermitian operator, see for instance equations (2.8b) (2.11) and (3.17c). If one quantizes the fields $\psi(\mathbf{r}) = \sum_{\mathbf{k},\lambda} c_{\mathbf{k},\lambda}\phi_{\mathbf{k},\lambda}(\mathbf{r})$, where $\mathbf{k}$ refers to the wave vector and λ to the other indices that characterize the wave functions of a complete basis, the components of current density operators in direction i contain terms of the form $\sum_{\mathbf{k},\mathbf{k}',\lambda,\lambda'} k'_i c^\dagger_{\mathbf{k},\lambda} c_{\mathbf{k}',\lambda'} \mathrm{Re}(\phi^\dagger_{\mathbf{k},\lambda}(\mathbf{r}) A \phi_{\mathbf{k}',\lambda'}(\mathbf{r}))$. Neglecting coherence[40] and using Bloch waves $\phi_{\mathbf{k},\lambda}(\mathbf{r}) = u_\lambda(\mathbf{r})\exp(i\mathbf{k}\cdot\mathbf{r})$, the average of such terms become $\sum_{\mathbf{k},\lambda} k_i f_{\mathbf{k},\lambda} \mathrm{Re}(u^\dagger_\lambda(\mathbf{r}) A u_\lambda(\mathbf{r}))$ with $f_{\mathbf{k},\lambda}$ the average occupation number. The average of current density operators is therefore different from zero only if $\sum_\lambda f_{\mathbf{k},\lambda} \mathrm{Re}(u^\dagger_\lambda(\mathbf{r}) A u_\lambda(\mathbf{r}))$ is different for certain wave vectors of opposite directions. This happens if there is some anisotropy in the average occupation number $f_{\mathbf{k},\lambda} \neq f_{-\mathbf{k},\lambda}$ and there can be further contributions if the average occupation numbers for an identical wave vector are different for different λ. This is for instance what is the cause of spin currents when A is a Pauli matrix. In a Boltzmann theory†, the average occupation numbers become distribution functions $f(\mathbf{r},\mathbf{k},t)$ and such anisotropy arises from spatial‡ gradients. Valet and Fert[159] made such a theory for diffusive transport and spin impurity scattering (neglecting electron-magnon scattering) considering anisotropy in wave vector due to the presence of an

*We wrote the spatial dependence while the time dependence depends on the quantum picture as usual.

†In the full quantum picture, one needs to work with a Wigner distribution function $F(\mathbf{r},\mathbf{k},t,\omega)$ instead of a Boltzmann distribution function[15,29].

‡Gradients in wave vector contribute in the presence of external forces which usually come from spatial gradients of a certain potential.

electric field and spin asymmetry, leading to the presence of charge and spin currents. Close to equilibrium, there can be gradients in the temperatures of electrons with up or down spin and the lattice as well as in chemical potentials for electrons with up and down spins and electric potential*. Writing down conservation equations for energy and charge, one may then obtain various generalizations of the 2TM depending on the thermal baths and gradients that are considered. In the case where exchange of energy and charge is linear in the various involved thermodynamic quantities, and for diffusive transport, the set of equations describing the system is[140,160]:

$$C\frac{\mathrm{d}\overline{X}}{\mathrm{d}t} = \boldsymbol{\nabla}\cdot\left(K\boldsymbol{\nabla}\overline{X}\right) + G\overline{X} + S \tag{3.25}$$

Where $\overline{X}$ is a vector storing the considered thermodynamic quantities, C is a matrix storing partial derivatives of energy and charge number density (capacities), K and G are matrices storing transport and coupling coefficients and S is a source term. The capacities and coupling coefficients are the same as in a local theory while K can be calculated from a linear response theory[29] or from a relaxation time approximation in a Boltzmann theory[50]. We are only interested in the case where there are gradients in the direction of the magnetization (we do not consider effects such as the anomalous Nernst effect). Then the various current densities in the direction z of the magnetization are[160–164]:

$$j_s = \frac{\sigma_s}{e}\partial_z\bar{\mu}_s - S_s\sigma_s\partial_z T_s \tag{3.26a}$$

$$q_s = -\kappa_s\partial_z T_s + \frac{S_s\sigma_s T_s}{e}\partial_z\bar{\mu}_s \tag{3.26b}$$

$$q_p = -\kappa_p\partial_z T_p \tag{3.26c}$$

Where j refers to charge current density, q to heat current density, s can be spin up or down, σ and S are conductivities and Seebeck coefficients, e is the (positive) electric charge and $\bar{\mu}_s = \mu_s - e\phi$ with μ referring to chemical potential and ϕ is the electric potential. The first term of equation (3.26a) is just Ohm's law while the second term gives the Spin Dependent Seebeck Effect (SDSE). The second term of equation (3.26b) gives the spin dependent Peltier effect which can be neglected[160]. To be more precise, the SDSE is the fact that the generated electric field $E_s = -S_s\partial_z T$ depends on spin through the spin dependence of the Seebeck coefficient. Thus a spin current density $j_\uparrow - j_\downarrow$ may be generated due the SDSE but it can also be created due to the standard Seebeck effect because conductivities are different for different spin directions

*This list is not exhaustive but contains the most important ones for our discussion. One could in general also consider gradients in magnon temperature (when magnons can be separated from electrons), density, chemical content, electric polarization, etc.

or also because temperature gradients for up and down spins may be different. The fact that the temperature for up and down spins may be different is called the spin heat accumulation and may be generated due to spin dependent interaction, for instance if electrons with different spins interact differently with phonons. Kimling and Cahill[160] argue that the presence of a spin heat accumulation may significantly enhance spin currents. One is also often interested in the spin accumulation $\mu_\uparrow - \mu_\downarrow$ rather than the spin current itself because it gives information about the spin polarization of conduction electrons at a specific location. In open circuit conditions such as in a thin film, charge currents relax after a few attoseconds[160] and lead to a charge accumulation. Kimling and Choi argue that this charge accumulation does not contribute much to the generated spin accumulation via the spin dependence of conductivities. However a spin accumulation can still exist in general due to spin currents (or local effects such as demagnetization[93]). In steady state, this spin accumulation will be mostly localized at the interfaces just as charge accumulation. This is shown in figure 3.3 in the presence of a temperature gradient*. The spin accumulation reduces exponentially as one goes away from the interface in a characteristic length l_s called the spin diffusion length (noted λ in the figure). In the ferromagnet, the spin accumulation has different signs on each side of the layer just like the charge accumulation due to the normal Seebeck effect. Because of the continuity of the spin dependent chemical potential at interfaces, there is a spin accumulation in a neighboring layer even if it is not ferromagnetic itself[159]. That way spin may be injected in a normal metal. In general, spin can not only be injected by conduction electrons as considered here but it can also be transported by magnons because of interfacial electron-magnon scattering[128,165,166] or even phonons[167]. It has been predicted that phonons can transport spin over very long distances (millimeter length scale) in insulators but the authors argue that the amplitude of the corresponding spin current might be small at room temperature[167]. This has never been investigated experimentally yet.

Choi and his coworkers measured the spin accumulation created in copper in various Ferromagnet(ferrimagnet)/Cu structures as a function of time after the ferromagnet was irradiated by a single (pump) laser pulse with duration around a picosecond[165,168–170]. The copper layer have thicknesses of at least one hundred nanometers such that the light from the probe pulse cannot reach the ferromagnetic layer, but it is still smaller than the spin diffusion length of copper (around 400nm[165]) such that a signal can be observed. The diffusive transport of the spin current in the copper layer can still change the amplitude and shape of the observed spin accumulation as a function of time[168]. The results are shown in figure 3.4. Choi and coworkers showed

*In this figure, the Seebeck coefficients have opposite signs in FM and NM. The heat flow is continuous at the interface but because the heat conductivities of both materials are different, this leads to a different temperature gradient at the interface and thus a difference of chemical potential $\Delta\mu$ due to the Seebeck effect.

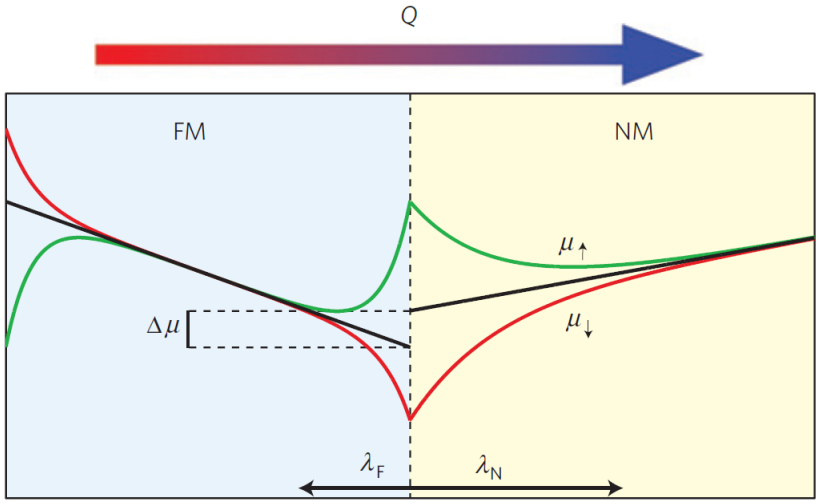

Figure 3.3: Representation of the spin dependent chemical potentials in a structure where a ferromagnetic metal (FM) is in contact with a non magnetic metal (NM) in the presence of a heat current $Q = -\kappa\partial_z T$. λ_F and λ_N are the spin diffusion lengths of FM and NM respectively. Figure taken from reference 163.

that the observed spin accumulation is mostly due to bulk spin generation because of electron-magnon scattering[128] (which can also be understood in a theory of electron-spin scattering where magnons are neglected[92,93]). Then a spin accumulation is generated in the ferromagnet at a rate proportional to $\mathrm{d}M/\mathrm{d}t$ where M is the magnetic layer magnetization amplitude. This spin accumulation is then assumed to obey a diffusive transport equation because the copper layer is thicker than the mean free path of copper (around 40nm[172]). They show that there is a smaller contribution due to SDSE but which lasts for hundreds of picoseconds that can be used to exert a torque on a magnetic layer[169]. The measured spin accumulation then has a positive peak at first due to the ultrafast demagnetization, followed by a second peak of opposite sign due to the remagnetization of the layer. In ferrimagnetic samples, one needs to consider two contributions to the magnetization. They showed that, for GdFeCo, the second peak cannot be only due to SDSE or remagnetization, but rather to the continuing slower demagnetization of gadolinium[105]. This is further evidenced by the fact that increasing the gadolinium concentration of the alloy, the amplitude of the second peak is increasing. We note that, doing so, the amplitude of the first positive peak is slightly reduced, possibly because gadolinium starts demagnetizing at the same time as iron and cobalt, thus counteracting the effect of these two components. Similar agreements were also obtained for iron, nickel and cobalt, thus further supporting the significant role of electron-magnon scattering in ultrafast demagnetization[165]. We note that in the measurements of Choi and Min presented in figure 3.4 (b), the second peak seems to reach its minimum (maximum amplitude) around 3 ps. This is because the spin accumulation measurements are

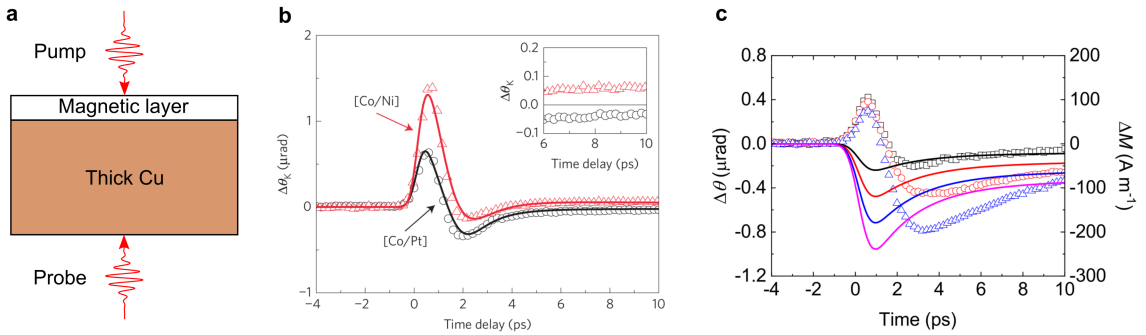

Figure 3.4: Kerr rotation measured on the copper side of various ferromagnetic(ferrimagnetic)/copper samples as shown in (a). The pump excites the magnetic layer while the spin accumulation is probed on the other side of the sample. Figure (b) is for ferromagnetic multilayers [Co/Ni] and [Co/Pt] as indicated while figure (c) is for ferrimagnetic layers $Tb_{20}Fe_{62}Co_{18}$ (black squares), $Gd_{22}Fe_{68.5}Co_{9.5}$ (red circles) and $Gd_{25}Fe_{65.6}Co_{9.4}$ (blue triangles). Solid lines are calculations considering both SDSE and spin currents due to ultrafast demagnetization in figure (b) while in figure (c) only the SDSE is considered for various SDSE coefficients. The spin accumulation due to the ultrafast demagnetization can be obtained from the change of magnetization as a function of time but this cannot be observed for GdFeCo alloys because one only probes the magnetization of Fe and Co[171]. Figures taken from references 169 and 170.

performed on the other side of the thick copper layer where spin transport is occurring. Choi and Min[170] actually estimate that the minimum of the second peak of the spin generation in the ferrimagnetic layer happens at around 1 ps.

Because of the thick layers (thicknesses are greater than the mean free paths[160]) and the relatively long laser pulse duration (∼1ps) used by Choi and his coworkers, it is reasonable to consider that electrons are thermalized (it is not necessarily so reasonable for phonons[62]) and that the transport is diffusive. However, in many cases, one uses laser pulses with a duration of around fifty femtoseconds and thin films thinner than the mean free path. In such cases, one may resort to the theory of superdiffusive spin transport[173,174] or solving the Boltzmann equation with less restrictive approximations[175,176] (such as thermalized distribution functions, or close to the thermalized ones, relaxation time approximations, etc.). We highlight again the fact that these approaches are fundamentally semiclassical, even though one may include quantum effects. In particular, they are not correct too far from equilibrium, especially for fast changes in time*. Both approaches rely on a transport equation for a distribution function, scattering ampli-

*The Boltzmann equation may be retrieved from the correct quantum kinetic equations if one performs the gradient approximation of the Wigner distribution function[15,29,42]. This approximation is correct when the Wigner distribution function is a slow function of time and space. Of course one may cast some doubts regarding this approximation for ultrafast dynamics.

tudes and group velocities that depend on spin and energy, and can consider electron cascades. For small systems and short period of times after the laser excitation (up to a few hundreds of femtoseconds) one can also use fully quantum calculations based on rt-TDDFT[177] or a density matrix approach[178] but we note that these approaches have not been able to include nuclei correctly yet. Here we note that these two works modeled a cobalt/copper interface. They were able to simulate the ultrafast injection of spin from the ferromagnetic layer into copper and it is also remarkable that both approaches predicted a backflow of minority spin from the copper layer into the cobalt layer.

It had been argued by Eschenlohr *et al.*[179] that this transport of angular momentum out of the magnetic sample could be sufficient to explain the observed laser induced ultrafast demagnetization. In their experiment, they compared the demagnetization of a nickel layer which was either capped with a thin platinum layer or by a thick gold layer such that it would significantly reduce light absorption in the magnetic layer. They could reproduce their experiments using the theory of spin superdiffusion notwithstanding with a smaller demagnetization amplitude. However, this mechanism cannot possibly be the only contribution to ultrafast demagnetization as demagnetization is also observed if the magnetic layer is sandwiched in between two insulating layers (see for instance reference 180). Nonetheless, this mechanism definitely plays a significant role as such ultrafast transport of angular momentum (or its consequences) has been observed on multiple occasions[180–186]. It is however worth mentioning that this mechanism is faster than the local transfer of angular momentum as one can reach demagnetization times around 40fs for nickel[180] and it has been shown that such transport dominates the demagnetization process at earlier times[183]. Finally, it has also been shown that light itself is not directly required. This was already expected from the results of Eschenlohr *et al.* (where seven percent of the light was still absorbed by the magnetic layer) but was clarified by Bergeard *et al.*[187] in samples with a thick copper layer (from 80 to 300nm) on top of a [Co/Pt] multilayer. That way the light absorption in the magnetic layer is already reduced by two orders of magnitude with 80nm of copper but an ultrafast demagnetization (with different amplitudes) was still observed up to 300nm of copper. Thus, what matters for ultrafast demagnetization is not the light itself but only the ultrafast transfer of energy to the electrons, no matter what the stimulus is.

To conclude this part, we argue that ultrafast demagnetization is a combination of spin dependent electronic transport (including OISTR), magnon generation due to electron-magnon interaction (in the presence of spin-orbit coupling) and various spin flip scattering mechanism, mostly due to direct electron-electron and electron-phonon interactions (also in the presence of spin-orbit coupling). Transport effects are the fastest, followed by magnon generation and

then spin flip mechanism. The angular momentum eventually ends up in the lattice even though not necessarily in a few hundreds of femtoseconds as measured in reference 115 for iron. This may depend on the material itself as it was observed in GdFeCo alloys that the total electronic angular momentum is conserved for more than a picosecond[120]. Also we note that transfer of angular momentum to or from the electromagnetic field itself is negligible although its effect may be visible for several laser pulses or on a sample that is almost completely demagnetized. Nevertheless, there are still some open questions[188] and the difficulty now resides in a better experimental and theoretical characterization of these various mechanisms.

3.4 Ultrafast magnetization reversal

Ultrafast magnetization reversal due to an ultrashort laser pulse excitation was first observed by Stanciu *et al.*[189]. In their work, they were able to reverse the magnetization of a ferrimagnetic GdFeCo alloy depending on the polarization of the laser pulse. Magnetization would reverse for one circular polarization and not for the other while linear polarization would only induce the formation of a multidomain parttern (for multiple laser shots). This AO-HDS was also later observed in a variety of other ferromagnetic and ferrimagnetic materials with perpendicular magnetic anisotropy[190,191]. A typical experiment for a [Co/Tb] multilayer is shown in figure 3.5. However, it was realized that there are actually two different mechanisms[192*] one where only a single pulse of any polarization is required (AO-HIS) and one where multiple pulses of circularly polarized light are necessary (AO-HDS). GdFeCo can actually exhibit both mechanisms[195] but in the case of the experiments of Stanciu *et al.*[189], where a single pulse was sufficient, it was demonstrated that the dependence on light polarization is due to Magnetic Circular Dichroism (MCD)[196] i.e. that fact that a material with a given magnetization absorbs more or less light depending on the polarization of the light (or equivalently the magnetization direction for a fixed light polarization). AO-HDS could also be explained in terms of MCD for granular media[197] and thin films[198]. Another commonly proposed mechanism for AO-HDS is the Inverse Faraday Effect (IFE) which was already demonstrated as a way to alter magnetization dynamics in materials with low absorption[199†]. Different theoretical approaches have been used to model IFE in

*We only consider magnetic materials with perpendicular magnetic anisotropy. It was discovered in 2017[193] that single pulse change of magnetization direction, which depends on the polarization axis of linearly polarized light, can be achieved in YIG:Co which has four easy magnetization axes. Also it was very recently observed that laser excitation of longitudinal optical phonons in YIG can also change the magnetization direction[194].

†The standard theory of IFE is only valid in a non absorbing medium.

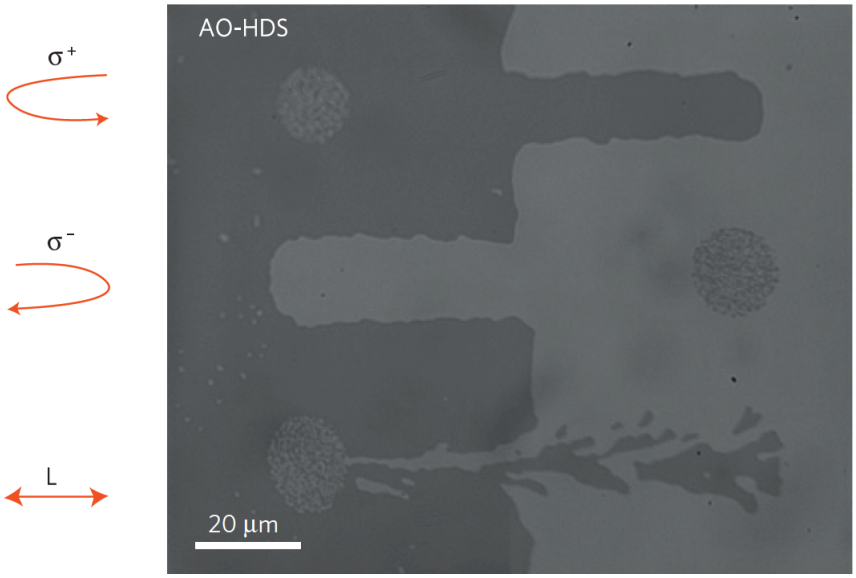

Figure 3.5: Magnetization of a [Co/Tb] multilayer observed using MOKE microscopy. A laser beam was swept on the sample, sending multiple pulses at a repetition rate of 1kHz and a given light polarization as indicated in the figure (σ^+, σ^- and L denote right circular polarization, left circular polarization and linear polarization respectively). Dark and light contrasts are due to the different orientation of magnetization. Figure taken from reference 190.

magnetic metals, either solely relying on the fact that IFE will produce an effective field[200,201] or by classical[202,203] and quantum[204–206] microscopic calculations. We also note recent *ab initio* rt-TDDFT calculations[207] where it is predicted that on top of the IFE, that only lasts during the direct interaction between light and the magnetic sample, there is another helicity dependent contribution due to absorption of the light by the material. AO-HDS is still investigated and in particular it is not clear yet, from an experimental point of view, what the exact effect of helicity is[208,209]. Finally, in the context of transfer of angular momentum discussed all along this thesis, it is also not clear whether AO-HDS is due to a transfer of angular momentum between the laser light and the magnetic material or not. It could be that helicity allows specific electronic transitions, which is what is considered in the quantum microscopic models, without actually transferring angular momentum to the system. Indeed, an electromagnetic wave with some helicity does not necessarily have angular momentum because plane waves can have helicity without carrying angular momentum[202,210,211]. Actual laser pulses have a gaussian spatial profile and so do carry angular momentum if they have a circular polarization, but the (spin) angular momentum is proportional to the derivative of the intensity profile[202] as can be obtained from equation (2.9b)[18]. In this context where angular momentum would be transferred from the

laser pulse to the magnetic system, it is predicted that the orbital angular momentum of light could induce IFE[202].

From now on, we will no longer be concerned by the helicity of light and so only focus on linearly polarized light. This seriously constrains the possibility of observing magnetization reversal. Indeed, because of conservation of angular momentum and because we argued that there is a negligible amount of angular momentum that is transferred to the electromagnetic field, the source of angular momentum that permits the magnetization reversal must come from the material itself. AO-HIS is then only expected in materials that possess two magnetic sublattices with opposite direction i.e. ferrimagnetic materials*. However, the mechanism is expected to be much faster than for AO-HDS in general, because only a single pulse of light is required. For several years, AO-HIS had only been observed in magnetic structures composed of gadolinium and some transition metals such as in Gd/Co bilayers[212]. It has now been observed for Mn_2Ru_xGa[213] and [Tb/Co] multilayers deposited on Ta/CoFeB[214]. We will shortly discuss the case of Mn_2Ru_xGa below because there is evidence that the AO-HIS mechanism in this material might share the same fundamental origin as gadolinium based ferrimagnetic structures. However, we will not discuss the case of [Tb/Co]/Ta/CoFeB because too little work has been done as of yet. There is some theoretical work based on the stochastic LLG equation which predicts a reversal of [Tb/Co] multilayers[215] but as for previous works in TbCo alloys[216], the predicted threshold fluences are too high to explain the experiments. Rather, we believe that there may be a spin current generated in the CoFeB (coupled antiferromagnetically to the [Tb/Co] by RKKY) that may cross the very thin (0.2nm) tantalum layer and cause the reversal of the multilayer as explained at the end of this section for GdFeCo/Cu/[Co/Pt] structures.

Rare Earth (RE) Transition Metals (TM) ferrimagnetic alloys, and notably GdFeCo, have been studied for a long time in the context of magneto-optical recording media due to their large MOKE signal[217]. They are amorphous alloys which exhibit perpendicular magnetic anisotropy. For RE such as terbium who have a non zero orbital angular momentum, this anisotropy is usually explained in terms of spin-orbit coupling due to the RE but for GdFeCo this explanation cannot hold and as far as we know, there is still not a complete explanation for this behavior[218]. An important feature of these ferrimagnetic alloys is that, because of the antiferromagnetic coupling between both sublattices, they can exhibit compensation temperatures (if they have certain

*Antiferromagnetic materials (regarding reversal of the Néel vector) can also be excluded because a reversal requires sublattices that are not equivalent. Indeed, from symmetry requirements, one sublattice has to be different in order to drive the reversal of the other sublattice. If both sublattices are equivalent, they will transfer angular momentum (to the other sublattice, phonons, etc.) in the same way and at best only a complete demagnetization can be achieved. In this case, an external source of angular momentum (coming from phonons, light, etc.) is required.

compositions) where angular momentum (at the angular momentum compensation temperature T_A) or magnetization (at the magnetization compensation temperature T_M) is zero. Below these temperatures, the total angular momentum or magnetization is dominated by the RE sublattice while above it it is dominated by the TM sublattice. Similarly, at a fixed temperature, these alloys may have compensation compositions. This implies that by changing composition or temperature, one can tune the magnetization (or angular momentum) and bring it very close to zero*. This feature has been used to modify the Gilbert damping as well as the precession frequency of the magnetization[219]. Both quantities were shown to diverge at the angular momentum temperature compensation, which is different from the magnetization compensation temperature because the RE and TM have different Landé g-factors. It was also suggested[220] that crossing the compensation temperature locally, due to a focused laser beam, could generate a demagnetization field of opposite direction (due to the reversed magnetization when the temperature exceeds T_M) to deterministically create magnetic domains and reverse them back. As far as we know, this exact mechanism has never been observed but we note that the demagnetizing field was successfully used to reverse a magnetic domain in TbFeCo with T_M close to room temperature[221]. This reversal mechanism is however rather slow (around a nanosecond), strongly depends on the energy of the pulse and does not allow the erasing of the magnetic domain with a second pulse (although, see reference 222). Faster reversal was obtained in GdFeCo due to a single laser pulse in the presence of an external magnetic field (around 200 picoseconds)[223]. For GdFeCo, the fastest way to reverse the magnetization was using single laser pulses without an external magnetic field[189] where it was shown[9], for $Gd_{25\%}Fe_{65.6}Co_{9.4}$, that the TM and RE sublattices demagnetizatize in around 100 and 400 femtoseconds respectively and the reversal is achieved with characteristic times of around 0.9 and 28 picoseconds respectively. Extrapolating the fitting function of Radu *et al.*, this leads to the total magnetization crossing zero in around 71 picoseconds and a complete reversal in around 150 picoseconds. This qualitatively agrees with the recent results of Wang *et al.*[224]. The experimental dynamics of GdFeCo observed by Radu *et al.* using Xray MCD (XMCD) is shown in figure 3.6. The observed different dynamics for both magnetization sublattices, also estimated to happen in Mn_2Ru_xGa[225], is fundamental for the magnetization reversal because it prevents a loss of memory of the original spin orientation and so permits the deterministic character of the reversal mechanism. It is sometimes characterized in terms of the relaxation time $\tau_R = \mu/(2\alpha\gamma k_B T)$[226] of each sublattice, where μ is the atomic magnetic moment, α determines the loss of angular momentum to the lattice via all pos-

*In practical situations, chemical inhomogeneities will lead to the formation of areas where the composition is above the compensation point while in other it will be below.

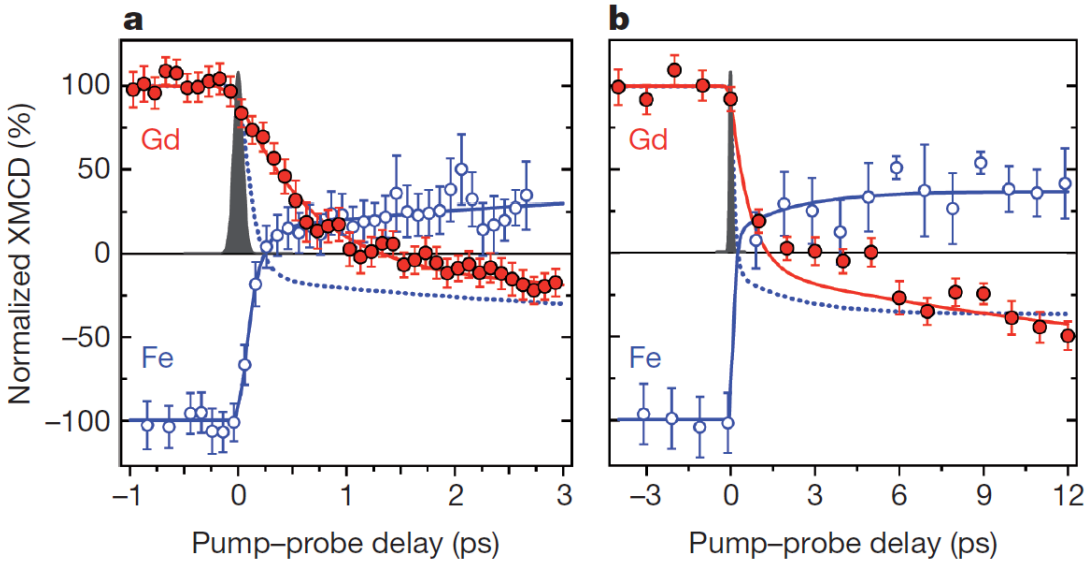

Figure 3.6: Magnetization dynamics of both sublattices of a GdFeCo alloy as observed using XMCD for a short timescale (a) and a longer one (b). Figure taken from reference 9.

sible mechanisms (i.e. Gilbert damping) and γ is the gyromagnetic ratio. What this essentially means, and it is confirmed from theoretical calculations using stochastic LLG[9], is that angular momentum is lost faster if the effective coupling to the lattice is higher and if there is less angular momentum to dissipate. It is then also often argued that in the very early stage of the AO-HIS dynamics (first few hundreds of femtoseconds), in either Mn_2Ru_xGa[227] or GdFeCo[226–228], both magnetic sublattices essentially demagnetize independently and angular momentum is then lost in the lattice. Although we agree that the demagnetization rate is fundamentally different for both sublattices because of their different atomic magnetic moments and differents couplings, we argue that both demagnetizations are not independent and that angular momentum mostly remains in the electronic degree of freedom. Indeed, it was measured by Bergeard *et al.*[120] that the total electronic angular momentum in a GdCo alloy (close to its angular momentum compensation) is conserved for at least a picosecond while it is lost in less than a picosecond for a TbCo alloy, potentially due to its greater spin-orbit coupling*. Hennecke *et al.*[125] performed similar measurements for GdFeCo and concluded that a complete transfer of the total electronic angular momentum to the lattice is achieved within the first few hundreds of femtoseconds because of the higher spin-orbit coupling of cobalt compared to iron. Their argumentation is based on the assumption that there is no transfer of angular momentum between gadolinium and the TM sublattice at these timescales[125]. However it has been observed that such an exchange of angular

*This could explain why AO-HIS has never been observed in such materials excepted transiently[229].

momentum happens within the first picosecond[10,230]. So we believe their argumentation is not valid and conclude that one cannot directly generalize the results of Dornes *et al.*[115] to another material than pure iron because other interactions and transfer of angular momentum channels might come into play. Rather we will argue that in GdFeCo and also probably in Mn_2Ru_xGa, the total electronic angular momentum is mostly conserved at this timescale. In this context, and because of the results of Choi and Min[170] which show that conduction electrons are being spin polarized by both magnetic sublattices, it seems necessary to include explicitly conduction electrons and their exchange of angular momentum with localized spins. This seems even more plausible considering that the ultrafast demagnetization happening right before the reversal might share the same nature than ferromagnetic materials, where, as we argued, electron-magnon scattering plays a significant role. This has been considered theoretically in several works[92,231–234]. In such models, one considers both magnetic sublattices as originating from localized spins (except in reference 231) which are then coupled to conduction electrons via an Hamiltonian given by equation (3.9). For GdFeCo, different coupling parameters and different values of spin are used. Typically J is greater for TM compared to gadolinium because of their less localized nature. The other interactions are also considered, typically the spin independent electron-phonon interaction which leads to a modified 2TM now that electrons can also exchange energy with localized spins[233], and other interactions that lead to spin transfer from conduction electrons to the lattice (Elliott-Yafet scattering, direct electron-electron scattering in the presence of spin-orbit coupling, impurity scattering, etc.) are treated phenomenologically through a spin-lattice relaxation time τ_s. Then the conservation equation for angular momentum of the conduction electrons is[92]:

$$\frac{\mathrm{d}s_z}{\mathrm{d}t} + \boldsymbol{\nabla}\cdot\mathbf{J}_{s_z} = -\frac{\mathrm{d}S}{\mathrm{d}t} - \frac{s_z(t) - s_z^{ie}(t)}{\tau_s} \tag{3.27}$$

Where s_z is the spin angular momentum* of the conduction electrons along the magnetization direction z, S is the total spin angular momentum of localized spins and $s_z^{ie}(t)$ is the (instantaneous) value of s_z if the conduction electrons were at equilibrium ($\mu_\uparrow = \mu_\downarrow$) at the electronic temperature $T_e(t)$ at a given instant t. The last term is then similar to what one has in the self-consistent Bloch equation[94,95] except that it is introduced phenomenologically here. We also added a current term which exists in general[93]. Because the spin value of the localized spin may be different than one half, there is not in general a single conservation equation for the localized spins. This will be discussed in some detail in chapter 5. The general picture of such models is depicted in figure 3.7 in the absence of current (local model). A laser pulse may heat up the con-

*Orbital angular momentum of the TM is neglected in these theories (although see reference 234 for a discussion).

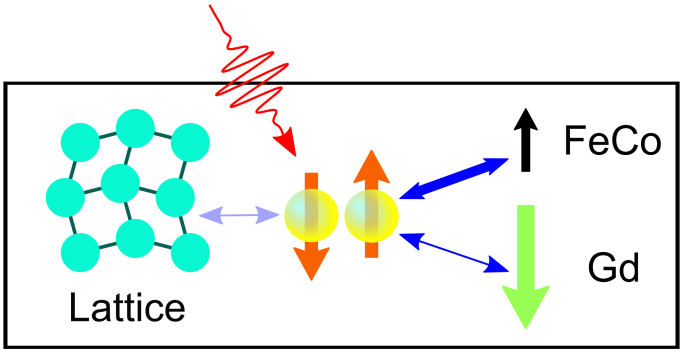

Figure 3.7: Representation of the transfers of energy and angular momentum for a model of AO-HIS in GdFeCo. A laser pulse transfers energy to conduction electrons (middle) which can then exchange energy and angular momentum with the lattice (left) and localized spins (right). The light blue arrow represents the fact that energy and angular momentum transfer with non electronic degrees of freedom is smaller than with localized spin (An exchange energy of around $\varepsilon = 10^{-21}$ joules[9] leads to a characteristic time of $\hbar/\varepsilon \sim$100 femtoseconds while the electron-phonon relaxation time is usually around a picosecond[58]). The transfer with TM is greater than with gadolinium because the magnetic d electrons of the transition metals are less localized.

duction electrons very quickly which will allow certain transitions to happen, transferring energy and angular momentum to the lattice and the localized spins. The transfer of angular momentum to the localized spin is given by $-\mathrm{d}S/\mathrm{d}t$ and the one to the lattice is $-(s_z(t) - s_z^{ie}(t))/(\tau_s)$. Because s-d Hamiltonians conserve the total angular momentum (it commutes with $\sum_i \mathbf{S}_i^{\mathrm{RE/TM}} + \mathbf{s}_i$), it is necessary to consider a mechanism to dissipates angular momentum, i.e. the transfer of angular momentum to the lattice, otherwise the model cannot reproduce magnetization reversal. However, at a short timescale (say a few hundreds of femtoseconds), this is not relevant to describe the magnetization dynamics[233]. Gridnev shows that at these timescales, neglecting the spin-lattice relaxation time that is set to 0.1ps, the spin angular momentum in the conduction electrons remains almost constant. Also, even though this spin-lattice relaxation time is small (and in agreement with the conclusions of Hennecke *et al.*[125]) most of the angular momentum still remains in the electronic system before 1 ps in these simulations[92,233,234]. This means that the angular momentum in one sublattice is almost directly transferred to the other sublattice $\mathrm{d}S^{\mathrm{RE}}/\mathrm{d}t \simeq -\mathrm{d}S^{\mathrm{TM}}/\mathrm{d}t$. Then, below the compensation temperature T_A, when there is more angular momentum in RE than in TM, the rare earth demagnetizes slower only because it has more angular momentum and not so much because the coupling parameters are different. The opposite is then expected above T_A. As noticed by Gridnev, this is not in disagreement with the results of Radu *et al.* because in the latter work, they observed the magnetization dynamics be-

low the compensation temperature. As far as we know, magnetization dynamics of the **reversal** of GdFeCo above its compensation point has never been reported although it has been reported that the magnetization reversal is more difficult above the compensation temperature than below it, and the required energy to achieve reversal is lower close to the compensation[235,236] (see also references 233, 234 for an explanation in this framework). It is also understood that gadolinium can in general demagnetize faster than TM, even in models that do not consider conduction electrons[228,237]. In all cases, one may reach a transient ferromagnetic like state as observed in figure 3.6 but it does not necessarily leads to a reversal of the total magnetization.

On longer timescales when spin dissipation becomes important, Gridnev shows[233] that reversal of the magnetization does occur. But it occurs above the compensation temperature only in a range of temperature that is higher for smaller values of τ_s[92] (but it also depends on the other parameters of the model[233]). With a spin-lattice relaxation time of 0.1ps, Gridnev shows that one can reverse magnetization for temperatures up to 70 Kelvins higher than the compensation temperature, which qualitatively agrees with what is observed experimentally[227]. For Mn_2Ru_xGa, τ_s is estimated to be around 10ps[227] which is then two orders of magnitude higher than for GdFeCo[233]. This could explain why no AO-HIS of this material is observed above its compensation temperature. We note that Baral and Schneider[231] used a similar model, without resorting to the Markov and secular approximations, and considering TM electrons as completely itinerant. They found that a criterion for magnetization reversal is the existence of a compensation temperature but do not discuss the importance of the initial temperature compared to this compensation temperature.

Earlier models of AO-HIS did not include the conduction electrons but only a direct exchange between localized spins[9,84,238–241]. We note however that the different couplings between spins of different nature was already taken into account and judged of importance in reference 241. An ultrafast magnetization reversal was also modeled but we believe that the microscopic mechanism was not sufficient because it cannot explain, for instance, the generation of spin currents[170]. However, even the current models including the role of conduction electrons are still not complete because they do not take several important effects into account such as the direct spin lattice coupling for localized spins in ferrimagnetic materials containing terbium (see the discussion in reference 92). Nevertheless, the role of direct exchange interaction between the less localized spins of TM is not clear and has been required to model magnetization reversal in multilayers[242*].

It was quickly understood that, just as in ultrafast demagnetization, the main role of the light

*Of course the problem is more complicated for TM because of the hybridization between sp and d bands. But if one wants to model such materials with a localized picture of spins, it seems reasonable to include a direct exchange interaction.

pulse is to quickly heat up the system to bring it out of equilibrium[238]. It was shown however that femtosecond laser pulses were not a requirement but that laser pulses with durations in the picosecond range are sufficient[228,243]. Also it was predicted[244] that one could reverse back the magnetization in GdFeCo with a second femtosecond laser pulse if it is delayed by a few picoseconds with respect to the first one, i.e. before the system reaches thermal equilibrium. However, so far, the minimum delay required between those two pulses to create a magnetic domain and reverse it back is 300ps[224]. In Mn_2Ru_xGa, however, this delay is much shorter and around 10ps[245].

Because fast heating is the only requirement for ultrafast magnetization reversal to happen in GdFeCo, it is actually not required to have a direct interaction between light and the magnetic material, similarly to ultrafast demagnetization. It was then observed that one could reverse the magnetization of GdFeCo using electronic pulses generated by laser induced hot electron generation* in a metallic layer[236,246] or using a photoswitch[247]. At the same time, it was also discovered that one could reverse a ferromagnetic [Co/Pt] multilayer with a single pulse of light by depositing it on a GdFeCo layer, taking advantage of the AO-HIS of the latter material[248]. Both magnetic materials were still strongly coupled thus such a reversal was not unexpected. However, Iihama *et al.*[249] discovered that one could reverse a ferromagnetic [Co/Pt] multilayer using the combined action of ultrafast heating and a spin current. The spin current can be generated during the AO-HIS of GdFeCo layer as observed by Choi and Min[170] which is deposited on top of a Cu(10nm)/[Co/Pt] structure (number in parenthesis always mean thicknesses). The ten nanometers of copper ensures that the observed reversal of the [Co/Pt] multilayer cannot be due to some magnetic coupling (such as RKKY or from dipolar origin). The mechanism for the single laser pulse magnetization reversal of the ferromagnetic multilayer may be explained by a combination of AO-HIS of GdFeCo[92,233,234], spin transport in copper and spin transfer in the ferromagnetic layer experiencing ultrafast demagnetization[93,128]. This is summarized in figure 3.8 and will be discussed extensively throughout this thesis.

3.5 Conclusion

We started this chapter by reviewing out of equilibrium phenomena in non magnetic metals

*Because charge currents disappear at the attosecond time scale, it might be more accurate to talk about heat pulses even though this heat pulse is composed of a charge current of hot electrons in one direction and a charge current of cold electrons in the other.

and how one can model these problems using the 2TM or its generalizations. We then moved on to an introduction of the basic concepts of magnetism and how one usually describes magnetization dynamics when the system is at equilibrium with an external reservoir. In particular, the stochastic LLG assumes that each (classical) atomic spin is at equilibrium even though the complete spin system is not at equilibrium. We then reviewed ultrafast magnetization dynamics where such approaches to magnetization dynamics is not sufficient for a complete description of the physics at play. We also reviewed the potential local angular momentum transfer channels that can explain ultrafast demagnetization and concluded that electron-magnon scattering has a predominant role in this phenomenon, together with other interactions involving electrons and phonons in the presence of spin-orbit coupling. However, we also reviewed other causes of ultrafast demagnetization which involves ultrafast transport of spin angular momentum such as spin superdiffusion or OISTR. Finally, we reviewed how magnetization can be very quickly reversed using either laser pulses, hot electrons or ultrafast demagnetization plus spin currents. In the case of ultrafast magnetization reversal induced by heating only, in ferrimagnets, we showed that one can understand the actual results in GdFeCo and MnRuGa using a theoretical approach[92] that involves conduction electrons through itinerant/localized spin coupling. In particular, we cast some doubts on the fact that most of the angular momentum may leak into the lattice for these two systems at the timescale of a few hundreds of femtosecond, supporting the view of Bergeard *et al.*[120] and not the one of Hennecke *et al.*[125] (even though the spin-lattice relaxation time might be shorter in GdFeCo compared to GdCo).

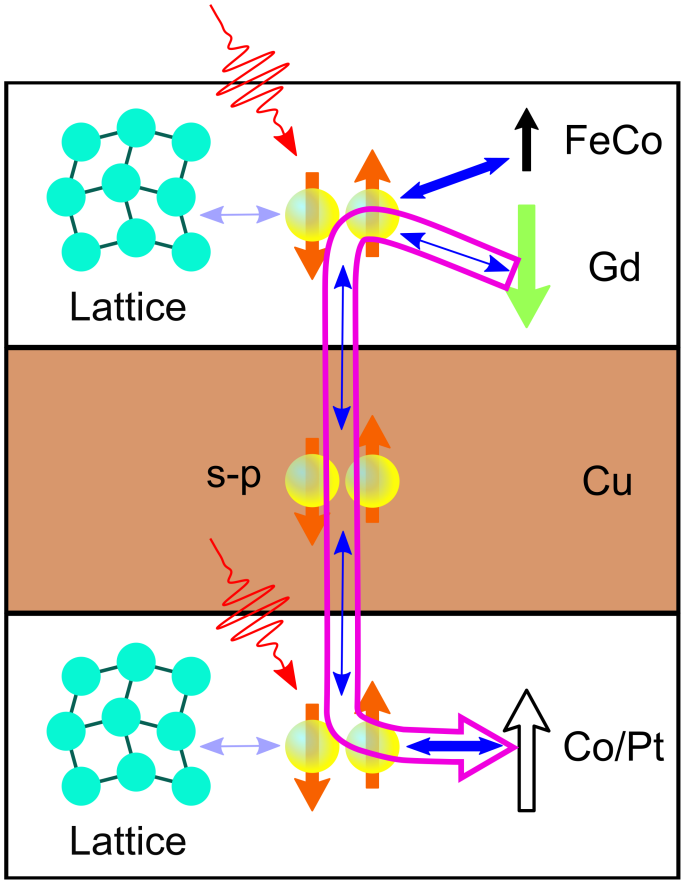

Figure 3.8: Representation of the transfers of energy and angular momentum for a model of AO-HIS (GdFeCo) and single pulse magnetization reversal of a ferromagnetic layer (Co/Pt). The color code is the same as in figure 3.7 except that there are two additional layer: a metallic (Cu) layer in which there is only spin transport (also possibly with some losses of angular momentum in the lattice if the layer thickness is not negligible compared to the spin diffusion length of the material) and a ferromagnetic layer (Co/Pt) where the mechanism is similar to the one for the ferrimagnetic layer except that there is only one magnetic lattice. The main angular momentum transport channel that explains the magnetization reversal of the ferromagnetic layer is highlighted by the open purple arrow.

Chapter 4

Experimental Methods

In this chapter, we will present the experimental setups and methods that have been used in the context of this thesis. We first start by a brief description of the types of samples that were used and we continue by the description of the optical setups that have been used to excite and probe the magnetization of our samples.

4.1 Samples characterization

The studied samples were grown using physical vapor deposition by Michel Hehn and Jean-Loïs Bello. The substrates were glass for all measurements except for the dynamics measurement presented in chapter 8 where double sided polished sapphire $(11\bar{2}0)$ substrates were used instead. Five nanometer of tantalum are always deposited first on the substrate as a buffer layer and five nanometers of platinum or tantalum are always deposited at the end as a capping layer to prevent oxidation of the materials. The magnetic materials that were grown were either $\mathrm{Gd}_x(\mathrm{Fe}_{90\%}\mathrm{Co}_{10\%})_{1-x}$ alloys where subscripts indicate the atomic concentrations in percent, or $\left[\mathrm{Co}_x\mathrm{Ni}_{(1-x)}(a)/\mathrm{Pt}(b)\right]_n$ multilayers where a and b indicate thicknesses in nanometers and n is the number of repetition of the bilayers. An additional cobalt layer is usually grown on top of the multilayer itself such that the material at the top and bottom of the multilayer is cobalt.

GdFeCo usually had a thickness fixed to five nanometers and was always deposited in between at least five nanometers of copper. It was realized that this configuration helps providing perpendicular magnetic anisotropy (PMA) to such thin layers and for alloy concentrations x between twenty to thirty four percents.

The ferromagnetic properties (anisotropy, magnetization and Curie temperature) can be tuned by changing the thicknesses b of platinum and the ferromagnetic alloy composition x and thickness a[250–254]. In the ferromagnetic multilayer, PMA mainly originates from interfacial anisotropy due to the induced magnetization in platinum by the ferromagnetic atoms at the interface[255].

The static magnetic properties where monitored using MOKE (introduced below) to obtain the coercive fields and verify that the sample indeed has PMA. When we needed magnetization or the Curie temperature, we used vibrating-sample magnetometry. Typical hysteresis loops obtained for GdFeCo and [Co/Pt] multilayers obtained with MOKE are shown in figure 4.1. The hysteresis loop on the left for $Gd_{27.3\%}FeCo(5)$ has a rather high coercive field compared to

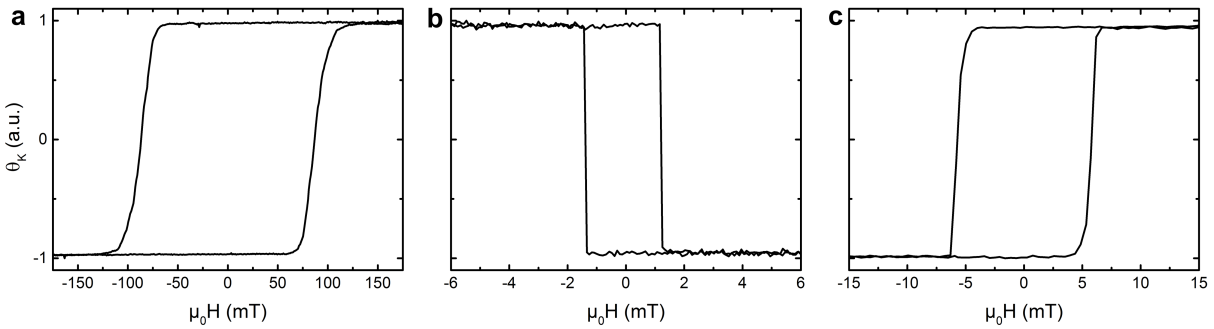

Figure 4.1: Magnetic hysteresis loops of three different magnetic samples obtained using MOKE. The measured Kerr rotation signal θ_K, proportional to the magnetization of the sample, has been normalized. The samples are (a): Glass / Ta(5) / Cu(5) / $Gd_{27.3\%}FeCo(5)$ / Cu(5) / Ta(5); (b): Glass / Ta(5) / Cu(5) / $Gd_{33\%}FeCo(5)$ / Cu(5) / Ta(5); (c): Glass / Ta(5) / Pt(4) / Cu(10) / $[Co(0.6)/Pt(1)]_2$ / Ta(5). Thicknesses in nanometers are indicated in parenthesis.

$Gd_{33\%}FeCo(5)$ in the middle because the alloy composition is very close to the compensation composition[236] which was found to be around 27% in these samples with copper interfaces. The hysteresis loop in the middle is inverted because the alloy magnetization is dominated by gadolinium which is not probed at optical wavelenghts.

4.2 Laser pulse characterization

Three different sources of laser light were used in this work. A cw helium neon laser (633nm wavelength), a Ti:sapphire femtosecond laser source with regenerative amplifier and an Yb femtosecond fiber laser with regenerative amplifier and optical parametric amplifiers (OPA). Not

much characterization is required regarding the cw laser because we only need to adjust its intensity with a neutral density filter and set its polarization with a polarizer. Regarding the pulsed laser we need to characterize its spatial and temporal profile. A pulse of laser light does not have a sharp location in time and space thus the uncertainty relations tell us that it also has a certain distribution in energy and wave vector. In order to obtain the electromagnetic field that corresponds to a beam (i.e. a mode with a spatially restricted distribution and a preferred direction of propagation) such as what is generated by a laser, one needs to find solutions to Maxwell's equations with a direction of propagation that is not sharp, meaning that the beam does not have a well defined wave vector (contrary to a plane wave). However, it is still required that the uncertainty on the wave vector is still rather small such as to allow us to perform a paraxial approximation[256,257]. In this case, one sees that at lowest order in λ/w_0, the electric field of such beam with wavelength λ (and thus sharp energy) and waist radius w_0 propagating in the z direction at an instant t in vacuum is:

$$\mathbf{E}_\perp(r,z,t) = E_0\mathbf{e}\frac{w_0}{w(z)}\exp\left(\frac{-r^2}{w(z)^2}\right)\exp\left(i\left(kz-\omega t+\frac{kr^2}{2R(z)}-\arctan\left(\frac{z}{z_R}\right)\right)\right) \quad (4.1)$$

Where $r = \sqrt{x^2+y^2}$ is the distance from the axis of propagation, E_0 is the electric field amplitude, $\mathbf{e}$ is its polarization direction perpendicular to the propagation vector $\mathbf{z}$, $w(z) = w_0\sqrt{1+(z/z_R)^2}$, $k = 2\pi/\lambda$, $\omega = kc$, $R(z) = z(1+(z_R/z)^2)$ and $z_R = kw_0^2/2$. Thus the electric field is transverse and gaussian at lowest order. However, because the beam is not a plane wave (unless $w_0 \to \infty$), there must be a longitudinal component to the electric field which is given by $\mathbf{E}_z(r,z,t) = \frac{-2ir}{kw_0w(z)}\exp(-i\arctan(z/z_R))E_\perp(r,z,t)\mathbf{z}$*. However this term is of first order in λ/w_0. The transverse component perpendicular to $\mathbf{e}$ is at least of second order. For our experimental setups, we have a waist radius around 50 micrometers and the wavelength is 800 nanometers. Thus $\lambda/w_0 = 0.016$ is indeed sufficiently small such that we may consider that the electric field is purely transverse. Actually, the electric field is a superposition of plane waves with the same energy but different wave vector directions. The time averaged intensity of this electromagnetic field, as obtained from Poynting's vector in the direction of the beam propagation, is:

$$I(r,z) = I_0\left(\frac{w_0}{w(z)}\right)^2\exp\left(\frac{-2r^2}{w(z)^2}\right) \quad (4.2)$$

Where $I_0 = \varepsilon_0 E_0^2/2\mu_0$ is the time averaged intensity at the center of the beam and at the focal point. At any distance z from the focal point $z = 0$ and at a distance $w(z)$ away from the propagation axis, $I(w(z),z) = I(0,z)e^{-2}$. Thus, it is natural to define experimentally the radius

*These electric fields are given in complex notation and one should take the real part of these fields to obtain the physical fields.

of a beam spot as the distance from the center of the beam where the intensity is divided by e^2. This is the convention that is taken in this work. The intensity of the beam as it would appear in a dusty environment is shown in figure 4.2 (a). A typical beam spot, corresponding to a fixed

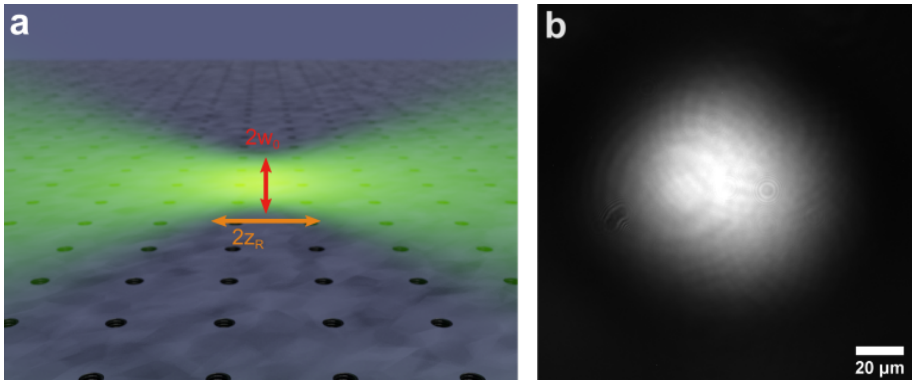

Figure 4.2: (a) Gaussian beam as it would be observed in a dusty environment. The defining parameters of the beam are shown. (b) Beam spot observed with a microscope. The diffraction fringes come from dust on the optics.

distance z, observed using the microscope setup described in the next section, is shown in figure 4.2 (b). Fitting a profile of this spot in a given direction by a gaussian function (possibly averaged over different directions or sections) gives the beam diameter of the spot. One can also use a razor blade and measure the transmitted power as a function of the distance between the razor blade edge and the center of the spot which should be an error function as given by the integral of equation (4.2). We also used a third method that we will now introduced and checked the consistency of these three methods*. The third method is based on the assumption that certain behaviors happen above a certain threshold fluence† (or certain threshold pulse energy) such as the formation of magnetic domains due to AO-HIS here. When a magnetic material with AO-HIS receives locally more energy than its threshold energy, the magnetization will reverse in

*We use different methods depending on the setup. For setups with camera we verified that using the razor blade method and a direct measurement with the camera provided similar results, for instance in one set of measurement, we obtained 86.2 ± 3.2 µm with the razor blade method and 86.6 ± 0.2 µm with the camera. This very good agreement comes from the fact that the beam spot was very circular. One may have a slight disagreement between both methods, for instance, if the beam is slightly elliptical and one does not measure the beam size along the same direction. The third method we introduce below neglects possible long timescale domain wall motion which changes the size of the domain. Nevertheless, we find that it also agrees really well with the camera measurement. For instance, for the static measurements of chapter 8, we find 92.9 ± 0.2 µm with the camera and 96.4 ± 0.7 µm with the third method.

†The fluence is the intensity integrated over the duration of the experiment i.e. the duration between two instants sufficiently before and after a laser pulse irradiates a measured sample.

this region. Because the spatial profile of the beam is gaussian, the material does not receive the same amount of energy everywhere. Magnetization will only reverse where the energy exceeded this threshold. This is illustrated in figure 4.3. The power P of the pulsed laser is determined

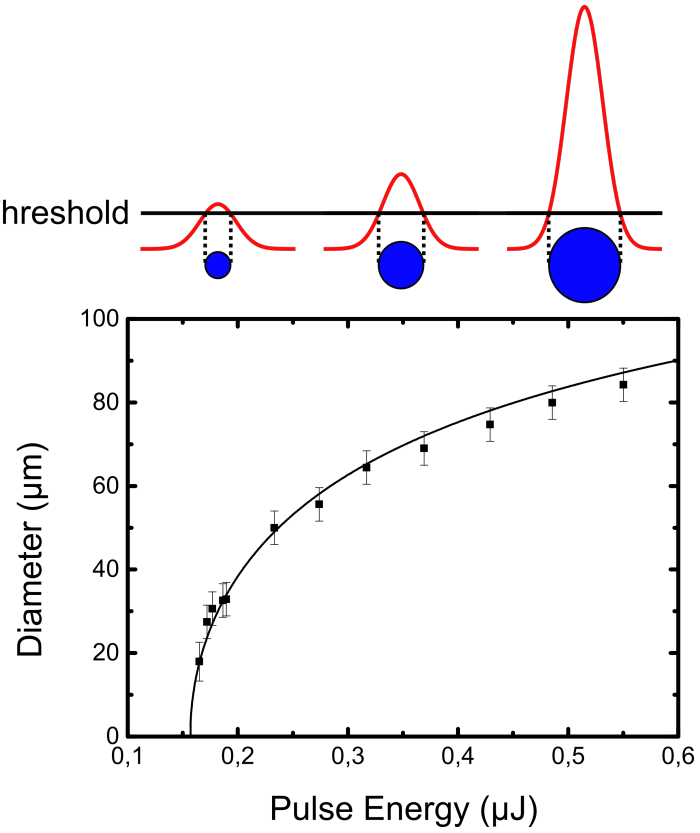

Figure 4.3: Reversed magnetic domain diameter as a function of the incident laser pulse energy. The top of the figure illustrates how the magnetic domain size changes when the amplitude of the gaussian intensity profile increases. The fit in the graph is made using equation (4.3)

using a power meter. Knowing the repetition rate f of the laser, the energy E of the pulse is given by $E = P/f$. The measured fluence $\overline{F}$ is defined using the beam radius w in the e^{-2} convention: $\overline{F} = E/(\pi w^2)$. The integral of the intensity profile $I(r, z_0)$ at the distance z_0 corresponding to the measurement (i.e. $w = w(z_0)$) over r must give the measured power P. Thus one obtains $I(0, z_0) = 2P/(\pi w^2)$ using the gaussian integral. Thus, the fluence profile is given by $F(r) = 2\overline{F} \exp\left(\frac{-2r^2}{w^2}\right)$ and one obtains that the peak fluence is twice the measured (averaged) fluence. The requirement that a magnetic domain is formed when the fluence exceeds a certain value $F_{\text{th}} = 2\overline{F}_{\text{th}}$ gives the magnetic domain diameter d as a function of the beam

diameter $D = 2w$, pulse energy and pulse energy threshold E_{th}[258]:

$$d = D\sqrt{\frac{1}{2}\ln\left(\frac{E}{E_{\text{th}}}\right)} \tag{4.3}$$

Fitting the domain diameter vs pulse energy curve with this function gives the beam diameter as well as the threshold energy. One can then also get the threshold fluence. It is preferable to work with energies rather than fluences because there is an additional source of uncertainty in the fluence as it relies on the measurement of the beam diameter (first measured with another method) on top of the laser power. Thresholds are then given as measured threshold fluences and not energies because AO-HIS depends only on the energy density provided to the material and not the total energy. Getting the energy density as a function of depth in the sample from the fluence requires knowing how the laser pulse is absorbed by the material. This depends on the optical indices of the multilayered sample, as will be discussed in the next chapter, and cannot be simply measured. Thus the interesting quantity is the measured threshold fluence. We note that the physically relevant quantity should be the threshold fluence F_{th} and not the measured one $\overline{F}_{\text{th}}$. However, it seems that it is the measured fluence that is always reported in the literature, thus we will also stick with this convention.

Up to know, we have not described the time dependence of pulsed electric fields (we just needed the repetition rate to convert experimentally measured powers into energy). Just as a beam emerges from the fact that confinement in space implies a certain distribution of wave vector (with identical amplitude given by the wavelength), a pulse emerges from confinement in time and implies a certain distribution in energy. Then just as a beam is a superposition of plane waves with fixed wavelength but slightly different directions of propagation, a pulse is a superposition of plane waves with slightly different wavelengths. A pulsed beam should be a superposition of beams given by equation (4.1) but for simplicity, we will always neglect the phase shift due to $kr^2/2R(z) - \arctan(z/z_R)$. This is reasonable because, assuming $\lambda = 800$ nm, a distance $z = 10$ cm away from the focal point, a maximum distance $r = w_0 = 50$µm away from the propagation axis, a distance variation $\Delta z = 100$ nm given by the maximum thickness of the samples that were used and a wavelength variation $\Delta\lambda = 0.1$ µm corresponding to a pulse duration of around 2 fs, we get $\Delta(\arctan(z/z_R)) \simeq 12$ and $\Delta(kr^2/2R(z)) \simeq 0.36$ which are much smaller than $\Delta(kz) \simeq 10^6$. Then, we can create pulsed laser beams by imagining a fictious amplification cavity of length L and which amplifies plane waves of pulsation ω by the following gain factor:

$$G(\omega) = \frac{\pi c}{\sqrt{2\pi}L\sigma_\omega} e^{-\frac{\omega - \omega_c}{2\sigma_\omega^2}} \tag{4.4}$$

Where σ_ω will be related to the laser pulse duration later and ω_c is related to the center wavelength λ_c of the pulsed beam by $\omega_c = k_c c = 2\pi c/\lambda_c$. The cavity is a Fabry-Pérot interferometer and thus prevents plane waves that do not have a pulsation that is an integer multiple of $\pi c/L$ from being amplified. Thus the electric field of the pulsed laser beam may be reasonably approximated by:

$$\mathbf{E}(r,z,t) = E_0 \mathbf{e} \frac{w_0}{w(z)} \exp\left(\frac{-r^2}{w(z)^2}\right) \sum_n G(\omega_n) \exp\left(i\left(k_n z - \omega_n t\right)\right) \tag{4.5}$$

Where $\omega_n = k_n c = n\pi c/L$. This electric field will give rise to pulses that are separated from each other with a distance $2L$ and thus the repetition rate of this unrealistic laser system is $f = c/2L$. When L becomes infinite, their will be only a single pulse and the sum becomes a Fourier transform. One gets* after a standard calculation:

$$\mathbf{E}(r,z,t) = E_0 \mathbf{e} \frac{w_0}{w(z)} \exp\left(\frac{-r^2}{w(z)^2}\right) \exp\left(-\frac{\sigma_\omega^2}{2}\left(\frac{z}{c} - t\right)^2\right) e^{i(k_c z - \omega_c t)} \tag{4.6}$$

Thus it is remarkable that the oscillatory part of the electric field is exactly given by a cosine with a frequency given by the center wavelength. The real factor that depends on z and t gives a gaussian envelope that propagates in time without attenuation or dispersion because we are considering that light propagates in vacuum (before irradiating the sample). This second gaussian factor allows us to define the pulse duration as its full width at half maximum. Its standard deviation is $\sigma_t^E = 1/\sigma_\omega$ where E refers to the electric field. We need to make this difference because the standard deviation for the intensity is $\sigma_t^I = 1/(\sqrt{2}\sigma_\omega)$. The pulse duration τ_l is defined as the full width at half maximum of the gaussian envelope of the intensity and is $\tau_l = 2\sqrt{2\ln(2)}\sigma_t^I = 2\sqrt{\ln(2)}/\sigma_\omega$.

This will be useful for modeling but real pulses are not always gaussian. In order to get information about the temporal evolution of the electric field, we use an optical autocorrelator to measure the intensity autocorrelation signal. A typical autocorrelation signal is given in figure 4.4. In this case, we found that a lorentzian fits the signal better. The corresponding pulse duration is around 20 fs but lorentzian fits tend to give smaller pulse duration values. In this case, one should modify the gain factor to the Fourier transform of a lorentzian. The pulse duration for the Ti:sapphire laser is around 35 fs while for the Yb laser it is around 70 fs.

*The factor $\pi c/L$ in the gain factor disappears when the sum becomes an integral: $\sum_n \frac{\pi c}{L} f(x_n) = \int f(x)\mathrm{d}x$

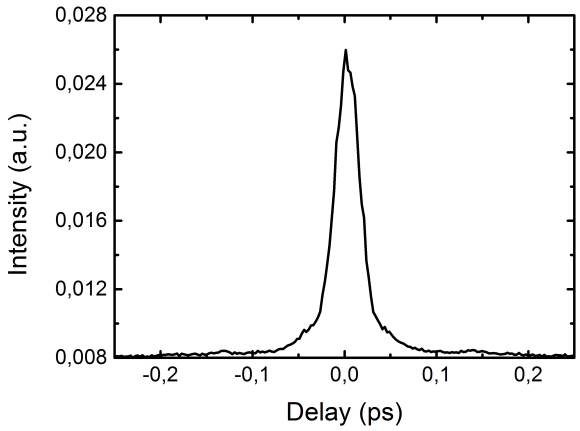

Figure 4.4: Intensity autocorrelation signal for a laser pulse of the Ti:sapphire laser.

4.3 MOKE and experimental setups

In this section, we present the four main experimental setups that have been used in this work. Those methods are quite standard and we refer to other works[259] for more details regarding the calculations underlying these methods. We will only cover the basics and the specificities of our setups. All measurements were performed at room temperature.

The theory of MOKE has been done by Argyres[260] and Oppeneer[261,262] used density functional theory to calculate magneto-optical coefficients. The idea of the theory of Argyres is to calculate the total current density generated by an electromagnetic radiation, using equation (2.11), in the presence of spin-orbit coupling and exchange splitting (and thus magnetization). Even in the presence of exchange splitting, spin-orbit coupling is required to have some MOKE signal. Then the total current density is calculated in first order in the potential vector and spin-orbit coupling. It is then found that a current density $\mathbf{J} = \boldsymbol{\sigma}\mathbf{E} + \boldsymbol{\alpha}\partial_t\mathbf{E}$ is generated by the electric field where $\boldsymbol{\sigma}$ and $\boldsymbol{\alpha}$ are conductivity and polarizability tensors with off diagonal elements proportional to the magnetization of the sample*. In this work, we are mostly interested in the polar MOKE geometry where the incident light beam is almost normal to the sample surface and the magnetization is out of plane. Working through standard electromagnetism in anisotropic media[46], one finds that the complex index of refraction for left and right circularly polarized light are different and upon reflection, the light polarization is rotated by a certain angle θ_K and acquires a certain ellipticity ε_K. It is a fundamental result that θ_K and ε_K are both proportional to

*The term proportional to the electric field should be seen as a free current term while the term proportional to the time derivative of the electric field should be seen as an electric polarization.

the magnetization of the sample M. However, the proportionality constants are not necessarily the same. It is also important to realize that MOKE is derived for equilibrium, thus, there is no guarantee that the proportionality between M and θ_K or ε_K is still valid out of equilibrium, and if it is, it is also possible that the proportionality constant varies in time. The experimental methods below are based on measuring either θ_K or ε_K. We will discuss below when this allows us to measure magnetization dynamics in the case of (out of equilibrium) time resolved measurements. At equilibrium, MOKE is sufficient to see whether a sample has PMA or not and what its coercive field is. However, when we need values of magnetization, vibrating-sample magnetometry is used.

4.3.1 MOKE magnetometry

We used MOKE magnetometry to measure hysteresis loops as presented for instance in figure 4.1. The experimental setup is depicted schematically in figure 4.5. The laser beam comes

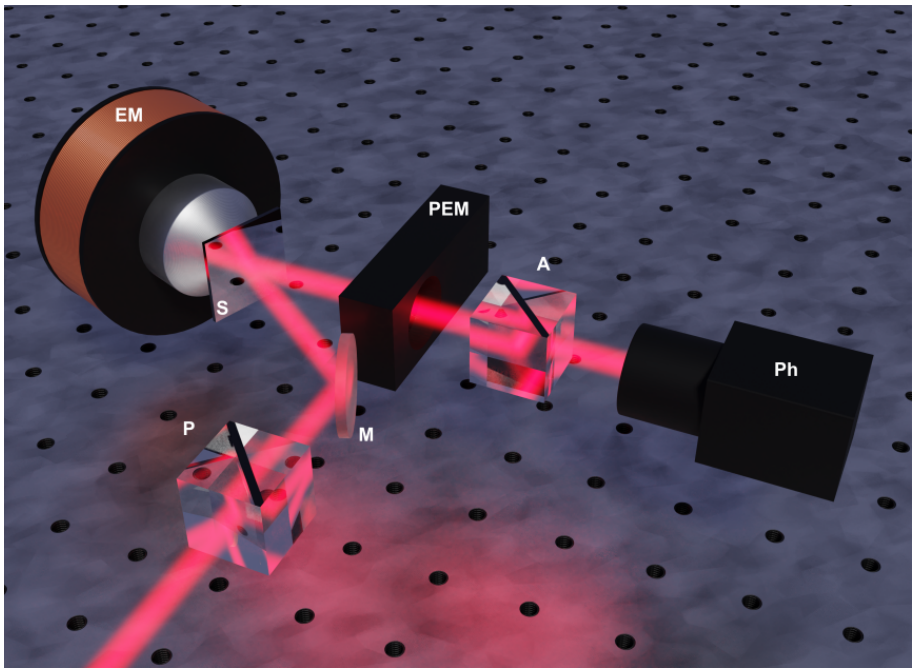

Figure 4.5: MOKE magnetometry setup with the following elements: electromagnet (EM); polarizer (P); mirror (M); sample (S); photoelastic modulator (PEM); analyzer (A) and photodetector (Ph).

from a helium neon laser and is linearly s-polarized before being reflected by the sample. The beam then passes through a photoelastic modulator (PEM) with vibration axis parallel to the table and an analyzer, at 45° with respect to the PEM axis, before being detected by a photode-

tector. The PEM frequency is 50kHz and is used as a reference frequency for a lock-in amplifier. The photodetector signal is fed into the input of the lock-in amplifier. The PEM modulation amplitude is set to 3.05 such that the second harmonic signal is optimized to give the Kerr rotation θ_K. Changing the external magnetic field with an electromagnet allows us to measure hysteresis loops. The output (complex) signal of the lock-in amplifier is given up to a certain phase. Because we only retrieve the real part of this signal (the X signal of the lock-in amplifier), one may change the lock-in internal phase such that the signal is maximized. However, there is *a priori* no way to decide if the signal (for a given external magnetic field) should be positive or negative when we study ferrimagnetic alloys because we only monitor the TM magnetization whereas the total magnetization may be dominated by either the TM or the RE. Thus in this case, the phase of the lock-in is calibrated, with a ferromagnetic [Co/Pt] multilayer or a GdFeCo alloy well below its compensation composition, such that the output signal be positive at positive external magnetic fields. Note that this calibration method relies on the fact that the Kerr rotation of the measured ferrimagnetic sample has the same Kerr rotation sign as one of the calibration sample. This is not an issue here because the only ferrimagnetic samples we studied are GdFeCo with compositions close to each other.

4.3.2 MOKE microscopy with femtosecond laser pulse irradiation

In order to see if a magnetic layer reverses its magnetization upon single pulse irradiation or not, and if it does, to see at which threshold fluence, we use MOKE microscopy to monitor the magnetization of the sample as we send laser pulses. The setup configuration is shown in figure 4.6. A pulse picker is used to send a (previously linearly polarized; not shown) single pulse through a half wave-plate and a polarizer. This allows us to control the fluence of the laser pulse. The pulse is then focused on the sample with a lens. Microscopy imaging is performed on the other side of the sample with a light emitting diode with center wavelength of around 630nm. A collector (Fresnel lens) sends the light through a field diaphragm which is then collimated by a lens. The collimated light is linearly polarized by a polarizer and send to the microscope objective with a beam splitter and a lens. After reflection on the magnetic sample, the light will acquire some Kerr rotation and ellipticity. It goes back through the objective and lens, partially crosses the beam splitter and is focused with a lens on the objective; A filter is used to prevent any laser light from reaching the Charge Coupled Device (CCD). An analyzer is put before the filter in order to complete the MOKE measurement. The polarizer and analyser must be almost crossed, such as to prevent any light that has not undergone a Kerr rotation from reaching the

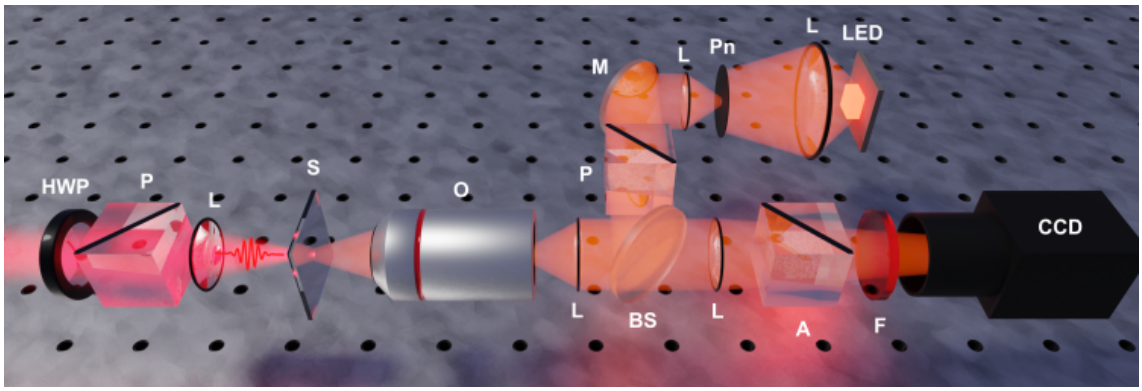

Figure 4.6: MOKE microscopy setup with single femtosecond laser pulse irradiation. The different optical elements are: half wave-plate (HWP); polarizer (P); lens (L); sample (S); objective (O); mirror (M); beam splitter (BS); pin hole (Pn); light emitting diode (LED); analyzer (A); filter (F) and charge coupled device (CCD). The color of the LED light has been changed for the purpose of illustration.

CCD. If the polarizer and analyzer are perfectly cross, no light will be transmitted to the CCD[259]. By making the difference between the light intensity for two opposite magnetizations at a given pixel of the microscope image, one gets a signal proportional to the magnetization of the sample. Typical raw images obtained on this setup by either applying an external magnetic field with a permanent magnet or after sending femtosecond laser pulses on a GdFeCo alloy (exhibiting AO-HIS) are shown in figure 4.7. The scale bars are determined thanks to a prior calibration using patterned samples of known dimensions. Because we often work with samples with two magnetically uncoupled magnetic layers, we need to know the magnetic signal of each magnetic layer. This is done in the following way: (i) finding the coercive field of individual layers using MOKE magnetometry on samples with just one magnetic layer and (ii) reproducing an hysteresis loop on the MOKE microscope setup for the bilayer structure. The change of signal obtained at a given coercive field is then proportional to the magnetization of the magnetic layer having this coercive field. Note that on samples with only one ferrimagnetic layer that is Gd dominant, one can identify the coercive fields of both layers directly from MOKE magnetometry hysteresis loops provided that the phase calibration has been done. If both magnetic layers have coercive fields that are too close to each other (a few mT), then it is most of the time not possible to distinguish both layers on our setup. We also note that the hysteresis loops performed on both setups are usually not identical, even though the wavelength of the LED and the cw laser are almost identical, because the LED does not generate coherent light and the distribution of wave vector directions is different in both setups. In order to get rid of the various non magnetic contributions to the microscope images, we always take a background image with the sample in a given

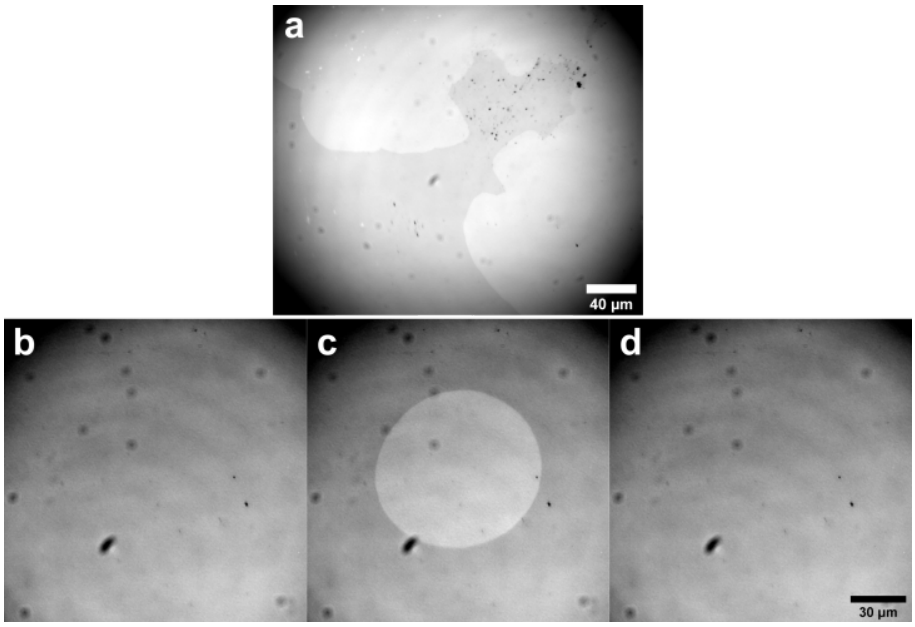

Figure 4.7: Glass / Ta(5) / Cu(5) / $Gd_{27.3\%}FeCo$(5) / Cu(5) / Ta(5) sample observed with the MOKE microscopy setup described in figure 4.6. In (a), we applied an external magnetic field such as to create a magnetic domains that is pinned on some defects. In (b), the sample is saturated. The resulting image obtained after sending a single laser pulse is shown in (c). Sending a second pulse, the magnetic domain created in (c) disappears.

magnetic configuration before sending any pulse of light and subtract this background image to any subsequent image. The images are always averaged sixteen times. After the subtraction, the contrast of the image is adjusted such that the difference between the maximum and the minimum displayed values correspond to the full amplitude of an hysteresis loop. The images are then colored using a red-white-blue ("phase") lookup table. The highest (positive) Kerr signal then appears as red while the lowest (negative) Kerr signal appears as blue. The image analysis is performed with the open source software ImageJ.

Two magnetic layers reversing their magnetization after a single pulse irradiation usually have different threshold fluences. If the fluence of an incident pulse is higher that the highest threshold fluence of these two layers, the observed domain is then a superposition of two concentric domains of different diameter. This results in a ring structure shown in figure 4.8 (a). For materials that do not exhibit AO-HIS, one usually observes a multidomain state shown in figure 4.8 (b). This results from the fact that the sample has been locally fully demagnetized and the demagnetizing field then generates random domain patterns as the sample cools down. The magnetic domains in this multidomain state can be of various shapes and sizes depending on the material itself as well as the nature and strength of the external stimuli.

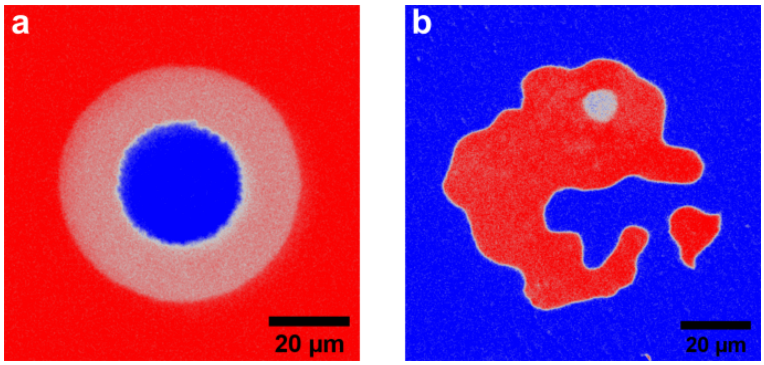

Figure 4.8: (a) Ring structure generated in Glass / Ta(5) / Pt(4) / $[Co(0,6)/Pt(1)]_2$ / Co(0,6) / Cu(20) / $Gd_{30\%}FeCo(5)$ / Cu(5) / Ta(5); The red color corresponds to the FeCo sublattice and [Co/Pt] magnetizations pointing upwards; The light red ring domain corresponds to only GdFeCo reversing its magnetization while the blue domain corresponds to both layers switching (b) Multidomain state in Glass / Ta(5) / Cu(5) / $Gd_{33\%}FeCo(5)$ / Cu(5) / Ta(5) that does not exhibit AO-HIS. The white domain corresponds two a domain that disappeared during the image averaging.

4.3.3 TR-MOKE

In order to measure magnetization dynamics, we use TR-MOKE which is a combination of MOKE with a pump-probe technique. Although we do not present many results obtained on this setup in this thesis, it was still used extensively and it allows us to introduce this technique which is essentially the same as for the TR-MOKE microscopy setup in the next section. The setup is shown in figure 4.9. In this case, the laser is continuously sending pulses at a repetition rate of 5kHZ and separated into two beams using a beam splitter. By letting one beam traveling a different distance between the beam splitter and the sample, it is possible to delay the arrival of one pulse on the sample compared to the other. Then one pulse is used to generate the out of equilibrium magnetization dynamics (the pump) while the other is used to probe it. The pump and probe beams powers are controlled using a half wave-plate and a polarizer. The probe power is fixed by the balanced photodiode linear response power threshold while the pump power is varied depending on what one wants to observe. Both beams are focused on the sample, at nearly normal incidence, using spherical mirrors such that the beam spot of the pump is roughly ten times higher than the probe beam spot. This ensures that the probed area corresponds to a roughly uniform pump fluence. The probe signal is retrieved and collimated with another spherical mirror and focused on a balance photodiode with a lens and a Wollaston prism. Because the Wollaston prism separates the s and p components of the electric field, a half wave-plate is used to balance the signal on the photodiodes. A filter is used to protect the photodiodes from

any potential signal of the pump beam. Signals from both diodes are then subtracted from each other which is (one of) the output of the device. When there is no Kerr rotation induced by the sample, this difference should be only noise if the half wave-plate was correctly set. However, if there is some Kerr rotation, there will be a bit more signal on the s component of the electric field compared to the p component (or the opposite depending on the Kerr rotation sign) and a signal can be measured. However, this signal is in practice rather small and one must resort to a modulation technique to increase the signal to noise ratio, such as what is done for MOKE magnetometry. In general, this modulation can be performed on any defining characteristic of

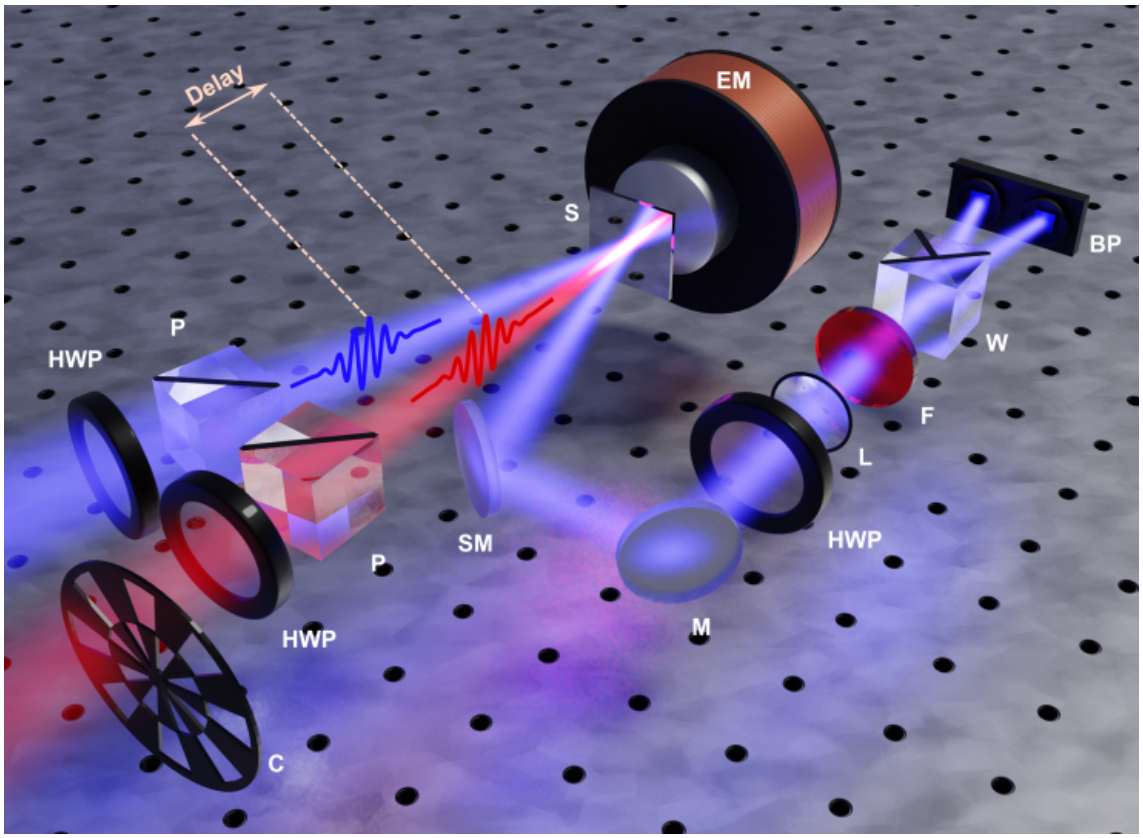

Figure 4.9: TR-MOKE setup with the following elements: half wave-plate (HWP); polarizer (P); chopper (C); sample (S); electromagnet (EM); spherical mirror (SM); mirror (M); lens (L); filter (F); Wollaston prism (W); balanced photodiodes (BP). The beam splitter separating the original beam (800 nm; red) into two beams, as well as the delay stage, are not shown. The blue (400nm; blue) probe beam is generated via second harmonic generation with a barium borate crystal (not shown). Additional spherical mirrors used to focus the beams on the sample are also not shown. The probe angle of incidence has been exaggerated for the purpose of illustration.

the beam (polarization, frequency, phase, spatial distribution, and intensity). The photoelastic modulator in our MOKE magnetometer performs a polarization modulation (by modulating the

phase of one component of the electric field). In this TR-MOKE setup, we perform intensity modulation using a chopper. If the probe beam is chopped, the balanced photodiode signal is then oscillating at the frequency of the chopper between zero and the signal one wants to measure (proportional to the Kerr rotation). The signal is then obtained using a lock-in amplifier to extract the first harmonic at the chopper frequency. By making this measurement for two opposites magnetizations, one gets a signal proportional to the magnetization*. This method can be used to measure hysteresis loops on this setup at equilibrium (if the pump beam is blocked) which is necessary to make calibrations, or one can also measure hysteresis loops as a function of pump-probe delay. To measure magnetization dynamics, it is however more convenient to chop the pump beam instead. That way, the balanced photodiodes output signal varies between a signal where the magnetization is unaffected by the pump and a signal where the magnetization is reduced. Two measurements with opposite magnetization directions are always performed in order to get rid of (some of) the signal that is not due to magnetization dynamics. From the lock-in outputs, one then obtains a signal proportional to a variation of magnetization $\beta\Delta M$, with respect to a certain initial state, that depends on the pump-probe delay. In order to make sure that this initial state is always the same, an external magnetic field is applied with an electromagnet during the measurement. A signal proportional to the equilibrium magnetization βM, with the same proportionality constant, can be obtained by chopping the probe beam and measuring an hysteresis loop. Taking the ratio of these two signals, we get the relative change of magnetization as a function of the pump-probe delay. This is shown in figure 4.10 for a $Gd_{20\%}FeCo$ alloy that does not exhibit AO-HIS. The zero time delay is obtained by fitting the results at early times with an exponential function convoluted with a gaussian function.

Soon after the measurement of Beaurepaire *et al.* of the ultrafast demagnetization of nickel, a debate started on whether TR-MOKE could be used to measure magnetization dynamics or not. Indeed, it was measured that both Kerr rotation and ellipticity do not have the same dynamics at short timescale[263–266] while they are both proportional to the magnetization at equilibrium and so should have an identical dynamics if this proportionality remains. The problem is that, compared to the equilibrium case, both the pump and the probe beams should be considered as perturbations to the system such that the measured response depends on the magnetization itself but also the pump and the probe beams[264,267]. Both beams (mainly the pump) will change the electronic structure of the sample by inducing certain transitions. Some of these transitions will affect the magnetization while others will not. However, as can be seen from the equilibrium case, MOKE does not only depend on magnetization but also on spin-orbit coupling. Thus, the

*See the discussion below about whether magnetization can be directly measured or not.

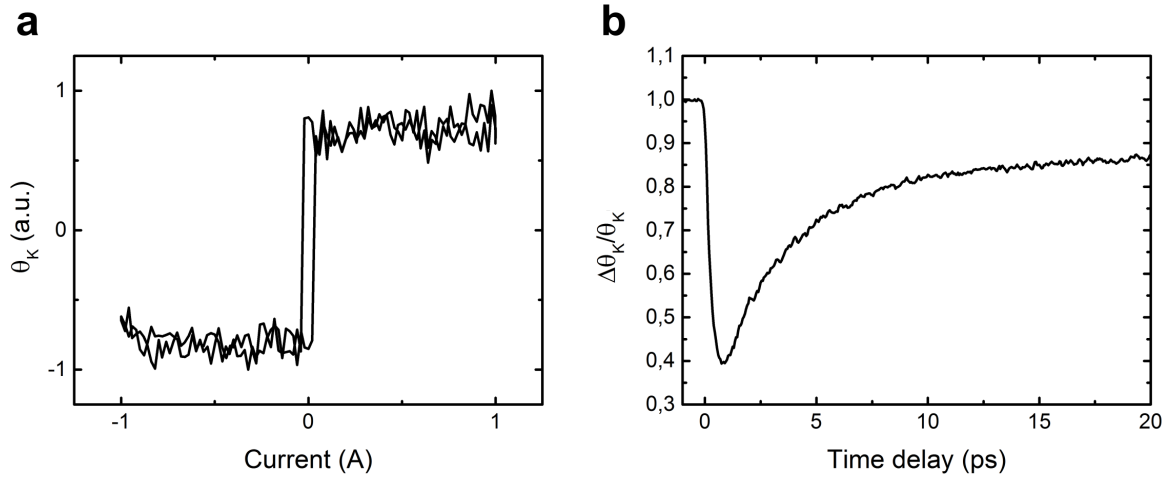

Figure 4.10: (a) Averaged hysteresis loop and (b) Kerr rotation dynamics for a Glass / Ta(5) / Cu(5) / $Gd_{20\%}$FeCo(5) / Cu(5) / Ta(5) sample as measured on the TR-MOKE setup. The hysteresis loop is given as a function of the current provided to the electromagnet.

measured MOKE signal may change because the spin-orbit dependent transitions in the system will change, and not only because magnetization changes. One can retrieve the real magnetization dynamics by assuming that the Kerr vector $\Theta_K(t) = F[M(t)] \simeq \alpha(t)M(t)$[265] where F is an unknown function, $\alpha = \alpha' + i\alpha''$ and $\Theta_K = \theta_K + i\varepsilon_K$, and one estimates the variation of both components of α by measuring both Kerr rotation and ellipticity[266]. Razdolski *et al.* then show that one can retrieve the true magnetization dynamics, provided that the magnetic film is thin compared to the light penetration depth and sandwiched in between two insulating layers. Because we work with rather thick films in general and because we do not use insulating films, this method is not applicable as is. Another way around consists in realizing that the various probe induced transitions, for a probe power sufficiently lower than the pump power, will not change the magnetization dynamics but will depend on wavelength[268]. Thus one can for instance use a probe with a different wavelength such that the transitions generated by the pump and the probe will be independent because of conservation of energy* and the probe induced transitions will be essentially the same as in equilibrium. This is what we use in this setup where the probe beam has its frequency doubled by a barium borate crystal. It is also possible to use various probe wavelengths and verify that the presumed magnetization dynamics (using the method of references 265 and 266 or not) remains unchanged.

*Of course for sufficiently short time intervals virtual transitions of any energy may happen. The problem is then to quantify the number of such transitions.

4.3.4 TR-MOKE microscopy

Another setup has been used, on the Yb laser, which is similar to the standard TR-MOKE setup except that it is also spatially resolved[221,269]. This is achieved by having the probe beam spot bigger than the pump beam spot and by imaging the probe reflection on a CCD camera. This setup is shown in figure 4.11. The pump laser pulse has a wavelength of 800 nm and its path is

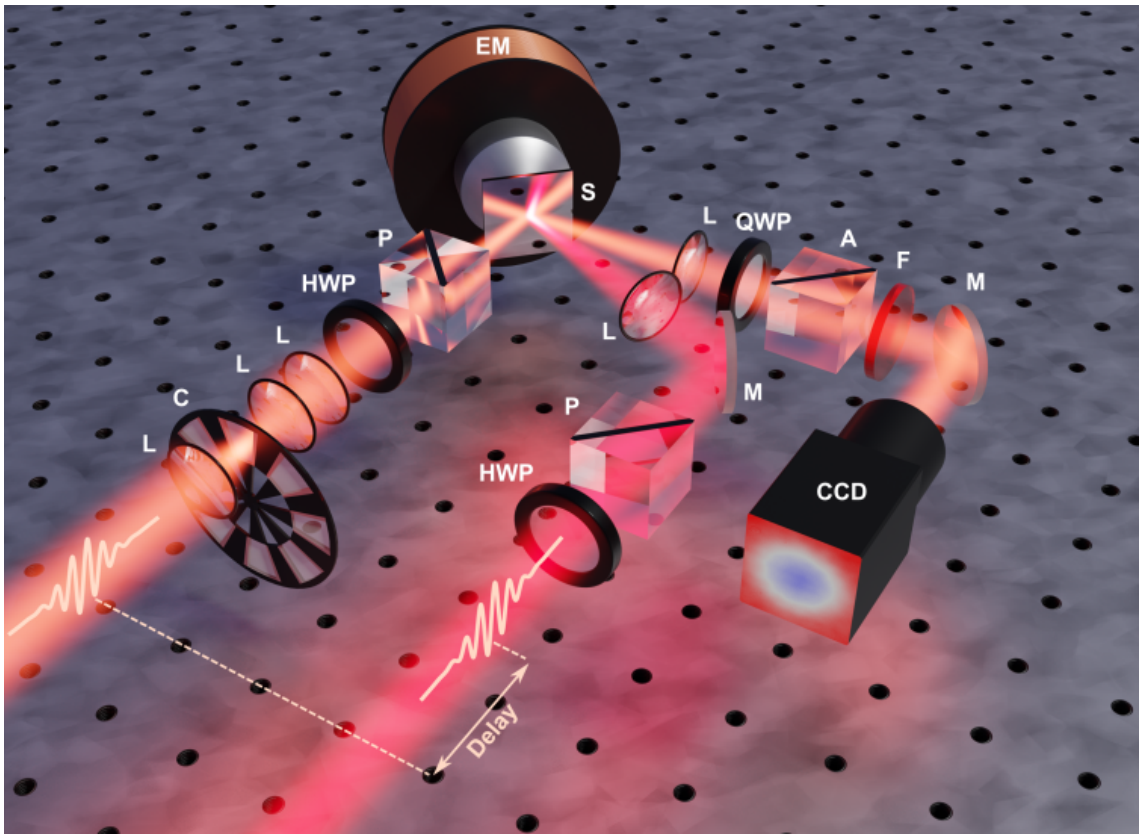

Figure 4.11: TR-MOKE microscopy setup with the following elements: half wave-plate (HWP); quarter wave-plate (QWP); polarizer (P); analyzer (A); chopper (C); sample (S); electromagnet (EM); mirror (M); lens (L); filter (F); charge coupled device (CCD). The pump (800 nm; red) and probe (850 nm; orange for the purpose of illustration) beam angles of incidence are realistic.

similar to the TR-MOKE setup except that it is focused using a lens. The pump pulse duration at the position of the sample is 100 fs. The probe laser pulse has a wavelength which was set to 850 nm, with a different OPA, for our experiments. Its path is similar to the LED light path of the MOKE microscopy setup. In particular, we did not use any modulation technique. The repetition rate is adjustable and was set to 50 kHz for the work presented in this thesis. A chopper with semi-transparent tape was used to destroy the coherence of the probe light which would create

interference patterns on the microscope images otherwise. As a result of chromatic dispersion in the tape, we measured that the probe laser pulse duration was increased to around 200 fs. This setup has been used to differentiate the magnetization dynamics of two magnetic layers in spin valve structures. The same information is in principle accessible on the standard TR-MOKE setup but the spatial resolution allows us, in principle, to directly recognize ring patterns and so greatly facilitates comparisons with static results obtained on the MOKE microscope. Moreover, one can have access to a complete set of fluence dependent dynamics in one measurement (with fluence uncertainty depending on the pump beam profile). A quarter wave-plate is used to use complex MOKE[270] which allows probing the magnetization of specific layers by measuring a certain linear combination of Kerr rotation and ellipticity *. Indeed, different magnetic layers usually have different Kerr vector directions which are determined by a single parameter. By adding a quarter wave-plate, we add an additional degree of freedom to completely cancel (in principle) the magnetic signal of any magnetic layer. This has been used on several occasions in ultrafast magnetization dynamics[157,180,248,271]. We note however that this technique also has a depth dependence for thick layers because of the non uniform light absorption profile in such layers[183]. The standard way of doing complex MOKE is to find a quarter wave-plate angle that suppresses the magnetic signal of one layer. However, there usually still is a little bit of signal from the other layer. To correct this, we repeat the measurements for different quarter wave plate angle and for the four possible initial magnetic configurations (two where the total magnetization is parallel (P) and two where it is antiparallel (AP)). Then for each quarter wave-plate angle θ_i, we have $\mathrm{P}_i(t) = \alpha_i(t)M_i^1(t) + \beta_i(t)M_i^2(t)$ and $\mathrm{AP}_i(t) = \alpha_i(t)M_i^1(t) - \beta_i(t)M_i^2(t)$ where $\mathrm{P}_i(t)$ and $\mathrm{AP}_i(t)$ are the total magnetic signal (difference of signals with opposite initial magnetizations) for the P and AP configuration with quarter wave-plate angle θ_i, M^1 and M^2 refer to the wanted normalized magnetizations of each layer and α and β are magneto-optical parameters that depend on the quarter wave-plate angle. The latter are determined from equilibrium hysteresis loops. Assuming α and β are known at all times, and laser fluence independent, one can get the dynamics of the magnetization of each layer with two quarter wave-plate angles. However, these parameters may depend on time because of the previously mentioned out of equilibrium effects or because of the thickness sensitivity of the method. Thus, to check the validity of this method, we use four quarter wave-plate angles. If the method is consistent, one should obtain the same dynamics for any pair of quarter wave-plate angles. We show in chapter 8 that, for our samples, the same dynamics is obtained at all times. In the context of this thesis, this method has only been used for two samples and the corresponding results will be shown in chapter 8.

*It has been verified that the measured intensity is proportional to the polarization axis rotation.

We note that in this setup, the pump and probe beam angles of incidence were 25.6 and 45.7 degrees respectively. The probe beam angle of incidence allows us to be sensitive to in plane magnetization. This may be a problem if the magnetization does not have a known direction at all times. However, our samples have PMA and AO-HIS is known to be a linear reversal process[241,272*]. Thus this angle of incidence is not a problem for our samples. The pump beam angle of incidence is more problematic. This angle implies that certain regions of the sample will be irradiated before others, resulting in a signal that moves spatially as a function of time. This is shown and well reproduced theoretically in chapter 8. However, the pump beam also has an intrinsic spatial motion due to short (a few seconds) and long (tens of minutes) timescale oscillations and drifts, which cannot be separated from the spatial motion due to the angle of incidence in general. The short timescale oscillations can be eliminated by a proper averaging. Regarding the long timescale drift, Yann Le Guen made a stabilization program that keeps track of any spatial displacement of the magnetic signal with respect to a reference image (usually the last image taken). Because the spatial displacement happens at the subpicosecond timescale, if the long timescale drift is sufficiently low, it is possible to separate both effects. Measurements were performed jointly with Julius Hohlfeld, Maxime Vergès and Yann Le Guen. Analysis of the measurements on this setup was performed together with Julius Hohlfeld.

4.4 Conclusion

This chapter was devoted to the introduction of our experimental methods. We started by explaing how our samples are grown and designed. We then extensively characterized the kind of pulsed laser beams that we use. In particular we verified that for the specific parameters that we use, it is safe to consider the light source as purely transverse. Finally, we presented the four different types of experimental setups that we used. They are all based on MOKE and we reviewed the conditions under which time resolved MOKE methods can be used to get information regarding magnetization and not some other magnetic field dependent out of equilibrium effects.

*Ultrafast demagnetization is also known to happen longitudinally although we do not know any published work that show this. Julius Hohlfeld made such experiments but they were never published.

Chapter 5

Model

In this chapter, we present the different theoretical approaches that have been used to understand the various physical phenomenon presented in this thesis. We start by exposing a theory of laser pulse absorption which is used to calculate time dependent absorption profiles in multilayer structures. This approach is valid for any sample thickness and pulse duration provided that one knows the wavelength dependence of optical indices. The various approximations are discussed. Then we shortly present our 2TM and its numerical implementation. Finally, the two last sections are devoted to Gridnev's model[92,233,234] of AO-HIS, Beens *et al.*[93] model of ultrafast demagnetization and a combination of both to understand the magnetization dynamics of our spin valve systems.

5.1 Theory of laser pulse absorption

For purely quantum calculations (usually *ab initio* like rt-TDDFT) of material systems interacting with pulses of light, one may just choose any transverse electromagnetic vector potential and use it as an input in the calculations with a given Hamiltonian. Not much issues arise if one neglects the spatial extension of the system (such that the electromagnetic four-vector potential does not depend on space) and if one is aware that the calculated energies are the eigenvalues of the total Hamiltonian which then includes the "energy" of the electromagnetic field, as long as it is still present in the material system. The problem is already more complicated when one uses semiclassical approaches because many phenomena that are intrinsically considered from quantum techniques lead to more complex equations to be solved. Such effects will be discussed.

We note that the great advantage of semiclassical techniques is that they can be used to consider spatially finite systems such as thin films, without requiring any periodic boundary condition. Thus, in this case, one may argue that it is required to correctly consider the spatial dependence of the interaction between light and matter. This is usually done using a Transfer Matrix Method (TMM)[54,273–275] or an equivalent approach[276] based on the propagation equation of light in a medium with a certain optical index and appropriate boundary conditions (Fresnel equations). However these methods are used for plane monochromatic waves. We note a first issue with these approaches, at least for an application in the out of equilibrium regime: Fresnel equations assume that there is no surface charges. This is obviously not the case in our samples. We will however assume the role of these surface charges is negligible.

If the optical index of each layer is known, one can then calculate the amplitude of the electric field (still assuming a plane monochromatic wave for now). However, there can be different approximations at this stage depending on the dependencies of these indices. Indeed, one may have in general frequency and wave vector dependences of the dielectric (and permeability) tensor $\boldsymbol{\varepsilon}(\mathbf{k},\omega)$ *, as well as anisotropy and temperature dependence. Anisotropy may come from birefringence or the fact that the material is gyrotropic[270,278]. One should also consider that s and p polarized light propagate differently because Fresnel equations for s and p polarizations are different. In principle, a realistic propagation of the electric field can be calculated, in any condition, as long as one knows the full dependence of the optical index. In practice however, it is difficult to have access to such data or to calculate it. Thus in this work, we will restrict ourselves to isotropic media with optical indices that only have a frequency dependence (i.e. chromatic dispersion). Such parameters are usually easily found in the literature. We note however that this prevents us from considering gyrotropic media correctly (such as our GdFeCo and [Co/Pt] layers) but this is what has been assumed so far in the context of ultrafast magnetization dynamics. Furthermore, as explained in chapter 2, we set the permeability $\mu = \mu_0$ for the considered optical wavelengths such that the optical index is $\mathbf{n} = \sqrt{\varepsilon/\varepsilon_0}$. Non linear effects are also neglected such that the light frequency is the same (for a given plane monochromatic wave) in all media. Finally, we only used linearly polarized pulses with either s or p polarization, thus we can restrict ourselves to the two by two TMM formalism. For circularly polarized light or other linear polarizations, one needs a four by four formalism in order to keep track of the forward and backward propagation of both s and p components which make up the total electric field.

Thus we start our calculations with a modified version of Byrnes TMM code[54] to include the

*It should actually be a non local function $\boldsymbol{\varepsilon}(r,r',t,t')$ in general, especially for thin films excited with a pulse[277]. The non locality in time can be seen from out of equilibrium variations of the dielectric tensor (see for instance references 59 and 264).

time factor $\exp(-i\omega t)$. This code gives us the electric field as a function of time and space for a plane monochromatic wave at a given angle of incidence. Then, we obtain the pulsed electric field at all times and depths in the sample using equation (4.5) with the same gaussian gain factor (L must be big enough such that the overlap between consecutive pulses is negligible). Note that now $k = 2\pi\mathbf{n}/\lambda = \mathbf{n}k_{\text{vacuum}}$ with $\mathbf{n}$ the complex index of refraction in the medium where the electric field is calculated. The factor $\frac{w_0}{w(z)} \exp\left(\frac{-r^2}{w(z)^2}\right)$ is neglected from the calculations and retrieved at the end by a change of the electric field amplitude for a given r because we can neglect the variation of z in the thickness of our layers compared to $z_R \simeq 1$ cm for optical wavelengths and $w_0 \simeq 50$ µm. E_0 is related to the measured fluence below. This electric field is still complex and thus one must take its real part to obtain the physical electric field. The envelope or profile of the electric field is given by the norm of the complex electric field.

Once the (real) electric field is known, one can then calculate the energy absorption. This is based on Poynting's theorem for which the most general form in the context of this thesis is given by the time component of equation (2.4). The tensor elements can be obtained from the integrand of equations (2.8) using the symmetry of Belinfante tensor. At the microscopic scale, it may always be written (even in the non relativistic case):

$$\frac{\partial u}{\partial t} + \boldsymbol{\nabla} \cdot \mathbf{S} \neq 0 \tag{5.1}$$

Where $u = \varepsilon_0 \mathbf{E}^2 + \mathbf{B}^2/\mu_0$ is the electromagnetic energy density (in the absence of matter) and the inequality sign originates from the energy of matter plus interaction between light and matter. We stress again that the only quantity that makes physical sense is the total energy, thus saying that the spatial integral of u is the energy of the electromagnetic field does not make sense in the presence of matter. However, this separation is the most natural one as it gives the total energy of the system when there is no matter and in this case the inequality becomes an equality. From the microscopic Maxwell equations, one usually derives[45]:

$$\frac{\partial u}{\partial t} + \boldsymbol{\nabla} \cdot \mathbf{S} = -\mathbf{J} \cdot \mathbf{E} \tag{5.2}$$

Where $\mathbf{J}$ is the charge current density. The term on the right hand side originates from the Lorentz force and the fact that the magnetic field does no work. It gives the amount of energy that is transferred from the charges to the electromagnetic field. However, as this energy is transferred, the energy of the charges changes which means that one needs another equation to fully describe the system. Models where a charge current is given as a constraint do not necessarily conserve energy, notably if the charge current is constant. As already mentioned, with this kind of separation and neglecting quantum mechanics, infinities may appear[20]. Considering the total energy does not lead to any issue in principle because conservation of energy is built in the

theory (2.4) but solving this problem is impossible in practice. One thus sticks to this type of energy separation but it should then be expected that issues may arise. Further problems arise when one does the macroscopic averaging of Maxwell's equations[277,279,280]. Indeed, in this case, using equations (2.17), equation (5.2) becomes:

$$\mathbf{E} \cdot \frac{\partial \mathbf{D}}{\partial t} + \mathbf{H} \cdot \frac{\partial \mathbf{B}}{\partial t} + \boldsymbol{\nabla} \cdot (\mathbf{E} \times \mathbf{H}) = -\mathbf{J} \cdot \mathbf{E} \tag{5.3}$$

As explained by Richter *et al.*[277], citing standard textbooks[45,46], the term $\mathbf{E} \cdot \partial_t \mathbf{D} + \mathbf{H} \cdot \partial_t \mathbf{B}$ cannot be written as the time derivative of any quantity in general and one cannot define an electromagnetic energy density just because of this fact. The separate energy of light or matter that one can define in the microscope theory does not have a physical sense in general as already discussed, but this is not an issue in principle because one can calculate the evolution of the total system. In the macroscopic Maxwell's equations approach, one wants to calculate how the electromagnetic field only evolves in the presence of matter. One can compute susceptibilities and conductivities from a microscopic point of view, but once this is done and used as an input in the macroscopic Maxwell's equations, one cannot retrieve the microscopic reaction of matter as a consequence of the interaction between light and matter.

Poynting's vector becomes $\mathbf{E} \times \mathbf{H}$ which is identical to the microscopic expression in non magnetic materials. This is the form of Poynting's vector that we will use in this theory. We note however that the validity of this expression in general is debated[277,279–281] but it should still be valid here because of the assumptions that we made (isotropic media with no spatial dispersion). Poynting's vector can then be used to calculate the flow of electromagnetic energy through any surface. $-\partial_z S_z$ gives the amount of electromagnetic energy that has been lost locally when the pulse propagates in the $+z$ direction, i.e. absorption. However, this energy will be absorbed by the total system made of matter and the (local) electromagnetic field. Thus there is *a priori* no way to say which amount of energy actually goes to matter because the notion of energy of matter is ill defined during the presence of the pulse*. However, as soon as the pulse is not present anymore, the total transferred energy will correspond to the total absorption by the material system. We will assume that this procedure gives the correct effective† energy absorption for a model that clearly separates electromagnetic and electronic energies such as the 2TM. Even though this

*We will not discuss possible reasonable separations of the energy between light and matter although this seems required to know what is the actual source input in a 2TM. We believe this debate is similar to the still ongoing Abraham-Minkowski controversy for momentum[19]. The best resolution for this issue should be to solve the full quantum problem. This problem is however not significant for our qualitative 2TM in this work.

†Because of our previous discussion, one should realize that the concept of light energy absorption by matter itself is ill defined.

might not be the case, this is still an improvement compared to the usual methods we are aware of. We know two such methods. First, one may multiply the absorption profiles obtained by the monochromatic TMM with a gaussian function corresponding to a certain pulse duration and with an amplitude obtained from the laser fluence. This completely neglects chromatic dispersion and the real time dependence of the energy transfer. Second, in the case where chromatic dispersion is small in the range of frequencies that make the pulse **and** when the pulse duration is large compared to the period of oscillation, one can approximate equation (5.3) by[45]:

$$\frac{\partial u_{\text{eff}}}{\partial t} + \boldsymbol{\nabla} \cdot \mathbf{S} = -\mathbf{J} \cdot \mathbf{E} - \omega_c \operatorname{Im}(\varepsilon(\omega_c)) \langle E^2 \rangle - \omega_c \operatorname{Im}(\mu(\omega_c)) \langle H^2 \rangle \tag{5.4}$$

Where ω_c is the central frequency of the pulsed electromagnetic field, the angular brackets denote an average over a period $2\pi/\omega_c$ and the effective electromagnetic energy u_{eff} is:

$$u_{\text{eff}} = \frac{1}{2} \operatorname{Re}\left(\frac{\mathrm{d}(\omega\varepsilon)}{\mathrm{d}\omega}(\omega_c)\right) \langle E^2 \rangle + \frac{1}{2} \operatorname{Re}\left(\frac{\mathrm{d}(\omega\mu)}{\mathrm{d}\omega}(\omega_c)\right) \langle H^2 \rangle \tag{5.5}$$

Note that the fields still depend on both time and space. The average only eliminates the fast oscillations of the fields. The term $-\mathbf{J} \cdot \mathbf{E}$ corresponds to Joule heating while $-\omega_c \operatorname{Im}(\varepsilon(\omega_c)) \langle E^2 \rangle$ and $-\omega_c \operatorname{Im}(\mu(\omega_c)) \langle H^2 \rangle$ correspond to losses due to excitations of electric and magnetic dipoles respectively.

The assumption that chromatic dispersion is small is in general not true, e.g. for frequencies close to the interband transition threshold of noble metals or at small frequencies in any conductor. The assumption that the pulse duration is large compared to the period of oscillation is also not valid for ultrashort pulses. In particular we cannot use the expression of the time averaged (over a period of oscillation) of Poynting's vector for planes waves $\operatorname{Re}(\mathbf{E} \times \mathbf{H}^*)/2$ (with complex fields) as in reference 54. This expression suppresses the oscillations in the absorption. These oscillations are actually existing, as can be seen when an electron is in an oscillating electric field. We stress that, when evaluating $\mathbf{S} = \mathbf{E} \times \mathbf{H}$, the total real electric and magnetic field must have been calculated beforehand. Summing Poynting's vectors for different monochromatic plane waves neglects interference terms.

We now present the calculations that give the laser pulse absorption as a function of time. The incident wave vector $\mathbf{k}^i$ of the pulse is in the $(\mathbf{x}, \mathbf{z})$ plane with an angle incidence θ^0. The situation is depicted in figure 5.1. We write the incident electric and magnetic fields as follows:

$$\mathbf{k}^i = \frac{2\pi}{\lambda}(\cos(\theta^0)\mathbf{z} + \sin(\theta^0)\mathbf{x}) \tag{5.6a}$$

$$E_n^i(\mathbf{r}, t) = E_0 G(\omega_n) \exp(i(\mathbf{k}^i \cdot \mathbf{r} - \omega_n t)) \tag{5.6b}$$

$$(\mathrm{s}): \quad \mathbf{E}^i(\mathbf{r},t) = \mathbf{y}\,\mathrm{Re}\left(\sum_n E_n^i(\mathbf{r},t)\right) \tag{5.6c}$$

$$\mathbf{H}^i(\mathbf{r},t) = \frac{1}{c\mu_0}(\sin(\theta^0)\mathbf{z} - \cos(\theta^0)\mathbf{x})\,\mathrm{Re}\left(\sum_n E_n^i(\mathbf{r},t)\right) \tag{5.6d}$$

$$(\mathrm{p}): \quad \mathbf{E}^i(\mathbf{r},t) = (-\sin(\theta^0)\mathbf{z} + \cos(\theta^0)\mathbf{x})\,\mathrm{Re}\left(\sum_n E_n^i(\mathbf{r},t)\right) \tag{5.6e}$$

$$\mathbf{H}^i(\mathbf{r},t) = \frac{1}{c\mu_0}\mathbf{y}\,\mathrm{Re}\left(\sum_n E_n^i(\mathbf{r},t)\right) \tag{5.6f}$$

With G given by equation (4.4). The magnetic field is obtained from Maxwell's equations as usual. (s) and (p) refer to s and p polarized light. Inside a medium, one must consider the wavelength dependent optical index $\mathbf{n}_n$ and angles θ_n which may both be complex in general because of Snell's law[54]. There is also forward and backward propagation due to reflections on interfaces. The various electric field amplitudes E_{0n}^f and E_{0n}^b of forward and backward monochromatic plane wave modes respectively, as well as the angles θ_n, are directly obtained from the TMM code of Byrnes[54*]. The total fields (separating forward and backward propagation) then

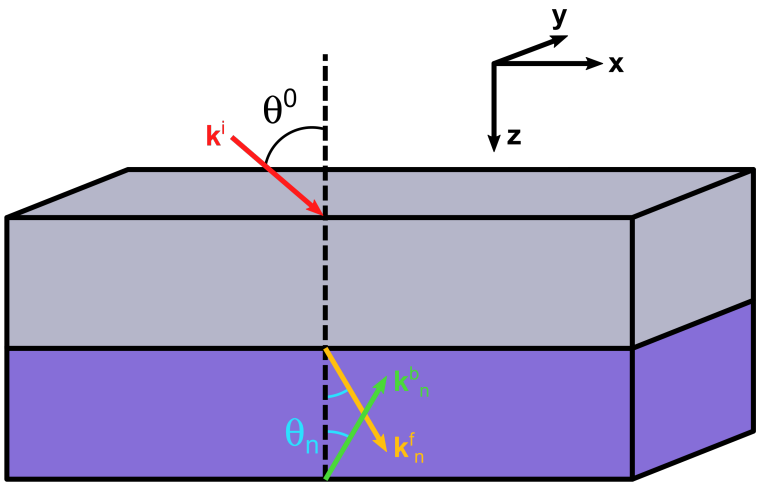

Figure 5.1: Geometrical configuration of wave vectors for light absorption calculations in multilayers. We represented the wave vector of the incident electromagnetic field as well as the wave vectors for forward and backward propagations in one of the layers and for one wavelength.

*In Byrnes' TMM code, the amplitudes are given for E_0=1.

are:

$$\mathbf{k}_n^f = \frac{2\pi \mathbf{n}_n}{\lambda}(\cos(\theta_n)\mathbf{z} + \sin(\theta_n)\mathbf{x}) \tag{5.7a}$$

$$\mathbf{k}_n^b = \frac{2\pi \mathbf{n}_n}{\lambda}(-\cos(\theta_n)\mathbf{z} + \sin(\theta_n)\mathbf{x}) \tag{5.7b}$$

$$E_n^f(\mathbf{r},t) = E_{0n}^f G(\omega_n)\exp(i(\mathbf{k}_n^f \cdot \mathbf{r} - \omega_n t)) \tag{5.7c}$$

$$E_n^b(\mathbf{r},t) = E_{0n}^b G(\omega_n)\exp(i(\mathbf{k}_n^b \cdot \mathbf{r} - \omega_n t)) \tag{5.7d}$$

$$\text{(s)}: \quad \mathbf{E}^f(\mathbf{r},t) = \mathbf{y}\,\mathrm{Re}\left(\sum_n E_n^f(\mathbf{r},t)\right) \tag{5.7e}$$

$$\mathbf{E}^b(\mathbf{r},t) = \mathbf{y}\,\mathrm{Re}\left(\sum_n E_n^b(\mathbf{r},t)\right) \tag{5.7f}$$

$$\mathbf{H}^f(\mathbf{r},t) = \mathrm{Re}\left(\sum_n \frac{\mathbf{n}_n}{c\mu_0}(\sin(\theta_n)\mathbf{z} - \cos(\theta_n)\mathbf{x})E_n^f(\mathbf{r},t)\right) \tag{5.7g}$$

$$\mathbf{H}^b(\mathbf{r},t) = \mathrm{Re}\left(\sum_n \frac{\mathbf{n}_n}{c\mu_0}(\sin(\theta_n)\mathbf{z} + \cos(\theta_n)\mathbf{x})E_n^b(\mathbf{r},t)\right) \tag{5.7h}$$

$$\text{(p)}: \quad \mathbf{E}^f(\mathbf{r},t) = \mathrm{Re}\left(\sum_n (-\sin(\theta_n)\mathbf{z} + \cos(\theta_n)\mathbf{x})E_n^f(\mathbf{r},t)\right) \tag{5.7i}$$

$$\mathbf{E}^b(\mathbf{r},t) = \mathrm{Re}\left(\sum_n (-\sin(\theta_n)\mathbf{z} - \cos(\theta_n)\mathbf{x})E_n^b(\mathbf{r},t)\right) \tag{5.7j}$$

$$\mathbf{H}^f(\mathbf{r},t) = \mathrm{Re}\left(\sum_n \frac{\mathbf{n}_n}{c\mu_0}\mathbf{y}E_n^f(\mathbf{r},t)\right) \tag{5.7k}$$

$$\mathbf{H}^b(\mathbf{r},t) = \mathrm{Re}\left(\sum_n \frac{\mathbf{n}_n}{c\mu_0}\mathbf{y}E_n^b(\mathbf{r},t)\right) \tag{5.7l}$$

The last layer is considered to be semi-infinite and there is only forward propagation. Calculating Poynting's vector $\mathbf{E}\times\mathbf{H}$ with $\mathbf{E} = \mathbf{E}^f + \mathbf{E}^b$ and $\mathbf{H} = \mathbf{H}^f + \mathbf{H}^b$ one gets for the normalized absorption $a(z,t) = -\partial_z S_z / S_z(\mathbf{r}=0, t=0)$:

$$\begin{aligned}\text{(s)}: \quad a(z,t) = \frac{-1}{S_z^0}\sum_{n,m} &\mathrm{Re}\left(ik_n(E_n^f - E_n^b)\right)\mathrm{Re}\left(\frac{\mathbf{n}_m}{c\mu_0}(E_m^f - E_m^b)\cos(\theta_m)\right) \\ &+ \sum_{n,m}\mathrm{Re}\left(E_n^f + E_n^b\right)\mathrm{Re}\left(\frac{\mathbf{n}_m}{c\mu_0}ik_m(E_m^f + E_m^b)\cos(\theta_m)\right)\end{aligned} \tag{5.8a}$$

$$\begin{aligned}(\mathrm{p}): \quad a(z,t) = \frac{-1}{S_z^0} \sum_{n,m} \mathrm{Re}\left(ik_n(E_n^f + E_n^b)\cos(\theta_n)\right) \mathrm{Re}\left(\frac{\mathbf{n}_m}{c\mu_0}(E_m^f + E_m^b)\right) \\ + \sum_{n,m} \mathrm{Re}\left((E_n^f - E_n^b)\cos(\theta_n)\right) \mathrm{Re}\left(\frac{\mathbf{n}_m}{c\mu_0} ik_m (E_m^f - E_m^b)\right)\end{aligned} \tag{5.8b}$$

$$S_z^0 \equiv S_z(\mathbf{r}=0, t=0) = \sum_{n,m} \frac{E_0^2}{c\mu_0} G(\omega_n) G(\omega_m) \cos(\theta^0) \tag{5.8c}$$

Where k is the z component of $\mathbf{k}$. The absorption only depends on the depth z as should be expected for a plane wave. In practical calculations, one multiplies the normalized absorption a by S_z^0. From equation (4.6), one finds that in vacuum and at normal incidence:

$$S_z(z,t) = A\cos(k_c z - \omega_c t)^2 \exp\left(\frac{-1}{2(\sigma_t^I)^2}\left(\frac{z}{c} - t\right)^2\right) \tag{5.9}$$

Where $A = S_z(0,0)$ is the wanted value S_z^0. The requirement that the integral of $S_z(0,t)$ over all times should be equal to the local fluence at the vacuum/sample interface leads to:

$$S_z^0 = \frac{2F\cos(\theta^0)}{\sqrt{2\pi}\sigma_t^I\left(1 + e^{-2(\sigma_t^I)^2\omega_c^2}\right)} \tag{5.10}$$

Where F is the fluence at normal incidence (such that the measured fluence is half of the maximum value of F) and the $\cos(\theta^0)$ factor then reduces the local fluence because of the angle of incidence. When ω_c goes to zero (such that one neglects oscillations), one retrieves the normalization that is used for a simple gaussian evolution in time of the absorption. These equations can be directly extended to the case where the incident pulse is in a medium that is not vacuum with an optical index $\mathbf{n^0}$. One should interpret results carefully however if $\mathrm{Im}(\mathbf{n^0}) \neq 0$[54]. The frequency dependence of the optical indices for the metals that we use and sapphire is taken from the literature[282–286] and we used 1.5136 for glass. It is in principle possible to combine this technique with the 2TM in the next section to consider temperature dependence of the optical indices as the sample is heated up. However one needs to know such dependence which we did not.

We now present some results of this method. Marie-Laure Chavazas contributed to the development of the code leading to these simulations. In figure 5.2, we report some calculations for a 1 µm thick slab of glass where a small complex part has been added to the optical index for illustration purposes. Both the electric field and its profile are shown. The profile allows us to clearly observe interferences between the forward and backward propagating fields (at $t = 0.25$ fs) because they induce oscillations in the profile. The profile can even reach zero certain instants. The electric field makes changes of wavelength clearly visible (inside the glass) as well

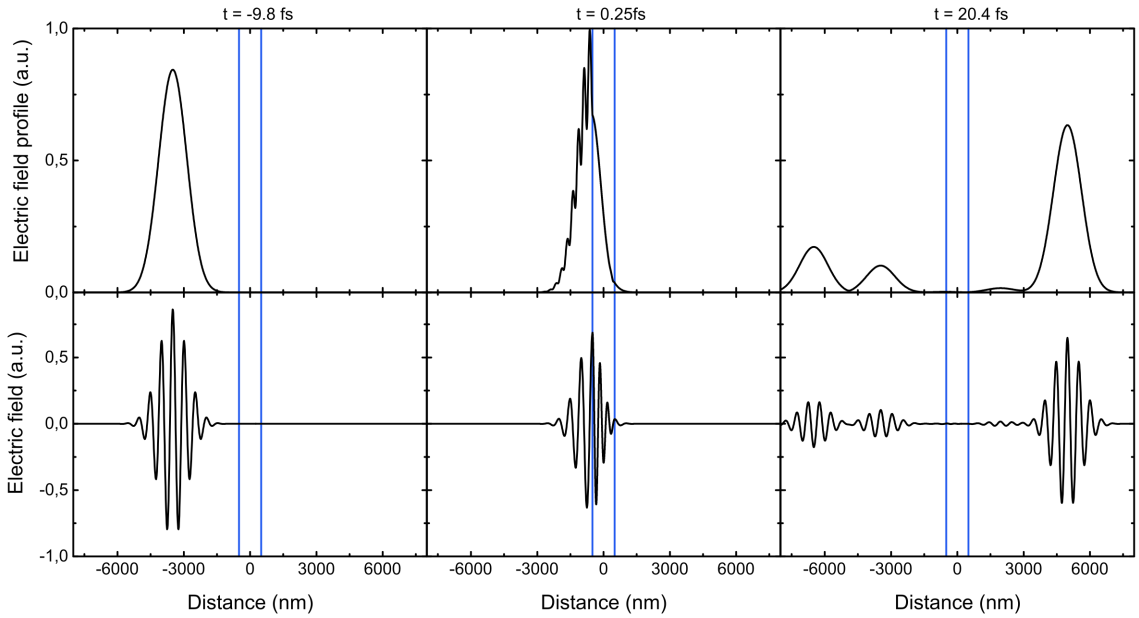

Figure 5.2: Electric field and its profile as a function of space for three different instants for a 5 fs pulse (duration of the electric field pulse and not of the intensity pulse) with 515nm wavelength. The time $t = 0$ is defined such that the laser pulse would be centered at a distance of 0 nm if it was propagating in vacuum only. The two blue vertical lines define the interfaces of a fictitious material (1000 nm thick) with constant optical index $\mathbf{n} = 1.5136 + 0.02i$.

as the π phase shift for the vacuum/glass reflection. The other three (visible) generated pulses do not exhibit this behavior, as expected from the fact that only the very first reflection experiences an interface with a greater optical index than the medium of incidence. The observed deformation of the pulse is due to the rather thick layer that we considered. Indeed, we did not consider chromatic dispersion in this case and the distance of around 3000 nm between two pulses propagating in the same direction matches well with twice the thickness of the layer times the real part of the optical index. This effect cannot happen with the rather thin layers that we consider in this thesis and the thickness of the substrate is much to big to cause any effect.

We now consider an extreme but realistic case with 100 nm of copper (deposited on a glass substrate) with the same laser pulse as for the previous example. The pulse duration was chosen such as to cover almost the entire range of wavelength provided by reference 286. The results are shown in figure 5.3. The results are rather similar to the previous example, except that one can see more interference around $t = 0$ fs, resulting in a lower electric field amplitude, and one can see that the tail of the pulse is elongated after its reflection on the copper layer. This will result in an effectively longer period of time where the material absorbs light compared to what would be predicted with at gaussian function. This effect is rather small but we expect that they may

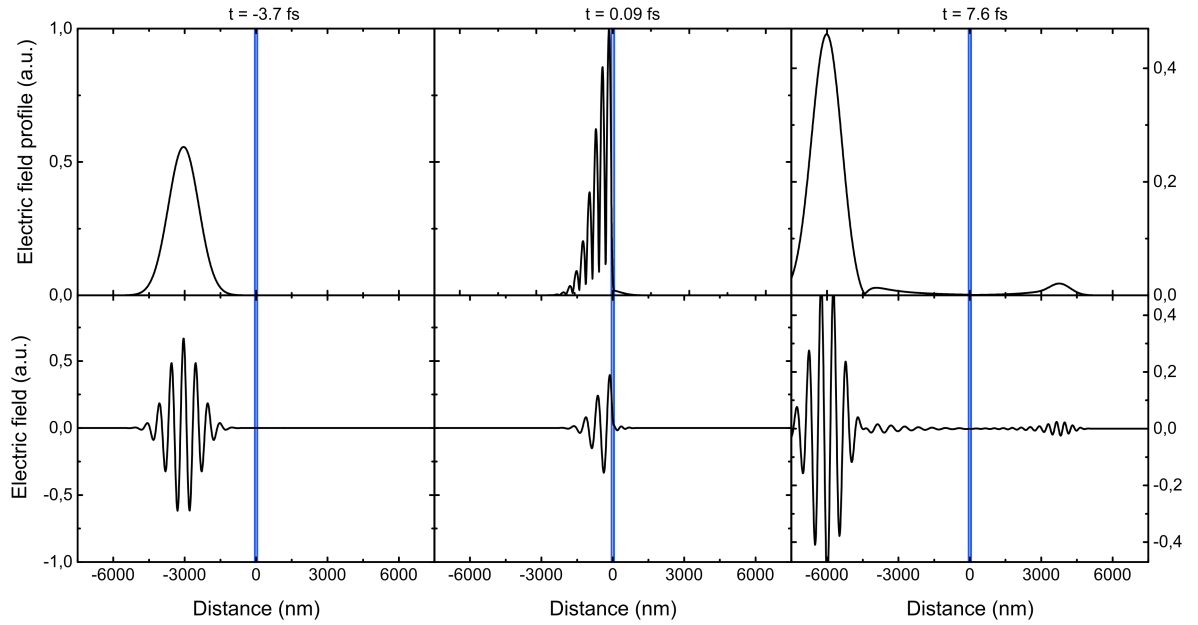

Figure 5.3: Electric field and its profile as a function of space for three different instants for a 5 fs pulse (duration of the electric field pulse and not of the intensity pulse) with 515nm wavelength. The time $t = 0$ is defined such that the laser pulse would be centered at of distance 0 nm if it was propagating in vacuum only. The two blue vertical lines define the interfaces of a 100 nm thick copper layer. The scale of the graphs at $t = 7.6$ fs is different to better see the effect of chromatic dispersion.

be in general much bigger for shorter pulses or for a more careful design of the sample. The fact that the pulse has been chirped is clearly seen from the fact that the oscillatory part of the pulse is not centered anymore with its envelope. We note that in general, this approach of calculating an electric pulse propagation is similar to what is done with the telegrapher's equation (a linear partial differential equation modeling dispersion and damping of propagating signals) except that our approach works for general multilayer structures and for an arbitrary frequency dependent propagation.

We now look at some results for light absorption. We consider a more complex structure studied in chapter 8: Glass / Ta(5) / Pt(4) / Cu(10) / $[\text{Co}(0.6)/\text{Pt}(1)]_2$ / Ta(5). We used a pulse duration of 100 fs, 25.6 degrees angle of incidence and 800 nm center wavelength as in chapter 8. In order to compare our theory with the standard static TMM for monochromatic waves, we define the time independent absorption $a(z)$ of our theory by the quantity such that the total energy density provided locally by the laser to the system is $u(z) = a(z)F$. For the standard TMM, this is the absorption that is given. In our theory, we need to first integrate the normalized absorption over time and then multiply it by $\frac{2}{\sqrt{2\pi}\sigma_t^I\left(1+e^{-2(\sigma_t^I)^2\omega_c^2}\right)}$. The comparison is shown in figure 5.4.

The difference between both theory is not big enough to create any qualitative difference in a

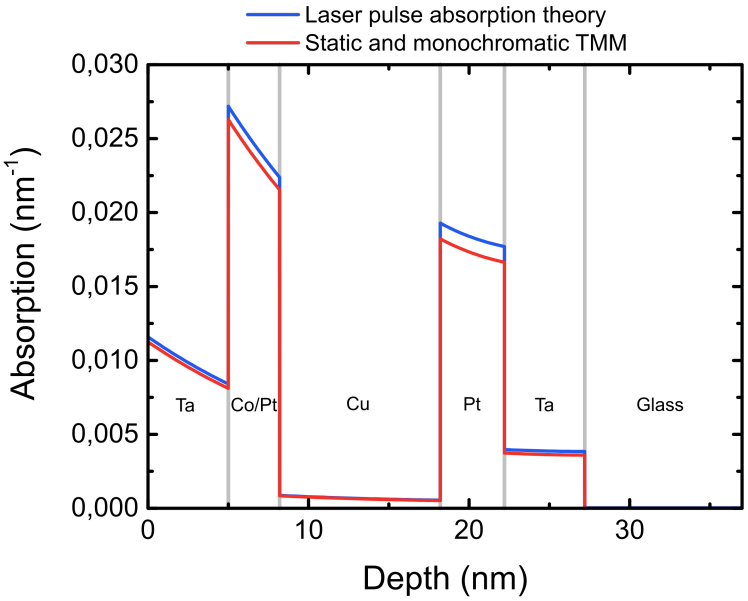

Figure 5.4: Comparison of the spatial absorption profile for our theory and the standard TMM method for Glass / Ta(5) / Pt(4) / Cu(10) / $[\text{Co}(0.6)/\text{Pt}(1)]_2$ / Ta(5). The incident pulse, propagating from left to right, has a duration of 100 fs, an angle of incidence of 25.6 degrees and a center wavelength of 800 nm.

model. However we note that the pulse duration used for these calculations is rather big here and one might expect much larger differences at lower pulse durations. We now look at some time dependent normalized absorption profiles, shown in figure 5.5. We remark that the shapes of

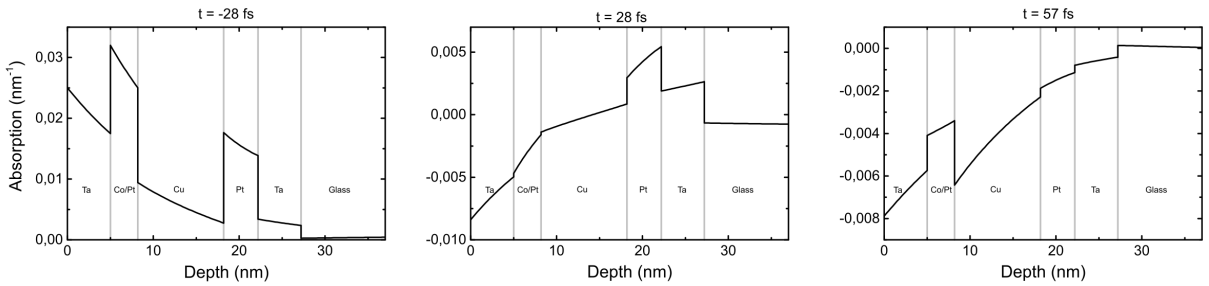

Figure 5.5: Time dependent normalized absorption profiles at three selected instants for Glass / Ta(5) / Pt(4) / Cu(10) / $[\text{Co}(0.6)/\text{Pt}(1)]_2$ / Ta(5). The incident pulse, propagating from left to right, has a duration of 100 fs, an angle of incidence of 25.6 degrees and a center wavelength of 800 nm.

these profiles are drastically different from the time independent ones. In particular, the absorption may be negative. This is because of the oscillation of the absorption as a function of time. This can be understood from Poynting's theorem in vacuum, equation (5.2) when $\mathbf{J} = 0$. Then

one directly sees that an absorption is accompanied with a local increases of electromagnetic energy density and reciprocally, a decrease of energy density gives a negative absorption. Then, the (time averaged) energy density at each point of space increases when the pulse arrives and it decreases as the pulse leaves, leading to a positive and then a negative time averaged absorption. The oscillating electric field adds oscillations to this absorption, as is directly seen from the derivative of equation (5.9) with respect to z. However at each point of space, the integral of the absorption over all times is zero. One could then subtract the rate of change of the local electromagnetic energy density to the absorption to obviously give a zero light absorption at all times (which is just the meaning of equation (5.2)). In matter, one cannot simply subtract from the absorption a corresponding fonction (that also gives zero when integrated over all times) that would correspond to the energy transferred to the local electromagnetic field because, as already stated, one cannot define such an energy (equation (5.3)).

To make this more visual, we plot the normalized absorption as a function of time for different depths in the sample. This is shown in figure 5.6. At the timescale of the pulse duration

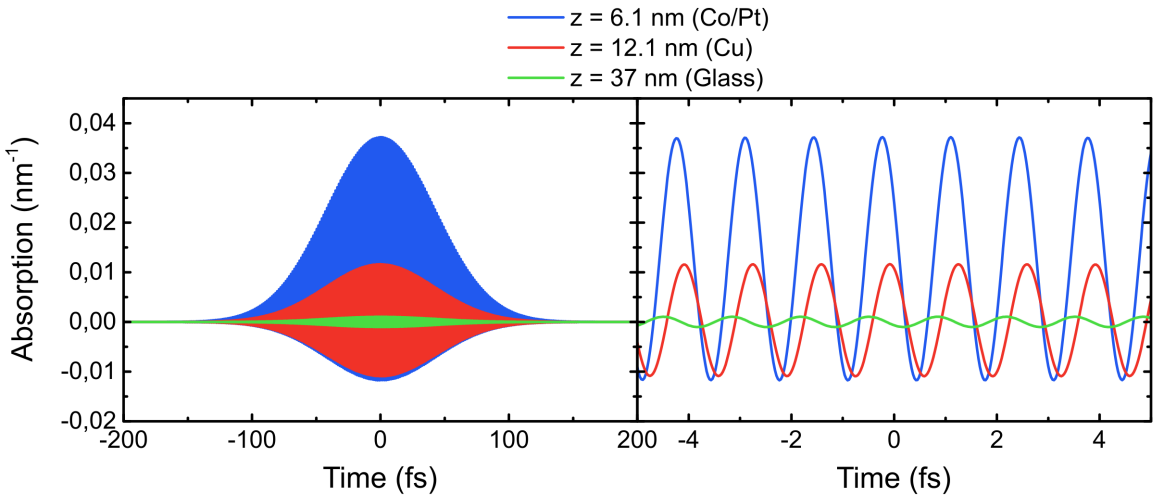

Figure 5.6: Time dependent normalized absorption profiles at three selected depths in Glass / Ta(5) / Pt(4) / Cu(10) / $[\text{Co}(0.6)/\text{Pt}(1)]_2$ / Ta(5). The incident pulse, propagating from left to right, has a duration of 100 fs, an angle of incidence of 25.6 degrees and a center wavelength of 800 nm.

(hundreds of femtoseconds), one sees clearly that the absorption can be either positive or negative. The positive and negative envelopes of these curves can be fitted by a function proportional to $\exp(\frac{-1}{2(\sigma_t^I)^2}(z/c-t)^2)$ really well. The difference between the amplitudes of the positive and negative part of the absorption is related to the total absorption (although we did not find any simple relation between these two quantities yet). Thus in the [Co/Pt] multilayer this difference is clear, leading to the $\sim$ 0,025 nm^{-1} absorption over time, while in copper this difference is

very small and it is zero in glass. The difference of sign of the absorption for different depths in the layer, at a given instant, is visible at the femtosecond timescale. There one can clearly see a phase difference between the absorption at different depths. This is simply due to the fact that the pulse propagates and thus the electric field reaches certain depths before others. In addition, we note that the amplitude of this absorption could be changed rather arbitrarily (as long as all energies are positive) without changing the total absorption profile of figure 5.4. This is again due to the fact one cannot separate/define the energies of the electromagnetic field and matter.

For our quantitative 2TM, the presence of theses rapid oscillations or not will not make much difference because their effect will cancel out in average as heat diffusion and electron-phonon scattering are slower processes (although we do see some small effects). It will still lead, however, to a slightly different deposited energy. This is unimportant in practice because there is a rather large uncertainty on the materials optical indices that depends a lot on the deposition conditions and the interfaces[286], and measuring these optical indices, with ellipsometry, can be challenging for such thin layers. As the pulse duration decreases however, and if one considers ballistic or superdiffusive transport, we suspect that the alternating energy density gradients we observe could have more important consequences. As far as we know, this has never been considered. When the pulse duration is not large compared to a period of oscillation anymore (such as in figure 5.3) and when the response of the system is also not slow compared to light absorption (such as in OISTR[8]), we suggest that one should not use an approach based on a macroscopic averaging of Maxwell's equations anymore. However, the spatial dependence of the electric field should be kept.

5.2 2TM implementation

In this section, we present the numerical implementation of our 2TM. For completeness, we write the system of equation as it has been used:

$$\gamma T_{\mathrm{e}} \frac{\partial T_{\mathrm{e}}}{\partial t} = \frac{\partial}{\partial z}\left(\kappa_{\mathrm{e}} \frac{T_{\mathrm{e}}}{T_{\mathrm{p}}} \frac{\partial T_{\mathrm{e}}}{\partial z}\right) - g_{\text{e-p}}\left(T_{\mathrm{e}} - T_{\mathrm{p}}\right) + a S_z^0 \tag{5.11a}$$

$$C_{\mathrm{p}} \frac{\partial T_{\mathrm{p}}}{\partial t} = \kappa_{\mathrm{p}} \frac{\partial^2 T_{\mathrm{p}}}{\partial z^2} + g_{\text{e-p}}\left(T_{\mathrm{e}} - T_{\mathrm{p}}\right) \tag{5.11b}$$

Where both electron and phonon temperatures depend on time t and depth z. The absorption and incident Poynting vector also depend on time and depth as derived in the previous section. We used standard boundary conditions[160] with all interfaces transparent to heat transport except

for the metal/substrate interface where an interfacial thermal conductance was assumed to exist. To model the boundary condition at an infinite depth in the substrate, we model a thin section of substrate (usually 10 nm) and ask that $T_\mathrm{p}(z+\Delta z)/T_\mathrm{p}(z) = T_\mathrm{p}(z)/T_\mathrm{p}(z-\Delta z)$ at the largest simulated depth $z+\Delta z$, for a spatial step Δz. This is the condition satisfied by gaussian and exponential solutions. This is required for long simulations (several tens of picoseconds) but not at short timescales (a few picoseconds) where temperature does not have time to increase significantly at the largest simulated depth. Because electrons do not carry heat in insulators, we set $T_\mathrm{e} = 0$ in the substrate. The parameters we used are shown in table 5.1. The initial temperature is always 300 Kelvins and the interfacial thermal conductance is $100\,10^6\,\mathrm{Wm^{-2}K^{-1}}$. This type of partial differential equation (PDE) is usually well solved using the Crank-Nicholson

Material	γ ($\mathrm{JK^{-2}m^{-3}}$)	κ_e ($\mathrm{WK^{-1}m^{-1}}$)	$g_\mathrm{e\text{-}p}$ ($10^{16}\,\mathrm{WK^{-1}m^{-3}}$)	C_p ($10^6\,\mathrm{JK^{-1}m^{-3}}$)	κ_p ($\mathrm{WK^{-1}m^{-1}}$)
[Co/Pt][160,187]	720	20	264	2.98	1
Cu[187,287,288]	98	300	7.5	2.63	5
Pt[187,287,288]	749	45	110	3.45	5
Ta	543	58	100	2.23	5
GdFeCo[243,287]	781	10.5	60	2.3	5
Sapphire[160]	0	0	0	3.16	30
Glass	0	0	0	2	2

Table 5.1: Table for the 2TM material parameters.

method. However, in our case, because this PDE is not linear (see the electronic heat diffusion term), the implicitness of the numerical scheme requires solving a non linear equation at each time step (instead of a standard matrix inversion for linear PDEs). Thus, to speed up calculations, we used a standard forward Euler method instead. The time Δt and spatial Δz steps are chosen such that the calculation converges. Because of the non linearity of the equation, there is in general no rule to find optimized time and spatial steps that ensures convergence. For a given spatial step, one can start from a given time step and decrease it until convergence is realized. The limit between the convergence and divergence regime seems to follow a quadratic law $\Delta t \propto (\Delta z)^2$ as Alexy Bertrand showed. In the calculations shown in this thesis, we used $\Delta t = 0.01$ fs and $\Delta z \simeq 0.25$ nm. The spatial step also depends on the thicknesses of the layers we used because they are not always multiples of 0.25 nm. At interfaces, we define two points at $\pm 10^{-3}$ nm away from the interface.

This theory can in principle be easily extended to consider the out of equilibrium dielectric tensor or its temperature dependence, as already mentioned. If one knows the time evolution of the dielectric tensor or its temperature dependence, then it suffices to repeat the calculations of the previous section for updated optical indices at each time step to obtain aS_z^0.

Results for the same laser pulse parameters and same structure as in the previous section Glass / Ta(5) / Pt(4) / Cu(10) / $[\text{Co}(0.6)/\text{Pt}(1)]_2$ / Ta(5) are shown in figure 5.7. These kind

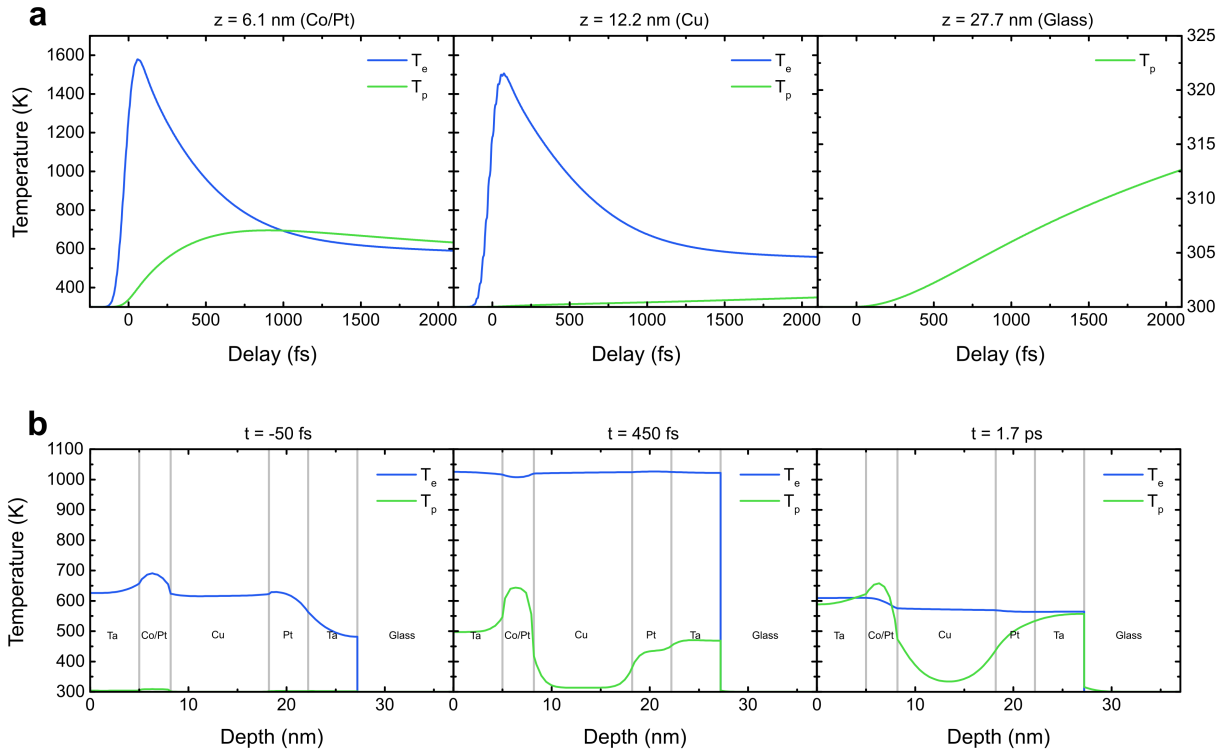

Figure 5.7: Electron (T_e) and phonon (T_p) temperature evolution in Glass / Ta(5) / Pt(4) / Cu(10) / $[\text{Co}(0.6)/\text{Pt}(1)]_2$ / Ta(5). The incident pulse, propagating from left to right, has a duration of 100 fs, an angle of incidence of 25.6 degrees and a center wavelength of 800 nm. The (peak) fluence is 6.6 mJ/cm^2. In (a), we show the temperature dynamics for given positions while in (b) we give the spatial profiles at given time delays. The temperature scale of the graph for $z = 27.7$ nm in (a) is different for illustration purposes.

of graphs are rather standard but we make some comments. First, one sees that in the [Co/Pt] multilayer, the phonon temperature can exceed the electron temperature. This behavior is due to the stronger electron-phonon coupling of this layer compared to tantalum and copper, together with an efficient heat diffusion which allows the electron temperature profile to flatten. Second, one can see some small oscillations in the electron temperature evolution in copper due to the oscillating laser pulse source term. This effect is indeed very small. Finally, the increase of

phonon temperature in the substrate is rather small and so the substrate boundary condition does indeed not play a role at such short timescales.

5.3 Ultrafast magnetization dynamics of ferrimagnets in a s-d model

We now include magnetism in the theory (orbital angular momentum is neglected). We start with the more complicated case of ferrimagnets[92,233,234] and we will see in the next section how one can retrieve the theory of ferromagnets[93] from it. The theory starts from a spin independent Hamiltonian that contains conduction electrons and phonons such that one can retrieve the 2TM from the previous section. On top of this, we assume that there exist some localized spins coupled to the spin of the conduction electrons as in equation (3.9). The spin in d bands is then assumed to be localized[92,93,240]. The spin operators are assumed to not contain a factor $\hbar$. Expanding the dot product, one sees that the interaction Hamiltonian is constituted of two terms, a transverse and a longitudinal term:

$$\hat{H} = -\sum_i J_i \left[\frac{1}{2} \left(S_i^+ s_i^- + S_i^- s_i^+ \right) + S_i^z s_i^z \right] \tag{5.12}$$

The exchange coupling parameter must now depend on lattice site as the material is ferrimagnetic. The conduction electrons have a spin of one half and thus their operators $\mathbf{s}_i$ are exactly described by equation (3.5) without the $\hbar$ factor. On the other hand, the localized spins may have a spin greater than one half and thus one needs another transformation as discussed above. The transformation that is used to consider electron-magnon scattering is usually the Holstein-Primakoff transformation[72,128]. However here we will not consider magnons. The theory presented here may be extended to consider this case and as far as we know, this has not been done in the literature. We doubt however this would be of interest to explain AO-HIS, because, as we will see in this section, the theory for ferrimagnets already relies on many parameters. Including magnons, especially for an amorphous material, would necessarily lead to more parameters. The role of the various coupling parameters in ferrimagnets is still studied[289] and not well understood for amorphous phases with chemical inhomogeneities[290]. Thus, the mean field approximation (MFA) is performed for the z components of the operators. It looks slightly different from the MFA in the Heisenberg model as one deals with two kinds of spin operators. The transverse part

is kept as is:

$$\hat{H} = -\sum_i J_i \left[\frac{1}{2} \left(S_i^+ s_i^- + S_i^- s_i^+ \right) + \langle S_i^z \rangle \, s_i^z + S_i^z \, \langle s_i^z \rangle \right] \tag{5.13}$$

This is an electron-spin Hamiltonian. Note that there is only one conduction electron per site for a s band in a metal. The first term will cause transitions that will in turn cause transfer of both energy and angular momentum between electrons and spins. The last term is similar to the Weiss model of ferromagnets except that it is for ferrimagnets here. It is solved similarly to what has been presented in chapter 3. The main difficulty comes from the second term which also looks like a Weiss Hamiltonian except that it will lead to an exchange splitting of the conduction electrons. The conduction electrons spin density* will depend on space. One cannot simply consider its average value over space (as in the case of localized spins in a ferromagnet) because the material is ferrimagnetic and different localized spins induce a different conduction electrons spin densities. This discussion is detailed by Gridnev[92]. We only give the resulting equations. One considers that the average value of a localized spin $\overline{S}_\nu^z$ only depends on the nature of the atom itself ($\nu = A$ or B with $A =$ Gd and $B =$ Fe or Co) and not on the lattice site i. Likewise, we only consider the averaged conduction electrons spin polarization $\bar{s}_A^z$ at an atom A or $\bar{s}_B^z$ at an atom B, as well as the spatially averaged conduction electrons spin polarization $\bar{s}^z$. The static effect of the exchange splitting $\Delta_\nu = -J_\nu \bar{s}_\nu^z$, where J_ν is the exchange coupling at an atom ν, is given by†:

$$\overline{S}_\nu^z = S_\nu \mathrm{B}_{S_\nu}(-\beta \Delta_\nu S_\nu) \tag{5.14}$$

Where S_ν is the spin of atom ν which corresponds to the average spin at zero Kelvin. This equation is similar to the ferromagnetic case except that the exchange splitting depends on the spin polarizations given by:

$$\bar{s}_A^z = x \chi_{AA} \overline{S}_A^z + (1-x) \chi_{AB} \overline{S}_B^z \tag{5.15a}$$

$$\bar{s}_B^z = x \chi_{BA} \overline{S}_A^z + (1-x) \chi_{BB} \overline{S}_B^z \tag{5.15b}$$

Where x is the concentration of atom A and $\chi_{\mu\nu}$ are parameters. The latter can in principle be obtained from the s-d Hamiltonian if one knows the electronic structure of the system. Because this task is rather complicated, especially in amorphous materials, they are adjusted so as to

*It is given by $\mathbf{s}(\mathbf{r}) = \frac{1}{2} \psi^\dagger(\mathbf{r}) \boldsymbol{\sigma} \psi(\mathbf{r})$ where the spinor wave function ψ describes all conduction electrons and is to be evaluated in an appropriate basis. Here we only refer to its z component. The integral of this quantity over all space and multiplied by $\hbar$ gives the spin angular momentum of the conduction electrons. The spin polarization at a given atomic site used below is the integral of the spin density over a given atomic cell.

†We note a typo in equation (11) of reference 92 where a minus sign is missing. As seen in equation (3.7), the molecular field and the factor in front of the spin operator in the Hamiltonian have opposite signs.

reproduce the experimental equilibrium properties of the material. This leads to effectively two different kinds of exchange couplings in this type of model even though they have the same origin[240,242]. We note however that they have distinct roles. The $\chi_{\mu\nu}$ parameters dictate the value of the conduction electrons exchange splitting for a given configuration of the localized spins. The coupling constant J_ν gives the localized spins exchange splitting in the longitudinal term while in the transverse term, it gives the amount of angular momentum that is transferred to the conduction electrons per unit of time. The latter kind of exchange is purely dynamical while the two former exist during the dynamics as well as in equilibrium. The spatially averaged conduction electrons spin polarization is given by:

$$\bar{s}^z = x\bar{s}^z_A + (1-x)\bar{s}^z_B \tag{5.16}$$

This quantity is related to the total spin angular momentum s_e stored in the conduction electrons via $s_\mathrm{e} = \hbar N \bar{s}^z$. As we will see, and as already mentioned in chapter 3, this quantity is usually rather small, which leads to the fact that the total angular momentum of both sublattices of localized spins is almost conserved. However, this does not mean that the spin polarization of the conduction electrons has an unimportant role. Rather than the angular momentum, it is the energy of the conduction electrons that will play a decisive role. The quantities of interest are then the exchange splitting and the spin accumulation (related to the conduction electrons spin polarization below) which are not small energies.

Equation (5.14) and (5.16) are only valid at equilibrium while equations (5.15) is valid at all times. The latter equation provides the general effect of the second term of equation (5.13) while the effect of the third term is the dynamical splitting $\Delta_\nu = -J_\nu \bar{s}^z_\nu$ of the energy levels of the localized spins. We now focus on the first term of this Hamiltonian. The effect of this term is to transfer angular momentum and energy between electrons and spin. The electrons are assumed to be in thermal equilibrium at all times, but because we need to keep track of the angular momentum and energy in the conduction electrons, the state of this thermal bath changes in time and the standard procedure[22] needs to be extended. This is discussed in reference 73. We only summarize the calculations. One starts with the Von Neumann equation (2.15) to calculate the dynamics of the density matrix. Any entanglement between the electronic and spin systems are neglected such that $\hat{\rho} = \hat{\rho}_\mathrm{e}\hat{\rho}_\mathrm{S}$ (understood as a direct product and not a matrix product) where $\hat{\rho}_\mathrm{e}$ is the density matrix that describes the electronic system and $\hat{\rho}_\mathrm{S}$ describes the localized spins. $\hat{\rho}_\mathrm{e}$ is assumed to be the equilibrium grand canonical density matrix. It is diagonal in the basis $|N\rangle$ of eigenvectors of the electronic Hamiltonian (without the transverse term of the electron-spin coupling). Its matrix elements are then $\rho_{NN'} = \delta_{NN'} e^{-\beta_\mathrm{e}\xi_N}$ where $\beta_\mathrm{e} = 1/(k_B T_\mathrm{e})$, $\xi_N = \sum_{\mathbf{k}s}(\varepsilon_{\mathbf{k}s} - \mu_s) n^N_{\mathbf{k}s} = E_N - \sum_{\mathbf{k}s} \mu_s n^N_{\mathbf{k}s}$ with $\varepsilon_{\mathbf{k}s}$ the energy of the single particle state with

wave vector $\mathbf{k}$ and spin projection s, μ_s the chemical potential for electrons of spin projection s and n^N refers to the occupation numbers when the electronic system is described by the many body state $|N\rangle$. The dynamics of the density matrix for the localized spins $\hat{\rho}_S$ is then obtained in the Markov and secular approximations[22]. This requires that the time resolution of the model be much larger than the correlation time of the thermal bath (the conduction electrons) **and** much larger than $\hbar/J$ respectively, while still being much smaller than the characteristic time of magnetization dynamics[22,73]. As noted by Beens *et al.*[93], this is probably not realizable because $\hbar/J \sim 10$ fs and typical demagnetization times are around 100 fs. We note that the localized spin density matrix is not assumed to be diagonal, as required if one wants to study coherent transverse dynamics[84]. However, magnetization dynamics at an ultrashort timescale is longitudinal and we do focus on longitudinal dynamics only. In this case, $\overline{S}^z_\nu = \langle S^z_\nu(t)\rangle = \mathrm{Tr}(\hat{\rho}_S(t)S^z_\nu)/\mathrm{Tr}(\hat{\rho}_S(t))$ only depends on the diagonal elements $\rho^\nu_m \equiv \rho_{S\nu m\nu m}$ of the localized spins density matrix, where m indexes one of the $2S_\nu + 1$ localized spin states $|\nu m\rangle$, because the z component of the localized spin operator is diagonal*. The master rate equations governing the dynamics of the localized spin density matrix is then[22]:

$$\frac{\mathrm{d}\rho^\nu_m}{\mathrm{d}t} = W^\nu_{m,m+1}\rho^\nu_{m+1} + W^\nu_{m,m-1}\rho^\nu_{m-1} - \left(W^\nu_{m+1,m} + W^\nu_{m-1,m}\right)\rho^\nu_m \tag{5.17}$$

Where the rates $W^\nu_{m,n}$ for transitions from a state where the localized spin ν has a spin projection n to a state where it is m are given by[22]:

$$W^\nu_{m\pm1,m} = \frac{2\pi}{\hbar}\sum_{NN'}\left|\left\langle (m\pm1)N\left|\sum_i \frac{-J_\nu}{2}\left(S^+_i s^-_i + S^-_i s^+_i\right)\right|mN'\right\rangle\right|^2 \frac{\rho_{N'N'}}{\Xi}\delta(E_N - E'_N \pm \Delta_\nu) \tag{5.18}$$

Where Ξ is the grand canonical partition function, the inner sum should be carried out over lattice sites belonging to the sublattice ν only (the terms for the other sublattice give zero) and we omitted the ν index in the states $|mN\rangle$. Only transitions where the spin projection changes by one unit are allowed in this first order theory. We discuss in appendix A how this expression can be simplified rigorously and especially compare it with what one gets from the standard intuitive derivation based on Fermi's golden rule where one introduces Fermi-Dirac distributions directly. Assuming that all the transitions happen in a range of energy around the Fermi energy where the

*We note that in the ferrimagnetic case, the localized spin density matrix is actually described in terms of states $|\nu m;\mu n\rangle$ (and thus with elements $\rho_{\nu m\mu n;\nu m'\mu n'}$) rather than $|\nu m\rangle$. This is not an issue in the first order approach presented here because only transitions where only one kind of localized spin changes its spin projection m are authorized. Thus one does not consider transitions $|\nu m;\mu n\rangle \to |\nu m';\mu n'\rangle$ and one may forget the second pair of indices when writing density matrix elements. Otherwise, because both localized spin subsystems are entangled, the transitions in one sublattice may depend on the state of the other sublattice.

densities of state $D_\uparrow$ and $D_\downarrow$, for spin up and spin down electrons respectively, are constant, one gets[92*]:

$$W^{\nu}_{m\pm1,m} = C_\nu S^{\nu\pm}_m(\Delta_\nu - \Delta\mu)\frac{\exp\left(\mp\beta_e(\Delta_\nu - \Delta\mu)/2\right)}{2\sinh\left(\beta_e(\Delta_\nu - \Delta\mu)/2\right)} \tag{5.19}$$

Where we denoted the spin accumulation $\mu_\uparrow - \mu_\downarrow$ by $\Delta\mu$ and $S^{\nu\pm}_m = S_\nu(S_\nu+1) - m(m\pm1)$. The expression of C_ν is given in appendix A. We note that it should depend on the exchange splitting itself if we did not assume that the densities of state were constant. Contrary the case where conduction electrons spin polarization is neglected[240], one actually needs three distinct sets of parameters because, as Gridnev argues, C_ν cannot be simply obtained from J_ν even though $C_\nu \propto J^2_\nu$. We also discuss this in appendix A. The average value of the localized spins is given by $\overline{S}^z_\nu = \sum_m m\rho^\nu_m / \sum_m \rho^{\nu\,\dagger}_m$. One then sees that there are $2S_\nu$ equations to solve in order to get the localized spin dynamics.

The spin accumulation depends on the conduction electrons spin polarization $\bar{s}^z$. The number of electrons with spin s is $N_s = \int f_s(E)D_s(E)\mathrm{d}E \simeq N_0 + D_s(\mu_s - E^0_s)$ where f_s is the Fermi-Dirac distribution for electrons with spin projection s and N_0 is the number obtained when integrating up to a certain reference energy E^0_s, close to the Fermi energy E_F but such that $E_F - E^0_s$ is larger than the conduction electron exchange splitting. Then $\bar{s}^z = (N_\uparrow - N_\downarrow)/(2N)$ and the total number of conduction electrons is $N = N_\uparrow + N_\downarrow$. Inverting this system of equation plus using the fact that at equilibrium when $\Delta\mu = 0$ we have $\bar{s}^z_{ie} \equiv (N_\uparrow(\mu_\uparrow = \mu) - N_\downarrow(\mu_\downarrow = \mu))/(2N)$, we get[128]:

$$\Delta\mu = (\bar{s}^z - \bar{s}^z_{ie})\frac{D_\uparrow + D_\downarrow}{D_\uparrow D_\downarrow} + \delta \tag{5.20}$$

Where the densities of states are now densities of states per atom (i.e. $D_s := ND_s$) and $\delta = (E^0_\uparrow - E^0_\downarrow) - (E^{0ie}_\uparrow - E^{0ie}_\downarrow)$ is the change of the conduction electron band exchange splitting $(E^0_\uparrow - E^0_\downarrow)$ which is related to the parameters $\chi_{\mu\nu}$. Gridnev does not consider this effect[92]. We will thus not consider this term anymore for ferrimagnetic systems. At all times, the instantaneous equilibrium spin polarization $\bar{s}^z_{ie}$ is given by the equilibrium equation (5.16) combined with (5.15). The true conduction electrons spin polarization is obtained from conservation of angular momentum as already explained in chapter 3. We give again the corresponding equation with the notations of this chapter, for completeness:

$$\frac{\mathrm{d}\bar{s}^z}{\mathrm{d}t} + \boldsymbol{\nabla}\cdot\mathbf{J}_{s^z} = -x\frac{\mathrm{d}\overline{S}^z_A}{\mathrm{d}t} - (1-x)\frac{\mathrm{d}\overline{S}^z_B}{\mathrm{d}t} - \frac{\bar{s}^z(t) - \bar{s}^z_{ie}(t)}{\tau_s} \tag{5.21}$$

*The expression we give is slightly different than the one found in references 92, 233, 234 but agrees with the one found in 93.

†We follow the convention introduced at the beginning of this thesis where the trace of the density matrix is not necessarily one.

$\mathbf{J}_{s^z}$ is now a spin polarization current instead of an angular momentum current. It is related to the spin current density $\mathbf{j}_\uparrow - \mathbf{j}_\downarrow$ via the electric charge $\mathbf{j}_\uparrow - \mathbf{j}_\downarrow = -e\mathbf{J}_{s^z}/V_{at}$ with V_{at} the average atomic volume*. In the case of diffusive transport, it is then obtained from equation (3.26a). The direct localized spin-lattice interaction is neglected although it might be significant when gadolinium is substituted by terbium[106]. The conduction spin-lattice relaxation originates from any kind of spin dependent interaction involving conduction electrons as discussed for ultrafast demagnetization. However, this particular form with a relaxation time is generally not correct. The 2TM must be supplemented by a term $-\mathrm{d}E_\mathrm{s}/\mathrm{d}t$ on the right hand side of equation (5.11a) in order to account for the transfer of energy from the localized spins to the conduction electrons. The energy density in the localized spin system is given by $E_\mathrm{s} = x\Delta_A \overline{S}^z_A/V_A + (1-x)\Delta_B \overline{S}^z_B/V_B$, with V_ν the atomic volume of atom ν, as directly obtained from the Hamiltonian.

The magnetization dynamics is obtained as follow. First one must determine the equilibrium values of $\overline{S}^z_\nu$, $\bar{s}^z$ and ρ^ν_m using equations (5.14) to (5.16) and the equilibrium density matrix for the localized spin system as in chapter 3. The coupled equations to be solved for the dynamics are equations (5.17) and (5.21). The transitions rates (5.19) require the knowledge of the exchange splitting, chemical potential and electron temperature obtained via equations (5.15) and (5.20) and with the 2TM respectively. The value of $\bar{s}^z_{ie}$ is obtained from equation (5.16) and δ is usually neglected. We note that the localized spins are never assumed to be in equilibrium with the conduction electrons bath during the dynamics contrary to stochastic LLG. Equilibrium of the localized spins is satisfied when $\mathrm{d}\rho^\nu_m/\mathrm{d}t = 0$ which is obviously not always the case from equation (5.17). It can be shown that when $\mathrm{d}\rho^\nu_m/\mathrm{d}t = 0$, the localized spin density matrix is given by the standard equilibrium density matrix[22,73], as it should.

Romain Billet has implemented the first version of Gridnev's model[92] under our supervision. Compared to the model presented here, it considers a simple biexponential evolution of the electron temperature $T_\mathrm{e}(t) = T_0 + \Delta T_\mathrm{e}(1 - \exp(-t/\tau_0))\exp(-t/\tau_E)$ where T_0 is the initial temperature, which increases by ΔT_e in a characteristic time τ_0 and relaxes with a characteristic time τ_E. We use the same parameters as Gridnev[92†], except for an initial temperature of 300 Kelvins, $C_A = 0.5$ ps^{-1}, $C_B = 5$ ps^{-1}, $\tau_0 = 100$ fs, $\Delta T_\mathrm{e} = 1578$ Kelvins and $\tau_E = 1$ ps. The spin of gadolinium is three while the one of the transition metals is one. The localized spin polarizations are displayed as a function of temperature for $x = 0.4$ in figure 5.8. One can observe the usual type of curves for RE-TM ferrimagnets[291]. Note however that we did not plot the contributions of conduction electrons. Considering these conduction electrons leads to various

*Note that the spin current density defined like this is not a current density of angular momentum. The current density of angular momentum is $\hbar\mathbf{J}_{s^z}/V_{at}$.

†The value of the density of state is given in reference 233.

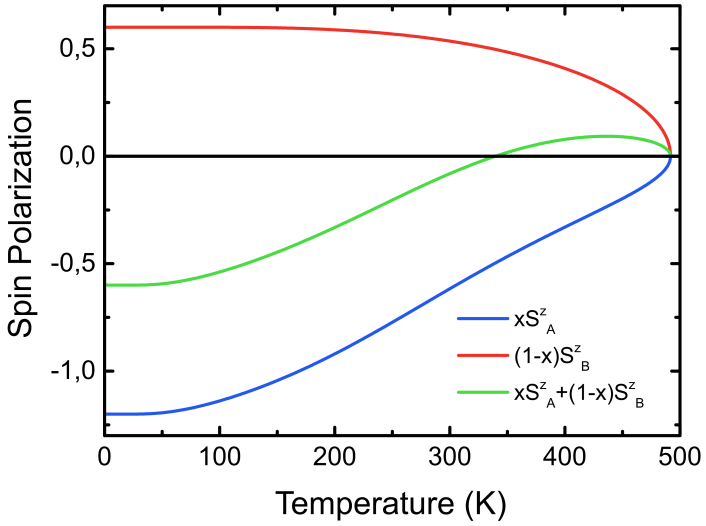

Figure 5.8: Spin polarization as a function of temperature for a GdFeCo alloy with a concentration $x = 0.4$.

compensation points as discussed in reference 234. In figure 5.9, we plot the dynamics for various spin polarizations in the absence of spin-lattice relaxation and with a spin-lattice relaxation time of 0.1 ps. Without spin-lattice relaxation, the total spin polarization $\bar{s}^z + x\bar{S}^z_A + (1-x)\bar{S}^z_B$ is conserved, as expected. In this case, both sublattice polarizations reverse, which is not always the case without spin-lattice relaxation, especially above the compensation temperature (the compensation temperature is here around 340 Kelvins). However, both sublattice cannot reach their equilibrium spin polarization, in order to conserve angular momentum. We notice that indeed

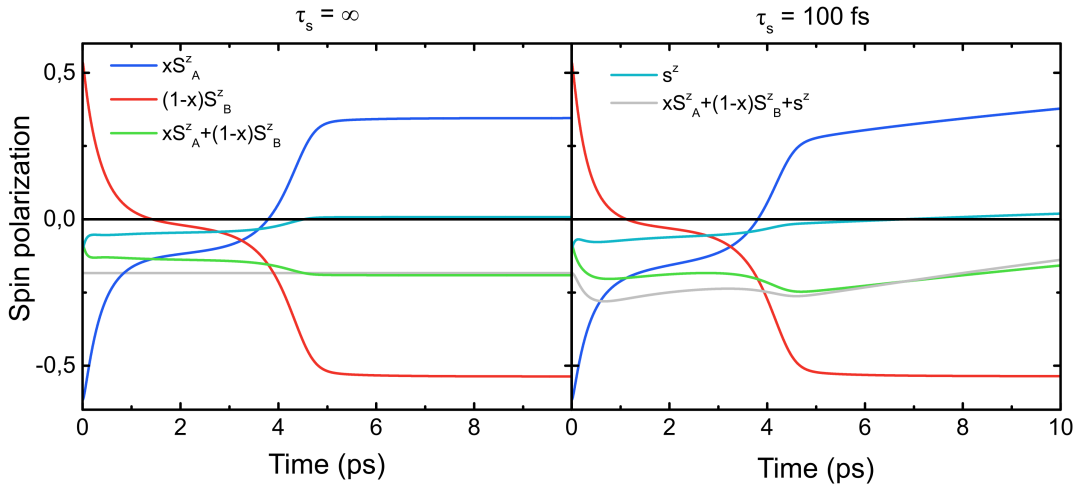

Figure 5.9: Spin polarization dynamics for a GdFeCo alloy with a concentration $x = 0.4$ and an initial temperature of 300K. Different spin polarizations are plotted as indicated by the legend.

the change of conduction electrons spin polarization is small compared to the change of localized spin polarization. When spin-lattice relaxation is allowed, the dynamics at short timescale (i.e. before the characteristic spin-lattice relaxation time) is almost identical to the case without it. However on a longer timescale, angular momentum will be lost to the lattice such that both sublattices may retrieve their equilibrium magnetization. In this case, the total spin polarization crosses zero at around 18 ps.

The quantity of interest that gives the generated spin accumulation by such a magnetic layer in ferrimagnetic/normal metal structures, as observed by Choi and Min[170], is the spin generation rate $-\frac{\mathrm{d}}{\mathrm{d}t}(x\overline{S}_A^z + (1-x)\overline{S}_B^z)$. This is seen from equation (5.21). We will see below that under certain assumptions regarding the transport equation (5.21), the generated spin accumulation is proportional to the spin generation rate. We plot these spin generation rates for various alloy concentrations in figure 5.10. We can see a general trend as in figure 3.4 (b) where there is first

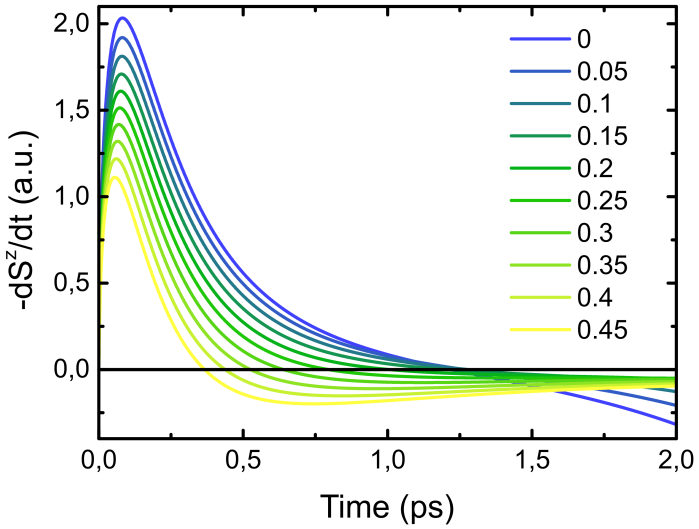

Figure 5.10: Spin generation rate in GdFeCo as predicted from Gridnev's model[92] for various concentrations x of gadolinium. The parameters are the same as in figure 5.9 except that we chose $\tau_s = 10$ fs for illustration purposes.

a positive peak followed later by a negative contribution. The negative peak is however absent for concentrations below 0.25*. We also observe that the first peak decreases in amplitude as the gadolinium concentration increases. The increase in the second peak amplitude is much less pronounced. One should be aware however that the actual measured spin accumulation will depend on spin transport. The model also shows that the details of the electron temperature dynam-

*There are in general other peaks at longer timescales due to a magnetization recovery or reversal. They happen at around 4 ps for our choice of parameters as may be seen from figure 5.9.

ics are important[92,233,234]. We argue that without any method to model such amorphous alloys without *ab initio* techniques, there exists no better general approach to model spin transport and dynamics in metallic heterostructures containing ferrimagnets.

5.4 Ultrafast magnetization dynamics of magnetic heterostructures in a s-d model

We now consider the simpler problem of ferromagnets. It is obtained directly from the theory for ferrimagnetic materials. We note that our approach is then slightly different from the approach of Beens *et al.*[93] where ferromagnetic order is assumed to arise from a Weiss model separated from the s-d Hamiltonian while in our case it is solely due to this Hamiltonian. There is no need to distinguish sublattices anymore but one still needs to discriminate the average conduction electrons spin polarization $\bar{s}_i^z$ at a lattice site i (identical for all lattice sites) from its spatially averaged value $\bar{s}^z$. $\bar{s}_i^z$ is related to the localized spin polarization by an electronic spin susceptibility as above:

$$\bar{s}_i^z = \chi \overline{S}^z \tag{5.22}$$

This equation is valid at all times, following what has been done for ferrimagnets. At equilibrium however, $\bar{s}_i^z = \bar{s}^z$. The exchange splitting may be related to the Curie temperature of the sample via $3\overline{S}^z k_B T_C = J\bar{s}_i^z S(S+1)$. This gives $\chi = 3k_B T_C/(JS(S+1))$. Out of equilibrium, the instantaneous equilibrium (spatially averaged) conduction electron spin polarization is given by equation (5.22) as $\bar{s}_i^z$. $\bar{s}^z$ on the other hand is given by equation (5.21). This equation may be expanded in the ferromagnetic case. In order to do so, we introduce the normalized magnetization $m = -\overline{S}^z/S$ and note that the conduction electron exchange splitting is $-J\overline{S}^z$. Here, we do not want to neglect δ as in Gridnev's model[92]. It is then given by:

$$\delta = -J(\overline{S}^z - \overline{S}_{ie}^z) \tag{5.23}$$

Where $\overline{S}_{ie}^z$ is the instantaneous equilibrium value of the localized spin obtained by solving equation (5.14) for ferromagnets or equivalently (3.7). Combining equations (5.20) and (5.21), we then find:

$$\frac{\mathrm{d}\Delta\mu}{\mathrm{d}t} = \frac{\mathrm{d}m}{\mathrm{d}t}\left(\frac{S}{\overline{D}}(1+\chi) + JS\right) - JS\frac{\mathrm{d}m_{ie}}{\mathrm{d}t} - \frac{\boldsymbol{\nabla}\cdot\mathbf{J}_{s^z}}{\overline{D}} - \frac{\Delta\mu}{\tau_s} + JS\frac{m - m_{ie}}{\tau_s} \tag{5.24}$$

Where $m_{ie} = -\overline{S}_{ie}^z/S$ and $\overline{D} = D_\uparrow D_\downarrow/(D_\uparrow + D_\downarrow)$. We note that we do not have exactly the same equation than Beens *et al.*[93] because we have additional terms on the right hand side that depend

on m_{ie} (the second and last terms). We believe this is due to the fact that they do not consider the longitudinal terms of the s-d Hamiltonian explicitly. Without these additional terms and for $\chi \simeq 1$, we retrieve the same equation*. One usually focuses on the case where $S = 1/2$ in ferromagnets. This does not affect equation (5.24) much but the dynamics of the localized spin is now given by a single equation. A little algebra using the equations of the previous section immediately gives the same equation as the one obtained by Beens *et al.*[93]:

$$\frac{\mathrm{d}m}{\mathrm{d}t} = \frac{1}{\tau}\left(m - \frac{\Delta\mu}{2k_B T_C}\right)\left[1 - m\coth\left(\frac{2mk_B T_C - \Delta\mu}{2k_B T_\mathrm{e}}\right)\right] \tag{5.25}$$

Where $1/\tau = 2k_B T_C C$ with C given in appendix A. Equations (5.24) and (5.25) together with a 2TM (with electron-spin coupling) and the instantaneous equilibrium equation $m_{ie} = \tanh(m_{ie}T_C/T_\mathrm{e})$† for the localized spin provide the full description of the spin transport and dynamics in any heterostructure with spin $1/2$ ferromagnets. However, one needs an additional model for $\mathbf{J}_{s^z}$. If the system also contains ferrimagnetic layers, one needs to use the equations of the previous section. The total spin polarization in a ferromagnetic layer is given by $\overline{S}^z + \bar{s}^z$. The corresponding total normalized magnetization is given by:

$$m_\mathrm{tot} = m - \frac{J\overline{D}m_{ie} + 2\overline{D}\Delta\mu}{1 + \chi + J\overline{D}} \tag{5.26}$$

When one neglects J and take $\chi = 1$ in this expression and in equation (5.24), the total magnetization is given by $m_\mathrm{tot} = m - \overline{D}\Delta\mu$ and is conserved. This is the assumption made by Beens *et al.*[93] and we will also make it from now on. We note that this model does not consider exchange interaction in real space and thus cannot describe systems with gradients of magnetization. This is an issue because the 2TM generates temperature gradient. In the magnetization reversal case that we will study in chapter 8, this can lead to unphysical results where only half of a magnetic layer has reversed its magnetization. Correcting this issue would require considering a layered magnetic system such as in reference 242.

The general theory presented in this chapter is applied in three different cases where we always consider GdFeCo/Cu/Ferromagnet(F) spin valves:

1. in section 7.1, we used the standard TMM together with the 2TM with heat diffusion as an input for the original microscopic three temperature model (m3TM)[107]. Only demagnetization of the ferromagnetic layer is then considered. The parameters used for the

*Note that in our case, there is a minus sign in front of the s-d Hamiltonian which explains the sign difference between $\rho = \overline{D}^{-1} - J/2$ in Beens *et al.*[93] compared to $\rho = \overline{D}^{-1}(1+\chi)/2 + J/2$ in our case.

†Note that in our derivation, m_{ie} is defined when $\Delta\mu = 0$ such that it is always given by $m_{ie} = \tanh((2m_{ie}k_B T_C - \Delta\mu)/(2k_B T_\mathrm{e}))$ together with the constraint the the spin accumulation must be zero.

demagnetization rate in this model are the same as the ones used in reference 187. These calculations were made in collaboration with Junta Igarashi from Tohoku University.

2. in section 7.4, we present simulations that have been performed by Maarten Beens from Eindhoven University of Technology in the context of a collaboration. It includes a 2TM without heat diffusion, Gridnev's model[92] of ferrimagnetic layers with the corrected expression for transition rates and Beens *et al.* model[93] of ferromagnets. Only the three layers GdFeCo, Cu and F are considered and light absorption in each layer was taken as a parameter. Spin transport is only modeled in the copper spacer layer and is assumed to be diffusive as the spacer layer is rather thick (> 20 nm). We note that this might actually not be the case in our samples.

3. in section 8.2, we used our theory of laser pulse absorption together with the 2TM and equation (5.25). Only the magnetization dynamics of the F layer was modeled. The spin accumulation was obtained from the magnetization dynamics of GdFeCo measured in reference 9 and is assumed to be instantly transferred to the F layer. Neglecting J and assuming that the spin polarization current term of equation (5.24) can be written as $\Delta\mu/\tau'$ for some characteristic time τ'[157], we get:

$$\Delta\mu = \frac{\tau'_s V_{at}}{\overline{D}\mu_B}\frac{\mathrm{d}M}{\mathrm{d}t} - \tau'_s\frac{\mathrm{d}\Delta\mu}{\mathrm{d}t} \tag{5.27}$$

Where $1/\tau'_s = 1/\tau' + 1/\tau_s$ and M is the total magnetization of GdFeCo. Replacing $\Delta\mu$ in the right hand side of this equation by the entire right hand side, one sees that $\tau'_s \mathrm{d}\Delta\mu/\mathrm{d}t$ is a much smaller term than $\tau'_s V_{at}/(\overline{D}\mu_B)\mathrm{d}M/\mathrm{d}t$, provided that τ'_s is much smaller than the characteristic magnetization dynamics time[157]. In our simulations, we use $\tau'_s \sim 35$ fs* (Choi and Min use 10 fs[170]) which is to be compared with the smallest timescale for GdFeCo dynamics (100 fs for the TM ultrafast demagnetization[9]). In this case we then used:

$$\Delta\mu = \frac{\tau'_s V_{at}}{\overline{D}\mu_B}\frac{\mathrm{d}M}{\mathrm{d}t} \tag{5.28}$$

This equation also allows to qualitatively reproduce the spin accumulation measured by Choi and Min[170] as shown in chapter 8. This model does not conserve angular momentum because of the constraint (5.28). It also neglects the spin accumulation generated by the F layer itself.

*The fact that this coincides with the laser pulse duration we use most of the time in this thesis is a coincidence. In fact when this model was applied, the laser pulse duration was around 100 fs for the experiments and set exactly to 100 fs for the modeling.

In all the 2TM models used, the exchange of energy between electrons and localized spins is neglected. This is experimentally justified for ferromagnetic systems subjected to a spin current in chapter 8.

5.5 Conclusion

In this chapter, we introduced the models that will be used in this thesis. First, we introduced our own theory of laser pulse absorption. This theory aims at generalizing the standard TMM. We showed how such an approach of calculating energy absorption from light for applications in models that sharply separate the energy from light and matter is devoted of physical sense in general. Still, it allows us to take chromatic dispersion into account as well as dynamical absorption gradients which may play a role in multilayered system when considering effects that happen at the femtosecond or subfemtosecond timescale such as charge transport. Then, we quickly presented the 2TM that we use and its numerical implementation. Afterwards, we presented Gridnev's model of AO-HIS[92,233,234] which will be used on several occasions in this thesis. Finally, we rederived Beens *et al.* model of ultrafast demagnetization of ferromagnets as a particular case of Gridnev's model. Considering dynamical exchange splitting explicitly, we arrived at a generalized equation for the dynamics of the spin accumulation in ferromagnetic systems for any value of the localized spin.

Chapter 6

Single laser pulse induced magnetization reversal of GdFeCo/Cu/GdFeCo spin valves

In this chapter, we focus on GdFeCo/Cu/GdFeCo spin valve structures where the gadolinium concentration x of the alloy is chosen to be far from the GdFeCo compensation composition x_{comp}. First we look at the behavior of single GdFeCo layers under the application of an external magnetic field or a single laser pulse. We worked with $x = 20.2\%$ and $x = 30.4\%$ (abbreviated to 20% and 30% respectively). Then, we put both layers in the same sample but separated by a copper layer of various thicknesses. We first study the static magnetic properties of these samples and explain the indirect exchange coupling between both magnetic layers in terms of RKKY and the equilibrium theory of GdFeCo presented in the previous chapter (equations (5.14) to (5.16)). Finally we study the effect of single laser pulses irradiation on these spin valves. In all this chapter, the laser pulse duration is 35 fs. We interpret our results through the generation of a spin current by both magnetic layers which can cross the thin copper layers that we use.

6.1 Single layers

The samples with a single layer of GdFeCo that we studied were Glass / Ta(5) / Cu(5) / Gd_xFeCo(5) / Cu(5) / Pt(5). We first consider the case $x = 20\%$ presented in figure 6.1. The hysteresis loop confirms the presence of PMA even for such a low value of x and its sign (positive

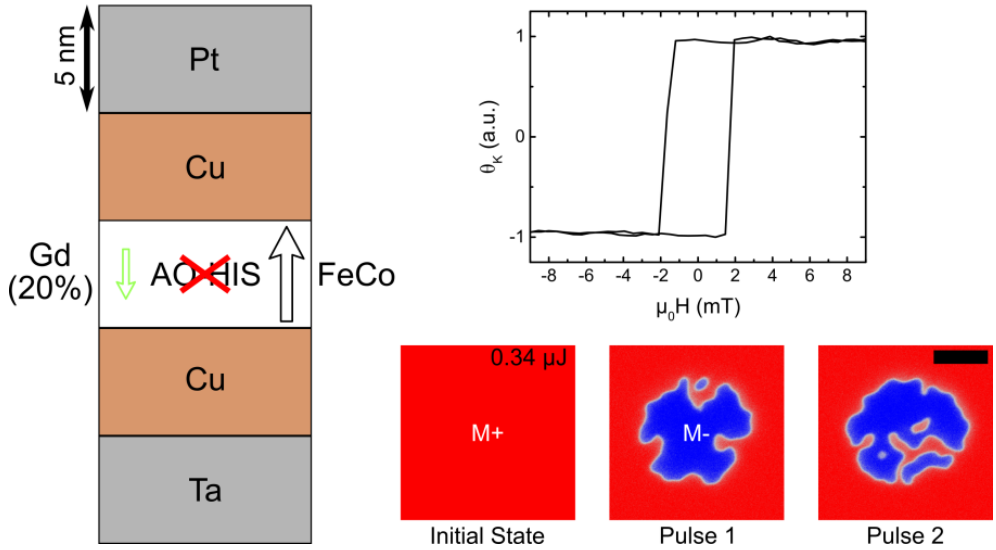

Figure 6.1: Behavior of the single layer structure with $x = 20\%$ under the application of an external magnetic field (top) and two consecutive laser pulses with an energy of 0.34 μJ and a duration of 35 fs (bottom). M+ and M- correspond to a positive and negative MOKE contrast respectively. The scale bar is 20 μm long and the pulse energy is 0.34 μJ.

Kerr rotation at high positive fields) is in agreement with the fact that the sublattice that dominates the total magnetization is the TM sublattice (the GdFeCo layer is said to be TM dominant). In the drawing on the left of figure 6.1, we represent the gadolinium sublattice magnetization by a green color while the black color always represents magnetization that originates from TM sublattices. Open arrows denote TM dominant layer while solid arrows, as in figure 6.2, denote a RE dominant layer. This is the convention used throughout the rest of this thesis. The microscope MOKE images obtained after single laser pulse irradiation (35 fs duration with a pulse energy of 0.34 μJ) show that for this alloy concentration x, there is no AO-HIS, similarly to the case with $x = 33\%$ shown in figure 4.8. This is consistent with the results of reference 236 even though our value of x_{comp} is around 27% against 26% in reference 236. This difference is attributed to the different interfaces of the GdFeCo layer in both works. In our work, the GdFeCo layers are sandwiched between two copper layers (unless otherwise mentioned) while in reference 236 one interface is with copper while the other one is with tantalum. In the case of $x = 30\%$, presented in figure 6.2, the magnetization is dominated by the gadolinium sublattice (the GdFeCo layer is said to be Gd or RE dominant) as seen by the fact that the hysteresis loop is inverted, and the sample exhibits AO-HIS with a threshold fluence around 1 mJ/cm^2. We note that the coercive fields we obtain are rather small (around 2 mT) because of the extreme alloy compositions that we use[236,292]. Thus, coercive fields are susceptible to have noticeable relative

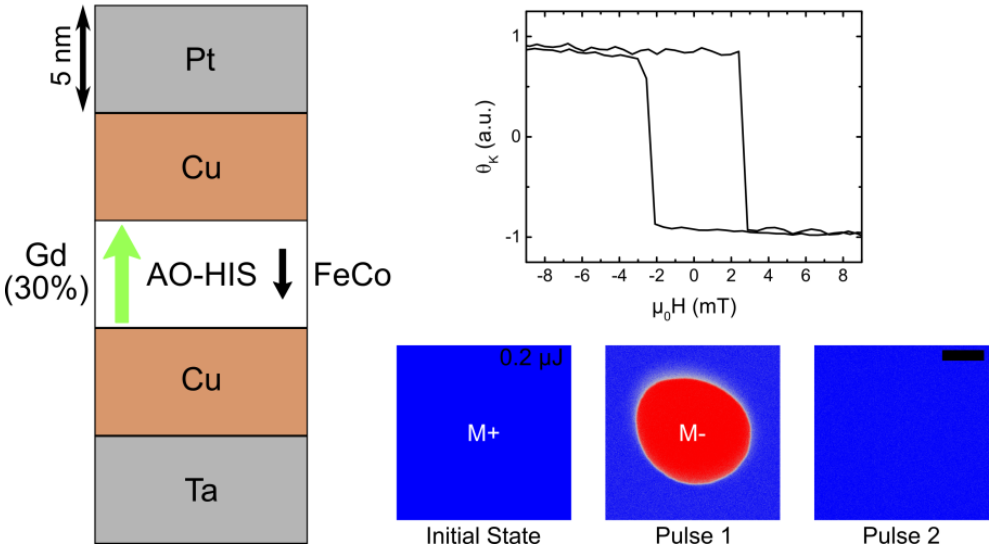

Figure 6.2: Behavior of the single layer structure with $x = 30\%$ under the application of an external magnetic field (top) and two consecutive laser pulses with an energy of 0.2 μJ and a duration of 35 fs (bottom). M+ and M- correspond to a positive and negative total magnetization respectively. The scale bar is 20 μm long and the pulse energy is 0.2 μJ.

variations from sample to sample. The hysteresis loops are also very sensitive to the history of the sample i.e. whether or not the sample is truly saturated. This is an issue because the coercive fields of both layers are similar. Then it is difficult to completely reverse the magnetization of only one layer using an external magnetic field.

6.2 Equilibrium properties of bilayers

We now move on to the study of Glass / Ta(5) / Cu(5) / Gd_xFeCo(5) / Cu(t) / Gd_yFeCo(5) / Cu(5) / (Pt or Ta)(5) spin valve structures. In the next section, we will study the influence of the capping layer (platinum or tantalum) and the position of the GdFeCo layers, i.e. either $x = 20\%$ and $y = 30\%$ or $x = 30\%$ and $y = 20\%$. This does not affect the equilibrium magnetic properties of the samples for the considered copper thicknesses t which are below 10 nm. Indeed, we observed that for $t \geq 60$ nm, the copper layer starts to become rough* and this can affect the magnetic properties of the layer that is directly deposited on this spacer. Then, in this section, we focus on Glass / Ta(5) / Cu(5) / $Gd_{20\%}$FeCo(5) / Cu(t) / $Gd_{30\%}$FeCo(5) / Cu(5) / Pt(5) samples with $t = 0$, 2, 3, 4, 6 and 10 nm. The hysteresis loop of the sample with $t = 0$ nm

*This was observed by Michel Hehn via atomic force microscopy measurements

is a standard hysteresis loop for a TM dominant GdFeCo. The coercive field is rather large for this material[236], around 80 mT, as for single GdFeCo layers with a composition close to x_{comp}. The samples with other thicknesses exhibit more complex behaviors. We show that in figure 6.3. The hysteresis loops for $t = 4$ and 10 nm are not shown and are almost identical to the hysteresis

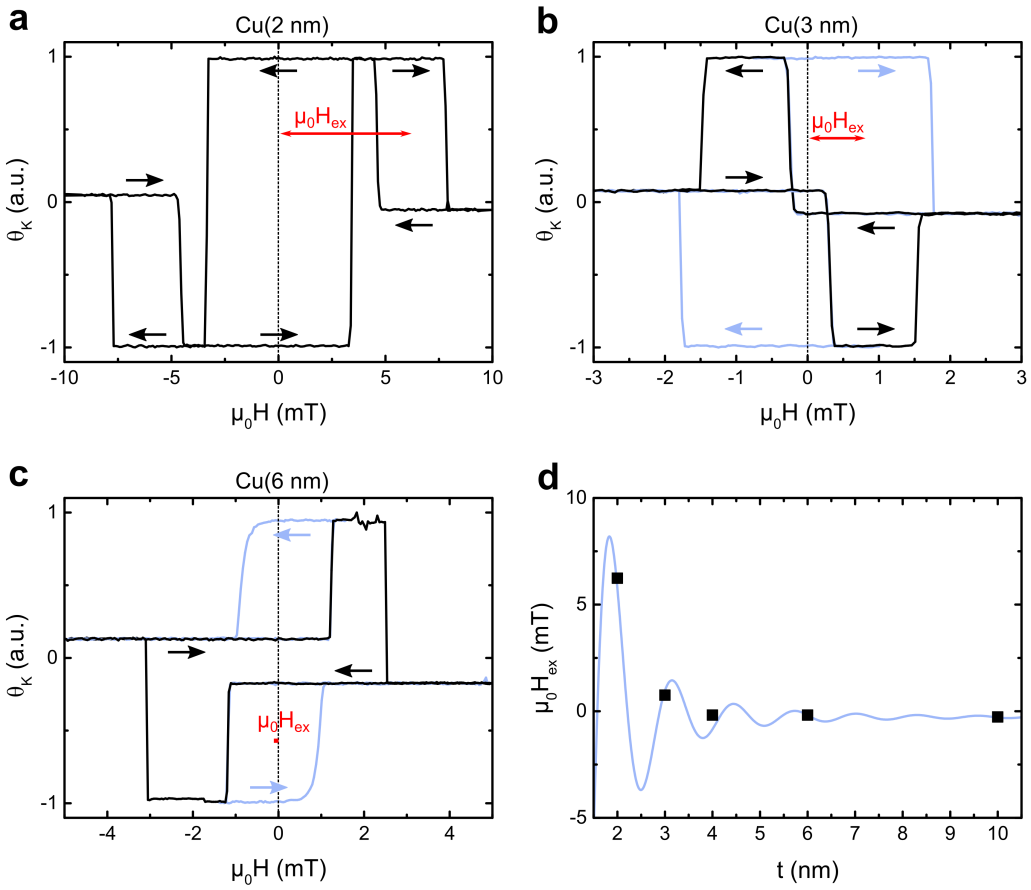

Figure 6.3: Hysteresis loop measurements of the GdFeCo/Cu(t)/GdFeCo samples with $t =$ (a) 2 nm, (b) 3 nm and (c) 6 nm. The light blue lines indicate minor hysteresis loop measurements. The black and light blue arrows indicate the sens of variation of the external magnetic field. The red arrows in figures (a) and (b) as well as the red bar in figure (c) show the exchange bias field $\mu_0 H_{ex}$ in the spin valve structures. These measurements were performed with the cw laser coming from the (top) sample side. Figure (d) shows the exchange bias field as a function of all copper thickness t except for $t = 0$ nm where this quantity cannot be measured. The light blue solid line is a fit using the function F, defined in the RKKY exchange parameter (3.10), plus a constant.

loop for $t = 6$ nm*. When the sample is saturated, one sees that the Kerr rotation signal is rather

*The coercive of both layers are closer to each other in these samples which makes the measurement of the minor loops very difficult.

small. This is because one layer, with $x = 30\%$, is RE dominant while the other is TM dominant, and because MOKE for a laser wavelength of 800 nm is only sensitive to the TM sublattice of GdFeCo[171]. Then when one layer reverses its magnetization and that the magnetizations of the TM sublattices of each layer are parallel, the Kerr rotation signal is much higher. When the spin valve is in this magnetic configuration we say that it is in a parallel (P) configuration. When both TM sublattices magnetizations are antiparallel we say that the spin valve is in an antiparallel (AP) configuration. We call such configurations positive (+) if the layer that does not exhibit AO-HIS has its TM sublattice magnetization pointing along the positive field direction (up in all figures) and we call it negative (-) otherwise. These configurations and definitions are summarized in figure 6.4.

For $t = 2$ nm, there is a strong indirect exchange coupling between both layers. The hysteresis loop of the GdFeCo layer with $x = 20\%$ is centered at 0 mT while the hysteresis loops (which are minor loops) corresponding to the GdFeCo layer with $x = 30\%$ are shifted by an exchange bias field of around 6 mT. This field is higher than the sum of the coercive field of both magnetic layers, resulting in three well separated loops. For $t = 3$ nm, the exchange bias field is smaller than the sum of both coercive fields and the hysteresis loops overlap. This means that a measurement of the minor hysteresis loops requires three different sets of measurements, one where both layers are reversed when the magnetic field is changing and two where only one layer reverses its magnetic field. The minor hysteresis loops measurements are shown in light blue in figure 6.3. In these measurements, after reversing one magnetic layer, the magnetic field needs to be increased even further (without reversing the other layer) such that the reversed magnetization is completely saturated, otherwise the hysteresis loop will not be symmetric. This happens if a small magnetic domain still remains. It suppresses the requirement that the external magnetic field be higher than the nucleation field of the magnetic layer. This is what happens for $t = 6$ nm where one can clearly see that the change of Kerr rotation in the minor hysteresis loop measurements is progressive while in the major hysteresis loop measurements, such variations are much sharper. We believe this is the cause for the small exchange bias field that we observe (around 0.2 mT for all layers with $t \geq 4$ nm). No indirect exchange coupling is expected for copper thicknesses larger than 10 nm[249]. We note that the relative amplitude of these loops depends on the absorption profile of the laser used for the MOKE measurement. In particular, copper is known have a high reflectivity[187,236]. Because we probe magnetization from the top side of the sample (the $x = 30\%$ side) the Kerr rotation signal of the layer with $x = 20\%$ tends to decrease, with respect to the one of the layer with $x = 30\%$, as the copper thicknesses increases.

We believe this indirect exchange coupling is due to a RKKY type of indirect exchange as

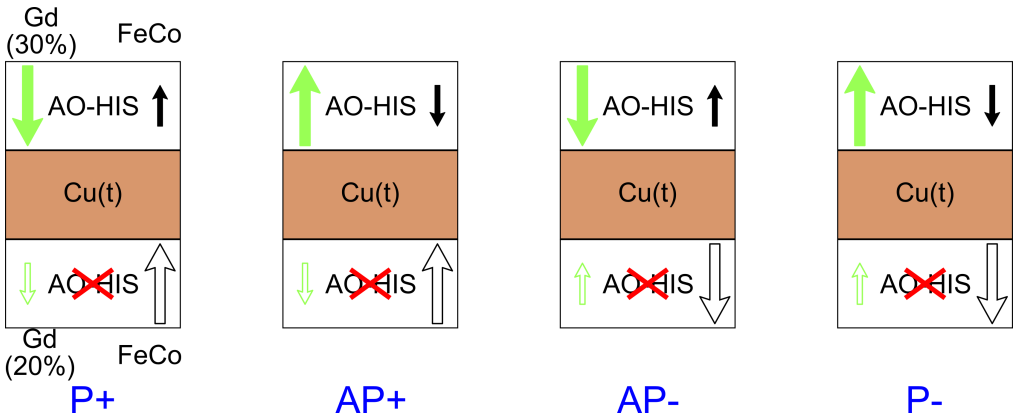

Figure 6.4: Summary of the four possible magnetic configurations in our spin valve structures with their corresponding designation (P+, AP+, AP- and P-).

observed in Co/Cu multilayers[293]. We fitted the measured exchange bias field as a function of the copper spacer thickness using the function F, defined in the RKKY exchange parameter (3.10). A small offset is added to this fit in order to take into account the very small exchange bias field measured for $t \geq 4$ nm. This offset is found to be 0.27 mT. The period of the RKKY oscillations are found to be around 1.28 nm which agrees well with the 1.2 nm reported in reference[293]. We note however that we do not have enough points to provide any relevant conclusion regarding this fit. Nevertheless, we do not know any other mechanism that can explain such indirect exchange coupling for thin films*.

One is however confronted to the issue that the peak observed around $t = 2$ nm in Co/Cu multilayers corresponds to an antiferromagnetic coupling between the cobalt magnetic moments of different cobalt layers, while in our case, it corresponds to a ferromagnetic coupling (parallel alignment). This is an issue because it is usually believed that the RKKY coupling is dictated by the TM atoms. Indeed, the 3d electrons of these atoms (carrying most of the magnetic moment) are much less localized than the 4f electrons of gadolinium (carrying most of the magnetic moment of this atom). We will however hypothesize that this is not the case. The reason, which is central in all the works presented in this thesis, is that the gadolinium atoms can also be very efficient at polarizing the conduction electrons. We note in this sense that the theory of RKKY[21] and the theory of AO-HIS[92,233,234] presented in the previous chapter are both based on the same Hamiltonian. The difference resides in the fact that in the theory of RKKY, one performs a time

*We note that the form of the RKKY exchange parameter given in equation (3.10) relies on the assumption that the electrons can be modeled as free electrons with an effective mass[21]. Thus the function F may not be the most suitable function to understand indirect exchange coupling in general. For noble metals such as copper, this seems however to be a reasonable approximation[175].

independent perturbation theory to second order to determine the $\chi_{\mu\nu}$ parameters while in the theory of GdFeCo presented in chapter 5 it is essentially time dependent perturbation theory to first order that is applied and the $\chi_{\mu\nu}$ are taken as parameters. In both theories, the spin polarization is determined by the exchange coupling parameters **and** the spin of the atom. While the exchange coupling of gadolinium with conduction electrons may be estimated to be about three[241] to ten[92,227] times smaller than the coupling for TM atoms, the spin of the gadolinium atoms is about four times larger than the spin of TM atoms[9]. Thus, it is possible that gadolinium could dominate the polarization of the conduction electrons and then the antiferromagnetic coupling would be between the TM sublattice of the TM dominant layer and the RE sublattice of the RE dominant layer. We show that gadolinium may dominantly polarize the conduction electrons in figure 6.5 where we simulated the spin polarization of the conduction electrons as a function of temperature and for three different alloy concentrations using the theory of chapter 5 with identical parameters. We can clearly see that there may exist a compensation temperature (or a

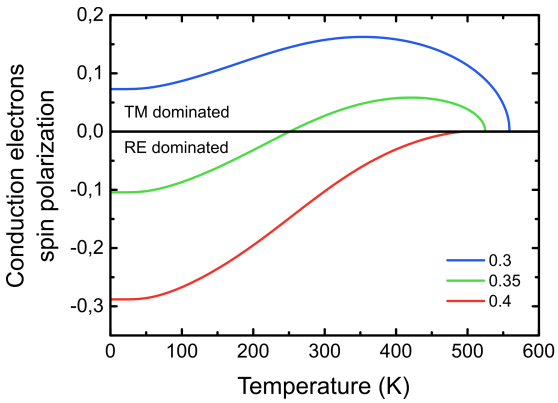

Figure 6.5: Conduction electrons spin polarization as a function of temperature for three different alloy concentrations x. A positive spin polarization means that the conduction electrons are mainly polarized by the TM sublattice while a negative polarization means that they are mainly polarized by the RE. Note that the spin polarization vanishes at the Curie temperature and that the Curie temperature depends on the alloy composition.

compensation composition) below (above) which the conduction electrons spin polarization can be dominated by the RE sublattice. It does not have to be equal to the magnetic compensation temperature. We believe that this hypothesis is further supported by the other results shown in this thesis.

6.3 Effect of a single laser pulse on bilayer structures

We now look at the results of sending single laser pulses on such heterostructures with MOKE microscopy. It is *a priori* expected that the layer with $x = 30\%$ should still exhibit AO-HIS but the behavior of the TM dominant layer may be influenced by non local effects such as spin currents generated in the RE dominant layer, stray fields and indirect exchange interaction. Moreover, spin currents can be due to ultrafast demagnetization of a magnetic layer or SDSE[160]. We will argue that magnetization reversal of the layer with $x = 20\%$ happens and is due to spin currents generated by the ultrafast demagnetization of the RE dominant layer while the other effects may play minor roles which do not explain the reversal by themselves. In all this section, laser pulse irradiation is performed from the substrate side except otherwise mentioned. MOKE microscopy is always performed on the other side (the sample side).

Magnetization reversal due to ultrafast spin currents

The cases with $t = 0$ nm and 2 nm are not very interesting because they exhibit AO-HIS just as single layers. This is understood because of the strong couplings between both magnetic layers[248]. The case with $t = 3$ nm and 4 nm are more interesting. Microscopy images obtained after exciting these samples with different number of pulses are shown in figure 6.6. We focus on what happens at the center of each image first. In both cases, the magnetic configuration changes

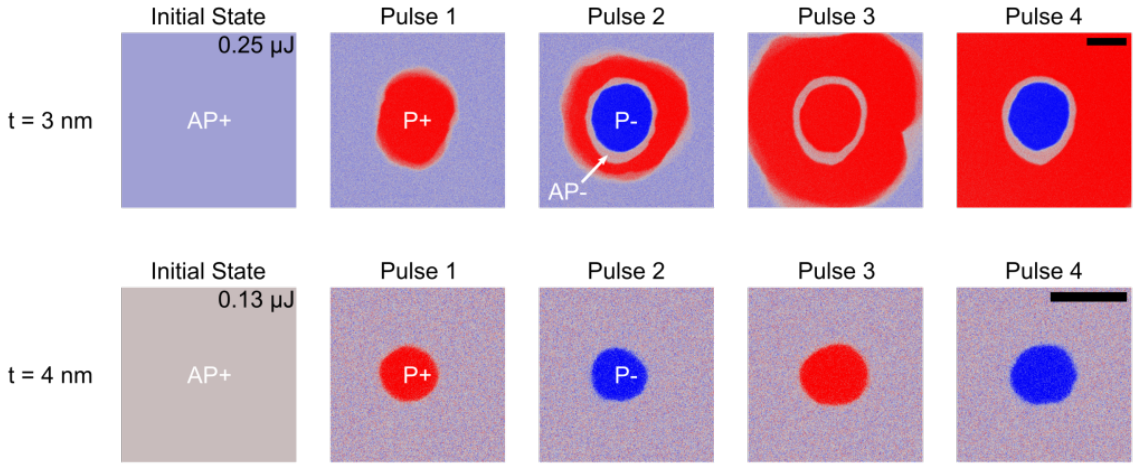

Figure 6.6: Results of sending single laser pulses on the GdFeCo/Cu(t)/GdFeCo spin valve structures for $t = 3$ nm and 4 nm. The magnetic configurations correspond to what is shown in figure 6.4. The scale bar is 20 µm long, the pulse energy is indicated in each case and the pulse duration is 35 fs. The almost grey color for $t = 4$ nm corresponds to a very small MOKE signal in this case for the AP+ configuration.

from AP+ to P+ after the first pulse. This corresponds to the reversal of the RE dominant layer which exhibits AO-HIS. After subsequent pulses, the magnetic configurations alternates between the P+ and the P- configuration, corresponding to a magnetization reversal of both layers. We hypothesize that this is due to a spin current generated by the ultrafast demagnetization of the RE dominant layer whose polarization would be mostly determined by the gadolinium sublattice as observed by Choi and Min[170]. This spin current would mostly interact with the TM sublattice of the TM dominant layer. This would explain why the TM dominant layer does not reverse its magnetization after the first pulse because the RE sublattice of the RE dominant layer is initially parallel to the TM sublattice of the TM dominant layer. After the first pulse however, they become antiparallel to each other which permits the magnetization reversal. We want to show that it is this mechanism which is happening. In the context of the theory presented in chapters 3 and 5, this mechanism is summarized in figure 6.7 where the main angular momentum transport channel is highlighted by the purple arrow. The spin current coming from the TM sublattice

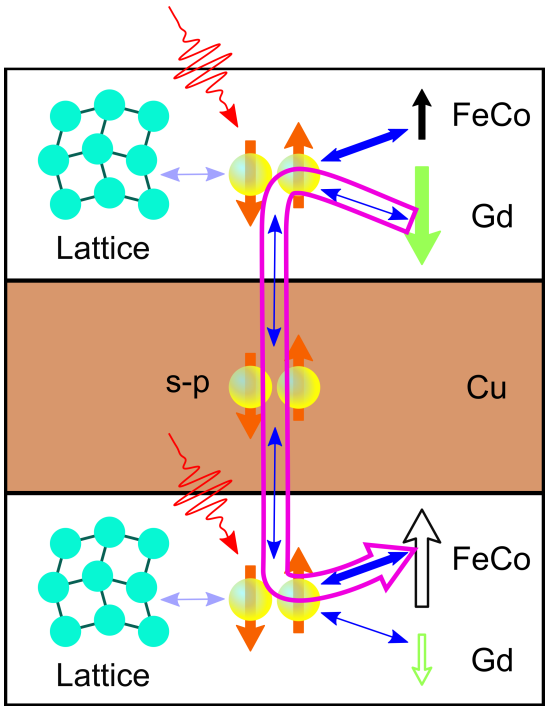

Figure 6.7: Representation of the transfer of angular momentum and energy in the GdFeCo/Cu/GdFeCo bilayer structures similar to figure 3.8. The main angular momentum transport channel we are supporting as the cause of the reversal of the TM dominant layer is highlighted by the purple arrow.

(the first positive peak from Choi and Min results[170]) is assumed to have a small effect because its amplitude is smaller and it arrives before in time. This will be further studied in the next chapters.

We now look at what is happening in the outer region of each image. Because of the gaussian profile of the beam, the sample receives less energy when moving away from the center. For $t = 4$ nm, nothing happens while for $t = 3$ nm, the magnetic domain that is generated after the first pulse is quickly expanding. This is attributed to the rather strong indirect exchange coupling in this case which favors a ferromagnetic coupling between TM sublattices as discussed in the previous section. A ring having an AP- configuration also appears and does not change after subsequent pulses. The fact that the same magnetization reversal behavior happens in the center of the image, independently of the indirect coupling, shows that, for these thicknesses, the RKKY coupling is not sufficient to explain the reversal of the TM dominant layer. In fact, similar behaviors are observed for samples with $t = 4$ nm and $t = 6$ nm. The reason for the formation of the AP- ring is discussed in more detail below for different structures and is also attributed to the same spin current mechanism. Indeed, the RE dominant layer does not need to reverse its magnetization to generate a spin current[170]. The spin generation rate is given by $-\mathrm{d}M/\mathrm{d}t$[92,170] which is higher in amplitude during the ultrafast demagnetization compared to the following reversal[9]. However, for subsequent pulses, the RE sublattice of the RE dominant layer is no longer antiparallel to the TM sublattice of the TM dominant layer and so no reversal can occur with the energies sent on this annular region of the sample. Finally, we note that for all these samples the threshold fluence for the reversal of the TM dominant layer, when starting from a P configuration was around 2.25 mJ/cm^2 except for the layer with $t = 0$ nm where it was around 1.48 mJ/cm^2. The obtained threshold fluences for the RE dominant layer are not relevant as the magnetization of the sample easily breaks into a multidomain state as the fluence is increased. This makes the method presented in chapter 4 unreliable in practice. We will present a more detailed analysis of the behavior of the RE dominant layer below for different samples.

Spin cooling and spin heating

We now look at the sample with $t = 10$ nm. For this thickness, starting from an AP configuration, the same behavior as for the samples with smaller thicknesses is observed. However, a first unexpected result is that the threshold fluence for the TM dominant layer reversal is around 1.54 mJ/cm^2 while we would expect it to be higher than for thinner copper spacer thicknesses. We have not found any reasonable explanation for this behavior. The second unexpected result is what happens when one sends a pulse starting from a P configuration. The comparison between P+ and AP+ is shown in figure 6.8. We show results for an identical pulse energy of 0.25 µJ. The AP- ring that appears when one starts from the P+ configuration is explained just as the AP- ring for $t = 3$ nm above. What is mostly interesting is the fact that while the RE dominant layer

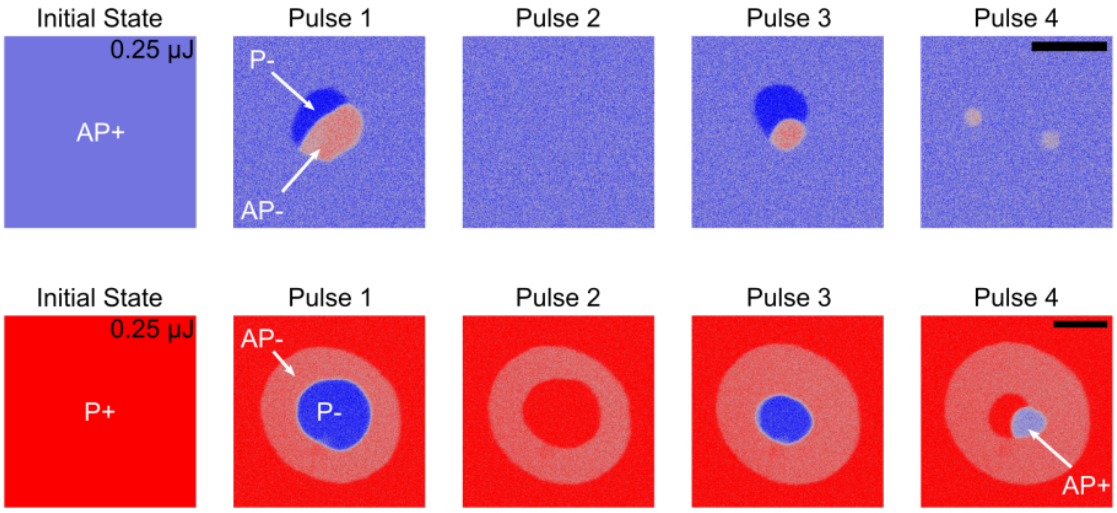

Figure 6.8: Results of sending single laser pulses on the GdFeCo/Cu(t)/GdFeCo spin valve structures for $t = 10$ nm. The magnetic configurations correspond to what is shown in figure 6.4. The scale bar is 20 µm long, the pulse energy is 0.25 µJ and the pulse duration is 35 fs.

reverses its magnetization together with the TM dominant layer in the center of the image when one starts from a P configurations, there is only a multidomain state (not necessarily stable) that appears from the AP configurations. This behavior is not observed for thinner copper spacers. Multidomain states appear from a saturated state (without any magnetic domains) if one heats up the sample locally such that the magnetization reaches almost zero. Then a gradient of magnetization appears meaning that the demagnetizing field may play a role[220] and stray fields are no longer zero (as it is for an infinite thin film). The demagnetizing field can generate magnetic domains. If the irradiated area is small enough, around the characteristic domain size, a single magnetic domain may be generated[221,222]. If the irradiated area is bigger than the characteristic domain size, fluctuations of the magnetization around zero in the center of the irradiated area will lead to a random magnetic pattern. In our samples, the characteristic domain size is difficult to determine experimentally because small domains are not stable. However we get stable magnetic domains smaller than 10 µm when irradiating the sample at high fluence, inevitably leading to a multidomain state. So we believe that the formation of any magnetic domain greater than 10 µm cannot be explained by the demagnetizing field. The stray field generated by magnetic domains in one layer could also explain the generation of magnetic domain in the other layer. However, we believe this cannot be the reason for the observed successive reversal in the center of the beam spot for a P+ initial configuration for two reasons: (i) we show below results for another sample with a thinner copper spacer where the annular domain pattern shown in figure

6.8, corresponding to the same magnetic behavior, is also present but for a much wider range of fluence (from around 3 to at least 9 mJ/cm^2 corresponding to domain sizes from around 25 to 65 µm); because stray fields are stronger close to domain edges we would expect that the magnetic behavior should be strongly affected by the size of the generated domains; we observe quite the opposite where the domain size depends only on the deposited energy as given by equation (4.3) and the thickness of the AP- ring goes towards zero as the fluence increases*; (ii) One can see that the magnetic domain at the center is not stable and disappears after several pulses; if this domain was due to the stray field of the larger AP- ring domain, it should still permit the formation of a magnetic domain at the center no matter how many pulses have been sent; on the other hand, while the system is in the AP- configuration, the RE sublattice of the RE dominant layer is parallel to the TM sublattice of the TM dominant layer such that a spin current may in principle hinder AO-HIS[294]. A direct proof that the observed magnetization reversals are not due to the magnetic dipolar interaction is the fact that these reversals can happen in less than a picosecond as shown in chapter 8 when the GdFeCo layer with $x = 20\%$ is replaced by a [Co/Pt] multilayer.

Thus, the behavior of the RE dominant layer is influenced by spin currents generated by the TM dominant layer. This has already been observed for Gd/Co bilayers where the spin current was generated by the ultrafast demagnetization of a Co/Ni multilayer[294]. In the latter case, the spin current was found to either hinder or assist AO-HIS by modifying threshold fluences. This is also something we describe below. However here the situation is much more stringent: the RE dominant layer reverses its magnetization for an initial P configuration while it is demagnetized (multidomain state) for an initial AP configuration. The spin current then generates a (full) disorder in the magnetic layer in the AP case while it brings more order in the P case. In the former case, we talk about spin heating (by a spin current) while in the latter we designates this as spin cooling (by a spin current). This concept of heating and cooling is related to the notion of spin temperature that is defined by disorder in the (localized) spin degree of freedom i.e. the effective temperature that needs to be put in equation (3.7) such that M is equal to the observed magnetization. Because the system is not necessarily at equilibrium, the spin temperature is not always equal to the electron temperature. We will also observe spin cooling and spin heating in the next chapters.

Another interesting point is that spin cooling of the RE dominant layer occurs in a P configuration when the RE sublattice of the RE dominant layer is antiparallel to the TM sublattice of the TM layer. The angular momentum transport channel is then the one shown in figure (6.7)

*One can show that $D\sqrt{\frac{1}{2}\ln\left(\frac{E}{E_{\text{th1}}}\right)} \sim D\sqrt{\frac{1}{2}\ln\left(\frac{E}{E_{\text{th2}}}\right)}$ as $E \to \infty$ for any two threshold energies E_{th1} and E_{th2}. This explain why the thickness of the ring decreases as fluence increases.

except that its direction is reversed. This means that the spin current of the TM layer acts on the RE sublattice of the RE dominant layer. This is consistent with the equilibrium properties of these samples that we reported in the previous section where it seemed that in the layer with $x = 30\%$, it is mostly the gadolinium sublattice that polarizes the conduction electrons. Another way to see it is by considering the form of the s-d hamiltonian (5.13). The transverse term depends on $S_i^+ s_i^-$ and $S_i^- s_i^+$. The latter term explains the generation of conduction electron spin polarization while the former describes absorption of spin polarization. This means that if the s-d model is really suitable to describe the magnetization dynamics of GdFeCo, the gadolinium sublattice should be as efficient to generate a spin current as to absorb one. Of course this will also depend on the dynamics of the system because this efficiency depends on temperature and spin populations as described by the transition rates in equation (5.19).

Finally, we note that we do not know the dynamics of this behavior and we did not make time resolved measurements for such systems. Because this behavior is only observed with laser irradiation through the substrate (see the next section on the impact of the capping layer), we cannot eliminate generation of spin currents due to SDSE (i.e. due to temperature gradients that are reversed when sending laser pulses from the other side of the sample) which can last for several hundreds of picosecond[169] and would thus generate a much slower dynamics than spin currents generated by ultrafast demagnetization.

Impact of the capping layer

So far we only studied the effect of sending a laser pulse through the susbtrate of the sample. The reason is that when one sends a pulse directly on the sample, a completely different behavior is observed. In particular, the RE dominant layer does not exhibit AO-HIS anymore. After a single pulse of light, the magnetic configuration will always change to a P configuration by reversing the magnetization of the RE dominant layer if the initial magnetic configuration is AP, but the magnetic configuration does not change anymore as long as it becomes P. This cannot be explained by some kind of magnetic coupling between both layers. Indeed, we compared the results of sending single laser pulses from the sample side on Glass / Ta(5) / Cu(5) / $Gd_{20\%}$FeCo(5) / Cu(10) / $Gd_{30\%}$FeCo(5) / Cu(5) / Pt(5) and Glass / Ta(5) / Cu(5) / $Gd_{20\%}$FeCo(5) / Cu(10) / $Gd_{30\%}$FeCo(5) / Cu(5) / Ta(5). That way, we could retrieve the AO-HIS of the RE dominant layer as shown in figure 6.9. We believe the reason for this difference of behavior is that in both samples, the heating is different due to a different generation of hot electrons. Indeed, 5 nm of platinum is quite close to the optimum (7 nm) found by Bergeard *et al.*[295] to induce a larger ultrafast demagnetization thanks to hot electrons. AO-HIS is a thermal driven process so one may

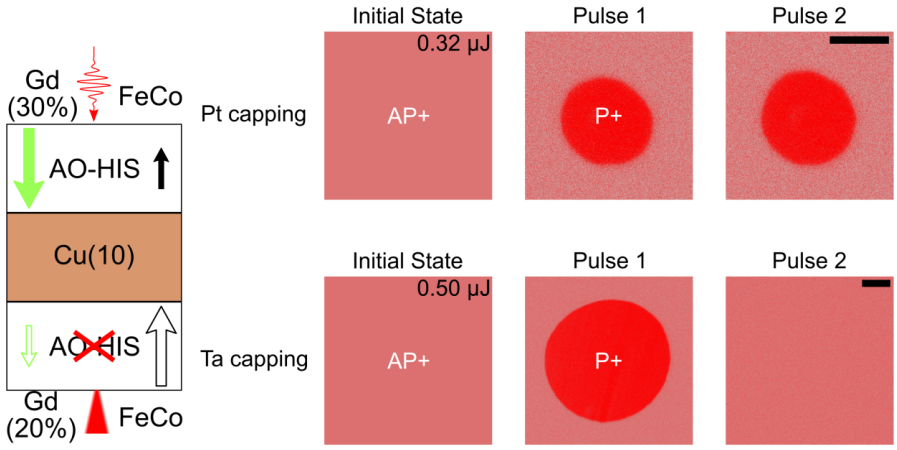

Figure 6.9: Results of sending single laser pulses on the GdFeCo/Cu(10)/GdFeCo spin valve structures with a Pt (0.32 μJ pulse energy) and Ta (0.50 μJ pulse energy) capping. The magnetic configurations correspond to what is shown in figure 6.4. The scale bar is 20 μm long and the pulse duration is 35 fs. The red cone indicates on which side MOKE microscopy is performed and the wiggly arrow indicates on which side we send single laser pulses.

believe that this process will be sensitive to the details of the heating dynamics, which seems to be a feature of Gridnev's model[233]*. We also note that the P configuration is not the one favored by the angular momentum transport channel that we highlighted in the previous part so we do not have any simple argument for this behavior and conclude that it must be a combination of a specific heating dynamics together with spin transport.

We found that inverting the order of the magnetic layers with a structure such as Glass / Ta(5) / Cu(5) / $Gd_{30\%}FeCo(5)$ / Cu(4) / $Gd_{20\%}FeCo(5)$ / Cu(5) / Pt(5) solves this issue. In the case of the latter sample, that we will use in the next section, the same behavior is observed no matter if the laser pulse is sent through the substrate or directly from the sample side. Thus in this case, we can discard SDSE as a possible effect to explain the magnetization reversal of the TM dominant layer.

Alloy concentration dependence

We now finish this chapter by studying the impact of the alloy concentration of the RE dominant layer. To do so, we studied two samples: Glass / Ta(5) / Cu(5) / $Gd_{30\%}FeCo(5)$ / Cu(4) / $Gd_{20\%}FeCo(5)$ / Cu(5) / Pt(5) and Glass / Ta(5) / Cu(5) / $Gd_{20\%}FeCo(5)$ / Cu(4) / $Gd_{27.3\%}FeCo(5)$ / Cu(5) / Pt(5) where both $Gd_{30\%}FeCo(5)$ and $Gd_{27.3\%}FeCo(5)$ (we now abbreviate 27.3% to 27%) exhibit AO-HIS. The magnetic layer with $x = 27\%$ has a composition that is very close to

*This has also been observed by Maarten Beens when he made the simulations that we present in chapter 7.

the compensation composition. Its threshold fluence for AO-HIS when it is in a single layer Glass / Ta(5) / Cu(5) / $Gd_{27.3\%}FeCo$(5) / Cu(5) / Ta(5) by itself is around 0.5 mJ/cm^2 (0.59 mJ/cm^2 when irradiating from the sample side and 0.46 mJ/cm^2 when irradiating from the substrate side) which is the lowest threshold fluence for AO-HIS we are aware of (the smallest reported value we are aware of is 0.76 mJ/cm^2[2269]).

Results of sending single laser pulses on these two samples are shown in figure 6.10. In all cases, in the center of the image, both magnetic layers reverse their magnetization as already shown several times. Our interpretation with spin currents is still consistent with these results. Something more interesting happens on the outer region. There, in the case where $x = 30\%$ for the RE dominant layer, only the TM dominant layer reverses its magnetization while when $x = 27\%$ only the RE dominant layer reverses its magnetization. The interpretation goes as follows: we know from Choi and Min results[170] as well as from Gridnev's model (see figure 5.10) that when one increases the gadolinium content in one magnetic layer, more spin current will be generated from gadolinium and this contributes to the second negative peak, which is assumed to drive the magnetization reversal. Moreover, no magnetization reversal of the GdFeCo layer is required to generate the spin current. Thus, in the $x = 30\%$ case, we have a higher threshold fluence for the RE dominant layer reversal and possibly more spin current while in the $x = 27\%$ case, we combine the effect of a lower threshold fluence for the RE dominant layer reversal with less spin current. For these samples, we believe that the most important factor is the threshold fluence of the RE dominant layer but still it shows that a spin current generated by ultrafast demagnetization is sufficent to induce magnetization reversal in another magnetic layer. In order to get more insight, we plot the magnetic domains diameters as a function of pulse energy. This is shown in figure 6.11. The corresponding threshold fluences are gathered in table 6.1. We

	Threshold Fluences (mJ/cm^2)			
x	RE dominant (P)	RE dominant (AP)	TM dominant (P)	TM dominant (AP)
30%	3,02 $\pm$ 0,12	3,33 $\pm$ 0,12	2,14 $\pm$ 0,09	-
27%	1,40 $\pm$ 0,03	1,17 $\pm$ 0,02	1,84 $\pm$ 0,03	1,82 $\pm$ 0,03

Table 6.1: Table for the threshold fluences of each magnetic layer in each sample for both RE dominant layer composition x. For $x = 27\%$, the threshold fluence for the TM dominant layer after the second pulse in the AP configuration is shown.

see that the threshold fluence for the reversal of the TM dominant layer is slightly smaller for $x = 27\%$. We hypothesize that the trend might be opposite is one uses $x \simeq 33\%$ instead of 30% because the spin current while be further increased in amplitude and because we observe

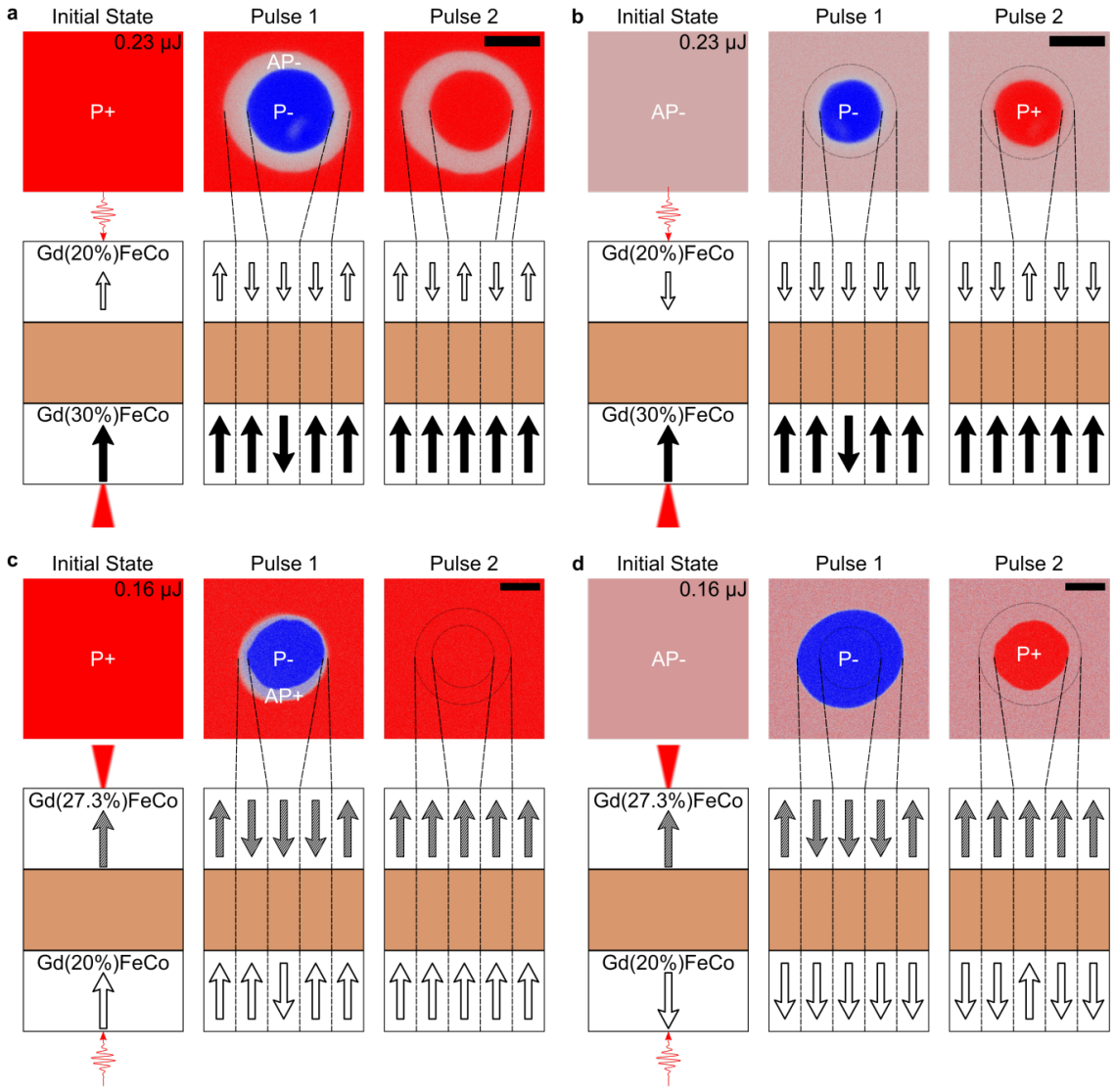

Figure 6.10: Results of sending single laser pulses on the GdFeCo/Cu(4)/GdFeCo spin valve structures with an alloy concentration in the RE dominant layer being 30% ((a) and (b) with a pulse energy of 0.23 μJ) and 27% ((c) and (d) with a pulse energy of 0.16 μJ). The initial magnetic configurations are P+ ((a) and (c)) and AP- ((b) and (d)). The magnetic configurations correspond to what is shown in figure 6.4. The scale bars are 20 μm long and the pulse duration is 35 fs. The red cone indicates on which side MOKE microscopy is performed and the wiggly arrow indicates on which side we send single laser pulses.

a smaller threshold fluence for this composition compared to $x = 27\%$ in the next chapter where the TM dominant layer is replaced by a ferromagnet. However we did not perform such measurements for the GdFeCo/Cu/GdFeCo structures. We checked that the reversal of the TM dominant layer after the second pulse in the case $x = 27\%$, with AP- as the initial configuration, is identical to the case with P+ as the initial configuration, as it should if the reversal only depends

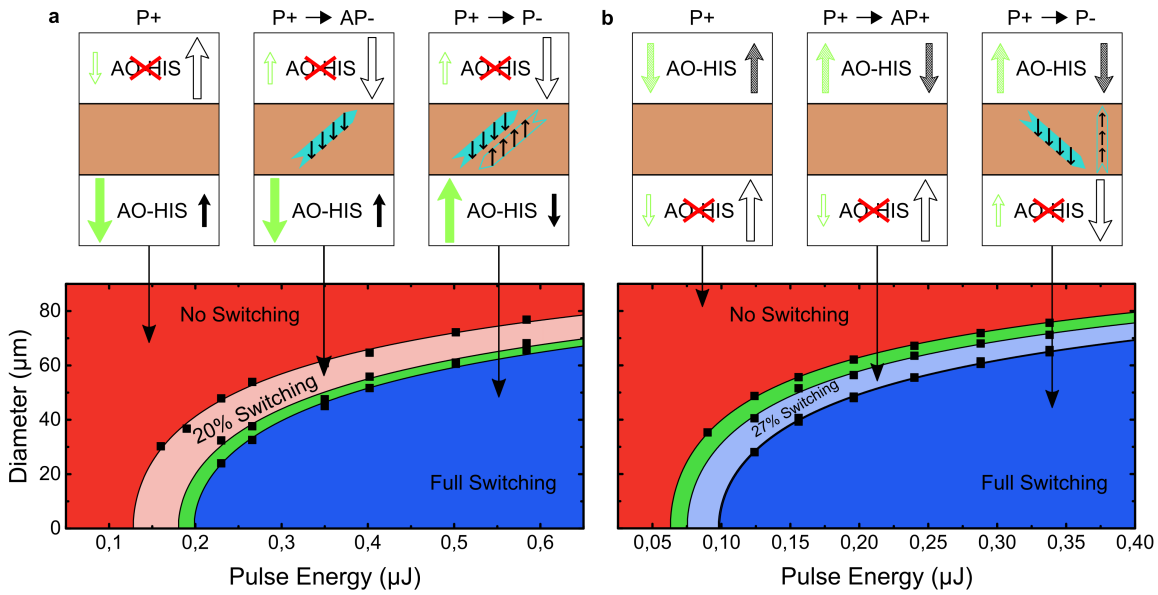

Figure 6.11: Magnetic domain diameter as a function of the laser pulse energy for (a) the sample with $x = 30\%$ and for (b) the sample with $x = 27\%$ starting from the P+ magnetic configuration. The colors in the graph represent the colors of figure 6.10 except the green color which represents the difference of magnetic domain size of the RE dominant layer between P+ and AP- initial configurations. Sketches above the graphs summarize the change of magnetic configuration after a single laser pulse irradiation starting from the initial configuration. The solid turquoise arrow represents the spin current going from the RE dominant layer to the TM dominant layer (with spin polarization indicated by the black arrows) and the open turquoise arrow represents the spin current going from the TM dominant layer to the RE dominant layer. The laser beam diameter is around 87 µm for $x = 30\%$ and around 83 µm for $x = 27\%$. The pulse duration is 35 fs.

on the deposited energy. Indeed, one sees from figure 6.10 that before the reversal of the TM dominant layer in the AP- initial configuration, a P- domain appears which could have an effect on the magnetization reversal of the TM dominant layer. Because we do not see any difference in the threshold fluences, this gives us another hint that stray fields do not play a role in the magnetic reversals we observe.

We drew the (hypothesized) main angular momentum transport channel in figure 6.11 for the reversal of the TM dominant layer (solid turquoise arrow). However, we also see a difference of threshold fluence for the RE dominant layer in P and AP configurations. The corresponding angular momentum transport channel is drawn as a solid turquoise arrow. In the case where $x = 30\%$, this difference corresponds to the fact that it is easier to reverse the RE dominant layer starting from a P configuration as is visible from figure 6.10. This corresponds to the same behavior that we observe for a copper thickness of 10 nm except that this time, it is still

possible to reverse that magnetic layer for both initial configurations. This is then similar to the work of reference 294 except that the spin current seem to interact mostly with the gadolinium sublattice. The opposite behavior is observed for $x = 27\%$ where the magnetization reversal of the RE dominant layer requires less energy when one starts from an AP configuration. This would correspond with the fact that this time, there is mostly a transport of angular momentum from the TM sublattice of the TM dominant layer towards the TM sublattice of the other layer (represented as an open turquoise arrow).

6.4 Conclusion

This chapter focused on GdFeCo/Cu/GdFeCo layers where one ferimagnetic layer is RE dominant and exhibits AO-HIS while the other is TM dominant and does not exhibit AO-HIS. We showed how spin currents generated by the ultrafast demagnetization of the gadolinium sublattice can permit magnetization reversal of the TM dominant layer. The possible role of dipolar couplings and SDSE were discussed and discarded as a possible explanation for the observed behaviors. We showed that the gadolinium sublattice can be the major source or receiver of angular momentum if the alloy composition is sufficiently high. This is consistent with the equilibrium hysteresis loops of these samples and is understood in the context of Gridnev's model[92]. Finally, we also introduced the concept of spin cooling where spin currents only can determine whether a magnetic sample is, for instance, demagnetized or not independently of the heat transport and dynamics.

Chapter 7

Single laser pulse induced magnetization reversal of GdFeCo/Cu/Ferromagnet spin valves

In the previous chapter, we studied the dynamics of GdFeCo bilayer spin valve structures and saw that it is possible to reverse the magnetization of a GdFeCo layer using spin currents while it is impossible to achieve such reversal without the presence of the spin current. That system was rather complicated to understand and a model would require many parameters. We simplify the system here by considering a ferromagnetic multilayer instead of the TM dominant GdFeCo layer. A GdFeCo layer is still used to generate a spin current but the focus is mostly on the behavior of the ferromagnetic multilayer in the presence of an ultrashort spin current. That way, the ferromagnetic multilayer is modeled as a spin 1/2 system subjected to heat and a spin accumulation. However, we still show some unexpected behaviors of the GdFeCo layer but we now limit their interpretations as it should be understood that this material is much more complex.

In a first part, we choose a standard GdFeCo layer with $x = 23.3\%$ and vary the properties (Curie temperature and interfaces) of the ferromagnetic multilayer. That way, the spin current generated by the ferrimagnetic layer is always the same and we study the role of heating and ultrafast demagnetization of the ferromagnetic multilayer on its ability to reverse its magnetization upon a single laser pulse irradiation. Then, we also affect the spin current by changing the laser pulse duration of the laser. Finally, we change the composition of the GdFeCo layer to play on the generated spin current. Then we also modify the copper spacer thickness and show that we

can still reverse the magnetization of the ferromagnetic multilayer for copper thicknesses up to 80 nm where direct light absorption is strongly reduced.

In all this chapter, the role of dipolar fields can be discarded to explain the magnetization reversal of the ferromagnetic multilayer (except for the formation of multidomain states) via a similar argumentation as what has been said in the previous chapter. See also the discussion in reference 249. We also discard a possible role of the SDSE by repeating the same experiment with laser irradiation on both sides of the sample in the third section. The final argument against the possible role of these effects will be the measured magnetization dynamics of the ferromagnetic multilayer which is shown to happen at the subpicosecond timescale. Such a fast reversal cannot be explained by the SDSE which plays a role at the timescale of several tens of picoseconds (in non colinear structure where the exerted torque is much larger)[169] or dipolar fields which permit magnetization reversal only after several nanoseconds[221] (for the TM in TbFeCo, where exchange of angular momentum between both sublattices may accelerate the dynamics) or even microseconds for [Co/Pt] multilayers[222].

The first two sections are the results of a work published in reference 296 while the results of the third section have been published in reference 297. Both works where the results of a collaboration with Tohoku University.

The definition of the magnetic configurations, similar to the one used in the previous chapter and that will also be used in the next chapter, is shown in figure 7.1.

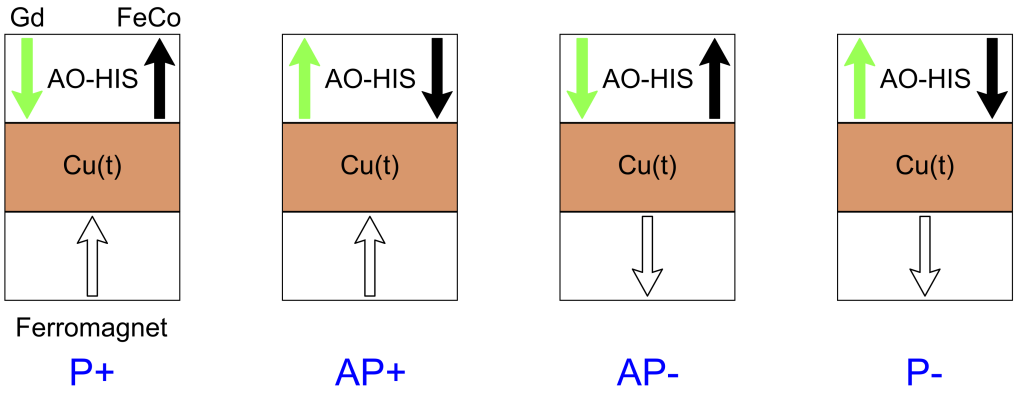

Figure 7.1: Summary of the four possible magnetic configurations in our spin valve structures with a ferromagnetic multilayer and with their corresponding designation (P+, AP+, AP- and P-).

7.1 Impact of the ferromagnetic multilayer properties

We start by studying Glass / Ta(5) / Pt(3) / $[Co_xNi_{1-x}(1)/Pt(1)]_3$ / $Co_xNi_{1-x}(1)$ / Cu(10) / $Gd_{23.3\%}FeCo(5)$ / Ta(5) samples with a TM dominant GdFeCo layer. We now abbreviate the alloy composition to 23%. Note that the GdFeCo layer has an interface with tantalum. This is the case only for this section and the next one (where we change the laser pulse duration). Jean-Loïs Bello demonstrated that this does not affect the compensation composition. By changing the ferromagnetic CoNi alloy concentration x, it is possible to change the Curie temperature of the ferromagnetic multilayer[251] and thus to affect the ultrafast demagnetization of this magnetic material[107]. This is shown in figure 7.2 (b). The Curie temperature varies between 448 Kelvins

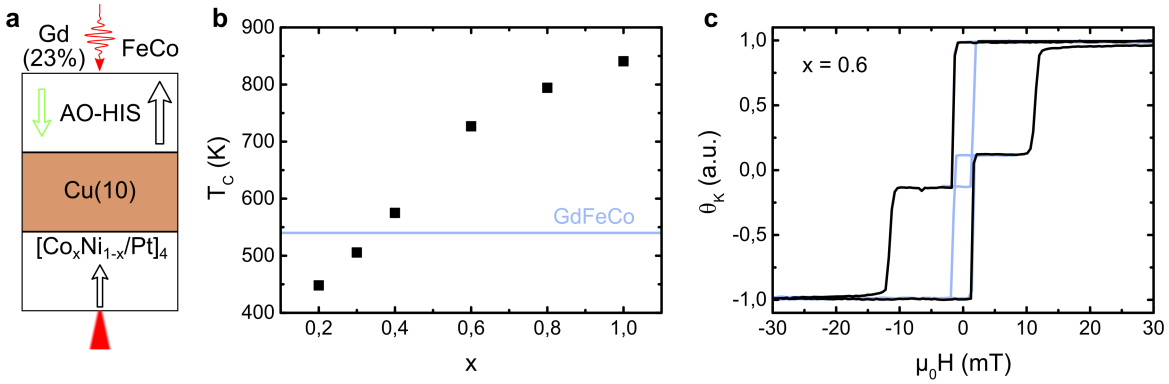

Figure 7.2: (a) Sketch of the sample and the experimental situation for MOKE microscopy. The red cone indicates on which side MOKE microscopy is performed and the wiggly arrow indicates on which side we send single laser pulses. (b) Curie temperature as a fonction of the ferromagnetic CoNi alloy composition x. The Curie temperature of the GdFeCo alloy is also shown and taken from references 238 and 243. (c) shows an hysteresis loop with minor loops (corresponding to GdFeCo) for the sample with $x = 0.6$.

for $x = 0.2$ to 841 Kelvins for $x = 1$. For measurements, MOKE microscopy was performed through the substrate side while laser pulses where send directly on the sample side as shown in figure 7.2 (a). An hysteresis loop of the sample with $x = 0.6$ is shown in figure 7.2 (c). Because MOKE magnetometry was performed on the sample side, the MOKE signal of the GdFeCo alloy was larger than the one of the ferromagnetic multilayer. The situation is reversed in the MOKE microscopy measurements. The laser beam diameter was around 94 μm and for now we use laser pulses with a duration of 35 fs.

The results of sending single laser pulses on these samples are shown in figure 7.3 (a). Except for the sample with $x = 0.2$ where only two magnetic levels are accessible, the samples behave similarly to the sample with 27% of gadolinium in the previous chapter: at low fluence, only

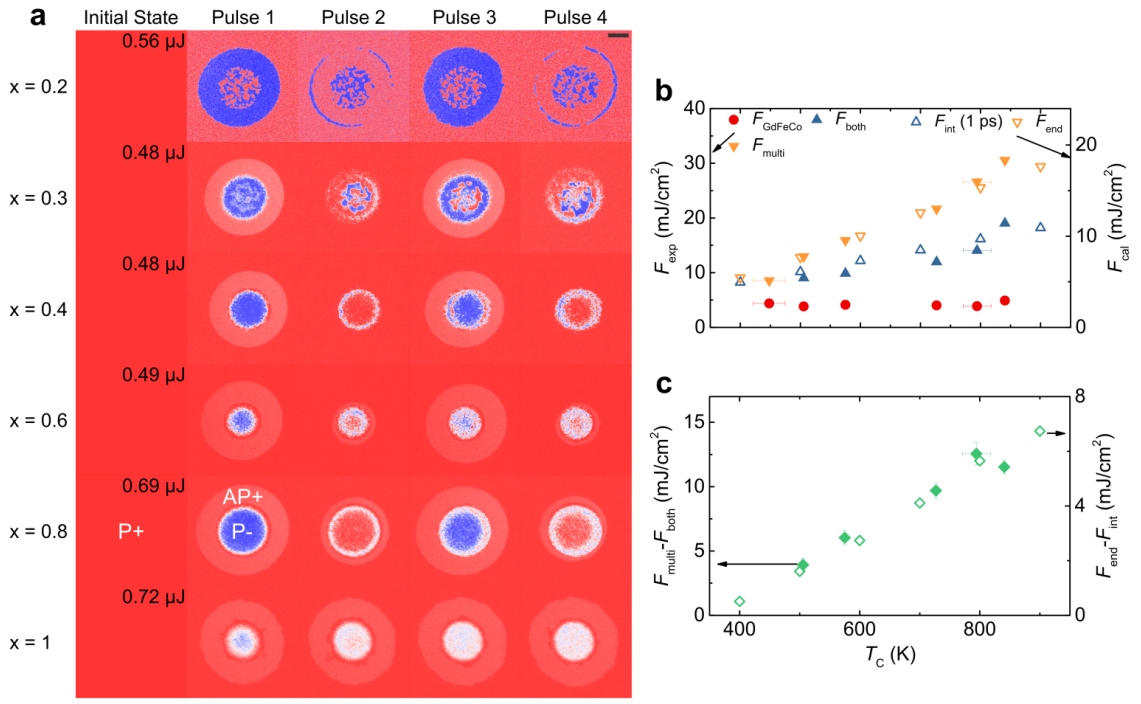

Figure 7.3: (a) Results of sending single laser pulses on the GdFeCo/Cu/$[Co_xNi_{1-x}/Pt]_4$ structures for various ferromagnetic alloy concentrations. The laser pulse duration is 35 fs and the pulse energy is shown in each case. The scale bar is 20 μm long and the magnetic configurations correspond to what is shown in figure 7.1. (b) Experimental (exp) and calculated (cal) (explained in the text) threshold fluences for the reversal of GdFeCo, the ferromagnetic multilayer (when both layers switch) and for the apparition of a multidomain state (multi). The results are plotted as a function of the Curie temperature of the ferromagnetic multilayer of each sample. Solid symbols represent experimental results (scale on the left axis) while open symbols represent calculated thresholds (scale on the right). (c) shows the difference of threshold fluence between the magnetization reversal of both layers and the apparition of a multidomain state in each sample as a function of Curie temperature.

the GdFeCo layer (exhibiting AO-HIS) is reversing its magnetization while at higher fluences, both magnetic layer switch. The threshold fluences for each reversal plus for the apparition of the multidomain state are shown in figure 7.3 (b). One sees that the threshold fluence for the reversal of the GdFeCo layer does not change when the Curie temperature of the ferromagnetic multilayer changes. This is not obvious because layers with a higher Curie temperature have a higher magnetization[296] and so could generate higher spin currents upon ultrafast demagnetization[294]. Nonetheless, we see that, after the second laser pulse for $x \geq 0.6$, there is a ring that appears where the GdFeCo does not reverse its magnetization back. For $x = 1$, the toggle switching behavior completely vanishes. This is also similar to what we have observed in the previous

chapter when also sending laser pulse directly on the sample. However, we have not been able to discriminate with enough certainty a single mechanism for this behavior*. The threshold fluence for the reversal of the ferromagnetic multilayer seems to increase more or less linearly with the Curie temperature from 9.03 mJ/cm^2 at 506 Kelvins to 19.03 mJ/cm^2 at 841 Kelvins. The threshold fluence for the reversal of the ferromagnetic multilayer with $x = 1$ is somewhat higher compared to the other samples but we note that the reversal of the ferromagnetic multilayer in this sample is much less clean. The threshold for the apparition of a multidomain state (visible for $x = 0.2$ and $x = 0.3$ in figure 7.3) also seems to increase linearly with the Curie temperature. We note that for fluences very close to the threshold fluence of the ferromagnetic multilayer switching, a multidomain state appears as a white ring around the blue P- domain. We believe this is due to the fact that around the threshold fluence, the magnetization of the system will be very close to zero and so critical slowdown[86,107] of the magnetization dynamics happens. This behavior has been observed in GdFeCo using TR-MOKE[243]. Depending on the material, this may or may not be visible. GdFeCo tends to form rather big domains in our samples (around 10 µm) while our ferromagnetic multilayers have characteristic domain sizes of 1 µm or smaller. This may explain why such white ring is not visible for samples with GdFeCo only. For the sample with $x = 0.6$, we show the results of sending a laser pulse with an energy slightly above the threshold fluence. In this case, the white ring is very visible because of the gaussian profile of the laser beam.

We calculated the threshold fluences using the model presented in chapter 5. In this case, we only used the 2TM as an input for the original m3TM[107]. This only allows us to compute ultrafast demagnetization of the ferromagnetic multilayer. Our idea is then to relate magnetic reversal to a sufficient amount of demagnetization. We use a qualitative criterion for the magnetic reversal which states that the remaining magnetization after 1 ps at the Cu/F interface $M_{\text{int}}(1\text{ps})$ should be less than the magnetization measured by Choi and Min[170]. This gives a threshold fluence $F_{\text{int}}(1\text{ps})$. Because we use fluences ten times higher than Choi and Min[170], this leads to the criterion that the magnetization reaches 1000 A/m at a delay of 1 ps after the laser pulse irradiates the sample. This corresponds to a value around a thousand times smaller than the measured saturation magnetizations with VSM. The criterion for the formation of a multidomain state is that the minimum of the magnetization in the ferromagnetic multilayer (corresponding to the

*A possible justification for this behavior in the sample with $x = 33\%$ in the previous chapter is to say that the TM sublattice of the TM dominant layer generates a spin current that transfers angular momentum to the RE sublattice of the RE dominant layer. This mechanism could also explain why the sample remains in the AP+ configuration here because in this magnetic configuration, the ferromagnetic multilayer has its magnetization parallel to the gadolinium magnetization. This is also consistent with other results shown later in this chapter.

magnetization M_{end} at the F/Pt interface) should reach 100 A/m. This gives a threshold fluence F_{end}. These criteria are very qualitative but they do not change our predictions qualitatively i.e. the trend we obtain is not sensitive to the values used for these criteria. In fact, the ferromagnetic multilayer magnetization reversal criterion is based on the fact that the gadolinium spin current peak happens 1 ps after the laser pulse irradiation in the measurements of Choi and Min[170]. We actually estimate in chapter 8 that this peak should reach its maximum value around 250 fs. The discrepancy comes from the fact that we use pump pulses with a duration of 35 fs which is much shorter than the 1.1 ps pulse durations of Choi and Min[170]. Overall, with only parameters taken from the literature and these two criteria, we arrive, without any fitting procedure, to the results shown as the open symbols in figures 7.3 (b) and (c). The values we get are around two times smaller than the measured values and they reproduce the linear increase as a function of Curie temperature. Figure 7.3 (c) shows that this also reproduces the linear increase in the fluence window where one can reverse the ferromagnetic multilayer without creating a multidomain state. Thus, even though this model is rather simple, its shows that the ultrafast demagnetization, induced by the provided energy, determines the energy efficiency of the magnetization reversal. Overall, materials with a higher Curie temperature (and a higher magnetization) will require more energy to be demagnetized which explains the increase in the threshold fluence. Even though the ultrafast demagnetization is not sufficient to reverse the magnetization, it is nonetheless required if one wants to achieve it.

We also performed the same type of measurements but on Glass / Ta(5) / Pt(3) / $[\text{Co}(0.6)/\text{Pt}(1)]_3$ / Co(t_{Co}) / Cu(10) / $\text{Gd}_{23.3\%}$FeCo(5) / Ta(5) samples where the thickness t_{Co} of the interfacial cobalt layer was set to 0.2, 0.6 and 1 nm. These results are shown in figure 7.4. We do not show what happens after the second pulse but the ferromagnetic multilayer switches after each pulse just as what happens in figure 7.3. We note however the presence of a ring for $t_{\text{Co}} = 1$ nm where the GdFeCo layer switches only after the first pulse as already observed several times. The point of this measurement is to the study the role of the Cu/Co interface. Indeed, we expect that the spin current mostly interacts with the first cobalt layer. Thicker cobalt layers will exhibit a higher Curie temperature[298] and thus would require more energy to be switched. After the first cobalt layer is switched, the other layers can follow due to exchange interaction between each cobalt layer[242,248]. This is indeed what is observed and this is also well reproduced by our model. We note however that it does not reproduce so well the threshold fluence for the multidomain state. In our model, the threshold fluence does not change much because of our criterion: the ultrafast demagnetization of the last cobalt layer will not depend much on the first cobalt layer because the change of Curie temperature of the first cobalt layer does not affect the

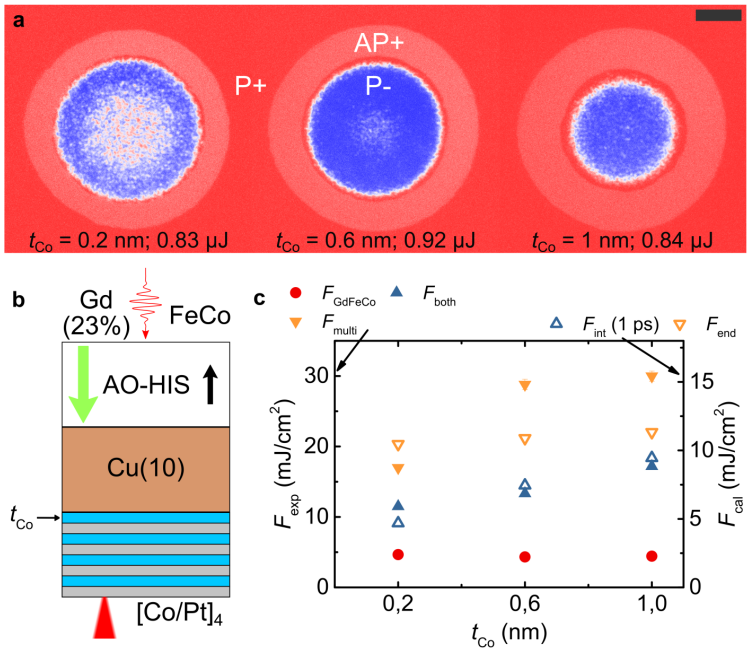

Figure 7.4: (a) Results of sending one single laser pulse on the GdFeCo/Cu/$[Co/Pt]_4$ structures for various interfacial cobalt thicknesses. The laser pulse duration is 35 fs and the pulse energy is shown in each case. The scale bar is 20 µm long and the magnetic configurations correspond to what is shown in figure 7.1. (b) shows the sample structure and the cobalt layer (blue) whose thickness is changed. The red cone indicates on which side MOKE microscopy is performed and the wiggly arrow indicates on which side we send single laser pulses. (c) Experimental (exp) and calculated (cal) (explained in the text) threshold fluences for the reversal of GdFeCo, the ferromagnetic multilayer (when both layers switch) and for the apparition of a multidomain state (multi). Solid symbols represent experimental results (scale on the left axis) while open symbols represent calculated thresholds (scale on the right).

magnetization dynamics of the last cobalt layer. The slight change of the first cobalt layer thickness will just slightly change temperature profiles. A better model would consider the exchange interaction between each cobalt layer such as in the layered m3TM[242].

7.2 Impact of the laser pulse duration

We now focus on the sample Glass / Ta(5) / Pt(3) / $[Co(0.6)/Pt(1)]_3$ / Co(0.6) / Cu(10) / $Gd_{23.3\%}FeCo(5)$ / Ta(5) with all identical cobalt layers. We want to study the role of the laser pulse duration. The same measurements but for different pulse durations are shown in figure 7.5. One does not see any difference for pulse durations between 35 fs and 100 fs. Starting at around 500 fs, one can clearly see that the ferromagnetic multilayer is not fully reversed anymore and some micron size magnetic domains start to appear in the blue area, until the ferromagnetic multilayer is only demagnetized (in a multidomain domain state) for 2 and 3 ps. For these pulse durations, the AO-HIS of the GdFeCo layer is also clearly affected, suggesting that AO-HIS and the generation of spin currents are strongly related.

Regarding the threshold fluences, they increase almost identically as a fonction of pulse duration for the reversal of GdFeCo and the ferromagnetic multilayer. Surprisingly, the threshold fluence for the apparition of a multidomain state decreases from 100 fs to 2 ps. For pulse durations of 2ps and above, the threshold fluence for the apparition of a multidomain state seems to continue the trend of the threshold fluence for the magnetization reversal of the ferromagnetic multilayer, trend which is identical to what one can observe for the GdFeCo threshold fluence. Our model can roughly reproduce the trend for the reversal of the ferromagnetic multilayer but completely fails in explaining the threshold fluence for the generation of a multidomain state, which predicts that the threshold fluence should increase.

We explain this discrepancy as follows: in order to achieve the magnetization reversal of the [Co/Pt] multilayer, the latter must be rather close to a fully demagnetized state in order for the spin current to permit the reversal. Thus, we believe that the threshold fluence for the reversal of the ferromagnetic multilayer must be very close to the threshold fluence for the demagnetization (apparition of a multidomain state) of the ferromagnetic multilayer **if** there was not a spin current generated by the GdFeCo (but still the same temperature dynamics). This explains why the threshold fluence for the apparition of a multidomain state at 2 and 3 ps seems to continue the trend of the [Co/Pt] reversal threshold fluence. Then, the difference between the threshold fluences for the apparition of a multidomain state and the reversal of the ferromagnetic multilayer is explained by the spin current generated by the gadolinium sublattice of the ferrimagnetic alloy. This means that the action of this spin current is twofold: (i) it permits the magnetization reversal and (ii) it prevents the formation of a multidomain state that one should observe, without a spin current, at these temperatures. We thus have an ultrafast spin cooling of the ferromagnetic layer by the GdFeCo spin current. We anticipate the fact that this is ultrafast from the results of the

next chapter plus the fact that this effect vanishes for pulse durations $\gtrsim 1$ ps. Indeed, the spin current is due to the spin generation rate which is proportional to $-\mathrm{d}M/\mathrm{d}t$. If the magnetization dynamics of the GdFeCo is slower (because of the longer pulse duration), the spin generation rate will be smaller and so will be the spin current and its impact on the ferromagnetic layer. We note that this spin cooling is slightly different from the one observed in the previous chapter. Indeed, in the previous chapter, when one starts from an AP configuration, a multidomain state appears while here the ferromagnetic layer remains in the same configuration (not shown; only

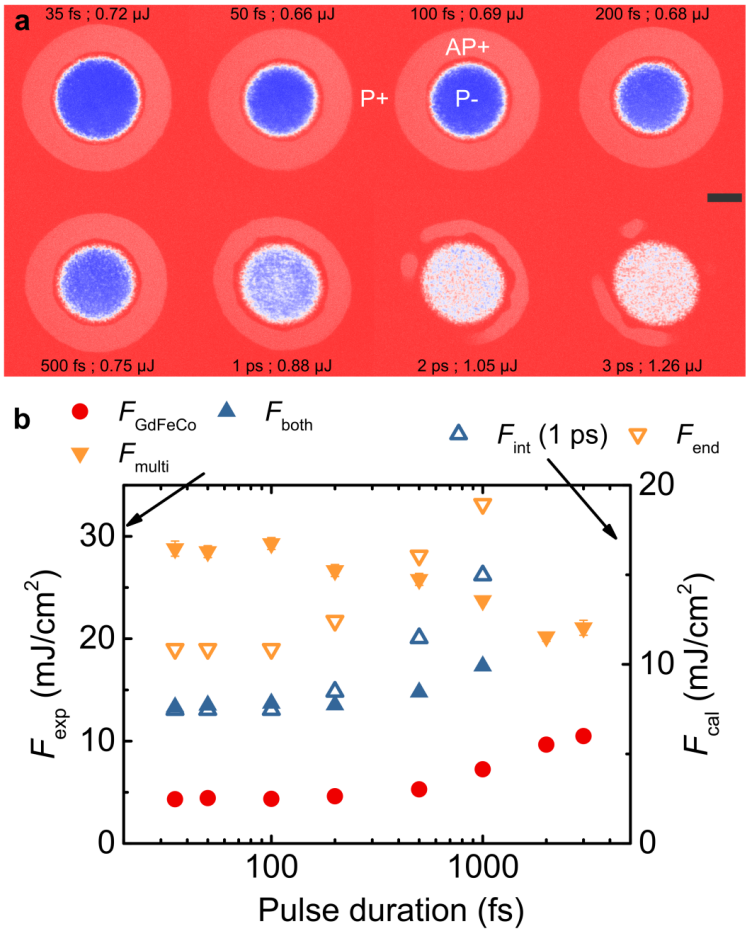

Figure 7.5: (a) Results of sending one single laser pulse on the GdFeCo/Cu/$[\mathrm{Co}(0.6)/\mathrm{Pt}]_4$ structures for various laser pulse durations. The pulse energy is shown in each case. The scale bar is 20 µm long and the magnetic configurations correspond to what is shown in figure 7.1. (b) Experimental (exp) and calculated (cal) (explained in the text) threshold fluences for the reversal of GdFeCo, the ferromagnetic multilayer (when both layers switch) and for the apparition of a multidomain state (multi). Solid symbols represent experimental results (scale on the left axis) while open symbols represent calculated thresholds (scale on the right).

the GdFeCo reverses its magnetization). We believe the reason is that the effect of the spin current on the magnetization is not necessarily symmetric, meaning that it is more or less efficient depending on the initial state of the magnetization. This is something we will observe in the next chapter. This asymmetry can be understood from the fact that, in the presence of a spin current, the ultrafast demagnetization is impacted by the spin current in the sense that it either hinders or assists it[93,181]. The situation in the previous chapter is also more complex because of the ferrimagnetic nature of the layer.

7.3 Impact of the ferrimagnet concentration

We now consider Glass / Ta(5) / Pt(4) / $[Co(0.4)/Pt(1)]_2$ / Co(0.4) / Cu(10) / $Gd_xFeCo(5)$ / Cu(5) / Ta(5) where $x = 20.4\%$ (abbreviated to 20%), 27.3% (abbreviated to 27%) and 33%. The case with $x = 20\%$ is rather different and is kept for the end of this section. The experimental configuration for MOKE microscopy and the sample's hysteresis loops are shown in figure 7.6. In this case, the GdFeCo layer with $x = 27\%$ is actually TM dominant because this composition is very close to the compensation composition. To clarify the different configuration, we remind the names of the magnetic configurations on the hysteresis loops (the hysteresis loop measurement was performed on the sample side just as for MOKE microscopy). Because we performed the measurements with laser pulse irradiation through the substrate (because it leads to lower threshold fluences) and MOKE microscopy on the other side, the light red color corresponds here to an AP- configuration instead of an AP+ configuration in the previous two sections. The results for a laser pulse irradiation directly on the sample side are shown below. In all this section, the laser pulse duration is 35 fs and the beam diameter is around 110 µm.

We start by focusing on the sample with $x = 33\%$ at low fluence and starting from a P configuration. We note the important fact that **the GdFeCo layer in this sample does not exhibit AO-HIS when it is in a layer by itself** as already shown in figure 4.8. The results are shown in figure 7.7. After irradiation with a single laser pulse of 35 fs duration, one sees that the [Co/Pt] multilayer only reverses its magnetization. Sending further pulses does not change the magnetization state of the sample. This is actually very similar to what we have already observed in figure 6.10 except that there is no magnetization reversal of the GdFeCo layer anywhere on the irradiated area and the GdFeCo layer does not exhibit AO-HIS by itself contrary to the sample with $x = 30\%$. The interpretation still follows what has been said before: the ultrafast demagnetization of the GdFeCo layer generates a spin current whose polarization is

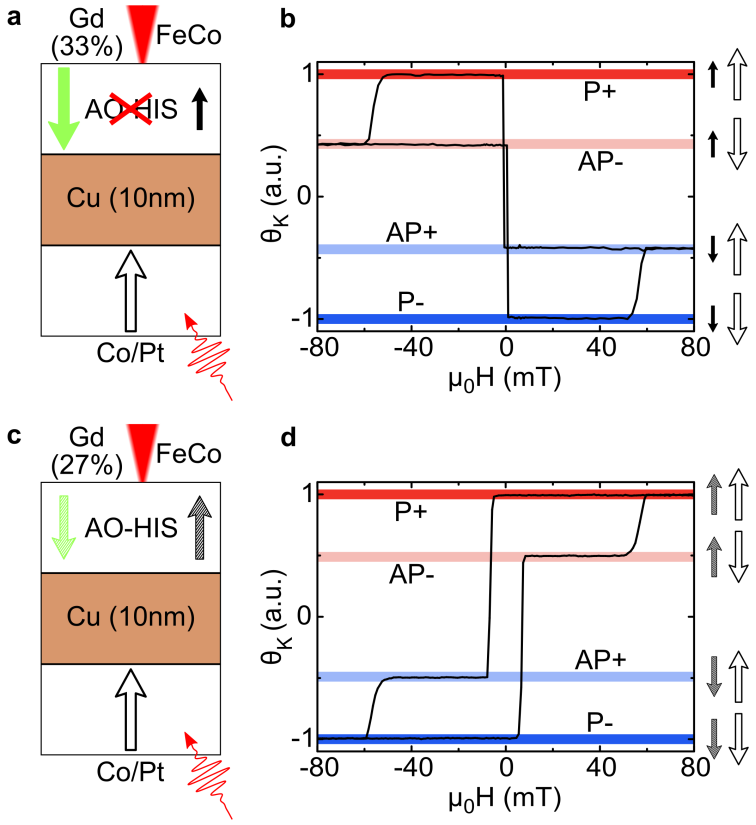

Figure 7.6: (a) and (c) show the simplified sample structures together with the experimental situation for MOKE microscopy. The red cone indicates on which side MOKE microscopy is performed and the wiggly arrow indicates on which side we send single laser pulses. (b) and (d) show the hysteresis loops, performed on the sample side just as MOKE microscopy. The colored horizontal bars represent the color of the magnetic configuration in the MOKE microscopy images.

mostly given by the RE sublattice (the second negative spin accumulation peak of Choi and Min measurements[170]); this spin currents then transfers its angular momentum to the magnetization of the (partially demagnetized) ferromagnetic multilayer which can then reverse. Thus, with a single laser pulse of light, we managed to reverse the magnetization of a ferromagnetic layer and only the magnetization of this layer, which had never been seen in previous measurements[249]. The reason why the reversal of the GdFeCo layer is not observed is threefold: (i) the [Co/Pt] multilayer is rather thin compared to what has been used in the two previous sections which means that it is easier to demagnetize and thus reverse as we showed above (ii) the GdFeCo layer does not exhibit AO-HIS by itself; this does not mean that it cannot reverse its magnetization in general (as we will see below) but it will still require more energy to reverse because its composition is far from the compensation composition[236] (iii) the higher gadolinium content means that the amplitude of the generated spin current is larger which further decreases the

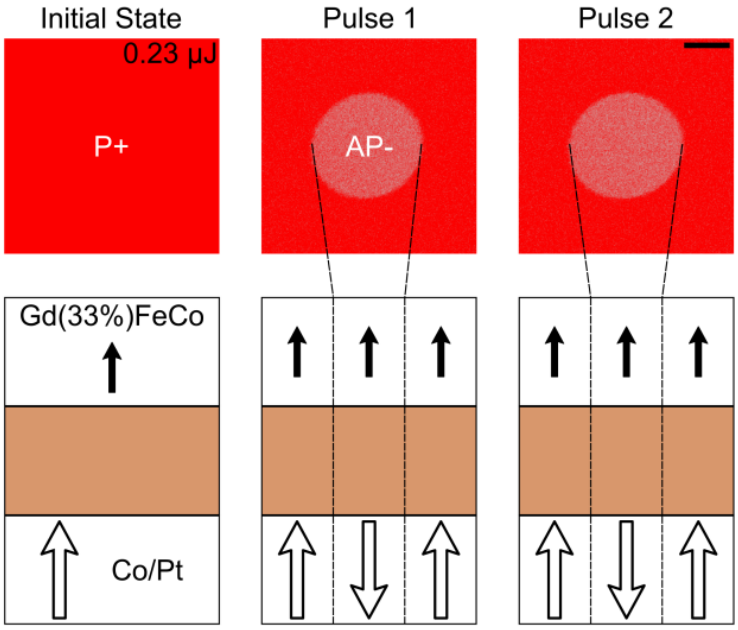

Figure 7.7: Results of sending single laser pulses of low fluence on the Gd_xFeCo/Cu/[Co/Pt] sample with $x = 33\%$ from a P+ configuration. The pulse duration is 35 fs and the pulse energy is 0.23 µJ. The scale bar is 20 µm long.

threshold fluence required to observe the magnetization reversal of the [Co/Pt] multilayer. This latter fact was not true for the GdFeCo bilayers in the previous chapter as it was still easier to reverse the TM dominant layer with $x = 27\%$ rather than with $x = 30\%$ (compare fluences).

In the case presented here we will now argue that the intensity of the spin current indeed allows the magnetization reversal to be more energy efficient*. To do so, we now also focus on the sample with $x = 27\%$. Apart from the different alloy composition, both samples are identical. From ellipsometry measurements, we could not see any difference in the optical indices of both magnetic layers and the change of Curie temperature is negligible in this range of composition[291]. Thus the heating in both samples will be identical and only the amount of angular momentum in each magnetic sublattices of GdFeCo will change. The results of sending single laser pulses on these two samples, at higher fluences and for both types of magnetic configurations are shown in figure 7.8. These results are qualitatively identical to the ones obtained in figure 6.10 for GdFeCo bilayers apart from some random magnetic patterns that appear on the rim of the inner region after the second pulse in figures 7.8 (a) and (b). Their origin is attributed to stray fields.

*This is a fact that can be easily reproduced by our model presented in chapter 8 by changing the amplitude of the input spin accumulation. We do not show it here but it results from the fact that spin currents enhance the ultrafast demagnetization which has already been shown experimentally[181] and theoretically[93].

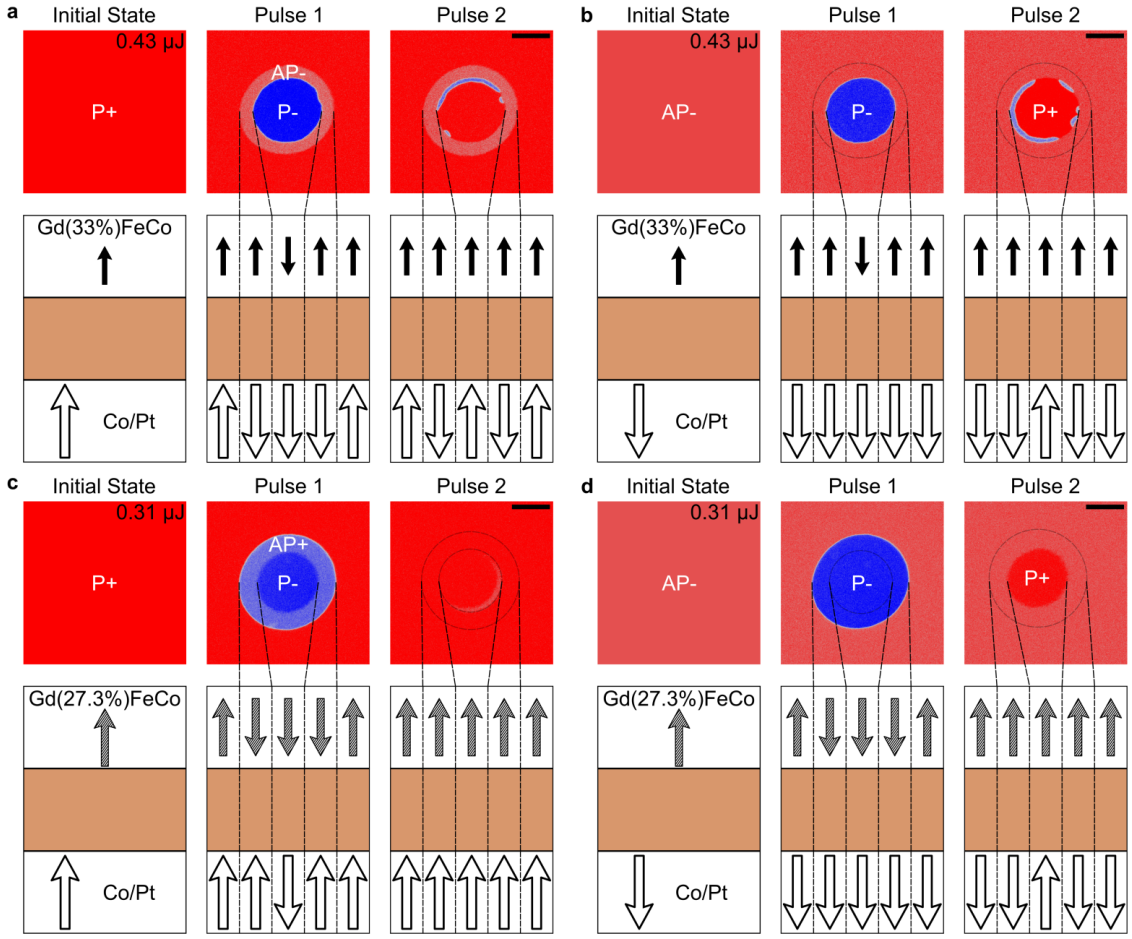

Figure 7.8: Results of sending single laser pulses of high fluence on the $Gd_xFeCo/Cu/[Co/Pt]$ samples with $x = 33\%$ ((a) and (b)) and 27% ((c) and (d)) from P+ ((a) and (c)) and AP- ((b) and (d)) configurations. The pulse duration is 35 fs and the pulse energy is shown in each case. The scale bars are 30 μm long.

Something unexpected is the magnetization reversal of the GdFeCo layer for $x = 33\%$. One could argue that it may be due to a spin current coming from the ultrafast demagnetization of the ferromagnetic multilayer as in the case of reference 294 (it is a synthetic ferrimagnetic Co/Gd bilayer in that reference). However, in our case, the reversal of the ferrimagnetic alloy happens at the same threshold fluence (within uncertainties; see below) no matter if the initial magnetic configuration is P or AP. We do not have a full explanation for this behavior but we believe it might be due to a more efficient heating of the ferrimagnetic layer in this spin valve structure compared to when it is in a structure by itself, as this magnetic layer is not far from the composition where AO-HIS starts to appear (around 31%) and AO-HIS is sensitive to heating. A more quantitative analysis is provided by looking at the fluence dependence of the magnetization

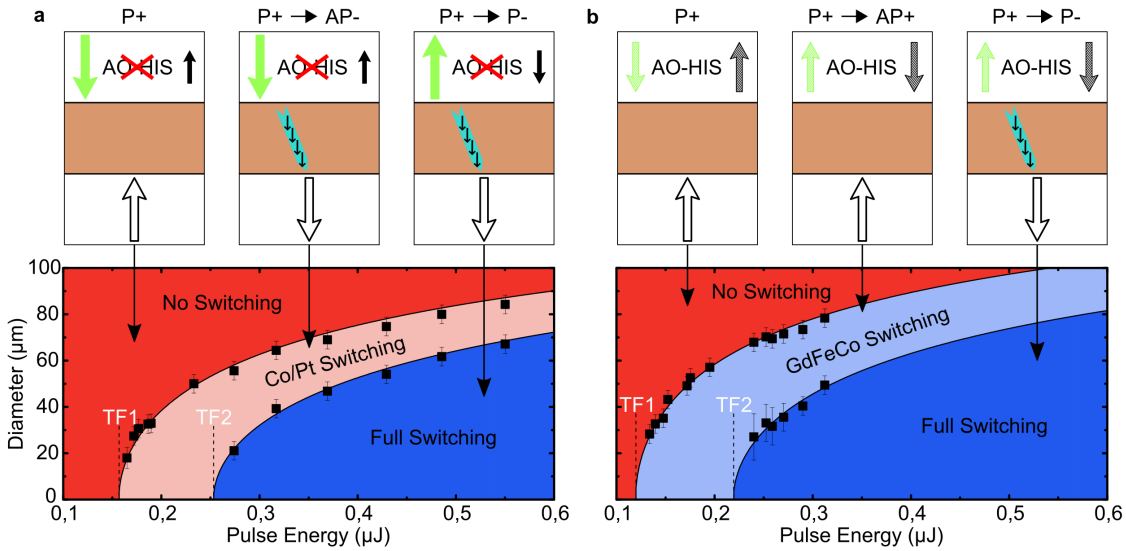

Figure 7.9: Magnetic domain diameter as a function of the laser pulse energy for (a) the GdFeCo/Cu/[Co/Pt] spin valve with $x = 33\%$ and for (b) the sample with $x = 27\%$ starting from the P+ magnetic configuration. The colors in the graph represent the colors of figure 7.8. Sketches above the graphs summarize the change of magnetic configuration after a single laser pulse irradiation starting from the initial configuration. The turquoise arrow represents the spin current going from the ferrimagnetic layer to the [Co/Pt] multilayer (with spin polarization indicated by the black arrows). The laser beam diameter is around 110 µm for $x = 33\%$ and around 115 µm for $x = 27\%$. The pulse duration is 35 fs.

reversal shown in figure 7.9. The corresponding threshold fluences are gathered in table 7.1. Contrary to the case with GdFeCo/Cu/GdFeCo spin valves, the AO-HIS of the GdFeCo layer, for both concentrations, does not seem to depend on the orientation of the magnetization in the ferromagnetic multilayer, possibly suggesting that the [Co/Pt] multilayer we consider does not generate much spin current, a fact that is consistent with the dynamics measurements of chapter 8. The reversal of the GdFeCo layer with $x = 27\%$ happens at lower fluences than for the ferrimagnetic layer with $x = 33\%$ but the threshold fluence for the latter layer is still lower than what could be expected from previous measurements[236]. We interpret this again by the fact that

	Threshold Fluences (mJ/cm^2)			
x	GdFeCo (P)	[Co/Pt] (P)	GdFeCo (AP)	[Co/Pt] (AP)
27.3%	1,15 ± 0,07	2.11 ± 0,12	1,16 ± 0,07	No reversal
33%	2,66 ± 0,31	1,65 ± 0,19	2,72 ± 0,31	No reversal

Table 7.1: Table for the threshold fluences of each magnetic layer in GdFeCo/Cu/[Co/Pt] spin valve for both ferrimagnetic alloy compositions x.

the heating in our structures is more efficient than in more conventional samples, where more of the energy provided by the light would contribute to the heating of the ferrimagnet, either directly or indirectly, for instance through hot electron generation in the ferromagnetic layer[295]. Finally, we clearly see a difference in the threshold fluence for the reversal of the [Co/Pt] multilayer which is around 22% smaller for the sample with the higher concentration in gadolinium, thus confirming our claims above.

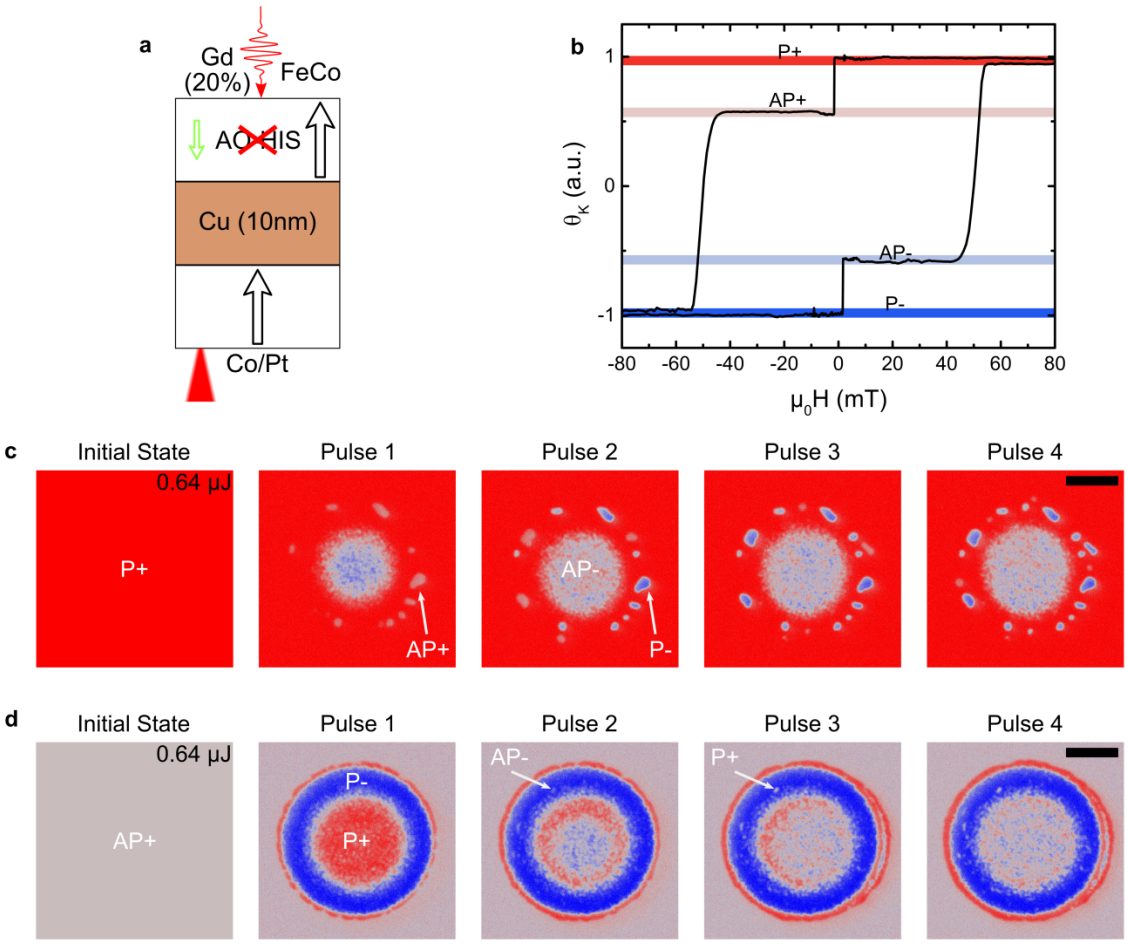

Figure 7.10: (a) shows the simplified sample structure for $x = 20\%$ together with the experimental situation for MOKE microscopy. The red cone indicates on which side MOKE microscopy is performed and the wiggly arrow indicates on which side we send single laser pulses. (b) shows the hysteresis loops performed through the substrate side just as MOKE microscopy. The colored horizontal bars represent the color of the magnetic configuration in the MOKE microscopy images ((c) and (d)). (c) and (d) show the results of sending single laser pulses on the GdFeCo/Cu/[Co/Pt] sample from P+ (c) and AP+ (d) configurations. The pulse duration is 35 fs and the pulse energy is 0.64 μJ for a beam diameter around 90 μm. The scale bars are 20 μm long. Two arrows in figure (c) and (d) indicate a magnetic domain which changes its magnetic configuration once after a single laser pulse irradiation.

For completeness, we show the results of sending laser pulses directly on the sample side in figures B.1 and B.2 in the appendix for $x = 33\%$ and $x = 27\%$ respectively. Because we qualitatively observe the same behavior in those cases and because temperature gradients will be reversed, we can rule out the role of SDSE as the cause of any magnetization reversal in our structures.

We finally focus on the sample with $x = 20\%$. The results are shown in figure 7.10. One can see that starting from a P configuration leads to a multidomain state in the GdFeCo layer (outer area) or in the [Co/Pt] multilayer (inner area) while starting from an AP configuration leads to magnetization reversal of the [Co/Pt] multilayer (outer area) or of the GdFeCo layer (inner area). This is another example of (probably ultrafast) spin cooling where only exchange of angular momentum between both magnetic layers decides whether a layer should reverse its magnetization, remain the same or create a multidomain state while enough energy is still provided to the system to generate a multidomain state. We note that this behavior clearly cannot be explained by an interaction of dipolar origin. Indeed, the magnetic domains generated in GdFeCo when one starts from a P configuration do not affect the magnetization of the ferromagnetic layer. Moreover, these magnetic domains are in an AP+ configuration and they can be reversed into a P- domain with a subsequent pulse (the magnetic domain keeping exactly the same shape and size). The reversal behavior being independent of the magnetic patterns, it cannot be explained by dipolar couplings. We note however, as before, that the dipolar coupling still is the cause of the formation of those magnetic domains. The annular magnetic domain formed after sending a laser pulse on the sample after initializing it in an AP configuration might be the reason why the generated domains in the AP- ring are smaller. However they can still be reversed to a P+ configuration as shown (domains appear white instead of red because they are small).

The [Co/Pt] multilayer reverses its magnetization only when the initial magnetic configuration is AP, indicating that the main source of angular momentum for this layer is the TM sublattice of the GdFeCo layer and not gadolinium, as already deduced from the results on GdFeCo/Cu/GdFeCo structures. This may be explained by the fact that the gadolinium content is very low and thus the first spin generation rate peak observed by Choi and Min[170] may dominate. Still, we do not fully understand these results. In particular, why is it a different magnetic layer that reverses above a certain fluence? Why does magnetization reversal happen in one layer for an AP configuration while a multidomain state appears in the other layer for a P configuration? We were not able to find satisfactory answers to these questions. There is also a P+ ring appearing for an initial AP+ configuration (the outermost ring) whose origin is not clear.

7.4 Impact of the Cu layer thickness

In this section, we study the influence of the copper spacer thickness on the magnetization reversal of the [Co/Pt] multilayer. For this purpose, the sample structure is Glass / Ta(5) / Pt(4) / [Co(0.6)/Pt(1)]$_2$ / Co(0.6) / Cu(t) / Gd$_x$FeCo(5) / Cu(5) / Ta(5) samples where t can be 20, 40, 60 and 80 nm. We also change the composition x of the ferrimagnetic alloy which can be 22%, 27.3% (abbreviated to 27%), 30% and 33%. In these structures, GdFeCo always exhibits AO-HIS, even for $x = 33\%$ at $t = 20$ nm similarly to what as been seen above. Note that we slightly increased the cobalt thickness in the ferromagnetic multilayer. This changes the coercive field of the ferromagnet (which is now around 30 mT instead of 60 mT) but does not affect the PMA of both magnetic layers. The hysteresis loops are similar to the ones shown in the previous section and in appendix B, the only difference being that the amplitude of the MOKE signal of one magnetic layer is reduced because of the thickness of the copper spacer. In all this section, we are only interested in the case where a single laser pulse (with a duration of 35 fs and beam diameter around 100 µm) is sent on the sample from the sample (GdFeCo) side while MOKE microscopy is performed through the substrate ([Co/Pt] side). In table 7.2 we report the absorption of the pump laser light by the Pt(4) / [Co(0.6)/Pt(1)]$_2$ / Co(0.6) multilayer for the different copper spacer thicknesses t. Including the tantalum buffer layer does not affect much these results. We used the standard TMM which requires much less computation time and provides similar results for these pulse durations as we showed. The point is that adding 20 nm of copper divides the direct

t (nm)	0	20	40	60	80
absorption	0.152	0,0434	0,00903	0,00181	0.000361

Table 7.2: Table for the absorption of the pump laser light by the [Co/Pt] multilayer for the different copper spacer thicknesses t.

light absorption in the ferromagnetic multilayer by around five. With 80 nm of copper, one can definitely neglect the direct interaction between the ferromagnetic layer and light[187]. We first look at the results for the sample with $t = 80$ nm and $x = 33\%$. They are shown in figure 7.11. In this case, only the MOKE signal from the ferromagnetic multilayer is visible. One sees that starting from a P configuration, the magnetization of the [Co/Pt] multilayer is reversed while it does not reverse for an AP configuration as above for smaller spacer thicknesses. Thus we conclude that hot electrons carrying spin (and then also heat), due to hot electron generation in the Ta/GdFeCo part of the sample and to the ultrafast demagnetization of GdFeCo, are sufficient

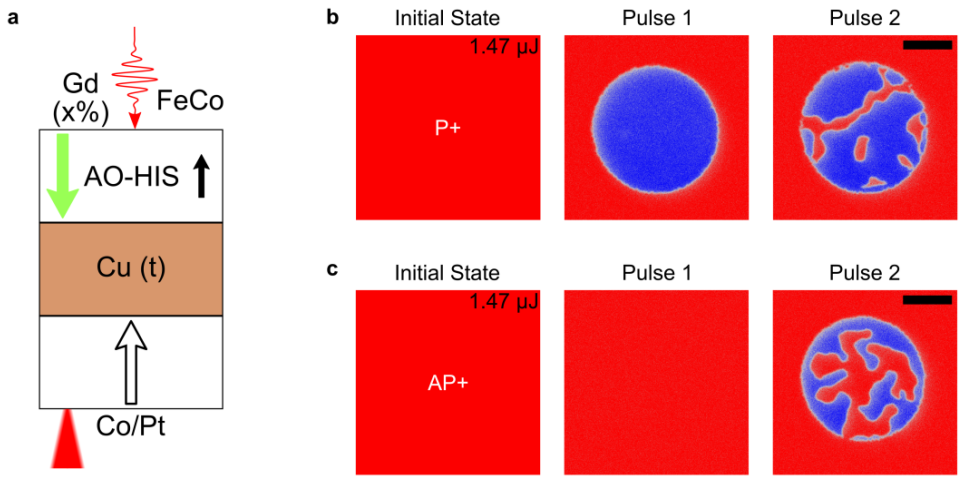

Figure 7.11: (a) shows the simplified sample structure together with the experimental situation for MOKE microscopy. The red cone indicates on which side MOKE microscopy is performed and the wiggly arrow indicates on which side we send single laser pulses. (b) and (c) show the results of sending single laser pulses on the $Gd_xFeCo/Cu(t)/[Co/Pt]$ sample with $x = 33\%$ and $t = 80$ nm from P+ (b) and AP+ (c) configurations. The pulse duration is 35 fs and the pulse energy is 1.47 μJ. The scale bars are 20 μm long.

to reverse the magnetization of a ferromagnetic layer. We were limited to $t = 80$ nm because then the Cu/GdFeCo interface starts becoming to rough and PMA of the ferrimagnetic layer is lost. The electronic transport for these thicknesses is sometimes understood as being ballistic[172,187*]. We note that these results are also consistent with the known spin diffusion lengths of copper which are usually greater than a hundred nanometers[299] but not with the spin transfer length of 13 nm[300], which is however measured for non collinear structures.

After the second pulse, the magnetization of [Co/Pt] does not switch back but exhibits a multidomain state that is unusual for this material. This pattern is actually the multidomain state of the GdFeCo generated after the first pulse (due to the high fluences required here to generate hot electrons[236]) which is being printed on the ferromagnetic multilayer. To see this, we now show the same results but for a copper thickness of 20 nm in figure 7.12. In these measurements, we used two different settings of the analyzer of the MOKE microscope. One setting was determined such as to optimize the MOKE signal of both magnetic layers (second analyzer setting) while the other one was determined by minimizing the signal coming from the ferrimagnetic layer (first analyzer setting)[†]. Thus one can reproduce the typical images observed

*This is however debated and certain phenomenon that show linear behavior, as here below, can also be understood in terms of heat diffusion[288].

[†]This is possible in single magnetic layers by perfectly crossing the polarizer and the analyzer[259]. In magnetic bilayers it is generally not possible to remove the signal of a magnetic layer without using additional optical elements

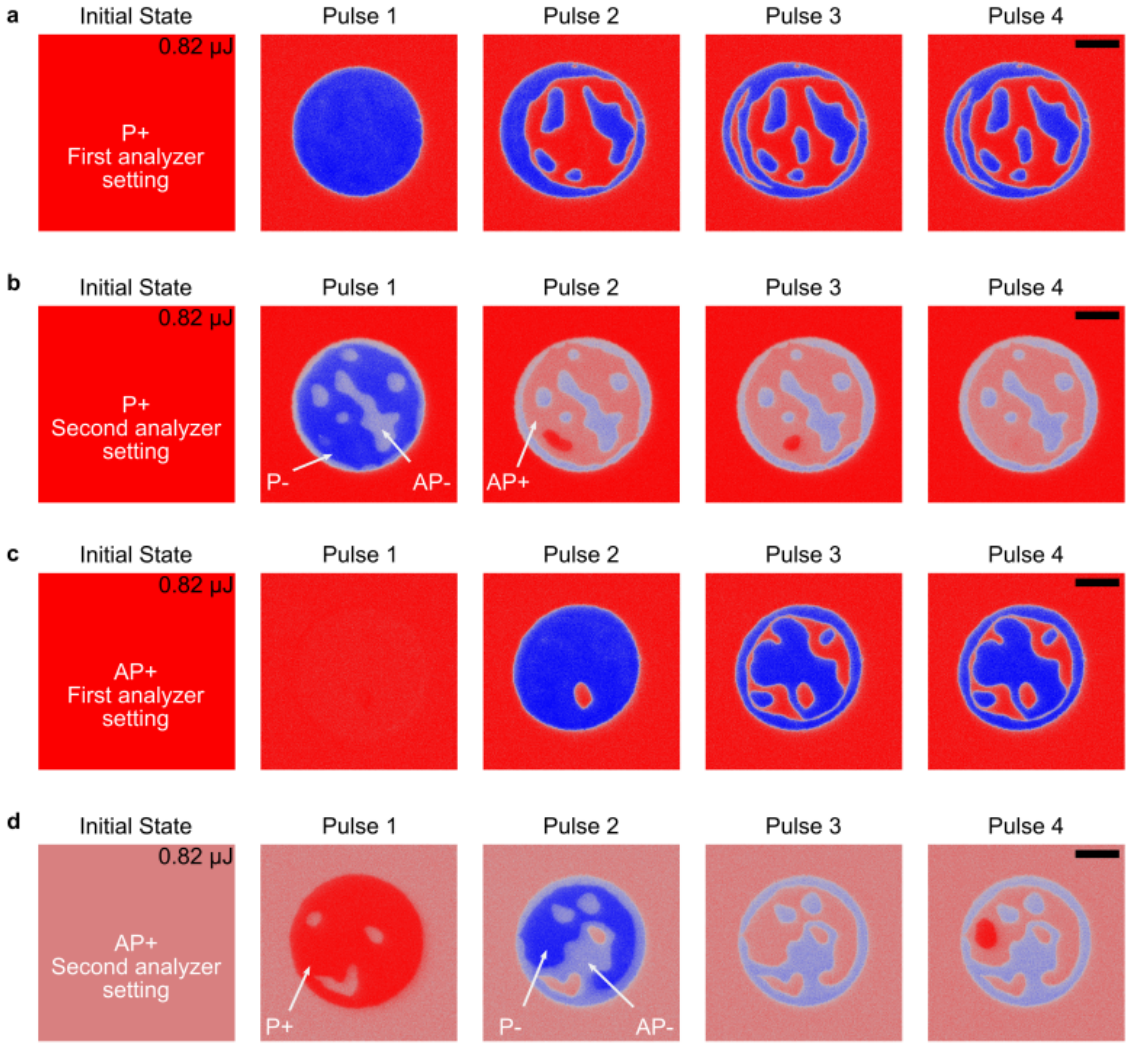

Figure 7.12: Results of sending single laser pulses on the $Gd_xFeCo/Cu(t)$/[Co/Pt] sample with $x = 33\%$ from P+ ((a) and (b)) and AP+ ((c) and (d)) configurations. Two different angles of the analyzer in the MOKE microscopy setup where used as explained in the text. The pulse duration is 35 fs and the pulse energy is 0.82 µJ. The scale bars are 20 µm long.

for thicker copper spacer and still see the GdFeCo layer at the same time. We could not use two different analyzer settings for the same batch of laser pulses because changing this setting changes the luminosity and thus the background. Still, one can see the previously mentioned

such as a quarter wave plate. However, it is possible to remove the signal of the deepest magnetic layer (here GdFeCo) because one mostly measure Kerr rotation of this layer. This is not the case for the first layer ([Co/Pt]) where one also measures Faraday rotation on top of Kerr rotation. The two Faraday rotation signals (coming from the forward and the backward propagation of light after reflection on the GdFeCo layer) do not cancel each other out similarly to what happens in optical isolators.

effect, for instance in figure 7.12 (b) where the P- domain after the first pulse (corresponding to a domain in the GdFeCo layer while the domain in [Co/Pt] is the full blue region made of the P- and AP- domains) becomes AP+ after the second pulse. After a certain number of pulses, the domains in the GdFeCo layer are not stable enough between the two instants where we record images so the magnetic pattern does not change anymore.

Finally, we present the various threshold fluences for the reversal of [Co/Pt] in all the samples. These results, together with Marteen Beens simulations, are shown in figure 7.13. For a given

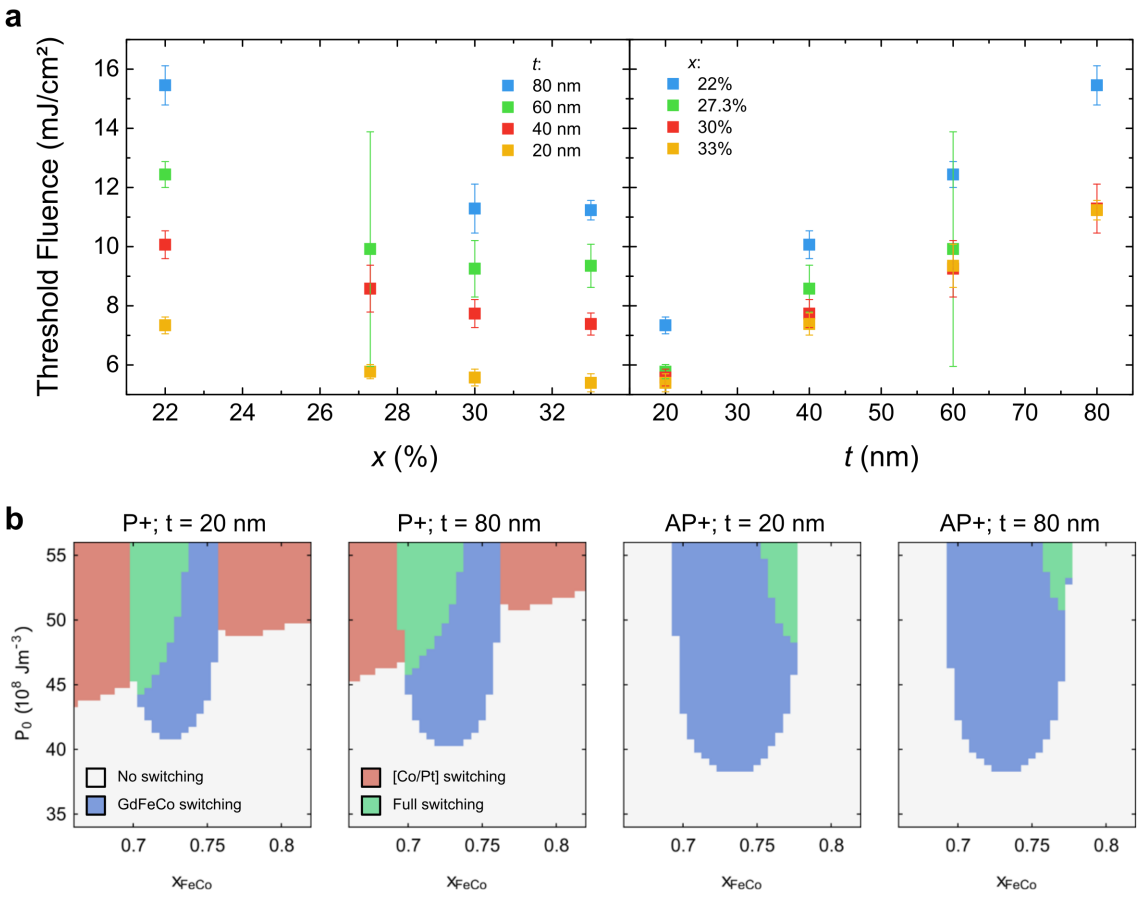

Figure 7.13: (a) Threshold fluences for [Co/Pt] in $Gd_xFeCo/Cu(t)$/[Co/Pt] spin valves for a P initial magnetic configuration. The results are presented either as a function of t or as a function of x. (b) Simulated state diagrams (absorbed energy density P_0 as a function of the TM content $x_{FeCo} = 1 - x$) for the reversal of the various magnetic layers in these samples for $t = 20$ or 80 nm and P and AP initial magnetic configurations. $10^8 Jm^3$ corresponds here to a fluence of around 0.5 mJ/cm^2. The color code is explained on the figure.

copper spacer thickness, one can see that the threshold fluence decreases as a function of x as already observed for smaller t. The observed decrease between 27% and 33% is however much

smaller and within uncertainties for all thicknesses except for $t = 40$ nm. In this latter case the relative decrease of threshold fluence between 27% and 33% is around 14%. We note that for $x = 22\%$, the reversal also happens for a P initial magnetic configuration, contrary to the case with $x = 20\%$ in the previous section, indicating that the transfer of angular momentum also mostly happens between the gadolinium sublattice and the [Co/Pt] multilayer at this composition. We therefore assume that the transition for the generation of a spin current which is mostly polarized by gadolinium to the case where it is mostly polarized by the TM sublattice should be between 20% and 22%. However, this is only an overall behavior and does not provide any information regarding the transient transfer of angular momentum*. We note that we had issues to determine threshold fluences for $x = 27\%$. In this case the coercive field of the GdFeCo is around 60 mT (against a few mT for other compositions) while the coercive field of the ferromagnetic multilayer is around 30 mT. Even though this difference is sufficient in principle to reach any magnetic configuration, we do not have a precise way to control the external magnetic field on our MOKE microscope setup (we use a permanent magnet) and we cannot know for sure whether the GdFeCo layer completely reversed because of the thick copper. In many situations, we found that magnetic domains were trapped (magnetization was not completely saturated) making the interpretation of the results difficult. For $t = 60$ nm, we managed to reverse a single magnetic domain whose size could me measured. The fluence threshold was determined from this single measurement hence the rather big uncertainty. It still seems to follow the trend one would expect from the results for thinner copper spacer. For 40 nm and below, it is possible to observe the GdFeCo layer making the measurements possible again.

From the plot as a function of copper thickness, one can see that the threshold fluence depends linearly on t. This is similar to the observations of Bergeard *et al.*[187] for ultrafast demagnetization of [Co/Pt] with hot electrons. In this range of thickness, they concluded that the electronic transport was ballistic (however see also the discussion in reference 288). One could assume that the hot spin transport that leads to the magnetization reversal is therefore also ballistic. We cannot ascertain this is indeed the case because it could still be that a ballistic hot (unpolarized) electron transport demagnetizes the ferromagnetic multilayer and then the reversal could happen much later. However, noting that we concluded that the spin current that reverses the magnetization comes from the ultrafast demagnetization of the ferrimagnet, we still hypothesize that the ferromagnetic multilayer switching is due to a ballistic hot spin current. We did not find any difference for the threshold fluences of GdFeCo between P and AP configurations, within

*The fact that we can obtain this transition is based on the fact that we know that the angular momentum from the GdFeCo layer can only be transferred to one sublattice in the ferromagnetic multilayer. The situation is more complicated for the samples of the previous chapter.

uncertainties, except for the case with $x = 22\%$ where the threshold fluence is smaller in the P configuration. It is consistent with the fact that for this composition, angular momentum transfer is mostly between the gadolinium sublattice and the ferromagnetic multilayer.

We now look at the simulations. We note that the absorbed energy density was always assumed to be P_0 in GdFeCo and $P_0/2$ for the ferromagnetic multilayer. This will prevent the model from predicting the correct threshold fluences but isolates the role of spin transport in the magnetization reversal. We want to highlight several points regarding these simulations, which we believe qualitatively agree with most of our experimental results:

1. It was found that the various shapes and sizes of the domains (red, blue and green) in these state diagrams depend on the temperature dynamics but the general qualitative behavior is always the same (presented in the next points).

2. The model predicts the reversal of the ferromagnetic multilayer (green and red areas) and even concentrations where only the [Co/Pt] multilayer will reverse.

3. Considering thicker copper spacers means, in the context of those simulations, that the spin current will lose some of its polarization as it diffuses through the spacer. For an identical temperature dynamics, one then sees that the threshold fluence for the ferromagnetic multilayer increases as spin angular momentum is lost in the copper spacer.

4. The model does not predict reversal only of the [Co/Pt] multilayer from an AP configuration at very low gadolinium content ($x = 20\%$) and also the general features of the sample at this composition that we did not understand. However it predicts such reversal at low Gd content from a P configuration, something that we did not observe but which we cannot exclude as a possibility.

5. The model shows that the GdFeCo layer reverses for smaller fluences in the AP configuration compared to the P configuration, for all compositions, while we found, for these samples, no effect of the spin current coming from the ferromagnetic multilayer or that the P configuration was more favorable for $x = 22\%$.

6. A great success of this model is the prediction of a critical concentration x_c (around $1 - x_{\text{FeCo}} = 25\%$ in these simulations) where the [Co/Pt] reverses its magnetization in the P configuration above x_c and in the AP configuration below x_c. This is something we have observed and we estimate $x_c \simeq 21\%$ from our experiments. The only disagreement is that such reversal of [Co/Pt] below x_c can happen without the reversal of GdFeCo in our experiments. At $x = x_c$ it is also predicted that the threshold fluence of the ferromagnetic

layer switching diverges which is consistent with the higher threshold fluences we observe for $x = 22\%$. We hypothesize that x_c might be related to the compensation composition for the spin polarization of the conduction electrons. However verifying this statement would require further investigation of this model.

Overall, we believe that this model contains all the key ingredients to explain the results presented in this chapter, apart from the sample with $x = 20\%$. This may be corrected if one considers a more realistic model by considering, for instance, electronic heat diffusion, absorption profiles with the TMM and a 2TM that considers exchange of energy between the conduction electrons and the localized spins. There are many other ways to improve this model (considering out of equilibrium magnons[128], several phonon temperatures[62], non thermal electrons[60], ballistic transport[187], etc.) but we believe that the essential assumption for the success of this model is the (out of equilibrium) exchange of angular momentum between itinerant and localized spins.

7.5 Conclusion

This chapter aimed at studying simpler systems compared to chapter 6 where one layer was replaced by a ferromagnetic layer. The purpose was then to study the conditions under which this magnetic layer could be switched using a single pulse of light. We first showed that the Curie temperature of the ferromagnet plays a major role as it allows us to tune the threshold fluence where single shot reversal can be achieved. This behavior could be well reproduced using our 2TM model coupled with the m3TM. Changing the duration of the laser pulse, we could also control threshold fluences by directly affecting the spin generation rate in GdFeCo. We also showed another example of (ultrafast) spin cooling where the generated spin current by GdFeCo, on top of reversing the magnetization of the [Co/Pt] layer (together with laser induced ultrafast demagnetization), prevents the formation of a multidomain state. The next part was then dedicated to the impact of the spin current itself on a given ferromagnet. We showed that increasing the gadolinium content in GdFeCo allows us to obtain lower threshold fluences for the reversal of the [Co/Pt] multilayer. In particular, AO-HIS of the GdFeCo layer itself is not required if a partial demagnetization of the ferrimagnetic layer generates enough angular momentum. We also found a similar behavior for GdFeCo layers with a very low content of gadolinium. This supports the fact that in this case, it is mostly the TM sublattice angular momentum that plays the role of reversing the magnetization of the ferromagnetic multilayer. This sample also shows spin cooling. The behavior of this sample is however far from being understood and possibly

suggests that gadolinium is not required in these samples. Finally, we increased the thickness of the spacer layer and saw that the same magnetization reversal is still happening for thicknesses up to 80 nm where the ferromagnetic multilayer does not interact with the laser light. This suggests that ultrashort (possibly ballistic) hot spin currents, i.e. spin polarized heat currents, may be sufficient to completely reverse the magnetization of a ferromagnetic system. These results were well understood using a combination of Gridnev[92] and Beens *et al.*[93] models of ultrafast magnetization dynamics.

Chapter 8

Ultrafast Dynamics of [Co/Pt] magnetization reversal

In the previous chapters, we only looked at magnetization several seconds after the laser pulse was sent and we deduced that the observed magnetization reversal must be ultrafast by eliminating slow processes as a possible way to cause the switching. Then, only the ultrafast demagnetization induced spin current can explain the magnetization reversal of the [Co/Pt] multilayer. Because this spin current was measured to be non zero only for a few picoseconds[170] for a pulse duration of 1.1 ps, we expect this magnetization reversal to happen in a few picoseconds at most. This is what we want to show experimentally and then theoretically in this chapter. It turns out that the reversal happens in less than a picosecond, with the magnetization crossing zero at around 400 $\pm$ 200 femtoseconds for a pump laser pulse duration of 100 fs.

8.1 Measurement of the dynamics

In order to measure the magnetization dynamics of [Co/Pt] in our spin valve structures, one must overcome several challenges. First, it is necessary to be able to separate the dynamics of GdFeCo from the dynamics of the ferromagnetic multilayer. This can usually be done either in standard TR-MOKE if both magnetic layers are identical[181], using complex TR-MOKE[157,180,248,270,271] or using an element sensitive method[186]. However, since we observe magnetization reversal even for a 80 nm thick copper spacer, one could try to pump the GdFeCo layer on one side and probe the [Co/Pt] multilayer on the other side. It turns out that this cannot

work because of the high fluences required to generate enough hot electrons (the only source of heating for thick copper spacers). After a few seconds of laser pulse irradiation, with a repetition rate of 5kHz on our MOKE microcopy setup, the GdFeCo layer is permanently damaged and no spin current can be generated anymore. In fact, even with most of our samples previously studied with 10 nm of copper, the GdFeCo layer is permanently damaged after a few minutes of continuous pulsed irradiation.

It is then required to provide the least possible amount of energy to the sample in order to avoid permanent damage. To do so, we only used two repetitions of Co/Pt in the [Co/Pt] multilayer, decreasing the number of hot electrons it can generate, and with the smallest cobalt thickness such that we could still obtain PMA for this layer. The latter fact allows us to reduce the threshold fluence for the reversal of that layer as demonstrated in chapter 7. We also use a high gadolinium content with $x = 33\%$. In order to enhance dissipation on a longer timescale, we also replaced glass by sapphire as a substrate. Because sapphire is birefringent and we probe with an angle of incidence for the TR-MOKE microscopy setup, the order of the spin valve structure is reversed i.e. the GdFeCo layer is grown first and the [Co/Pt] multilayer is then directly accessible from the sample side. Finally, our TR-MOKE setup uses an external magnetic field to reinitialize the magnetic configuration between two consecutive laser pulses (which is required anyways because the [Co/Pt] multilayer reverses its magnetization only after the first pulse; see below). Because the GdFeCo layer we choose is RE dominant, saturating the sample with a magnetic field initializes it in an AP configuration where the [Co/Pt] switching is not observed. We thus grow a ferromagnetic layer next to the ferrimagnetic layer to make it TM dominant while still keeping its ability to generate spin currents. Finally, the sample that we study is the following: Sapphire / Ta(5) / Pt(4) / $[\text{Co(1)/Pt(1)}]_2$ / Co(0,6) / $\text{Gd}_{33\%}\text{FeCo(5)}$ / Cu(10) / $[\text{Co(0.6)/Pt(1)}]_2$ / Ta(5). For comparisons, we also grew Glass / Ta(5) / Pt(4) / Cu(10) / $[\text{Co(0.6)/Pt(1)}]_2$ / Ta(5) as a reference which does not have the RE based multilayer that generates the spin current. In all this section, when we talk about the [Co/Pt] ferromagnetic multilayer, we talk about the $[\text{Co(0.6)/Pt(1)}]_2$ multilayer at the top and when we talk about the ferrimagnetic or GdFeCo layer, we actually talk about the $[\text{Co(1)/Pt(1)}]_2$ / Co(0,6) / $\text{Gd}_{33\%}\text{FeCo(5)}$ multilayer. The sample with GdFeCo is referred to as the spin valve sample while the other sample is referred to as the reference sample.

The magnetic hysteresis loops of these two samples (measured from the sample side) are shown in figure 8.1 (a) and (b). Both magnetic layers exhibit PMA. The coercive field of the [Co/Pt] multilayer is rather small (around 5.7 mT) compared to the previous ferromagnetic multilayers we have considered. This is explained by the fact that it is grown directly on copper,

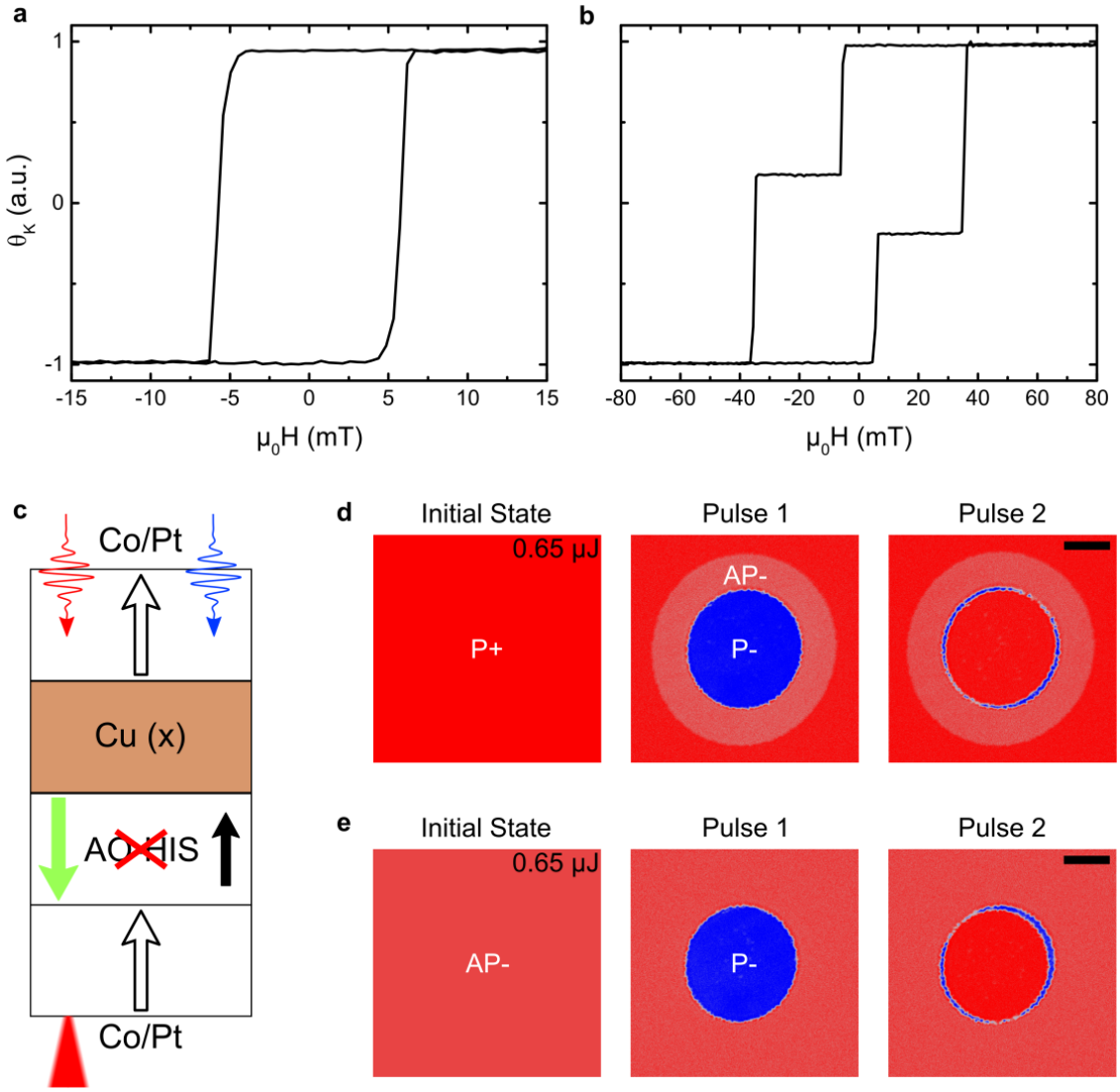

Figure 8.1: (a) and (b) show the hysteresis loops for the single [Co/Pt] and the spin valve samples respectively. The cw laser irradiates from the sample side as the probe in both TR-MOKE setups. (c) shows the simplified sample structure in the P+ configuration together with the experimental situation for MOKE microscopy and TR-MOKE microscopy. The red cone indicates on which side MOKE microscopy is performed and the red wiggly arrow indicates on which side we send single laser pulses whose characteristics depend on the experimental setup (see text). The blue wiggly line represents the probe pulse in the TR-MOKE microscopy setup. (d) and (e) show the results of sending single laser pulses on the spin valve from P+ (d) and AP- (e) initial configurations. The pulse duration is 35 fs, the beam spot size is 93 μm and the pulse energy is 0.44 μJ. The scale bars are 20 μm long.

therefore removing one Pt/Co interface. The GdFeCo layer on the other hand has a much higher coercive field (around 35 mT) due to the additional [Co/Pt] multilayer next to it. The situation is

thus reversed compared to previous samples studied above. The convention for the names of the magnetic configurations is still the same as in figure 7.1 with positive and negative referring to the orientation of the top [Co/Pt] multilayer and not the bottom one in direct contact with GdFeCo. Figure 8.1 (c) represents the experimental situation. For MOKE microscopy, magnetization of the sample is probed from the substrate side while for TR-MOKE microscopy it is probed from the sample side. Static results obtained from the MOKE microscopy setup are shown in figure 8.1 (d) and (e) for P+ and AP- initial magnetic configurations respectively. Note that compared to the results presented in the appendix, the color representing AP- is different because the order of the spin valve is reversed. The qualitative behavior is otherwise identical. From figure 8.1 (d), we conclude that the [Co/Pt] multilayer reverses its magnetization for lower fluences than the ferrimagnetic layer, as in the previous chapter. The threshold fluence for the [Co/Pt] multilayer reversal is 2.19 ± 0.05 mJ/cm^2 and the one for GdFeCo is 5.39 ± 0.11 mJ/cm^2 independently of whether the magnetic configuration is P or AP (within our uncertainty). The fact that the [Co/Pt] multilayer reverses for a lower fluence than the GdFeCo layer is useful because it *a priori* means that we can be sure that if we observe a magnetization reversal, even if we probe both magnetic layers, the reversal will correspond to [Co/Pt]. This is not so straightforward in practice because one needs to make sure that the threshold fluences observed with our static MOKE microscopy setup coincides with the actual (short timescale) threshold fluences.

We now look at magnetization dynamics with the TR-MOKE microscopy setup. First, we show some time dependent MOKE images where we subtracted data for opposite external magnetic field directions and a common background was subtracted for each delay. The image was also scaled along the horizontal direction x to take into account the probe angle of incidence. This is shown in figure 8.2. The beam spot is elliptical, with a major horizontal (x) diameter of 246 µm and a minor vertical (y) diameter of 220 µm. The signal on the images also has a wider characteristic size in the x direction due to the pump angle of incidence in the x-z plane (z being the direction normal to the sample surface). One can clearly see the consequence of the pump angle of incidence because the signal first appears on the left side of the image. The speed at which the signal extends to the right is $c/(\sin(\theta_{\text{pump}}) + \sin(\theta_{\text{probe}}))$ where θ_{pump} and θ_{probe} are the pump and probe angles of incidence respectively*. From the previous formula, we calculate a speed of around 26 µm per 100 fs which agrees well with the data. In the AP configuration, the TM magnetizations are in opposite directions resulting in an overall smaller signal. We adjusted the contrast of the images in figure 8.2 such as the signal pattern is clearly visible. In particular,

*The signal delay, between two points on the sample separated by a distance Δx, induced by the angle of incidence θ of one beam is $\Delta t = \Delta x \sin(\theta)/c$. When the angle of incidence is zero, the "speed" is infinite because the beam irradiates the sample everywhere at the same time.

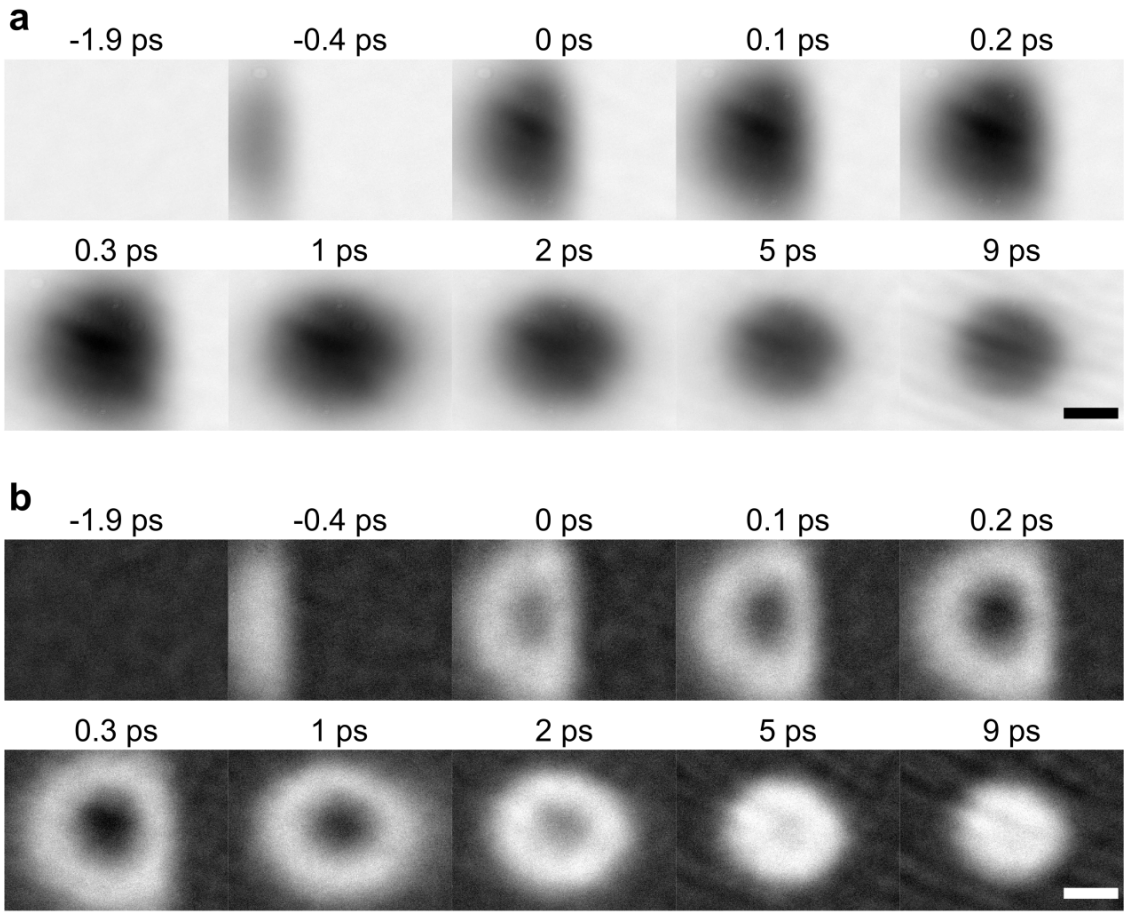

Figure 8.2: Time dependent MOKE images of the spin valve sample for various pump-probe delays for an initial magnetic configuration which is either P (a) or AP (b) and a given quarter wave-plate setting. The scale bars are 100 μm long. The image contrast was adjusted such that one can clearly see the magnetization pattern in each case. In (b), the color code is such that a brighter contrast corresponds to a signal dominated by [Co/Pt] while a darker one corresponds to a signal dominated by GdFeCo.

the signal forms a ring like shape because of the different magnetization dynamics of both layers. The signal cannot be related to the magnetization of a given layer without performing the analysis explained in chapter 4. The external magnetic field is adjusted such that the observed signal vanishes after a few nanoseconds, ensuring that one starts with a saturated state before the next pulse arrives. An external field of around 14.6 mT was required. We also repeated the measurements with an external field of 146 mT which only changes the long time dynamics. The pulse energy of 2.4 μJ, corresponding to a measured (average) fluence of 5.09 mJ/cm^2, is below the threshold fluence of GdFeCo*. We verified this fact by looking at the magnetization

*Note that one cannot directly compare these two values in general because of the different angles of incidence in TR-MOKE microscopy and MOKE microscopy in our setups. We found that, in this sample, the total absorption

on a long time scale (with the pump turned off). AP measurements where also made with an external magnetic field of 14.6 mT. We verified that the system remains in the AP configuration on a long timescale for this value of the external magnetic field. To obtain the magnetization dynamics as a function of fluence, we choose the position along the x direction that corresponds to the center of the reversed domain at a long time scale. We then vary the position along the y axis to get magnetization dynamics at different fluences. We verified that changing position along the x direction leads to identical results (but the maximum fluence will be lower in these cases). The data is averaged over a square of 10 µm side. This leads to a fluence uncertainty ranging from around 0.01 to around 0.3 mJ/cm^2 depending on position.

Let us first focus on the magnetization dynamics of [Co/Pt] measured in the P configuration. Results are shown in figure 8.3 (a) for a fluence of 5.08 $\pm$ 0.01 mJ/cm^2 (we always present the corresponding "measured" fluence $\overline{F}(r) = P/(f\pi w^2)\exp(-2r^2/w^2)$; the actual fluence as given in chapter 4 is $F(r) = 2\overline{F}(r)$). We clearly see that the magnetization crosses zero at around 400 fs (see figure 8.3 (b)) where the uncertainty should be $\pm$ 200 fs because of the probe laser pulse duration. The error bars are the standard deviations coming from the average of the magnetization dynamics obtained from different pairs of quarter wave-plate angles as explained in chapter 4. The results for such pairs of quarter wave-plate angles are shown in figure 8.3 (c). Only five out of the six possible pairs (with 4 different wave-plate angles) are shown because the other one leads to too much noise*. One sees that they give the same magnetization dynamics (up to the uncertainty shown in figure 8.3). The quarter wave-plate angles corresponds to various possible ratios of [Co/Pt] to GdFeCo MOKE signals. The fact that we obtain the same dynamics at all times means that we are indeed able to separate the signal of both magnetic layers. Moreover, this also confirms that our assumption about the time independence of the magneto-optical parameters α or β is verified (note also that we use the same magneto-optical parameters for all fluences). This in general not true because it could still be that one has the same magnetic artifacts[266] for all pairs of quarter wave-plate angles. However, because both our magnetic layers are different, they should exhibit different magnetic artifacts. The same argumentation shows that the magnetization dynamics we see is independent of any possible depth

is around 20% at normal incidence and 22% at 25.6 degrees from TMM calculations. This difference is small. However, note that we cannot estimate the correction to the threshold fluence of GdFeCo from TMM calculations because the magnetization dynamics does not only depends on the total light absorbed or the light absorbed in the [Co/Pt] layer but on the complete absorption profile. Especially, the threshold fluence may differ because more or less hot electrons can be generated in each layer for different angles of incidence.

*This happens when some of the magneto-optical parameters α or β introduced in chapter 4 are too close to each other as one can see by solving the system of equation for M^1 or M^2.

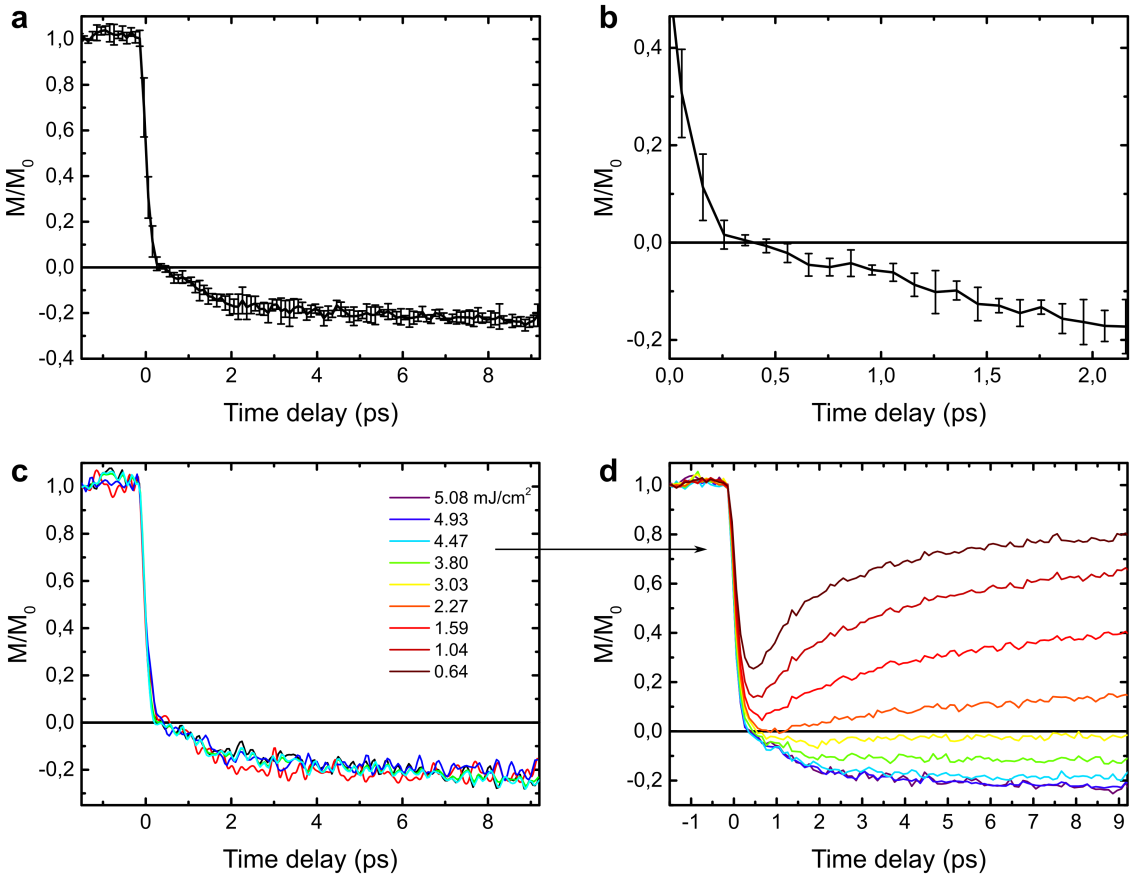

Figure 8.3: (a) Normalized magnetization M/M_0 dynamics of [Co/Pt] for an initial P configuration, where M_0 is the magnetization at negative delay, as a function of pump-probe delay and for a fluence of 5.08 $\pm$ 0.01 mJ/cm^2. (b) is a zoom on the region around the magnetization reversal. (c) shows the individual magnetization dynamics resulting from the analysis with five different pairs of quarter wave-plate angles. (d) shows the normalized magnetization dynamics for several fluences. In the latter figure, error bars have been removed for visibility.

sensitivity. We thus conclude that, within error bars, we are able to extract the true magnetization dynamics of each magnetic layer. We could reproduce the same measurements for different probe wavelengths to further confirm this but this has not been done yet. Figure 8.3 (d) shows the [Co/Pt] magnetization dynamics for various fluences. At low fluence, we observe standard ultrafast demagnetization curves with a fast reduction of magnetization followed by a rather fast but still slower recovery. At high fluence however, the behavior is drastically different. The magnetization goes to zero in around 400 fs and then the magnetization continues to decrease (increase in the opposite direction) but slower. One can clearly see the rupture of the magnetization dynamics at $M/M_0 = 0$ in figure 8.3. Then the magnetization seems to evolve linearly

in time up to around 2 ps after which the magnetization dynamics slows down even more. We believe this transient evolution between 400 fs and 2 ps is the signature that the magnetization is not in equilibrium with the electronic system, as it is during the ultrafast demagnetization before 400 fs. More precisely, the magnetization is smaller (in amplitude) than the instantaneous equilibrium magnetization given by the electron temperature. This is something that we will reproduce theoretically in the next section. Thus we claim that a complete reversal of the magnetization is achieved in around 2 ps. The magnetization does not have its room temperature value at this time delay because the sample is still hot. The threshold fluence we can estimate from these results is in between 2.27 ± 0.26 and 3.03 ± 0.28 mJ/cm^2 which is in agreement with our MOKE microscopy measurements. When the fluence is around that threshold, the magnetization dynamics is slowed down and remains around zero. In this case, one would expect the formation of a multidomain state at a longer timescale if there is no external magnetic field.

We now look at the dynamics of [Co/Pt] in the AP configuration and at the dynamics of GdFeCo. This is shown in figure 8.4. At low fluence, the magnetization dynamics of [Co/Pt] in the AP configuration is similar to what is observed for ultrafast demagnetization. However, compared to the low fluence case in the P configuration, the magnetization recovery onsets sharply. At high fluence, the magnetization overshoots zero and transiently reverses (see the zoom in figure 8.5 (b)). This transient reversal happens at around 200 fs at the highest fluence. However, the magnetization recovers and we do not observe a critical slow down of the magnetization dynamics[84,107,301]. This is explained by the presence of the spin current which prevents a complete spin disorder in the magnetic layer, as explained in chapter 3. This is something that is well explained within the models introduced in chapter 5 as we will discuss in the next section*. The fact that the magnetization crosses zero is attributed to the spin current coming from the TM sublattice of GdFeCo (the first spin generation peak observed by Choi and Min[170]). At first glance this does not seem right because this overshoot happens in less than a picosecond just as the magnetization reversal in the P configuration. We will show however that this is a feature that

*In the context of the s-d model, the dynamics of the localized spins is modeled by an interaction of the form $-J\sum_i \mathbf{S}_i \cdot \mathbf{s}_i$. The total magnetization of the sample is given by both localized $\mathbf{S}_i$ and itinerant $\mathbf{s}_i$ spin operators. When there is no external source of itinerant spin, heating of the sample may reduce the magnetization of the sample near zero such that the expectation value of both types of operators is nearly zero as well. Then, there can be no transitions due to the s-d interaction on average and the magnetization dynamics slows down. In the presence of a spin current, this means that $\mathbf{s}_i$ is not zero on average and its effect will also be to induce a polarization in the localized spins. Then, the transitions rates are never equal to zero, even when the total magnetization itself is zero. Mathematically, one can see from equation (5.25) that $\mathrm{d}m/\mathrm{d}t \neq 0$ as long as $\Delta\mu \neq 0$. In the particular case $m = \Delta\mu/(2k_BT_C)$, the prefactor on the right hand side of (5.25) is zero but the last factor is equal to infinity. A Taylor expansion of $\coth$ directly shows that $\mathrm{d}m/\mathrm{d}t \neq 0$ even in this case.

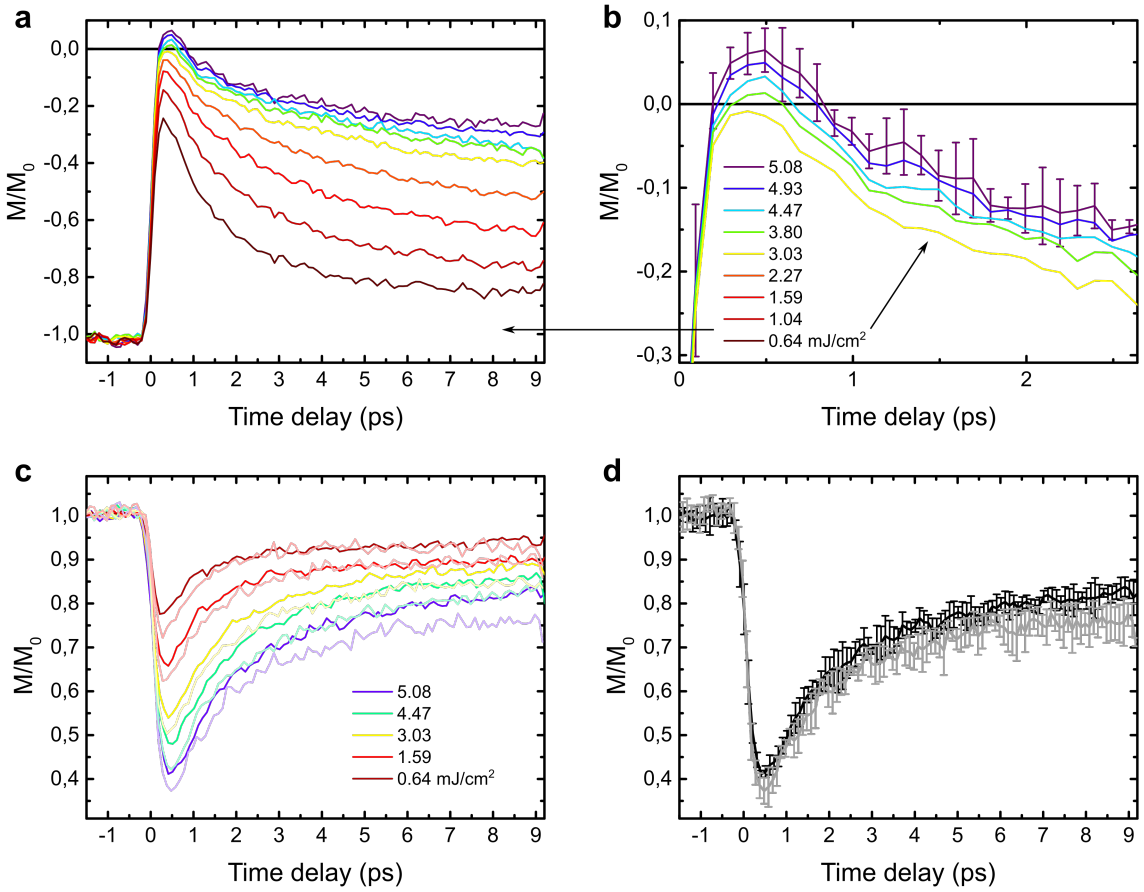

Figure 8.4: (a) Normalized magnetization M/M_0 dynamics of [Co/Pt] for an initial AP configuration, where M_0 is the magnetization at negative delay, as a function of pump-probe delay and for a fluence of 5.08 ± 0.01 mJ/cm^2. (b) is a zoom on the region around the magnetization overshoot. (c) Normalized magnetization M/M_0 dynamics of GdFeCo for both initial P (saturated colors) and AP (light colors) configurations, as a function of pump-probe delay. (d) shows the normalized magnetization dynamics for one fluence and both initial magnetic configurations (P in black and AP in gray) with error bars. For visibility, error bars for certain fluences were removed in other figures.

is reproduced by our model below. The magnetization recovers due to the spin current generated by the gadolinium sublattice. Regarding the GdFeCo dynamics shown in figure 8.4 (c), we see first that we indeed do not have reversal and only (partial) ultrafast demagnetization of that magnetic layer for all the considered fluences. Second, we see that the demagnetization amplitude is systematically larger in the AP configuration compared to the P configuration. This feature is explained by a spin current generated by the [Co/Pt] multilayer which, at the subpicosecond timescale, would mostly interact with the TM sublattice just as the [Co/Pt] dynamics is affected by the spin current generated by the TM sublattice in the AP configuration, for identical delays.

This is however a feature that we will not be able to reproduce given that we do not consider that magnetization dynamics of GdFeCo explicitly. Note however that the difference between the GdFeCo dynamics for P and AP configurations is rather small and within our error bars (see figure 8.4 (d)) which is consistent with the fact that we do not observe a difference of threshold fluence with the MOKE microscopy measurements for the reversal of that layer. Because we did not make measurements of the magnetization reversal of GdFeCo in this system, we cannot conclude whether this difference remains small at higher fluences.

In order to compare the [Co/Pt] multilayer dynamics when it is subjected to different spin current polarizations, we plot the previous results for both P and AP initial magnetic configurations in the same graph 8.5. We also show the magnetization dynamics at a longer timescale in the same figure. At low fluence, one sees that the magnetization dynamics is nearly identical in

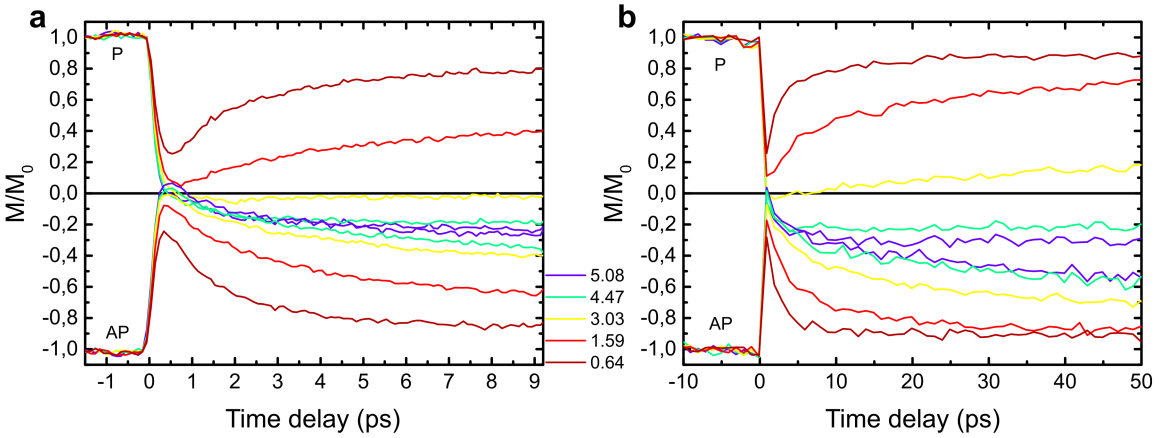

Figure 8.5: (a) Normalized magnetization M/M_0 dynamics of [Co/Pt] for both initial magnetic configurations, where M_0 is the magnetization at negative delay, as a function of pump-probe delay and for several fluences. (b) shows the same results but for longer pump-probe delays.

both magnetic configurations. However, as the fluence increases, the effect of the GdFeCo spin current becomes more visible. There are two reasons for this. First, the demagnetization amplitude of GdFeCo increases and thus so does the amplitude of the generated spin. Second, as the demagnetization in the [Co/Pt] multilayer increases, the magnetization becomes more sensitive to the effect of the spin current*. Up to 3.03 ± 0.28 mJ/cm^2, the spin current heats up the magnetization in the P configuration (spin heating) while in the AP configuration it cools it down (spin cooling). Above this fluence, magnetization is quickly reversed in the P configuration and then the spin current cools down magnetization in both cases. This results in an almost identical mag-

*This is seen in equation (5.25), when m is large compared to $\Delta\mu/(2k_BT_C)$, m dominates the magnetization dynamics while when m is small, the term that depends on the spin accumulation dominates.

netization in both magnetic configurations at higher fluences as can be seen in figure 8.5 (a) for 5.08 ± 0.01 mJ/cm^2. At longer delays, both magnetization curves separate from each other due to the action of the external magnetic field. For 5.08 ± 0.01 mJ/cm^2, we can see that the reversed magnetization is around 20% of its room temperature equilibrium value after a few picoseconds and around 40% percent of it after 50 ps (we suppress the contribution of the external magnetic field by averaging the normalized magnetization for both magnetic configurations). These values can be increased in principle if one increases the Curie temperature of the ferromagnetic layer because then the instantaneous equilibrium magnetization will be larger. However, as we showed in the previous chapter, this will require a higher laser fluence or a larger spin current amplitude to achieve the magnetization reversal. One must then face a trade off between energy efficiency and a higher reversed magnetization amplitude.

Finally, in order to better appreciate this spin cooling effect, we compare the results we have for the spin valve with the results for the reference sample. This is shown in figure 8.6. Figure 8.6 (a) shows the magnetization dynamics of the reference sample for several fluences. We recover the usual ultrafast demagnetization behavior[302]. In order to compare these results with what we get for the AP configuration in the spin valve sample, we change the peak fluence for the measurement of the reference sample until we get the same normalized magnetization dynamics. This is what we obtained in figure 8.6 (c) for 0.53 ± 0.08 mJ/cm^2. The displayed values of fluence correspond to the fluences used for the reference sample which are then found to be half as high as the ones for the spin valve sample. Starting at around 1.52 ± 0.14 mJ/cm^2, a clear difference between both magnetization dynamics appears which keeps increasing as the fluence increases, showing again the increasing efficiency of the spin current generation (in the GdFeCo layer) and absorption (in the [Co/Pt] layer) as fluence increases. To quantify this effect, we define the spin cooling as the difference between the [Co/Pt] normalized magnetization in both cases i.e. $(|M_{\text{AP [Co/Pt]}}(t)| - |M_{\text{single [Co/Pt]}}(t)|)/M_0$ where $M_{\text{AP [Co/Pt]}}(t)$ is the magnetization of the [Co/Pt] multilayer in the spin valve for the AP configuration while $M_{\text{single [Co/Pt]}}(t)$ is its magnetization in the reference sample. The spin cooling as a function of pump-probe delay is plotted in figure 8.6 (b) for various fluences. At low fluences, there is no spin cooling but one can see an ultrashort transient spin heating (i.e. negative spin cooling) at 1 ps of around 10%. This spin heating is due to the already observed sharp onset on the magnetization recovery. Just as the magnetization overshoot, it is attributed to the spin current coming from the TM sublattice of GdFeCo*. This measurement confirms this hypothesis as the spin cooling is the difference of

*Even though we observe this spin heating for only one data point, because of the lower time resolution of these measurements, we believe this effect is real. Indeed, at high fluence, it is the signature of the magnetization overshoot which we also observed with the higher time resolution of figure 8.4.

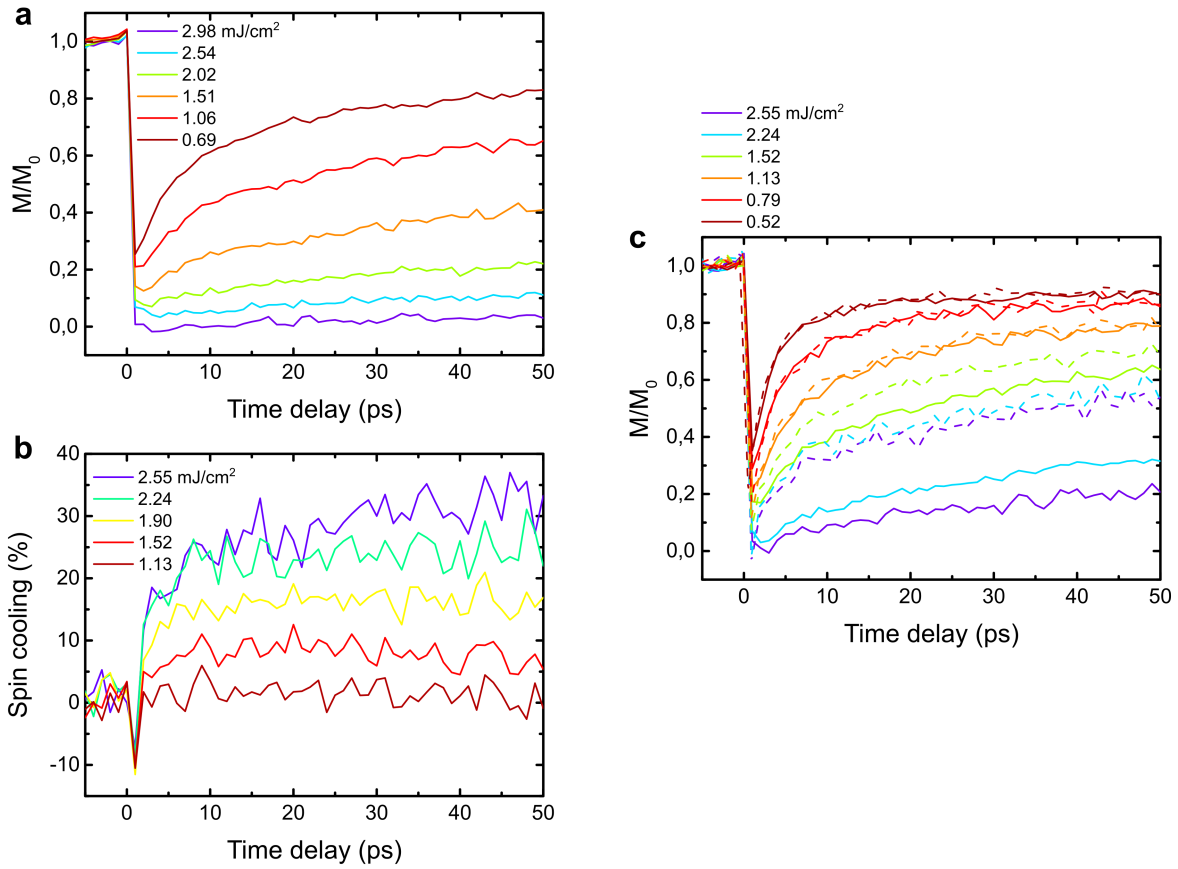

Figure 8.6: (a) Normalized magnetization M/M_0 dynamics of the reference sample, where M_0 is the magnetization at negative delay, as a function of pump-probe delay and for several fluences. The measurements were also made with an external magnetic field of 14.6 mT. (b) shows the spin cooling, defined in the text, as a function of pump-probe delay for several fluences (corresponding to the reference sample; see text). (c) Normalized magnetization dynamics for the reference sample (solid lines) and the spin valve sample in the AP configuration (dashed lines) as a function of pump-probe delay for several fluences (corresponding to the reference sample).

the magnetization dynamics of the [Co/Pt] multilayer with and without spin current. At higher fluences, a spin cooling starts to appear. At the highest fluence we used, a spin cooling of around 18% is reached within 3 ps and it even reaches around 32% at 50 ps.

8.2 Modeling and discussion

We now focus on modeling the previous results and use these simulations to draw conclusions regarding the physics at play. We use our model introduced in chapter 5 which is a combina-

tion of our theory of laser pulse absorption, a 2TM with heat diffusion, Beens *et al.*[93] model of ultrafast magnetization dynamics for ferromagnets (for $S = 1/2$) and a model for the spin accumulation generated by the GdFeCo ultrafast demagnetization. We consider that the generated spin accumulation in [Co/Pt] due to its own demagnetization is negligible due to a short spin-lattice relaxation time. We take the Curie temperature of the [Co/Pt] multilayer to be 500 Kelvins and the characteristic demagnetization time $\tau = 0.132$ ps as given by the standard m3TM[107] with the parameters used by Bergeard *et al.* as for chapter 7. We choose the room temperature to be 300 Kelvins, $\overline{D} = 1$ eV^{-1} as in reference 93 and all the other parameters are given in chapter 5 or taken from the experimental conditions. The only exception is the pump beam which was assumed to be circular with a diameter of 288 µm. We explain how we estimated the spin accumulation below. The normalized magnetization we plot is the one given at the center (in the z direction) of the [Co/Pt] multilayer*.

First, we focus on what this model predicts for the reference sample. This is shown in figure 8.7. Note that the normalized magnetization we are now talking about is different from the

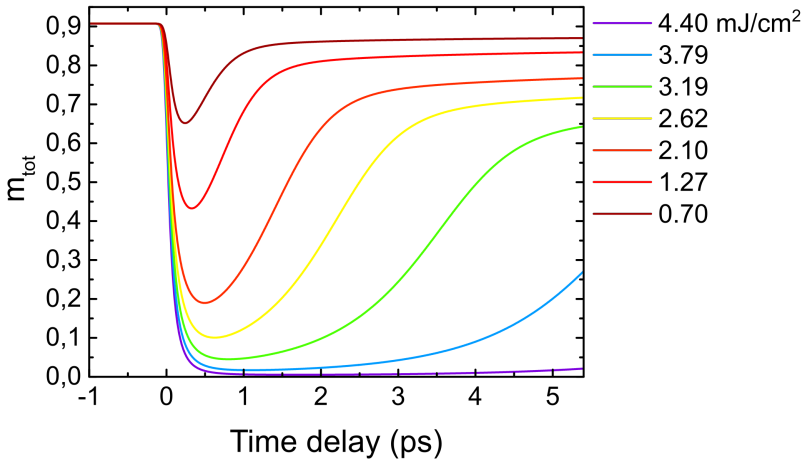

Figure 8.7: Predicted total normalized magnetization m_{tot} of the reference sample as a function of time delay for various fluences.

normalized magnetization in the previous section. In the previous section, magnetization was normalized with respect to the equilibrium magnetization at room temperature while here it is normalized by the magnetization at zero Kelvin as usual. One observes the standard ultrafast demagnetization dynamics with critical slowdown at high fluence. We note that the fluence we

*Here we calculate the magnetization dynamics at each point of our spatial grid. Because we neglect exchange interaction between magnetic moments at different depths, a cleaner approach would calculate the average electron temperature over the [Co/Pt] multilayer thickness at each time step and use this as an input for equation (5.25). However, this is not going to affect our results qualitatively.

find are higher than the experimental ones but we do not aim at making quantitative predictions. There is a factor two of difference between our predicted fluences and the experimental ones. This is similar to the factor two that we also had for the simulations in section 7.1.

We now consider the spin valve sample. In order to model the spin accumulation, we use equation (5.28) with the density of state per unit volume given by Sommerfeld's model[51] and $\tau_s' = 35$ fs*. We just need to know the dynamics of the magnetization of GdFeCo. We get the magnetic moment dynamics of each sublattice from the fits used in reference 9, assuming it is still valid for $x = 33\%$, and the atomic magnetic moments also given in this reference. We note that they used a pulse duration of 60 fs which is closer to our 100 fs than the 1.1 ps of Choi and Min[170]. To get magnetization, we estimate the number of atoms per unit volume from the measured magnetization of GdFeCo at 300 Kelvins measured in reference 303. We take $2.5\ 10^{28}$ atoms per cubic meters. The obtained magnetization dynamics is valid for positive delays. We then assume it is given by its equilibrium value at negative delays and take the convolution of the resulting function with a gaussian function with full width at half maximum of 100 fs (the pump laser pulse duration) as the true magnetization. The fits of reference 9 are obtained from reversal dynamics but we assume one has the same characteristic times for magnetization recovery. The effect of fluence on the amplitude of the generated spin accumulation is taken into account by assuming that the demagnetization amplitude of each sublattice scales linearly with fluence and that a complete quenching is achieved at the threshold fluence for GdFeCo switching that we found in the previous section. Thus, the resulting spin accumulation as a function of time to be used as an input in equation (5.25) is shown in figure 8.8. We retrieve a curve similar to the one measured by Choi and Min[170] through a thick layer of copper. The main difference is that the signal lasts for a shorter period of time of around 2 ps instead of several tens of picoseconds. This difference is attributed to the different pump laser duration as well as the diffusion in the thick copper in the case of Choi and Min[170]. It results that the gadolinium peak has its maximum amplitude at around 300 fs. The amplitude of the gadolinium peak is around $2.23\ 10^{-21}$ J which leads to $\Delta\mu/(2k_BT_C) \simeq 16\%$ and $\overline{D}\Delta\mu \simeq 1.4\%$. Thus, $\Delta\mu/(2k_BT_C)$ may indeed affect the magnetization dynamic when the normalized magnetization of the localized spins is sufficiently reduced. The impact of $\overline{D}\Delta\mu$ on the total magnetization is however small. As stated in chapter 5, this modeling of the spin accumulation breaks conservation of angular momentum. This model also neglect the spin accumulation generated by [Co/Pt] and especially the possible feedback this spin accumulation might have on the magnetization dynamics[93]. We note however that

*This value was tuned such as too reproduced the experimentally observed threshold fluence but choosing a different value with the same order of magnitude does not change the qualitative behavior we will describe.

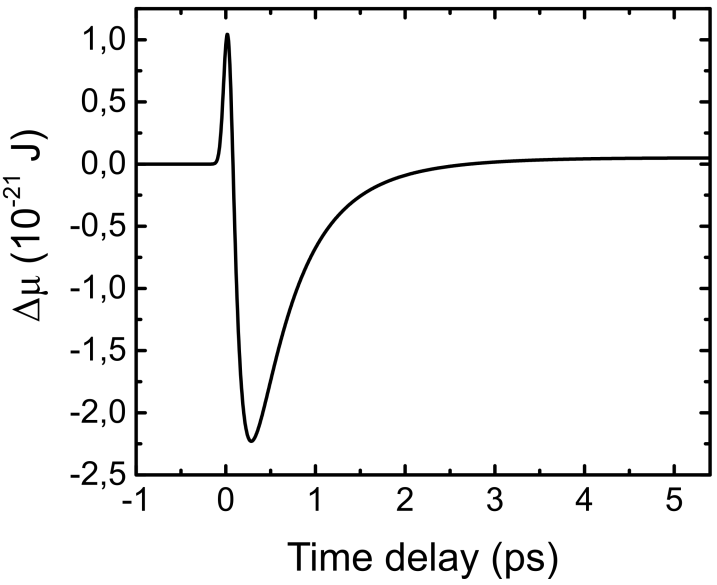

Figure 8.8: Predicted spin accumulation in the [Co/Pt] multilayer as a function of time delay for a fluence of 6.64 mJ/cm^2.

the spin accumulation generated by [Co/Pt] will be small at around 2 ps[93] when our input spin accumulation becomes negligibly small. Thus one should see the spin accumulation plotted in figure 8.8 as an effective total spin accumulation. Because we observed that the impact of the [Co/Pt] spin current on GdFeCo is small (which is however not directly related to the spin accumulation [Co/Pt] generates locally) we believe that it is reasonable to assume that the spin accumulation dynamics in [Co/Pt] is mostly given by GdFeCo.

Thus, we now give the predicted magnetization dynamics in [Co/Pt] in the P and AP configurations for various fluences in figure 8.9. One can see that our model indeed reproduces magnetization reversal in the P configuration and it also reproduces the lack of reversal in the AP configuration. The detailed behavior is however not quite right, especially because the amplitude of the normalized magnetization, just above the threshold fluence, reaches around 0.8 after a few ps. We give the equilibrium normalized magnetization which is around 0.91 for our parameters. In the P configuration, as fluences increases, the amplitude of the reversed magnetization decreases. This is simply explained by the fact that the temperature of the system increases and thus the corresponding equilibrium magnetization is lower in amplitude. This is not something we observed, perhaps because we did not try high enough fluences. Apart from the wrong amplitude, the magnetization dynamics for the P configuration is similar in trend to what we observe experimentally: (i) an ultrafast demagnetization (ii) magnetization crosses zero

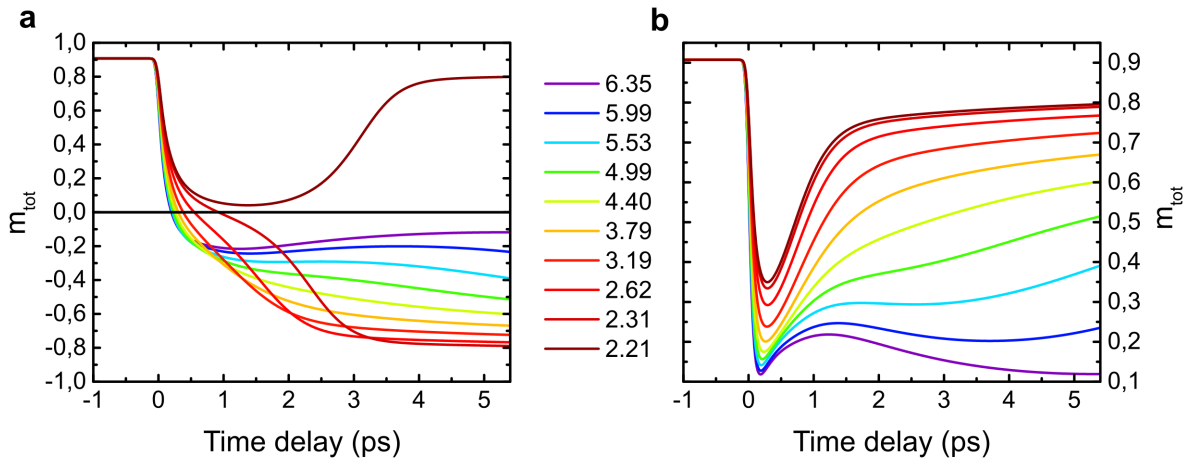

Figure 8.9: Predicted total normalized magnetization dynamics of the [Co/Pt] multilayer as a function of time delay for an initial P (a) or AP (b) magnetic configuration. Results for various fluence (indicated in the center of the figure in mJ/cm^2) are shown.

in less than a picosecond and increases in the other direction rather linearly until (iii) around 2 or 3 ps, the magnetization dynamics decelerate. This is especially visible for fluences between 2.62 and 3.79 mJ/cm^2. We show in figure 8.10 below that this third step happens as soon as the magnetization reaches equilibrium with the electronic system. We note that the overestimation in the reversed magnetization amplitude could be corrected by changing the Curie temperature or the intensity of the spin current. We tried several other set of parameters and we always found that the magnetization crosses zero in around a picosecond or less, which seems to show that this ultrafast reversal is a general behavior as long as one can sufficiently demagnetize the ferromagnetic layer and send a spin current on it at the right instant. We also note that our model is not able to reproduce magnetization dynamics where the magnetization remains stuck around zero, for fluences around the threshold fluence, as in figure 8.5. This behavior must exist in our model, by continuity, but the range of fluence where this happens might be very small while it seems to be easily reachable in experiments. In the AP configuration, we are not able to reproduce the overshoot. This makes sense because the reversed magnetization amplitude in the P configuration is too large and so we would expect the same to be true for the magnetization that is prevented from demagnetizing because of a spin current*. We are able however to reproduce a peak at around 200 fs which might play the role of this overshoot in the case of our simulations. In the simulations, this peak is due to the spin accumulation generated by the ultrafast

*This may be corrected by modifying the alloy concentration in the estimation of the spin accumulation given in figure 8.8. We believe that we are probably overestimating the spin current generated by gadolinium compared to the TM sublattice.

demagnetization of the TM sublattice which supports our interpretation that it is indeed the spin current coming from the TM sublattice of GdFeCo that generates this peak. Right after this peak and at high fluence, the magnetization suddenly increases because of the contribution of gadolinium. However, because the system is still very hot at these fluences, the magnetization decreases again after around 1 ps. This deformation of the magnetization curve as fluence increases shows that the magnetization is more sensitive to the spin current (spin accumulation) when the magnetization is reduced.

Our simulations also reproduce a counter intuitive result we obtained experimentally: the magnetization reversal in around 400 fs in the P configuration is explained by the spin current generated by gadolinium but at the same time the magnetization overshoot in AP is also around 500 fs but is explained by the spin current coming from the TM sublattice. In our simulations, the magnetization reversal also happens in less than a picosecond and the TM spin current peak in the AP configuration also happens in less than a picosecond (note the slight deviation of the magnetization minimum towards earlier delays as the fluence increases which is a signature that the TM spin accumulation happens at even earlier times). We believe the reason for this apparent contradiction is that the normalized magnetization dynamics lags behind the effect of the spin current/spin accumulation. To explain this and also prove our claim above that the magnetization is at equilibrium in around 2 ps, we plot the instantaneous equilibrium magnetization m_{eq} defined as the solution of $m_{eq}(t) = \tanh((2m_{eq}(t)k_BT_C - \Delta\mu(t))/(2k_BT_e(t)))$ which is different from m_{ie} defined in chapter 5. Equation (5.25) states that, at each instant, m tends towards m_{eq} with a certain characteristic time τ. This instantaneous equilibrium magnetization should be equal to the normalized magnetization (neglecting the small $\overline{D}\Delta\mu$ contribution to m_{tot}) when the localized spins are in equilibrium with the electronic system. A necessary and sufficient condition for this equilibrium is : $m = m_{eq}$ and $\mathrm{d}m/\mathrm{d}t = \mathrm{d}m_{eq}/\mathrm{d}t$. We plot the normalized magnetization dynamics and its time dependent equilibrium value for both magnetic configuration, and also in a fictitious case where the spin accumulation is always zero (but still for the same sample and same 2TM modeling), for two different fluences in figure 8.10. We first focus on the lowest fluence. In this case, without spin accumulation, the equilibrium magnetization reaches zero (note the almost vertical dashed line reaching zero) because the electron temperature exceeds the Curie temperature*. However, the magnetization lags behind this equilibrium value and a full quenching is not achieved. In the P case, the equilibrium magnetization does not reach zero right away because of the TM spin accumulation. The equilibrium magnetization thus slows

*We note that it is not required in this model that the electron temperature transiently exceeds the Curie temperature in order to reverse the magnetization of the ferromagnet. This is possible if the spin accumulation is sufficiently high.

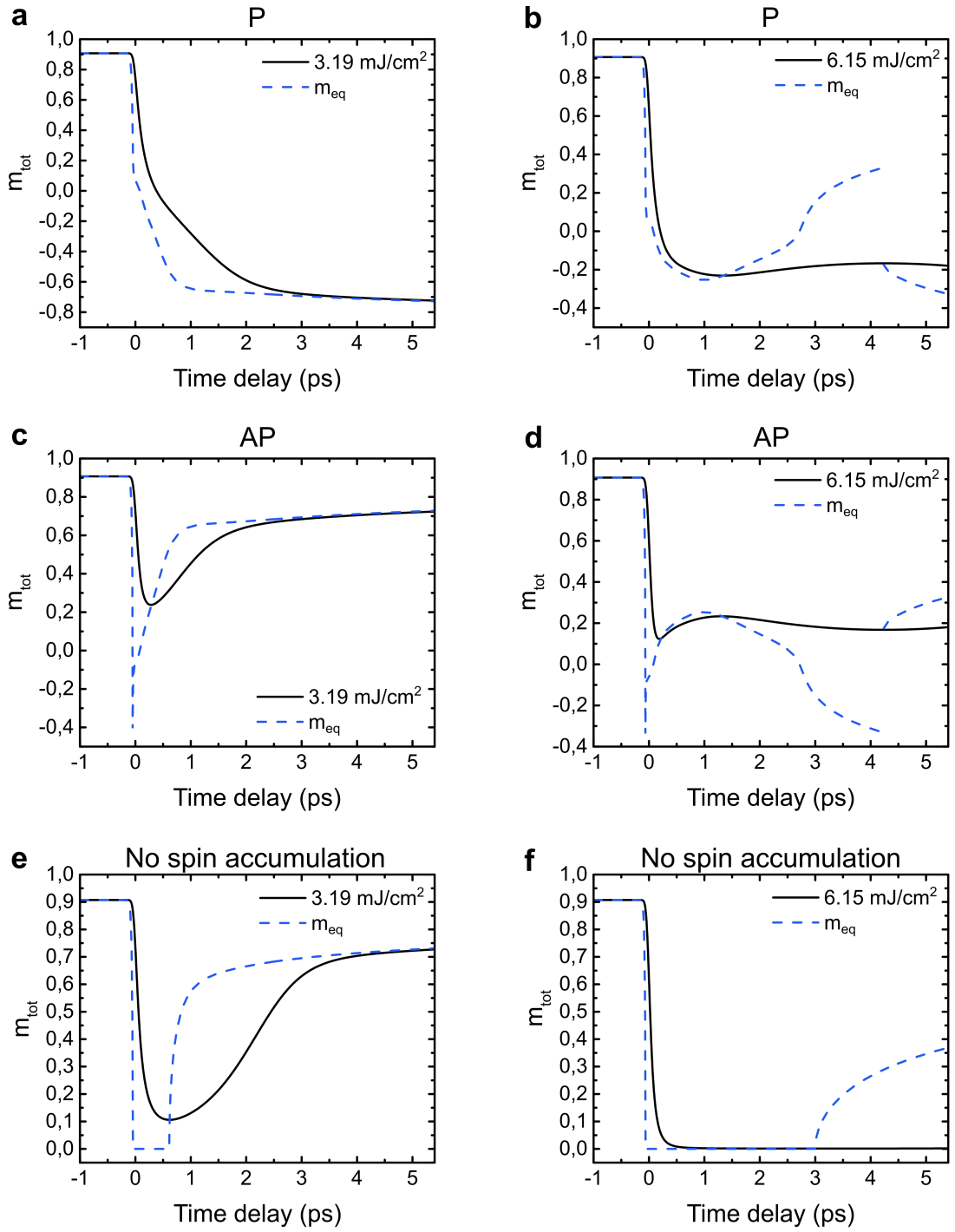

Figure 8.10: Predicted total normalized magnetization dynamics of the [Co/Pt] multilayer, and its time dependent equilibrium value, as a function of time delay for an initial P ((a) and (b)) or AP ((c) and (d)) magnetic configuration as well as for the fictitious case where no spin accumulation is present ((e) and (f)). The results for two fluences, as indicated in the figure, are shown.

down but still crosses zero because of the gadolinium spin accumulation. The normalized magnetization then follows and as soon as it is sufficiently close to the equilibrium magnetization, it slows down even more. This is very similar to what we observed experimentally and justifies our claim that the magnetization is at equilibrium with the electrons at around 2 ps. The system could still possibly not be at equilibrium because both electron and phonon temepratures could still be different as seen in figure 5.7. In the AP case, the equilibrium magnetization very quickly crosses zero because of the TM spin accumulation but it comes back because of the gadolinium contribution to the spin accumulation. Because the normalized magnetization lags behind, it is still going down as the equilibrium magnetization goes back up and the effect of the spin accumulation is barely visible. As one increases the fluence however, the magnetization follows the equilibrium magnetization more closely and the signature of the TM spin accumulation starts to appear. We note that in the case of this high fluence in P and AP configurations, the equilibrium magnetization is not always continuous. This comes from the fact that the self consistent equation we need to solve has either one or three roots and under certain conditions, for instance if the spin accumulation is relatively large, two such roots may disappear as time changes resulting in the convergence towards another root. This is similar to what happens when one models magnetic hysteresis loops with a Weiss model[79].

We now look at the spin cooling our model predicts. To see this, we either plot the magnetization dynamics in the P and AP magnetic configurations together with the dynamics without spin accumulation, or we plot the difference between the magnetization dynamics in the AP configuration and the magnetization dynamics without spin accumulation (i.e. the spin cooling as defined above). This is shown in figure 8.11. One sees that our model is not able to reproduce the long term asymmetry that is observed in figure 8.5 between the [Co/Pt] magnetization dynamics in the P and AP configurations at intermediate fluences. The high fluence (5.53 mJ/cm^2) case seems to reproduce qualitatively what we experimentally measure at 5.08 $\pm$ 0.01 mJ/cm^2. That is a subpicosecond magnetization reversal in P and both magnetization dynamics for P and AP become identical after some time. The magnetization in P and AP would not be identical at long delays if the electronic temperature of the [Co/Pt] multilayer were different in both configurations. The latter fact happens if the localized spins transfer a different amount of energy to the conduction electrons depending on their orientation. We do not observe such difference of magnetization between P and AP at high fluence, however this does not exclude an exchange of energy between conduction electrons and localized spins which should be included in our 2TM. For lower fluences (2.31 and 3.19 mJ/cm^2), an asymmetry persists only during the time interval required for the [Co/Pt] magnetization to switch and we cannot reproduce the fact that

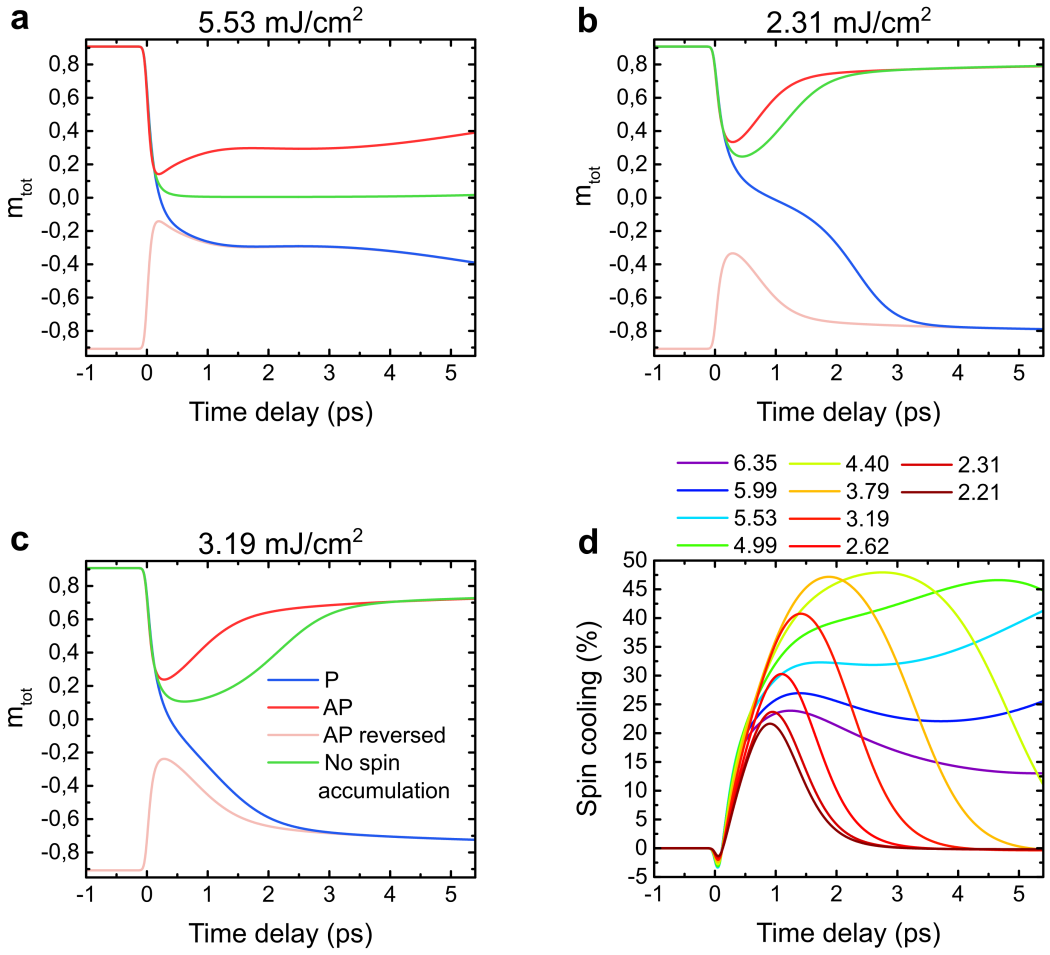

Figure 8.11: Superimposed magnetization dynamics in the P and AP (standard and reversed) magnetic configurations as well as the magnetization dynamics without spin accumulation for three different fluences as indicated in (a), (b) and (c). (d) shows the predicted spin cooling for this sample as a function of time delay.

the magnetization can remain around zero for several tens of picoseconds. We believe this is because the MFA prevents us to consider magnetization slow down due to out of equilibrium states that comes with complex magnetic textures[86*]. In this sense, atomistic stochastic LLG simulations are more suitable. Of course for much lower fluences, the spin accumulation has a negligible effect and we will obtain the same magnetization dynamics for both P and AP configurations, as in the experiments. Apart from this behavior around the threshold fluence of the ferromagnet, the magnetization reversal is well reproduced qualitatively. The results obtained

*This could also be partially due to the fact that, in our measurements, (i) there is a small fluctuation of the position of the beam and (ii) we average data over a square of finite size. This would result, at the threshold fluence, to data that are the average of magnetization reversal and recovery thus canceling out each other.

for the spin cooling show common features with the experimental one in figure 8.6. In particular, we model the spin heating peak (even though its amplitude is rather small). In our model, it is indeed due to the TM sublattice contribution to the spin accumulation. This spin accumulation will slightly increase the ultrafast demagnetization rate in the AP configuration compared to the case without spin accumulation. The behavior at longer times appears to be more complex in the case of the simulation with various non monotonous behaviors and higher spin cooling values. Nevertheless, we conclude that our model allows us to explain many features of our experiments.

Finally, we present some simulations of TR-MOKE microscopy images if there was no GdFeCo in the system. To do so, we reproduced our calculations for various fluences following a gaussian spatial profile. The angle of incidence of the pump laser beam is then taken into account to correct the incident laser fluence (see equation(5.10)) as well as the time delay for the arrival of the pulse along the x axis of the sample (the plane of incidence is the (x, z) plane). The angle of incidence of the probe is also taken into account because there will also be a time delay due to the fact that certain regions of the sample are probed earlier. According to what we explained in chapter 4, we should then obtain the exact effect of a pulsed laser beam on the sample (up to the fact that we neglected some small contributions to the electric field). These results are shown in figure 8.12. We can clearly see that we reproduced the fact that the signal starts appearing from the left and then propagates towards the right. At longer time delays, a sharper magnetic domain forms. However we note that this is faster than in our experiments because we saw that the simulations cannot reproduce the slowdown of the magnetization around the threshold fluence. We also note that the center of the reversed magnetic domain is hotter, leading to a slower magnetization recovery to its room temperature value.

8.3 Conclusion

In this chapter, we unveiled the true magnetization dynamics of the [Co/Pt] multilayer in the GdFeCo/Cu/[Co/Pt] spin valve structures using TR-MOKE microscopy. We saw that the magnetization crosses zero in less than a picosecond and reaches equilibrium in around 2 picoseconds. Both peaks of the spin accumulation were shown to contribute to the dynamics but it is the spin accumulation arising from the gadolinium sublattice that drives the reversal. We also showed that the spin accumulation efficiently cools down the local magnetization already at a subpicosecond timescale and can change the magnetization by around 30% at the picosecond timescale. These results were understood thanks to a model of ultrafast magnetization dynamics

with heat transport in multilayer structures and a spin current source. The model successfully reproduces qualitatively many features of the experiments apart from the slowdown of the magnetization dynamics around the threshold fluence.

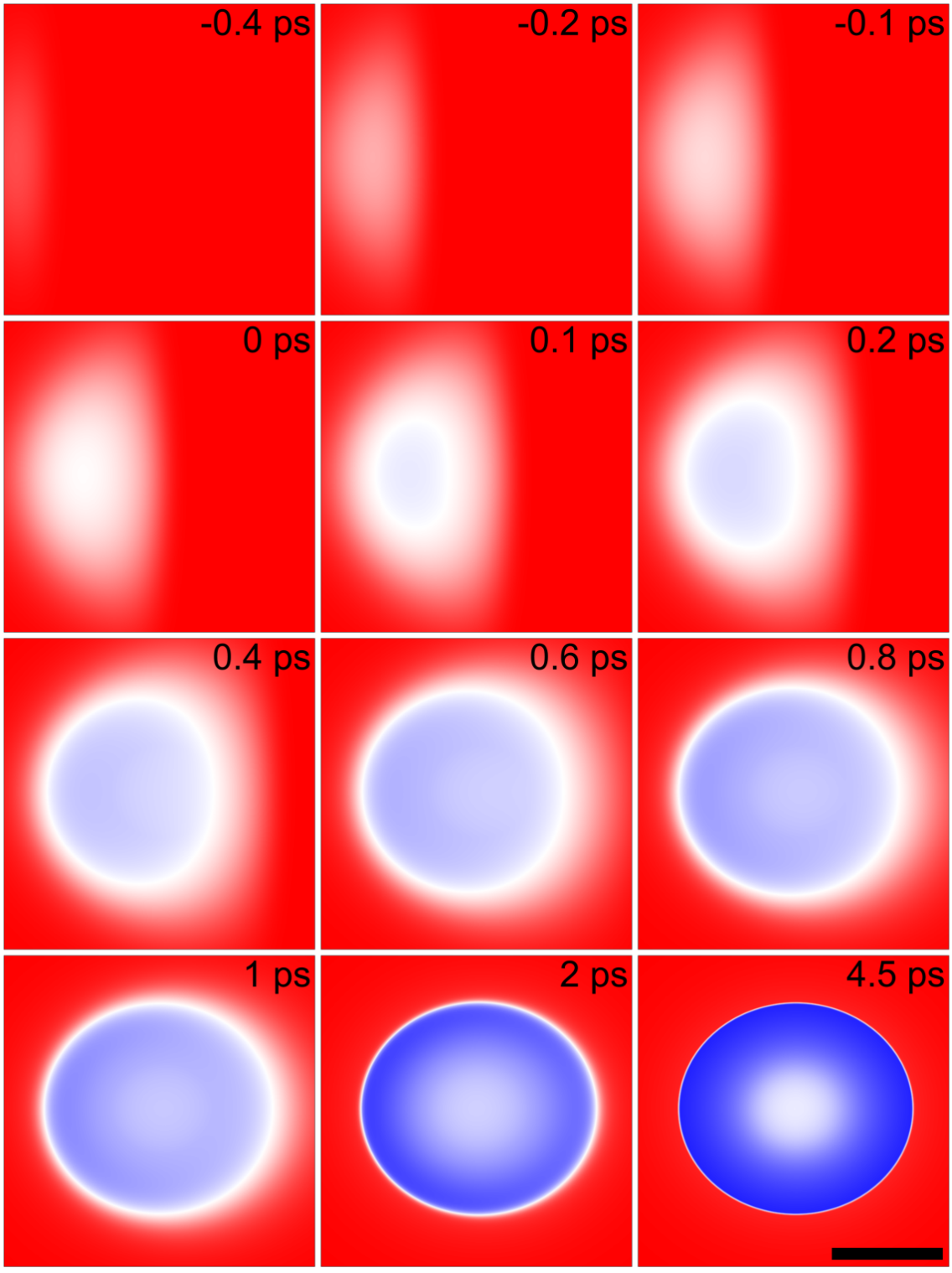

Figure 8.12: Simulations of the TR-MOKE microscopy images for different pump-probe delays (defined as zero when the peak of the laser pulse reaches the center of the image) for a laser power of 120 mW and the other experimental parameters are mentioned in the text. The scale bar is 100 μm long and the color code is the same as for MOKE microscopy images.

Chapter 9

Conclusion

This thesis focused on the ultrafast transport and dynamics of spin. We started by discussing the general conservation laws and dynamics equations satisfied by conserved quantities such as angular momentum. From these general considerations, one can tackle the problem of magnetization or spin dynamics in various approaches that we reviewed. In particular we discussed ultrafast demagnetization and where the angular goes during such experiments. Even though the details of such mechanisms are still the subject of intensive work, we argue that ultrafast spin transport, loss of magnetization accompanied by magnon generation and spin flip scatterings (all in the presence of spin orbit coupling) are the most important microscopic mechanisms. They may however contribute more or less depending on the sample and the experimental method (for instance which region of the Brillouin zone is probed). We also discussed extensively AO-HIS and presented our understanding of this mechanism which is at the base of the models we used in this work. Finally we presented the works that had already been done on the reversal of magnetization due to ultrashort spin currents, which is the main phenomenon that was investigated in the remaining part of this thesis.

The next part focused on the experimental and theoretical methods used to investigate magnetization dynamics. We presented a detailed characterization of the pulsed laser beams that we used and discussed the various approximations that are commonly made implicitly. The MOKE setups that we used were then presented and we explained why such methods allow us to probe magnetization even under non equilibrium conditions. The theoretical part aimed at providing a full (essentially semiclassical) treatment of magnetization dynamics in general heterostructures irradiated with ultrashort pulses of light. We extended the TMM to consider the absorption of laser pulses instead of monochromatic waves and extensively discussed why these types of ap-

proaches fundamentally lack physical sense because they sharply separate electromagnetic and electronic conserved quantities. We also presented Gridnev's model[92] of ultrafast magnetization dynamics which was then used to provide a slightly different derivation of Beens *et al.* model of ultrafast magnetization dynamics in ferromagnets. In particular, we obtained a generalized equation for the spin accumulation dynamics.

The remaining part of this thesis was then focused on experimental results together with simulations of them. First we considered GdFeCo/Cu/GdFeCo structures where we showed that spin currents due to ultrafast demagnetization modify the behavior of GdFeCo under single laser pulse irradiation. In particular, the RE dominant GdFeCo generates a spin current whose effect on the other GdFeCo is mostly determined by the gadolinium sublattice. Conversely, the gadolinium sublattice of the RE dominant layer is the one most sensitive to spin currents. This was explained by the fact that at high concentration of gadolinium, it is gadolinium that might polarize conduction electrons and not the TM sublattice. These results where shown to be consistent with measurements of exchange bias fields due to RKKY coupling. It is the TM sublattice of the TM dominant layer on the other hand that polarizes conduction electrons. We estimate in chapter 7 that the transition, which would correspond to the conduction electron spin polarization compensation composition, happens at $x_c \simeq 21\%$. It comes from Gridnev's model[92] of ferrimagnets that this compensation does not have to be the same as the magnetization compensation point[234]. This system is rather complex due to all the possible channels for the transfer of angular momentum. To simplify the problem, and also in prevision for more practical applications, we replaced the TM dominant GdFeCo by various ferromagnetic multilayers. We showed that by playing with Curie temperatures, one can tune the threshold fluence for the single pulse reversal of the ferromagnetic layer. This was explained by a 2TM with heat diffusion that is coupled to a model for light absorption and another one for ultrafast magnetization dynamics. Without fitting any parameter, we could explain the increase of threshold fluence with increasing Curie temperature of a [Co_xNi_{1-x}(1)/Pt(1)] multilayer or with increasing thickness of the interfacial cobalt layer in a [Co/Pt] multilayer. The impact of the spin current generated by GdFeCo could be directly tuned by changing the laser pulse duration and the spin current was shown to cause spin cooling i.e. increase of the magnetization amplitude due to spin currents. Another way to modify the spin current is to change the GdFeCo alloy composition. For 33% of gadolinium, we not only showed that no magnetization reversal of the ferrimagnetic alloy is required but also that higher spin current intensities lead to lower threshold fluences, which is another manifestation of spin cooling. The control of magnetism was pushed even further after we considered samples with copper spacer thicknesses up to 80 nm. There, we showed that one

can still achieve single shot magnetization reversal of the ferromagnetic layer even if there is no direct laser irradiation of the layer. Up to that point, the ultrafast dynamics of magnetization was deduced from the inability of other explanations to explain our experimental results. However in the last chapter, we used TR-MOKE microscopy to show that the magnetization reversal (zero crossing) happens in around 400 fs. A spin cooling of around 30% was observed after 50 ps, meaning that the spin current can enhance the magnetization by up to 30% compared to a sample with no spin current. Moreover this spin cooling is ultrafast and already becomes sizable after a few picoseconds. We were also able to qualitatively reproduce these results with a model that combines laser pulse absorption, a 2TM model with heat diffusion, a phenomenological model for the spin accumulation and Beens *et al.*[93] model of ultrafast magnetization dynamics for ferromagnets. This model also allowed us to understand the subpicosecond magnetization dynamics in P and AP magnetic configurations and in particular we could ascertain what was the role of the TM sublattice contribution to the spin accumulation.

Overall, we were able to manipulate magnetization of ferrimagnetic and ferromagnetic materials at the picosecond and subpicosecond timescales using light, heat and spin pulses. Our results could be explained by conservation of energy and angular momentum. However, several points remain unclear. The principle ones are: a complete understanding of the GdFeCo/Cu/[Co/Pt] sample for an alloy composition $x = 20\%$, the precise role of heating in the AO-HIS of GdFeCo, the magnetization dynamics for samples with a thick copper, whether one can increase the reversed magnetization amplitude of [Co/Pt] as observed in TR-MOKE microscopy (for instance by increasing the Curie temperature of the spin current amplitude) and what is the minimum delay between two consecutive pump laser pulses such that the magnetization reversal occurs for each pulse. Also, one should improve the presented model for the ultrafast magnetization dynamics such that it considers an improved 2TM (at least including the exchange of energy with localized spins) and also magnons. Indeed, we saw that our model does not reproduce the correct magnetization behavior around the [Co/Pt] switching threshold fluence. We explained this by the fact that we use a MFA. One would need to consider spin-spin correlations in order to consider non equilibrium of the spin system itself[86] on top of the out of equilibrium situation between individual spins and the electronic system. Also, because the magnetization reversal happens on timescales comparable with ultrafast demagnetization, it might be required to consider microscopic mechanisms for the spin lattice relaxation explicitly and not simply take it into account through a relaxation time approximation.

From a more practical point of view, we want to propose the design shown in figure 9.1. In this design, one uses two GdFeCo with a high gadolinium content (typically $x = 33\%$). They are

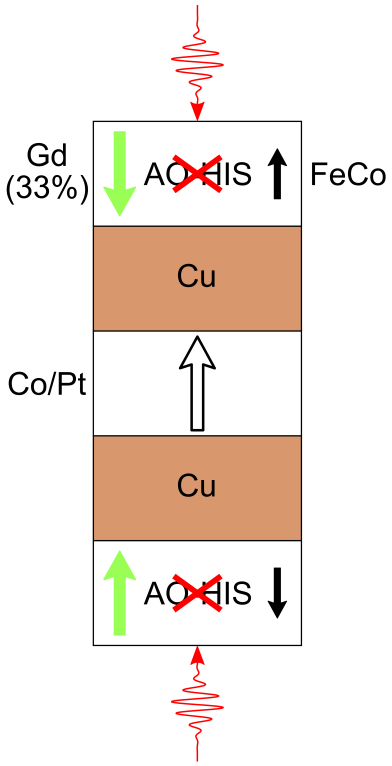

Figure 9.1: Proposed multilayer design for subpicosecond single pulse toggle switching of [Co/Pt].

positioned on each side of a Cu(10)/[Co/Pt]/Cu(10) multilayer. One then sets the magnetization of the GdFeCo layers such that their magnetizations are pointing in opposite directions. Then, exciting one GdFeCo layer or the other (the simplest way would be to send a laser pulse on one side of the sample or the other) one could generate a hot spin current of a given direction and thus set the magnetization of the ferromagnetic multilayer in the wanted direction. Because the threshold fluence of the [Co/Pt] multilayer can be made smaller than the ones of the GdFeCo layers, the direction of the magnetization would always be given by which GdFeCo layer one excites.

Bibliography

[1] Froning, F. N. *et al.* Ultrafast hole spin qubit with gate-tunable spin–orbit switch functionality. *Nature Nanotechnology* **16**, 308–312 (2021). URL https://doi.org/10.1038/s41565-020-00828-6.

[2] Landau, L. & Lifshitz, E. On the theory of the dispersion of magnetic permeability in ferromagnetic bodies. *Phys Z Sowjetunion* **8**, 153 (1935).

[3] Gilbert, T. L. A phenomenological theory of damping in ferromagnetic materials. *IEEE Transactions on Magnetics* **40**, 3443–3449 (2004). URL http://ieeexplore.ieee.org/lpdocs/epic03/wrapper.htm?arnumber=1353448. arXiv:1011.1669v3.

[4] Neeraj, K. *et al.* Inertial spin dynamics in ferromagnets. *Nature Physics* **17**, 245–250 (2021). URL http://www.nature.com/articles/s41567-020-01040-y.

[5] Tudosa, I. *et al.* The ultimate speed of magnetic switching in granular recording media. *Nature* **428**, 831–833 (2004). URL http://www.nature.com/articles/nature02438.

[6] Kimel, A. V. & Li, M. Writing magnetic memory with ultrashort light pulses. *Nature Reviews Materials* **4**, 189–200 (2019). URL http://www.nature.com/articles/s41578-019-0086-3.

[7] Chen, Z. & Wang, L.-W. Role of initial magnetic disorder: A time-dependent ab initio study of ultrafast demagnetization mechanisms. *Science Advances* **5**, eaau8000 (2019). URL https://advances.sciencemag.org/lookup/doi/10.1126/sciadv.aau8000.

[8] Siegrist, F. *et al.* Light-wave dynamic control of magnetism. *Nature* **571**, 240–244 (2019). URL https://doi.org/10.1038/s41586-019-1333-x.

[9] Radu, I. *et al.* Transient ferromagnetic-like state mediating ultrafast reversal of antiferromagnetically coupled spins. *Nature* **472**, 205–208 (2011). URL http://www.nature.com/articles/nature09901.

[10] Graves, C. E. *et al.* Nanoscale spin reversal by non-local angular momentum transfer following ultrafast laser excitation in ferrimagnetic GdFeCo. *Nature Materials* **12**, 293–298 (2013). URL http://www.nature.com/articles/nmat3597.

[11] Heitler, W. *The Quantum Theory of Radiation* (Clarendon Press, Oxford, 1954), 3rd edn.

[12] Schwartz, M. D. *Quantum field theory and the standard model* (Cambridge University Press, 2014).

[13] Peskin, M. E. & Schroeder, D. V. *An introduction to quantum field theory* (CRC Press, 2018).

[14] Weinberg, S. *The quantum theory of fields (Vol. 1)* (Cambridge university press, 1995).

[15] Kamenev, A. *Field Theory of Non-Equilibrium Systems* (Cambridge University Press, Cambridge, 2011).

[16] Villars, F. On the Energy-Momentum Tensor of the Electron. *Physical Review* **79**, 122–128 (1950). URL https://link.aps.org/doi/10.1103/PhysRev.79.122.

[17] Streib, S. Difference between angular momentum and pseudoangular momentum. *Physical Review B* **103**, L100409 (2021). URL https://link.aps.org/doi/10.1103/PhysRevB.103.L100409. 2010.15616.

[18] Ohanian, H. C. What is spin? *American Journal of Physics* **54**, 500–505 (1986). URL http://aapt.scitation.org/doi/10.1119/1.14580. 0308027.

[19] Mcdonald, K. T. Bibliography on the Abraham-Minkowski Debate. Tech. Rep. (2017). URL http://kirkmcd.princeton.edu/examples/EM/poynting_pm_9_169_05.pdf.

[20] Campos, I. & Jimenez, J. L. About Poynting's theorem. *European Journal of Physics* **13**, 117–121 (1992). URL https://iopscience.iop.org/article/10.1088/0143-0807/13/3/003.

[21] Nolting, W. & Ramakanth, A. *Quantum Theory of Magnetism* (Springer Berlin Heidelberg, Berlin, Heidelberg, 2009). URL http://link.springer.com/10.1007/978-3-540-85416-6.

[22] Blum, K. *Density Matrix Theory and Applications*, vol. 64 of *Springer Series on Atomic, Optical, and Plasma Physics* (Springer Berlin Heidelberg, Berlin, Heidelberg, 2012), 3rd edn. URL http://link.springer.com/10.1007/978-3-642-20561-3.

[23] Mondal, R. *Relativistic theory of laser-induced magnetization dynamics*. Ph.D. thesis, Uppsala Universitet (2017).

[24] Berestetskii, V. B., Pitaevskii, L. P. & Lifshitz, E. *Quantum Electrodynamics* (Elsevier, 1982), 2nd edn.

[25] Greiner, W. *Relativistic Quantum Mechanics. Wave Equations* (Springer Berlin Heidelberg, Berlin, Heidelberg, 2000), third edn. URL http://link.springer.com/10.1007/978-3-662-04275-5.

[26] Zawadzki, W. On the v2/c2 expansion of the Dirac equation with external potentials. *American Journal of Physics* **73**, 756–758 (2005). URL http://aapt.scitation.org/doi/10.1119/1.1927548. 0408065.

[27] Hickey, M. C. & Moodera, J. S. Origin of Intrinsic Gilbert Damping. *Physical Review Letters* **102**, 137601 (2009). URL https://link.aps.org/doi/10.1103/PhysRevLett.102.137601. 0812.3184.

[28] Hinschberger, Y. & Hervieux, P.-A. Foldy–Wouthuysen transformation applied to the interaction of an electron with ultrafast electromagnetic fields. *Physics Letters A* **376**, 813–819 (2012). URL https://linkinghub.elsevier.com/retrieve/pii/S0375960112000485.

[29] Mahan, G. D. *Many-Particle Physics* (Springer Science & Business Media., 2000), 3rd edn.

[30] Landau, L. & Lifshitz, E. *Quantum Mechanics* (Elsevier, 1977), 3rd edn. URL https://linkinghub.elsevier.com/retrieve/pii/C20130027934.

[31] Grimvall, G. *The Electron-Phonon Interaction in Metals* (North-Holland Publishing Co., Amsterdam, New York, Oxford, 1981).

[32] Kittel, C. *Quantum theory of solids* (John Wiley & Sons, 1987).

[33] Fetter, A. L. & Walecka, J. D. *Quantum theory of many-particle systems* (McGraw-Hill, 1971).

[34] Mattuck, R. D. *A Guide to Feynman Diagrams in the Many-Body Problem* (Dover Publications, New York, 1992), 2nd edn.

[35] Baral, A., Vollmar, S., Kaltenborn, S. & Schneider, H. C. Re-examination of the Elliott–Yafet spin-relaxation mechanism. *New Journal of Physics* **18**, 023012 (2016). URL https://iopscience.iop.org/article/10.1088/1367-2630/18/2/023012.

[36] Belitz, D. & Kirkpatrick, T. R. Quantum electrodynamics and the origins of the exchange, dipole-dipole, and Dzyaloshinsky-Moriya interactions in itinerant fermion systems. *Physical Review B* **81**, 184419 (2010). URL https://link.aps.org/doi/10.1103/PhysRevB.81.184419. 1002.2008.

[37] Müller, T., Sharma, S., Gross, E. K. U. & Dewhurst, J. K. Extending Solid-State Calculations to Ultra-Long-Range Length Scales. *Physical Review Letters* **125**, 256402 (2020). URL https://link.aps.org/doi/10.1103/PhysRevLett.125.256402.

[38] Huang, K. *Statistical Mechanics, 2nd Edition* (John Wiley & Sons, 1987), 2nd edn.

[39] Iotti, R. C., Ciancio, E. & Rossi, F. Quantum transport theory for semiconductor nanostructures: A density-matrix formulation. *Physical Review B* **72**, 125347 (2005). URL https://link.aps.org/doi/10.1103/PhysRevB.72.125347. 0509054.

[40] Snoke, D., Liu, G. & Girvin, S. The basis of the Second Law of thermodynamics in quantum field theory. *Annals of Physics* **327**, 1825–1851 (2012). URL https://linkinghub.elsevier.com/retrieve/pii/S0003491611002211. 1112.3009.

[41] Zurek, W. H. Decoherence and the Transition from Quantum to Classical — Revisited. In *Quantum Decoherence*, vol. 48, 1–31 (Birkhäuser Basel, Basel, 2006). URL http://link.springer.com/10.1007/978-3-7643-7808-0_1. 0306072.

[42] Maciejko, J. An Introduction to Nonequilibrium Many-Body Theory (2007). URL http://www.physics.arizona.edu/$\sim$stafford/Courses/560A/nonequilibrium.pdf.

[43] Haug, H. J. W. & Jauho, A.-P. *Quantum Kinetics in Transport and Optics of Semiconductors*, vol. 123 of *Solid-State Sciences* (Springer Berlin Heidelberg, Berlin, Heidelberg, 2008). URL http://link.springer.com/10.1007/978-3-540-73564-9.

[44] Wagner, M. Expansions of nonequilibrium Green's functions. *Physical Review B* **44**, 6104–6117 (1991). URL https://link.aps.org/doi/10.1103/PhysRevB.44.6104.

[45] Jackson, J. D. *Classical Electrodynamics* (John Wiley & Sons, 1999), 3rd edn.

[46] Landau, L. & Lifshitz, E. *Electrodynamics of Continuous Media* (Elsevier, 1984).

[47] Kaganov, M., Lifshitz, I. & Tanatarov, L. Relaxation between Electrons and the Crystalline Lattice. *Soviet Physics JETP* **4**, 173–178 (1955). URL http://www.jetp.ac.ru/cgi-bin/e/index/e/4/2/p173?a=list.

[48] Anisimov, S., Kapeliovich, B. & Perel'man, T. Electron emission from metal surfaces exposed to ultrashort laser pulses. *Soviet Physics JETP* **39**, 776–781 (1974). URL http://www.jetp.ac.ru/cgi-bin/e/index/e/39/2/p375?a=list.

[49] Chen, J., Tzou, D. & Beraun, J. A semiclassical two-temperature model for ultrafast laser heating. *International Journal of Heat and Mass Transfer* **49**, 307–316 (2006). URL https://linkinghub.elsevier.com/retrieve/pii/S001793100500445X.

[50] Qiu, T. Q. & Tien, C. L. Heat Transfer Mechanisms During Short-Pulse Laser Heating of Metals. *Journal of Heat Transfer* **115**, 835–841 (1993). URL https://asmedigitalcollection.asme.org/heattransfer/article/115/4/835/411500/Heat-Transfer-Mechanisms-During-ShortPulse-Laser.

[51] Ashcroft, N. W. & Mermin, N. D. *Solid State Physics* (Saunders College Publishing, 1976).

[52] Allen, P. B. Theory of thermal relaxation of electrons in metals. *Physical Review Letters* **59**, 1460–1463 (1987). URL https://link.aps.org/doi/10.1103/PhysRevLett.59.1460.

[53] Schilp, J., Kuhn, T. & Mahler, G. Electron-phonon quantum kinetics in pulse-excited semiconductors: Memory and renormalization effects. *Physical Review B* **50**, 5435–5447 (1994). URL https://link.aps.org/doi/10.1103/PhysRevB.50.5435.

[54] Byrnes, S. J. Multilayer optical calculations arXiv:1603.02720 [physics.comp–ph] (2016). URL http://arxiv.org/abs/1603.02720. 1603.02720.

[55] Lin, Z., Zhigilei, L. V. & Celli, V. Electron-phonon coupling and electron heat capacity of metals under conditions of strong electron-phonon nonequilibrium. *Physical Review B - Condensed Matter and Materials Physics* **77**, 075133 (2008). URL https://link.aps.org/doi/10.1103/PhysRevB.77.075133.

[56] Scheid, P., Malinowski, G., Mangin, S. & Lebègue, S. Ab initio study of electronic temperature effects on magnetic materials properties. *Physical Review B* **99**, 174415 (2019). URL https://link.aps.org/doi/10.1103/PhysRevB.99.174415.

[57] Fann, W. S., Storz, R., Tom, H. W. K. & Bokor, J. Direct measurement of nonequilibrium electron-energy distributions in subpicosecond laser-heated gold films. *Physical Review Letters* **68**, 2834–2837 (1992). URL https://link.aps.org/doi/10.1103/PhysRevLett.68.2834.

[58] Sun, C.-K., Vallée, F., Acioli, L. H., Ippen, E. P. & Fujimoto, J. G. Femtosecond-tunable measurement of electron thermalization in gold. *Physical Review B* **50**, 15337–15348 (1994). URL https://link.aps.org/doi/10.1103/PhysRevB.50.15337.

[59] Del Fatti, N. *et al.* Nonequilibrium electron dynamics in noble metals. *Physical Review B* **61**, 16956–16966 (2000). URL https://link.aps.org/doi/10.1103/PhysRevB.61.16956.

[60] Carpene, E. Ultrafast laser irradiation of metals: Beyond the two-temperature model. *Physical Review B* **74**, 024301 (2006). URL https://link.aps.org/doi/10.1103/PhysRevB.74.024301.

[61] Shim, J. H. *et al.* Role of non-thermal electrons in ultrafast spin dynamics of ferromagnetic multilayer. *Scientific Reports* **10** (2020). URL https://doi.org/10.1038/s41598-020-63452-3.

[62] Maldonado, P., Carva, K., Flammer, M. & Oppeneer, P. M. Theory of out-of-equilibrium ultrafast relaxation dynamics in metals. *Physical Review B* **96**, 174439 (2017). URL https://link.aps.org/doi/10.1103/PhysRevB.96.174439. 1708.01470.

[63] Ritzmann, U., Oppeneer, P. M. & Maldonado, P. Theory of out-of-equilibrium electron and phonon dynamics in metals after femtosecond laser excitation. *Physical Review B*

102, 214305 (2020). URL https://link.aps.org/doi/10.1103/PhysRevB.102.214305. 1911.12414.

[64] Hohlfeld, J., Grosenick, D., Conrad, U. & Matthias, E. Femtosecond time-resolved reflection second-harmonic generation on polycrystalline copper. *Applied Physics A Materials Science and Processing* **60**, 137–142 (1995). URL http://link.springer.com/10.1007/BF01538238.

[65] Hohlfeld, J. *et al.* Electron and lattice dynamics following optical excitation of metals. *Chemical Physics* **251**, 237–258 (2000). URL https://linkinghub.elsevier.com/retrieve/pii/S0301010499003304.

[66] J. K. Chen, J. E. B. NUMERICAL STUDY OF ULTRASHORT LASER PULSE INTERACTIONS WITH METAL FILMS. *Numerical Heat Transfer, Part A: Applications* **40**, 1–20 (2001). URL http://www.tandfonline.com/doi/abs/10.1080/104077801300348842.

[67] Metzler, R. & Klafter, J. The random walk's guide to anomalous diffusion: a fractional dynamics approach. *Physics Reports* **339**, 1–77 (2000). URL https://linkinghub.elsevier.com/retrieve/pii/S0370157300000703.

[68] Majlis, N. *The quantum theory of magnetism, second edition* (World Scientific, 2007), 2nd edn.

[69] Mentink, J. H., Katsnelson, M. I. & Lemeshko, M. Quantum many-body dynamics of the Einstein–de Haas effect. *Physical Review B* **99**, 064428 (2019). URL https://link.aps.org/doi/10.1103/PhysRevB.99.064428. 1802.01638.

[70] Mitchell, A. H. Ferromagnetic Relaxation by the Exchange Interaction between Ferromagnetic Electrons and Conduction Electrons. *Physical Review* **105**, 1439–1444 (1957). URL https://link.aps.org/doi/10.1103/PhysRev.105.1439.

[71] Auerbach, A. & Arovas, D. P. Schwinger Bosons Approaches to Quantum Antiferromagnetism (2008). URL https://arxiv.org/abs/0809.4836v2. 0809.4836.

[72] Manchon, A., Li, Q., Xu, L. & Zhang, S. Theory of laser-induced demagnetization at high temperatures. *Physical Review B* **85**, 064408 (2012). URL https://link.aps.org/doi/10.1103/PhysRevB.85.064408. 1112.2428.

[73] Cywiński, Ł. & Sham, L. J. Ultrafast demagnetization in the sp-d model: A theoretical study. *Physical Review B* **76**, 045205 (2007). URL https://link.aps.org/doi/10.1103/PhysRevB.76.045205.

[74] Hertz, J. A. & Edwards, D. M. Electron-magnon interactions in itinerant ferromagnetism. I. Formal theory. *Journal of Physics F: Metal Physics* **3**, 2174–2190 (1973). URL https://iopscience.iop.org/article/10.1088/0305-4608/3/12/018.

[75] Müller, M. C., Blügel, S. & Friedrich, C. Electron-magnon scattering in elementary ferromagnets from first principles: Lifetime broadening and band anomalies. *Physical Review B* **100**, 045130 (2019). URL https://link.aps.org/doi/10.1103/PhysRevB.100.045130. 1809.02395.

[76] Cleveland, C. L. & Medina A., R. Obtaining a Heisenberg Hamiltonian from the Hubbard model. *American Journal of Physics* **44**, 44–46 (1976). URL http://aapt.scitation.org/doi/10.1119/1.10537.

[77] Balucani, U. & Stasch, A. Magnon-phonon and exciton-phonon interactions in FeCl2. *Journal of Magnetism and Magnetic Materials* **54-57**, 1157–1158 (1986). URL https://linkinghub.elsevier.com/retrieve/pii/0304885386907614.

[78] Streib, S., Vidal-Silva, N., Shen, K. & Bauer, G. E. W. Magnon-phonon interactions in magnetic insulators. *Physical Review B* **99**, 184442 (2019). URL https://link.aps.org/doi/10.1103/PhysRevB.99.184442. 1906.01042.

[79] Harrison, R. G. Calculating the spontaneous magnetization and defining the Curie temperature using a positive-feedback model. *Journal of Applied Physics* **115**, 033901 (2014). URL http://aip.scitation.org/doi/10.1063/1.4861869.

[80] Tannous, C. & Gieraltowski, J. A Stoner–Wohlfarth model Redux: Static properties. *Physica B: Condensed Matter* **403**, 3563–3570 (2008). URL https://linkinghub.elsevier.com/retrieve/pii/S0921452608002482.

[81] Tannous, C. & Gieraltowski, J. A Stoner–Wohlfarth model redux: Dynamic and statistical properties. *Physica B: Condensed Matter* **403**, 3578–3584 (2008). URL https://linkinghub.elsevier.com/retrieve/pii/S0921452608002500.

[82] Exl, L., Suess, D. & Schrefl, T. Micromagnetism. URL https://homepage.univie.ac.at/lukas.exl/files/mic_intro.pdf.

[83] Stiles, M. D. & Zangwill, A. Anatomy of spin-transfer torque. *Physical Review B* **66**, 014407 (2002). URL https://link.aps.org/doi/10.1103/PhysRevB.66.014407. 0202397.

[84] Atxitia, U., Hinzke, D. & Nowak, U. Fundamentals and applications of the Landau–Lifshitz–Bloch equation. *Journal of Physics D: Applied Physics* **50**, 033003 (2017). URL https://iopscience.iop.org/article/10.1088/1361-6463/50/3/033003.

[85] Skubic, B., Hellsvik, J., Nordström, L. & Eriksson, O. A method for atomistic spin dynamics simulations: implementation and examples. *Journal of Physics: Condensed Matter* **20**, 315203 (2008). URL https://iopscience.iop.org/article/10.1088/0953-8984/20/31/315203. 0806.1582.

[86] Kazantseva, N., Nowak, U., Chantrell, R. W., Hohlfeld, J. & Rebei, A. Slow recovery of the magnetisation after a sub-picosecond heat pulse. *EPL (Europhysics Letters)* **81**, 27004 (2008). URL https://iopscience.iop.org/article/10.1209/0295-5075/81/27004.

[87] Garanin, D. A. Fokker-Planck and Landau-Lifshitz-Bloch equations for classical ferromagnets. *Physical Review B* **55**, 3050–3057 (1997). URL https://link.aps.org/doi/10.1103/PhysRevB.55.3050. 9805054.

[88] Kazantseva, N. *et al.* Towards multiscale modeling of magnetic materials: Simulations of FePt. *Physical Review B* **77**, 184428 (2008). URL https://link.aps.org/doi/10.1103/PhysRevB.77.184428.

[89] Hinzke, D. *et al.* Multiscale modeling of ultrafast element-specific magnetization dynamics of ferromagnetic alloys. *Physical Review B* **92**, 054412 (2015). URL https://link.aps.org/doi/10.1103/PhysRevB.92.054412. 1504.00199.

[90] Bloch, F. Nuclear Induction. *Physical Review* **70**, 460–474 (1946). URL https://link.aps.org/doi/10.1103/PhysRev.70.460.

[91] Garanin, D. Generalized equation of motion for a ferromagnet. *Physica A: Statistical Mechanics and its Applications* **172**, 470–491 (1991). URL https://linkinghub.elsevier.com/retrieve/pii/037843719190395S.

[92] Gridnev, V. N. Ultrafast heating-induced magnetization switching in ferrimagnets. *Journal of Physics: Condensed Matter* **28**, 476007 (2016). URL https://iopscience.iop.org/article/10.1088/0953-8984/28/47/476007.

[93] Beens, M., Duine, R. A. & Koopmans, B. S-d model for local and nonlocal spin dynamics in laser-excited magnetic heterostructures. *Physical Review B* **102**, 054442 (2020). URL https://doi.org/10.1103/PhysRevB.102.054442. 2005.03905.

[94] Xu, L. & Zhang, S. Magnetization dynamics at elevated temperatures. *Physica E: Low-dimensional Systems and Nanostructures* **45**, 72–76 (2012). URL https://linkinghub.elsevier.com/retrieve/pii/S1386947712002743.

[95] Xu, L. & Zhang, S. Self-consistent Bloch equation and Landau-Lifshitz-Bloch equation of ferromagnets: A comparison. *Journal of Applied Physics* **113**, 163911 (2013). URL http://dx.doi.org/10.1063/1.4803150].

[96] Fähnle, M. Comparison of theories of fast and ultrafast magnetization dynamics. *Journal of Magnetism and Magnetic Materials* **469**, 28–29 (2019). URL https://linkinghub.elsevier.com/retrieve/pii/S0304885318313258.

[97] Beaurepaire, E., Merle, J.-C., Daunois, A. & Bigot, J.-Y. Ultrafast Spin Dynamics in Ferromagnetic Nickel. *Physical Review Letters* **76**, 4250–4253 (1996). URL https://link.aps.org/doi/10.1103/PhysRevLett.76.4250.

[98] Hohlfeld, J., Matthias, E., Knorren, R. & Bennemann, K. H. Nonequilibrium Magnetization Dynamics of Nickel. *Physical Review Letters* **78**, 4861–4864 (1997). URL https://link.aps.org/doi/10.1103/PhysRevLett.78.4861.

[99] Conrad, U., Güdde, J., Jähnke, V. & Matthias, E. Ultrafast electron and magnetization dynamics of thin Ni and Co films on Cu(001) observed by time-resolved SHG. *Applied Physics B: Lasers and Optics* **68**, 511–517 (1999). URL http://link.springer.com/10.1007/s003400050658.

[100] Scholl, A., Baumgarten, L., Jacquemin, R. & Eberhardt, W. Ultrafast Spin Dynamics of Ferromagnetic Thin Films Observed by fs Spin-Resolved Two-Photon Photoemission. *Physical Review Letters* **79**, 5146–5149 (1997). URL https://link.aps.org/doi/10.1103/PhysRevLett.79.5146.

[101] Stamm, C. *et al.* Femtosecond modification of electron localization and transfer of angular momentum in nickel. *Nature Materials* **6**, 740–743 (2007). URL http://www.nature.com/articles/nmat1985.

[102] Agranat, M., Ashitkov, S., Granovskii, A. & Rukman, G. Interaction of picosecond laser pulses with the electron, spin, and phonon subsystems of nickel. *Zh. Eksp. Teor. Fiz* **86**, 10 (1984). URL http://www.jetp.ac.ru/cgi-bin/e/index/e/59/4/p804?a=list.

[103] Vaterlaus, A., Beutler, T. & Meier, F. Spin-lattice relaxation time of ferromagnetic gadolinium determined with time-resolved spin-polarized photoemission. *Physical Review Letters* **67**, 3314–3317 (1991). URL https://link.aps.org/doi/10.1103/PhysRevLett.67.3314.

[104] Melnikov, A. *et al.* Nonequilibrium Magnetization Dynamics of Gadolinium Studied by Magnetic Linear Dichroism in Time-Resolved 4f Core-Level Photoemission. *Physical Review Letters* **100**, 107202 (2008). URL https://link.aps.org/doi/10.1103/PhysRevLett.100.107202.

[105] Wietstruk, M. *et al.* Hot-Electron-Driven Enhancement of Spin-Lattice Coupling in Gd and Tb 4f Ferromagnets Observed by Femtosecond X-Ray Magnetic Circular Dichroism. *Physical Review Letters* **106**, 127401 (2011). URL https://link.aps.org/doi/10.1103/PhysRevLett.106.127401. 1010.1374.

[106] Frietsch, B. *et al.* The role of ultrafast magnon generation in the magnetization dynamics of rare-earth metals. *Science Advances* **6**, eabb1601 (2020). URL https://advances.sciencemag.org/lookup/doi/10.1126/sciadv.abb1601.

[107] Koopmans, B. *et al.* Explaining the paradoxical diversity of ultrafast laser-induced demagnetization. *Nature Materials* **9**, 259–265 (2010). URL http://www.nature.com/articles/nmat2593.

[108] Eich, S. *et al.* Band structure evolution during the ultrafast ferromagnetic-paramagnetic phase transition in cobalt. *Science Advances* **3** (2017). URL http://advances.sciencemag.org/.

[109] Haag, M., Illg, C. & Fähnle, M. Theory of scattering of crystal electrons at magnons. *Physical Review B* **87**, 214427 (2013). URL https://link.aps.org/doi/10.1103/PhysRevB.87.214427.

[110] Scheid, P. *Investigation of light – induced ultrafast magnetization dynamics using ab initio methods*. Ph.D. thesis, Université de Lorraine (2020).

[111] Fähnle, M. & Illg, C. Electron theory of fast and ultrafast dissipative magnetization dynamics. *Journal of Physics: Condensed Matter* **23**, 493201 (2011). URL https://iopscience.iop.org/article/10.1088/0953-8984/23/49/493201.

[112] Fähnle, M., Haag, M. & Illg, C. Is the angular momentum of a ferromagnetic sample after exposure to a fs laser pulse conserved? *Journal of Magnetism and Magnetic Materials* **347**, 45–46 (2013). URL https://linkinghub.elsevier.com/retrieve/pii/S0304885313005404.

[113] Illg, C., Haag, M. & Fähnle, M. Ultrafast demagnetization after laser irradiation in transition metals: Ab initio calculations of the spin-flip electron-phonon scattering with reduced exchange splitting. *Physical Review B* **88**, 214404 (2013). URL https://link.aps.org/doi/10.1103/PhysRevB.88.214404.

[114] Fähnle, M. Review of Ultrafast Demagnetization After Femtosecond Laser Pulses: A Complex Interaction of Light with Quantum Matter. *American Journal of Modern Physics* **7**, 68 (2018). URL http://www.sciencepublishinggroup.com/journal/paperinfo?journalid=122&doi=10.11648/j.ajmp.20180702.12.

[115] Dornes, C. *et al.* The ultrafast Einstein–de Haas effect. *Nature* **565**, 209–212 (2019). URL http://www.nature.com/articles/s41586-018-0822-7. 1804.07159.

[116] Zhang, W. *et al.* Ultrafast terahertz magnetometry. *Nature Communications* **11**, 4247 (2020). URL http://www.nature.com/articles/s41467-020-17935-6.

[117] Kanda, N. *et al.* The vectorial control of magnetization by light. *Nature Communications* **2**, 362 (2011). URL http://www.nature.com/articles/ncomms1366.

[118] Elliott, R. J. Theory of the Effect of Spin-Orbit Coupling on Magnetic Resonance in Some Semiconductors. *Physical Review* **96**, 266–279 (1954). URL https://link.aps.org/doi/10.1103/PhysRev.96.266.

[119] Yafet, Y. g Factors and Spin-Lattice Relaxation of Conduction Electrons. *Solid State Physics - Advances in Research and Applications* **14**, 1–98 (1963). URL https://linkinghub.elsevier.com/retrieve/pii/S0081194708602593.

[120] Bergeard, N. *et al.* Ultrafast angular momentum transfer in multisublattice ferrimagnets. *Nature Communications* **5**, 3466 (2014). URL http://www.nature.com/articles/ncomms4466.

[121] Zhang, L. & Niu, Q. Angular Momentum of Phonons and the Einstein–de Haas Effect. *Physical Review Letters* **112**, 085503 (2014). URL https://link.aps.org/doi/10.1103/PhysRevLett.112.085503. 1308.6036.

[122] Garanin, D. A. & Chudnovsky, E. M. Angular momentum in spin-phonon processes. *Physical Review B* **92**, 024421 (2015). URL https://link.aps.org/doi/10.1103/PhysRevB.92.024421. 1505.08057.

[123] Nakane, J. J. & Kohno, H. Angular momentum of phonons and its application to single-spin relaxation. *Physical Review B* **97**, 174403 (2018). URL https://link.aps.org/doi/10.1103/PhysRevB.97.174403.

[124] Fähnle, M. *et al.* Ultrafast Demagnetization After Femtosecond Laser Pulses: Transfer of Angular Momentum from the Electronic System to Magnetoelastic Spin-Phonon Modes. *Journal of Superconductivity and Novel Magnetism* **30**, 1381–1387 (2017). URL http://link.springer.com/10.1007/s10948-016-3950-z.

[125] Hennecke, M. *et al.* Angular Momentum Flow During Ultrafast Demagnetization of a Ferrimagnet. *Physical Review Letters* **122**, 157202 (2019). URL https://link.aps.org/doi/10.1103/PhysRevLett.122.157202.

[126] Krauß, M. *et al.* Ultrafast demagnetization of ferromagnetic transition metals: The role of the Coulomb interaction. *Physical Review B* **80**, 180407 (2009). URL https://link.aps.org/doi/10.1103/PhysRevB.80.180407.

[127] Haag, M., Illg, C. & Fähnle, M. Role of electron-magnon scatterings in ultrafast demagnetization. *Physical Review B* **90**, 014417 (2014). URL https://link.aps.org/doi/10.1103/PhysRevB.90.014417.

[128] Tveten, E. G., Brataas, A. & Tserkovnyak, Y. Electron-magnon scattering in magnetic heterostructures far out of equilibrium. *Physical Review B* **92**, 180412 (2015). URL https://link.aps.org/doi/10.1103/PhysRevB.92.180412. 1504.00511.

[129] Dewhurst, J. K., Elliott, P., Shallcross, S., Gross, E. K. U. & Sharma, S. Laser-Induced Intersite Spin Transfer. *Nano Letters* **18**, 1842–1848 (2018). URL https://pubs.acs.org/doi/10.1021/acs.nanolett.7b05118.

[130] Hofherr, M. *et al.* Induced versus intrinsic magnetic moments in ultrafast magnetization dynamics. *Physical Review B* **98**, 174419 (2018). URL https://link.aps.org/doi/10.1103/PhysRevB.98.174419.

[131] Borchert, M. *et al.* Manipulation of ultrafast demagnetization dynamics by optically induced intersite spin transfer in magnetic compounds with distinct density of states (2020). URL http://arxiv.org/abs/2008.12612. 2008.12612.

[132] Willems, F. *et al.* Optical inter-site spin transfer probed by energy and spin-resolved transient absorption spectroscopy. *Nature Communications* **11**, 871 (2020). URL http://www.nature.com/articles/s41467-020-14691-5.

[133] Hofherr, M. *et al.* Ultrafast optically induced spin transfer in ferromagnetic alloys. *Science Advances* **6**, eaay8717 (2020). URL https://advances.sciencemag.org/lookup/doi/10.1126/sciadv.aay8717.

[134] Shokeen, V. *et al.* Spin Flips versus Spin Transport in Nonthermal Electrons Excited by Ultrashort Optical Pulses in Transition Metals. *Physical Review Letters* **119**, 107203 (2017). URL https://link.aps.org/doi/10.1103/PhysRevLett.119.107203.

[135] Turgut, E. *et al.* Stoner versus Heisenberg: Ultrafast exchange reduction and magnon generation during laser-induced demagnetization. *Physical Review B* **94**, 220408 (2016). URL https://link.aps.org/doi/10.1103/PhysRevB.94.220408.

[136] Tengdin, P. *et al.* Critical behavior within 20 fs drives the out-of-equilibrium laser-induced magnetic phase transition in nickel. *Science Advances* **4**, eaap9744 (2018). URL https://advances.sciencemag.org/lookup/doi/10.1126/sciadv.aap9744.

[137] Młyńczak, E. *et al.* Kink far below the Fermi level reveals new electron-magnon scattering channel in Fe. *Nature Communications* **10**, 505 (2019). URL http://www.nature.com/articles/s41467-019-08445-1. 1808.02682.

[138] Schellekens, A. J. & Koopmans, B. Comparing Ultrafast Demagnetization Rates Between Competing Models for Finite Temperature Magnetism. *Physical Review Letters* **110**, 217204 (2013). URL https://link.aps.org/doi/10.1103/PhysRevLett.110.217204.

[139] Mueller, B. Y. *et al.* Feedback Effect during Ultrafast Demagnetization Dynamics in Ferromagnets. *Physical Review Letters* **111**, 167204 (2013). URL https://link.aps.org/doi/10.1103/PhysRevLett.111.167204.

[140] Mueller, B. Y. & Rethfeld, B. Thermodynamic μT model of ultrafast magnetization dynamics. *Physical Review B* **90**, 144420 (2014). URL https://link.aps.org/doi/10.1103/PhysRevB.90.144420.

[141] Töws, W. & Pastor, G. M. Many-Body Theory of Ultrafast Demagnetization and Angular Momentum Transfer in Ferromagnetic Transition Metals. *Physical Review Letters* **115**, 217204 (2015). URL https://link.aps.org/doi/10.1103/PhysRevLett.115.217204. 1508.00983.

[142] Weng, W. *et al.* Unexpectedly marginal effect of electronic correlations on ultrafast demagnetization after femtosecond laser-pulse excitation. *Physical Review B* **95**, 224439 (2017). URL http://link.aps.org/doi/10.1103/PhysRevB.95.224439.

[143] Acharya, S. R., Turkowski, V., Zhang, G. P. & Rahman, T. S. Ultrafast Electron Correlations and Memory Effects at Work: Femtosecond Demagnetization in Ni. *Physical Review Letters* **125**, 017202 (2020). URL https://doi.org/10.1103/PhysRevLett.125.017202%0Ahttps://link.aps.org/doi/10.1103/PhysRevLett.125.017202.

[144] Mueller, B. Y. & Rethfeld, B. Relaxation dynamics in laser-excited metals under nonequilibrium conditions. *Physical Review B* **87**, 035139 (2013). URL https://link.aps.org/doi/10.1103/PhysRevB.87.035139.

[145] Krieger, K., Dewhurst, J. K., Elliott, P., Sharma, S. & Gross, E. K. U. Laser-Induced Demagnetization at Ultrashort Time Scales: Predictions of TDDFT. *Journal of Chemical Theory and Computation* **11**, 4870–4874 (2015). URL https://pubs.acs.org/doi/10.1021/acs.jctc.5b00621.

[146] Secchi, A., Brener, S., Lichtenstein, A. & Katsnelson, M. Non-equilibrium magnetic interactions in strongly correlated systems. *Annals of Physics* **333**, 221–271 (2013). URL https://linkinghub.elsevier.com/retrieve/pii/S0003491613000547. 1212.3671.

[147] Secchi, A., Lichtenstein, A. & Katsnelson, M. Magnetic interactions in strongly correlated systems: Spin and orbital contributions. *Annals of Physics* **360**, 61–97 (2015). URL https://linkinghub.elsevier.com/retrieve/pii/S0003491615001864.

[148] Secchi, A., Lichtenstein, A. I. & Katsnelson, M. I. Nonequilibrium itinerant-electron magnetism: A time-dependent mean-field theory. *Physical Review B* **94**, 085153 (2016). URL https://link.aps.org/doi/10.1103/PhysRevB.94.085153.

[149] Frietsch, B. *et al.* Disparate ultrafast dynamics of itinerant and localized magnetic moments in gadolinium metal. *Nature Communications* **6**, 8262 (2015). URL http://www.nature.com/articles/ncomms9262.

[150] Nieves, P., Serantes, D., Atxitia, U. & Chubykalo-Fesenko, O. Quantum Landau-Lifshitz-Bloch equation and its comparison with the classical case. *Physical Review B* **90**, 104428 (2014). URL https://link.aps.org/doi/10.1103/PhysRevB.90.104428. 1404.6922.

[151] Ma, P.-W., Dudarev, S. L. & Woo, C. H. Spin-lattice-electron dynamics simulations of magnetic materials. *Physical Review B* **85**, 184301 (2012). URL https://link.aps.org/doi/10.1103/PhysRevB.85.184301.

[152] Strungaru, M. *et al.* Spin-lattice dynamics model with angular momentum transfer for canonical and microcanonical ensembles. *Physical Review B* **103**, 024429 (2021). URL https://link.aps.org/doi/10.1103/PhysRevB.103.024429.

[153] Brataas, A., Bauer, G. & Kelly, P. Non-collinear magnetoelectronics. *Physics Reports* **427**, 157–255 (2006). URL https://linkinghub.elsevier.com/retrieve/pii/S0370157306000238.

[154] Berger, L. Emission of spin waves by a magnetic multilayer traversed by a current. *Physical Review B* **54**, 9353–9358 (1996). URL https://link.aps.org/doi/10.1103/PhysRevB.54.9353.

[155] Slonczewski, J. Current-driven excitation of magnetic multilayers. *Journal of Magnetism and Magnetic Materials* **159**, L1–L7 (1996). URL https://linkinghub.elsevier.com/retrieve/pii/0304885396000625.

[156] Schellekens, A. J., Kuiper, K. C., de Wit, R. & Koopmans, B. Ultrafast spin-transfer torque driven by femtosecond pulsed-laser excitation. *Nature Communications* **5**, 4333 (2014). URL http://www.nature.com/articles/ncomms5333.

[157] Lichtenberg, T., Beens, M., Jansen, M. H., Duine, R. A. & Koopmans, B. Probing optical spin-currents using THz spin-waves in noncollinear magnetic bilayers (2021). URL http://arxiv.org/abs/2103.06029. 2103.06029.

[158] Diao, Z. *et al.* Spin-transfer torque switching in magnetic tunnel junctions and spin-transfer torque random access memory. *Journal of Physics: Condensed Mat-*

ter **19**, 165209 (2007). URL https://iopscience.iop.org/article/10.1088/0953-8984/19/16/165209.

[159] Valet, T. & Fert, A. Theory of the perpendicular magnetoresistance in magnetic multilayers. *Physical Review B* **48**, 7099–7113 (1993). URL https://link.aps.org/doi/10.1103/PhysRevB.48.7099.

[160] Kimling, J. & Cahill, D. G. Spin diffusion induced by pulsed-laser heating and the role of spin heat accumulation. *Physical Review B* **95**, 014402 (2017). URL https://link.aps.org/doi/10.1103/PhysRevB.95.014402.

[161] Johnson, M. & Silsbee, R. H. Thermodynamic analysis of interfacial transport and of the thermomagnetoelectric system. *Physical Review B* **35**, 4959–4972 (1987). URL https://link.aps.org/doi/10.1103/PhysRevB.35.4959.

[162] Hatami, M., Bauer, G. E. W., Zhang, Q. & Kelly, P. J. Thermal Spin-Transfer Torque in Magnetoelectronic Devices. *Physical Review Letters* **99**, 066603 (2007). URL https://link.aps.org/doi/10.1103/PhysRevLett.99.066603.

[163] Slachter, A., Bakker, F. L., Adam, J.-P. & van Wees, B. J. Thermally driven spin injection from a ferromagnet into a non-magnetic metal. *Nature Physics* **6**, 879–882 (2010). URL http://www.nature.com/articles/nphys1767. 1004.1566.

[164] Bauer, G. E. W., Saitoh, E. & van Wees, B. J. Spin caloritronics. *Nature Materials* **11**, 391–399 (2012). URL http://www.nature.com/articles/nmat3301. 1107.4395.

[165] Shin, I. H., Min, B. C., Ju, B. K. & Choi, G. M. Ultrafast spin current generated by electron-magnon scattering in bulk of ferromagnets. *Japanese Journal of Applied Physics* **57**, 090307 (2018). URL https://iopscience.iop.org/article/10.7567/JJAP.57.090307.

[166] Beens, M., Heremans, J. P., Tserkovnyak, Y. & Duine, R. A. Magnons versus electrons in thermal spin transport through metallic interfaces. *Journal of Physics D: Applied Physics* **51**, 394002 (2018). URL https://iopscience.iop.org/article/10.1088/1361-6463/aad520. 1804.02172.

[167] Rückriegel, A. & Duine, R. A. Long-Range Phonon Spin Transport in Ferromagnet–Nonmagnetic Insulator Heterostructures. *Physical Review Letters* **124**, 117201 (2020). URL https://link.aps.org/doi/10.1103/PhysRevLett.124.117201.

[168] Choi, G.-M., Min, B.-C., Lee, K.-J. & Cahill, D. G. Spin current generated by thermally driven ultrafast demagnetization. *Nature Communications* **5**, 4334 (2014). URL http://www.nature.com/articles/ncomms5334.

[169] Choi, G.-M., Moon, C.-H., Min, B.-C., Lee, K.-J. & Cahill, D. G. Thermal spin-transfer torque driven by the spin-dependent Seebeck effect in metallic spin-valves. *Nature Physics* **11**, 576–581 (2015). URL http://www.nature.com/articles/nphys3355.

[170] Choi, G.-M. & Min, B.-C. Laser-driven spin generation in the conduction bands of ferrimagnetic metals. *Physical Review B* **97**, 014410 (2018). URL https://link.aps.org/doi/10.1103/PhysRevB.97.014410.

[171] Sato, K. & Togami, Y. Magneto-optical spectra of RF-sputtered amorphous Gd-Co and Gd-Fe films. *Journal of Magnetism and Magnetic Materials* **35**, 181–182 (1983). URL https://linkinghub.elsevier.com/retrieve/pii/0304885383904900.

[172] Gall, D. Electron mean free path in elemental metals. *Journal of Applied Physics* **119**, 085101 (2016). URL http://aip.scitation.org/doi/10.1063/1.4942216.

[173] Battiato, M., Carva, K. & Oppeneer, P. M. Superdiffusive Spin Transport as a Mechanism of Ultrafast Demagnetization. *Physical Review Letters* **105**, 027203 (2010). URL https://link.aps.org/doi/10.1103/PhysRevLett.105.027203. 1106.2117.

[174] Battiato, M., Carva, K. & Oppeneer, P. M. Theory of laser-induced ultrafast superdiffusive spin transport in layered heterostructures. *Physical Review B* **86**, 024404 (2012). URL https://link.aps.org/doi/10.1103/PhysRevB.86.024404.

[175] Nenno, D. M., Kaltenborn, S. & Schneider, H. C. Boltzmann transport calculation of collinear spin transport on short timescales. *Physical Review B* **94**, 115102 (2016). URL https://link.aps.org/doi/10.1103/PhysRevB.94.115102.

[176] Nenno, D. M., Rethfeld, B. & Schneider, H. C. Particle-in-cell simulation of ultrafast hot-carrier transport in Fe/Au heterostructures. *Physical Review B* **98**, 224416 (2018). URL https://link.aps.org/doi/10.1103/PhysRevB.98.224416.

[177] Chen, J. *et al.* Competing Spin Transfer and Dissipation at Co/Cu(001) Interfaces on Femtosecond Timescales. *Physical Review Letters* **122**, 067202 (2019). URL https://link.aps.org/doi/10.1103/PhysRevLett.122.067202.

[178] Töpler, F., Henk, J. & Mertig, I. Ultrafast spin dynamics in inhomogeneous systems: a density-matrix approach applied to Co/Cu interfaces. *New Journal of Physics* **23**, 033042 (2021). URL https://iopscience.iop.org/article/10.1088/1367-2630/abe72b. 2011.13763.

[179] Eschenlohr, A. *et al.* Ultrafast spin transport as key to femtosecond demagnetization. *Nature Materials* **12**, 332–336 (2013). URL http://www.nature.com/articles/nmat3546.

[180] Hofherr, M. *et al.* Speed and efficiency of femtosecond spin current injection into a nonmagnetic material. *Physical Review B* **96**, 100403 (2017). URL https://link.aps.org/doi/10.1103/PhysRevB.96.100403.

[181] Malinowski, G. *et al.* Control of speed and efficiency of ultrafast demagnetization by direct transfer of spin angular momentum. *Nature Physics* **4**, 855–858 (2008). URL http://www.nature.com/articles/nphys1092.

[182] Melnikov, A. *et al.* Ultrafast Transport of Laser-Excited Spin-Polarized Carriers in Au/Fe/MgO(001). *Physical Review Letters* **107**, 076601 (2011). URL https://link.aps.org/doi/10.1103/PhysRevLett.107.076601.

[183] Wieczorek, J. *et al.* Separation of ultrafast spin currents and spin-flip scattering in Co/Cu(001) driven by femtosecond laser excitation employing the complex magneto-optical Kerr effect. *Physical Review B* **92**, 174410 (2015). URL https://link.aps.org/doi/10.1103/PhysRevB.92.174410. 1503.01979.

[184] Alekhin, A. *et al.* Femtosecond Spin Current Pulses Generated by the Nonthermal Spin-Dependent Seebeck Effect and Interacting with Ferromagnets in Spin Valves. *Physical Review Letters* **119**, 017202 (2017). URL http://link.aps.org/doi/10.1103/PhysRevLett.119.017202. 1606.03614.

[185] Kumberg, I. *et al.* Accelerating the laser-induced demagnetization of a ferromagnetic film by antiferromagnetic order in an adjacent layer. *Physical Review B* **102**, 214418 (2020). URL https://link.aps.org/doi/10.1103/PhysRevB.102.214418. 2008.05268.

[186] Stamm, C. *et al.* X-ray detection of ultrashort spin current pulses in synthetic antiferromagnets. *Journal of Applied Physics* **127**, 223902 (2020). URL http://aip.scitation.org/doi/10.1063/5.0006095.

[187] Bergeard, N. *et al.* Hot-Electron-Induced Ultrafast Demagnetization in Co / Pt Multilayers. *Physical Review Letters* **117**, 147203 (2016). URL https://link.aps.org/doi/10.1103/PhysRevLett.117.147203.

[188] Lloyd-Hughes, J. *et al.* The 2021 Ultrafast Spectroscopic Probes of Condensed Matter Roadmap. *Journal of Physics: Condensed Matter* (2021). URL https://iopscience.iop.org/article/10.1088/1361-648X/abfe21.

[189] Stanciu, C. D. *et al.* All-Optical Magnetic Recording with Circularly Polarized Light. *Physical Review Letters* **99**, 047601 (2007). URL https://link.aps.org/doi/10.1103/PhysRevLett.99.047601.

[190] Mangin, S. *et al.* Engineered materials for all-optical helicity-dependent magnetic switching. *Nature Materials* **13**, 286–292 (2014). URL http://www.nature.com/articles/nmat3864.

[191] Lambert, C.-H. *et al.* All-optical control of ferromagnetic thin films and nanostructures. *Science* **345**, 1337–1340 (2014). URL https://www.sciencemag.org/lookup/doi/10.1126/science.1253493.

[192] El Hadri, M. S. *et al.* Two types of all-optical magnetization switching mechanisms using femtosecond laser pulses. *Physical Review B* **94**, 064412 (2016). URL https://link.aps.org/doi/10.1103/PhysRevB.94.064412. 1602.08525.

[193] Stupakiewicz, A., Szerenos, K., Afanasiev, D., Kirilyuk, A. & Kimel, A. V. Ultrafast nonthermal photo-magnetic recording in a transparent medium. *Nature* **542**, 71–74 (2017). URL http://www.nature.com/articles/nature20807.

[194] Stupakiewicz, A. *et al.* Ultrafast phononic switching of magnetization. *Nature Physics* **17**, 489–492 (2021). URL http://www.nature.com/articles/s41567-020-01124-9. 2010.13671.

[195] Xu, Y. *et al.* From single to multiple pulse all-optical switching in GdFeCo thin films. *Physical Review B* **100**, 064424 (2019). URL https://link.aps.org/doi/10.1103/PhysRevB.100.064424.

[196] Khorsand, A. R. *et al.* Role of Magnetic Circular Dichroism in All-Optical Magnetic Recording. *Physical Review Letters* **108**, 127205 (2012). URL https://link.aps.org/doi/10.1103/PhysRevLett.108.127205.

[197] Gorchon, J., Yang, Y. & Bokor, J. Model for multishot all-thermal all-optical switching in ferromagnets. *Physical Review B* **94**, 020409 (2016). URL https://link.aps.org/doi/10.1103/PhysRevB.94.020409.

[198] Quessab, Y. *et al.* Helicity-dependent all-optical domain wall motion in ferromagnetic thin films. *Physical Review B* **97**, 054419 (2018). URL https://link.aps.org/doi/10.1103/PhysRevB.97.054419. 1709.07645.

[199] Kimel, A. V. *et al.* Ultrafast non-thermal control of magnetization by instantaneous photomagnetic pulses. *Nature* **435**, 655–657 (2005). URL http://www.nature.com/articles/nature03564.

[200] Cornelissen, T. D., Córdoba, R. & Koopmans, B. Microscopic model for all optical switching in ferromagnets. *Applied Physics Letters* **108**, 142405 (2016). URL https://doi.org/10.1063/1.4945660http://aip.scitation.org/doi/10.1063/1.4945660.

[201] Du, Z., Chen, C., Cheng, F., Liu, Y. & Pan, L. Prediction of Deterministic All-Optical Switching of Ferromagnetic Thin Film by Ultrafast Optothermal and Optomagnetic Couplings. *Scientific Reports* **7**, 13513 (2017). URL http://www.nature.com/articles/s41598-017-13568-w.

[202] Ali, S., Davies, J. R. & Mendonca, J. T. Inverse Faraday Effect with Linearly Polarized Laser Pulses. *Physical Review Letters* **105**, 035001 (2010). URL https://link.aps.org/doi/10.1103/PhysRevLett.105.035001.

[203] Zhang, G. P., Latta, T., Babyak, Z., Bai, Y. H. & George, T. F. All-optical spin switching: A new frontier in femtomagnetism — A short review and a simple theory. *Modern Physics Letters B* **30**, 16300052 (2016). URL https://www.worldscientific.com/doi/abs/10.1142/S0217984916300052. 1609.09139.

[204] Kurkin, M. I., Bakulina, N. B. & Pisarev, R. V. Transient inverse Faraday effect and ultrafast optical switching of magnetization. *Physical Review B* **78**, 134430 (2008). URL https://link.aps.org/doi/10.1103/PhysRevB.78.134430.

[205] Battiato, M., Barbalinardo, G. & Oppeneer, P. M. Quantum theory of the inverse Faraday effect. *Physical Review B* **89**, 014413 (2014). URL https://link.aps.org/doi/10.1103/PhysRevB.89.014413.

[206] Berritta, M., Mondal, R., Carva, K. & Oppeneer, P. M. Ab Initio Theory of Coherent Laser-Induced Magnetization in Metals. *Physical Review Letters* **117**, 137203 (2016). URL https://link.aps.org/doi/10.1103/PhysRevLett.117.137203. 1604.01188.

[207] Scheid, P., Sharma, S., Malinowski, G., Mangin, S. & Lebègue, S. Ab Initio Study of Helicity-Dependent Light-Induced Demagnetization: From the Optical Regime to the Extreme Ultraviolet Regime. *Nano Letters* **21**, 1943–1947 (2021). URL https://dx.doi.org/10.1021/acs.nanolett.0c04166.

[208] Kichin, G. *et al.* From Multiple- to Single-Pulse All-Optical Helicity-Dependent Switching in Ferromagnetic Co / Pt Multilayers. *Physical Review Applied* **12**, 024019 (2019). URL https://link.aps.org/doi/10.1103/PhysRevApplied.12.024019.

[209] Li, G. *et al.* Timescales and contribution of heating and helicity effect in helicity-dependent all-optical switching (2020). URL https://arxiv.org/abs/2009.12816. 2009.12816v1[cond-mat.mtrl-sci].

[210] Khrapko, R. I. Question 79. Does plane wave not carry a spin? *American Journal of Physics* **69**, 405–405 (2001). URL http://aapt.scitation.org/doi/10.1119/1.1352719.

[211] Yurchenko, V. B. Answer to Question 79. Does plane wave not carry a spin? *American Journal of Physics* **70**, 568–569 (2002). URL http://aapt.scitation.org/doi/10.1119/1.1463741.

[212] Lalieu, M. L. M., Peeters, M. J. G., Haenen, S. R. R., Lavrijsen, R. & Koopmans, B. Deterministic all-optical switching of synthetic ferrimagnets using single femtosecond laser pulses. *Physical Review B* **96**, 220411 (2017). URL https://link.aps.org/doi/10.1103/PhysRevB.96.220411.

[213] Banerjee, C. *et al.* Single pulse all-optical toggle switching of magnetization without gadolinium in the ferrimagnet Mn2RuxGa. *Nature Communications* **11**, 4444 (2020). URL http://www.nature.com/articles/s41467-020-18340-9.

[214] Avilés-Félix, L. *et al.* Single-shot all-optical switching of magnetization in Tb/Co multilayer-based electrodes. *Scientific Reports* **10**, 5211 (2020). URL http://www.nature.com/articles/s41598-020-62104-w.

[215] Avilés-Félix, L. *et al.* All-optical spin switching probability in [Tb/Co] multilayers (2021). URL http://arxiv.org/abs/2103.05066. 2103.05066.

[216] Moreno, R., Ostler, T. A., Chantrell, R. W. & Chubykalo-Fesenko, O. Conditions for thermally induced all-optical switching in ferrimagnetic alloys: Modeling of TbCo. *Physical Review B* **96**, 014409 (2017). URL http://link.aps.org/doi/10.1103/PhysRevB.96.014409.

[217] Awano, H. *et al.* Magnetic domain expansion readout for amplification of an ultra high density magneto-optical recording signal. *Applied Physics Letters* **69**, 4257–4259 (1996). URL http://aip.scitation.org/doi/10.1063/1.116963.

[218] Ostler, T. A. *et al.* Crystallographically amorphous ferrimagnetic alloys: Comparing a localized atomistic spin model with experiments. *Physical Review B* **84**, 024407 (2011). URL https://link.aps.org/doi/10.1103/PhysRevB.84.024407.

[219] Stanciu, C. D. *et al.* Ultrafast spin dynamics across compensation points in ferrimagnetic GdFeCo : The role of angular momentum compensation. *Physical Review B* **73**, 220402 (2006). URL https://link.aps.org/doi/10.1103/PhysRevB.73.220402.

[220] Shieh, H. D. & Kryder, M. H. Magneto-optic recording materials with direct overwrite capability. *Applied Physics Letters* **49**, 473–474 (1986). URL http://aip.scitation.org/doi/10.1063/1.97120.

[221] Ogasawara, T., Iwata, N., Murakami, Y., Okamoto, H. & Tokura, Y. Submicron-scale spatial feature of ultrafast photoinduced magnetization reversal in TbFeCo thin film. *Applied Physics Letters* **94**, 162507 (2009). URL https://doi.org/10.1063/1.3123256.

[222] Vomir, M., Albrecht, M. & Bigot, J.-Y. Single shot all optical switching of intrinsic micron size magnetic domains of a Pt/Co/Pt ferromagnetic stack. *Applied Physics Letters* **111**, 242404 (2017). URL http://aip.scitation.org/doi/10.1063/1.5010915. 1710.10341.

[223] Hohlfeld, J. *et al.* Fast magnetization reversal of GdFeCo induced by femtosecond laser pulses. *Physical Review B* **65**, 012413 (2001). URL https://link.aps.org/doi/10.1103/PhysRevB.65.012413.

[224] Wang, S. *et al.* Dual-shot dynamics and ultimate frequency of all-optical magnetic recording on GdFeCo. *Light: Science and Applications* **10**, 8 (2021). URL http://www.nature.com/articles/s41377-020-00451-z.

[225] Bonfiglio, G. *et al.* Sub-picosecond exchange–relaxation in the compensated ferrimagnet Mn 2 Ru x Ga. *Journal of Physics: Condensed Matter* **33**, 135804 (2021). URL https://iopscience.iop.org/article/10.1088/1361-648X/abda7c.

[226] Mentink, J. H. *et al.* Ultrafast spin dynamics in multisublattice magnets. *Physical Review Letters* **108**, 057202 (2012). URL https://journals.aps.org/prl/pdf/10.1103/PhysRevLett.108.057202.

[227] Davies, C. S. *et al.* Exchange-driven all-optical magnetic switching in compensated 3d ferrimagnets. *Physical Review Research* **2**, 032044 (2020). URL https://link.aps.org/doi/10.1103/PhysRevResearch.2.032044.

[228] Davies, C. *et al.* Pathways for Single-Shot All-Optical Switching of Magnetization in Ferrimagnets. *Physical Review Applied* **13**, 024064 (2020). URL https://link.aps.org/doi/10.1103/PhysRevApplied.13.024064.

[229] Alebrand, S. *et al.* Subpicosecond magnetization dynamics in TbCo alloys. *Physical Review B* **89**, 144404 (2014). URL https://link.aps.org/doi/10.1103/PhysRevB.89.144404.

[230] Iacocca, E. *et al.* Spin-current-mediated rapid magnon localisation and coalescence after ultrafast optical pumping of ferrimagnetic alloys. *Nature Communications* **10**, 1756 (2019). URL http://www.nature.com/articles/s41467-019-09577-0. 1809.02076.

[231] Baral, A. & Schneider, H. C. Magnetic switching dynamics due to ultrafast exchange scattering: A model study. *Physical Review B* **91**, 100402 (2015). URL https://link.aps.org/doi/10.1103/PhysRevB.91.100402.

[232] Kalashnikova, A. M. & Kozub, V. I. Exchange scattering as the driving force for ultrafast all-optical and bias-controlled reversal in ferrimagnetic metallic structures. *Physical Review B* **93**, 054424 (2016). URL https://link.aps.org/doi/10.1103/PhysRevB.93.054424. 1506.06585.

[233] Gridnev, V. N. Ferromagneticlike states and all-optical magnetization switching in ferrimagnets. *Physical Review B* **98**, 014427 (2018). URL https://link.aps.org/doi/10.1103/PhysRevB.98.014427.

[234] Gridnev, V. N. Role of compensation points in all-optical magnetization switching. *Physical Review B* **100**, 174405 (2019). URL https://link.aps.org/doi/10.1103/PhysRevB.100.174405.

[235] Medapalli, R. *et al.* The role of magnetization compensation point for efficient ultrafast control of magnetization in Gd24Fe66.5Co9.5 alloy. *The European Physical Journal B* **86**, 183 (2013). URL http://link.springer.com/10.1140/epjb/e2013-30682-6.

[236] Xu, Y. *et al.* Ultrafast Magnetization Manipulation Using Single Femtosecond Light and Hot-Electron Pulses. *Advanced Materials* **29**, 1703474 (2017). URL http://doi.wiley.com/10.1002/adma.201703474.

[237] Atxitia, U., Barker, J., Chantrell, R. W. & Chubykalo-Fesenko, O. Controlling the polarity of the transient ferromagneticlike state in ferrimagnets. *Physical Review B* **89**, 224421 (2014). URL https://link.aps.org/doi/10.1103/PhysRevB.89.224421.

[238] Ostler, T. A. *et al.* Ultrafast heating as a sufficient stimulus for magnetization reversal in a ferrimagnet. *Nature Communications* **3**, 666 (2012). URL www.nature.com/naturecommunications.

[239] Atxitia, U., Nieves, P. & Chubykalo-Fesenko, O. Landau-Lifshitz-Bloch equation for ferrimagnetic materials. *Physical Review B* **86**, 104414 (2012). URL https://link.aps.org/doi/10.1103/PhysRevB.86.104414. 1206.6672.

[240] Schellekens, A. J. & Koopmans, B. Microscopic model for ultrafast magnetization dynamics of multisublattice magnets. *Physical Review B* **87**, 020407 (2013). URL https://link.aps.org/doi/10.1103/PhysRevB.87.020407.

[241] Wienholdt, S., Hinzke, D., Carva, K., Oppeneer, P. M. & Nowak, U. Orbital-resolved spin model for thermal magnetization switching in rare-earth-based ferrimagnets. *Physical Review B* **88**, 020406 (2013). URL https://link.aps.org/doi/10.1103/PhysRevB.88.020406.

[242] Beens, M., Lalieu, M. L. M., Deenen, A. J. M., Duine, R. A. & Koopmans, B. Comparing all-optical switching in synthetic-ferrimagnetic multilayers and alloys. *Physical Review B* **100**, 220409 (2019). URL https://link.aps.org/doi/10.1103/PhysRevB.100.220409. 1908.07292.

[243] Gorchon, J. *et al.* Role of electron and phonon temperatures in the helicity-independent all-optical switching of GdFeCo. *Physical Review B* **94**, 184406 (2016). URL https://link.aps.org/doi/10.1103/PhysRevB.94.184406. 1605.09764.

[244] Atxitia, U. & Ostler, T. A. Ultrafast double magnetization switching in GdFeCo with two picosecond-delayed femtosecond pump pulses. *Applied Physics Letters* **113**, 062402 (2018). URL http://aip.scitation.org/doi/10.1063/1.5044272.

[245] Banerjee, C. *et al.* Ultrafast Double Pulse All-Optical Reswitching of a Ferrimagnet. *Physical Review Letters* **126**, 177202 (2021). URL https://link.aps.org/doi/10.1103/PhysRevLett.126.177202.

[246] Wilson, R. B. *et al.* Ultrafast magnetic switching of GdFeCo with electronic heat currents. *Physical Review B* **95**, 180409 (2017). URL http://link.aps.org/doi/10.1103/PhysRevB.95.180409.

[247] Yang, Y. *et al.* Ultrafast magnetization reversal by picosecond electrical pulses. *Science Advances* **3**, e1603117 (2017). URL https://advances.sciencemag.org/lookup/doi/10.1126/sciadv.1603117. 1609.06392.

[248] Gorchon, J. *et al.* Single shot ultrafast all optical magnetization switching of ferromagnetic Co/Pt multilayers. *Applied Physics Letters* **111**, 042401 (2017). URL http://aip.scitation.org/doi/10.1063/1.4994802.

[249] Iihama, S. *et al.* Single-Shot Multi-Level All-Optical Magnetization Switching Mediated by Spin Transport. *Advanced Materials* **30**, 1804004 (2018). URL http://doi.wiley.com/10.1002/adma.201804004. 1805.02432.

[250] Lin, C.-J. *et al.* Magnetic and structural properties of Co/Pt multilayers. *Journal of Magnetism and Magnetic Materials* **93**, 194–206 (1991). URL https://linkinghub.elsevier.com/retrieve/pii/0304885391903299.

[251] Hashimoto, S. Adding elements to the Co layer in Co/Pt multilayers. *Journal of Applied Physics* **75**, 438–441 (1994). URL http://aip.scitation.org/doi/10.1063/1.355870.

[252] Krishnan, R., Lassri, H., Seddat, M., Porte, M. & Tessier, M. Magnetic properties of Co x Ni 1 - x /Pt multilayers. *Applied Physics Letters* **64**, 2312–2314 (1994). URL http://aip.scitation.org/doi/10.1063/1.111628.

[253] Koyama, T. *et al.* Dependence of Curie temperature on Pt layer thickness in Co/Pt system. *Applied Physics Letters* **106**, 132409 (2015). URL http://aip.scitation.org/doi/10.1063/1.4916824.

[254] Parakkat, V. M., Ganesh, K. R. & Anil Kumar, P. S. Tailoring Curie temperature and magnetic anisotropy in ultrathin Pt/Co/Pt films. *AIP Advances* **6**, 056118 (2016). URL http://aip.scitation.org/doi/10.1063/1.4944343.

[255] Menzinger, F. & Paoletti, A. Magnetic Moments and Unpaired-Electron Densities in CoPt3. *Physical Review* **143**, 365–372 (1966). URL https://link.aps.org/doi/10.1103/PhysRev.143.365.

[256] Lax, M., Louisell, W. H. & McKnight, W. B. From Maxwell to paraxial wave optics. *Physical Review A* **11**, 1365–1370 (1975). URL https://link.aps.org/doi/10.1103/PhysRevA.11.1365.

[257] Davis, L. W. Theory of electromagnetic beams. *Physical Review A* **19**, 1177–1179 (1979). URL https://link.aps.org/doi/10.1103/PhysRevA.19.1177.

[258] Liu, J. M. Simple technique for measurements of pulsed Gaussian-beam spot sizes. *Optics Letters* **7**, 196 (1982). URL https://www.osapublishing.org/abstract.cfm?URI=ol-7-5-196.

[259] Schellekens, S. *Manipulating spins novel methods for controlling magnetization dynamics on the ultimate timescale*. Ph.D. thesis, Eindhoven University of Technology (2014). URL www.tue.nl/taverne.

[260] Argyres, P. N. Theory of the Faraday and Kerr Effects in Ferromagnetics. *Physical Review* **97**, 334–345 (1955). URL https://link.aps.org/doi/10.1103/PhysRev.97.334.

[261] Oppeneer, P. M., Maurer, T., Sticht, J. & Kübler, J. Ab initio calculated magneto-optical Kerr effect of ferromagnetic metals: Fe and Ni. *Physical Review B* **45**, 10924–10933 (1992). URL https://link.aps.org/doi/10.1103/PhysRevB.45.10924.

[262] Oppeneer, P. M. Magneto-optical kerr spectra. In Buschow, K. (ed.) *Handbook of Magnetic Materials*, vol. 13, chap. 3, 229–422 (North Holland, 2001), 1st edn.

[263] Koopmans, B., van Kampen, M., Kohlhepp, J. T. & de Jonge, W. J. M. Ultrafast Magneto-Optics in Nickel: Magnetism or Optics? *Physical Review Letters* **85**, 844–847 (2000). URL https://link.aps.org/doi/10.1103/PhysRevLett.85.844.

[264] Guidoni, L., Beaurepaire, E. & Bigot, J.-Y. Magneto-optics in the Ultrafast Regime: Thermalization of Spin Populations in Ferromagnetic Films. *Physical Review Letters* **89**, 017401 (2002). URL https://link.aps.org/doi/10.1103/PhysRevLett.89.017401.

[265] Koopmans, B., van Kampen, M. & de Jonge, W. J. M. Experimental access to femtosecond spin dynamics. *Journal of Physics: Condensed Matter* **15**, S723–S736 (2003). URL https://iopscience.iop.org/article/10.1088/0953-8984/15/5/324.

[266] Razdolski, I. *et al.* Analysis of the time-resolved magneto-optical Kerr effect for ultrafast magnetization dynamics in ferromagnetic thin films. *Journal of Physics: Condensed Matter* **29**, 174002 (2017). URL https://iopscience.iop.org/article/10.1088/1361-648X/aa63c6.

[267] Vernes, A. & Weinberger, P. Formally linear response theory of pump-probe experiments. *Physical Review B* **71**, 165108 (2005). URL https://link.aps.org/doi/10.1103/PhysRevB.71.165108.

[268] Zhang, G. P., Hübner, W., Lefkidis, G., Bai, Y. & George, T. F. Paradigm of the time-resolved magneto-optical Kerr effect for femtosecond magnetism. *Nature Physics* **5**, 499–502 (2009). URL http://www.nature.com/articles/nphys1315.

[269] Vahaplar, K. *et al.* All-optical magnetization reversal by circularly polarized laser pulses: Experiment and multiscale modeling. *Physical Review B* **85**, 104402 (2012). URL https://link.aps.org/doi/10.1103/PhysRevB.85.104402.

[270] Hamrle, J. *Magneto-optical determination of the in-depth magnetization profile in magnetic multilayers*. Ph.D. thesis, Université Paris-Sud XI (2003).

[271] Schellekens, A. J., de Vries, N., Lucassen, J. & Koopmans, B. Exploring laser-induced interlayer spin transfer by an all-optical method. *Physical Review B* **90**, 104429 (2014). URL https://link.aps.org/doi/10.1103/PhysRevB.90.104429.

[272] Kazantseva, N., Hinzke, D., Chantrell, R. W. & Nowak, U. Linear and elliptical magnetization reversal close to the Curie temperature. *EPL (Europhysics Letters)* **86**, 27006 (2009). URL https://iopscience.iop.org/article/10.1209/0295-5075/86/27006.

[273] Schubert, M. Polarization-dependent optical parameters of arbitrarily anisotropic homogeneous layered systems. *Physical Review B* **53**, 4265–4274 (1996). URL https://link.aps.org/doi/10.1103/PhysRevB.53.4265.

[274] Katsidis, C. C. & Siapkas, D. I. Systems With Coherent , Partially Coherent , and Incoherent Interference. *Applied Optics* **41**, 3978–3987 (2002).

[275] Passler, N. C. & Paarmann, A. Generalized 4 × 4 matrix formalism for light propagation in anisotropic stratified media: study of surface phonon polaritons in polar dielectric heterostructures. *Journal of the Optical Society of America B* **34**, 2128 (2017). URL http://dx.doi.org/10.1364/JOSAB.34.002128https://www.osapublishing.org/abstract.cfm?URI=josab-34-10-2128. 1707.00462.

[276] Windt, D. L. IMD—Software for modeling the optical properties of multilayer films. *Computers in Physics* **12**, 360 (1998). URL http://scitation.aip.org/content/aip/journal/cip/12/4/10.1063/1.168689.

[277] Richter, F., Henneberger, K. & Florian, M. Comment on "Poynting vector, heating rate, and stored energy in structured materials: A first-principles derivation". *Physical Review B* **82**, 037103 (2010). URL https://link.aps.org/doi/10.1103/PhysRevB.82.037103.

[278] Zak, J., Moog, E. R., Liu, C. & Bader, S. D. Magneto-optics of multilayers with arbitrary magnetization directions. *Physical Review B* **43**, 6423–6429 (1991). URL https://link.aps.org/doi/10.1103/PhysRevB.43.6423.

[279] Silveirinha, M. G. Poynting vector, heating rate, and stored energy in structured materials: A first-principles derivation. *Physical Review B* **80**, 235120 (2009). URL https://link.aps.org/doi/10.1103/PhysRevB.80.235120.

[280] Silveirinha, M. G. Reply to "Comment on 'Poynting vector, heating rate, and stored energy in structured materials: A first-principles derivation' ". *Physical Review B* **82**, 037104 (2010). URL https://link.aps.org/doi/10.1103/PhysRevB.82.037104.

[281] Wang, C. Electromagnetic power flow, Fermat's principle, and special theory of relativity. *Optik* **126**, 2703–2705 (2015). URL https://linkinghub.elsevier.com/retrieve/pii/S0030402615005252.

[282] Kelly, R. L. Program of the 1972 Annual Meeting of the Optical Society of America. *Journal of the Optical Society of America* **62**, 1336 (1972). URL https://www.osapublishing.org/abstract.cfm?URI=josa-62-11-1336.

[283] Atkinson, R. *et al.* Fundamental optical and magneto-optical constants of Co/Pt and CoNi/Pt multilayered films. *Journal of Magnetism and Magnetic Materials* **162**, 131–138 (1996). URL https://linkinghub.elsevier.com/retrieve/pii/0304885396003356.

[284] Hendren, W. R. *et al.* Optical and magneto-optical characterization of TbFeCo and GdFeCo thin films for high-density recording. *Journal of Physics: Condensed Matter* **15**, 1461–1468 (2003). URL https://iopscience.iop.org/article/10.1088/0953-8984/15/9/310.

[285] Werner, W. S. M., Glantschnig, K. & Ambrosch-Draxl, C. Optical Constants and Inelastic Electron-Scattering Data for 17 Elemental Metals. *Journal of Physical and Chemical Reference Data* **38**, 1013–1092 (2009). URL https://doi.org/10.1063/1.3243762http://aip.scitation.org/doi/10.1063/1.3243762.

[286] McPeak, K. M. *et al.* Plasmonic Films Can Easily Be Better: Rules and Recipes. *ACS Photonics* **2**, 326–333 (2015). URL https://pubs.acs.org/sharingguidelineshttps://pubs.acs.org/doi/10.1021/ph5004237.

[287] Kittel, C. *Introduction to Solid State Physics* (John Wiley & Sons, 2005), 8th edn. 1011.1669.

[288] Pudell, J. *et al.* Heat Transport without Heating?—An Ultrafast X-Ray Perspective into a Metal Heterostructure. *Advanced Functional Materials* **30**, 2004555 (2020). URL https://onlinelibrary.wiley.com/doi/10.1002/adfm.202004555.

[289] Moreno, R., Khmelevskyi, S. & Chubykalo-Fesenko, O. Role of exchange parameters for ultrafast thermally induced magnetization switching in ferrimagnets. *Physical Review B* **99**, 184401 (2019). URL https://link.aps.org/doi/10.1103/PhysRevB.99.184401.

[290] Chimata, R. *et al.* All-thermal switching of amorphous Gd-Fe alloys: Analysis of structural properties and magnetization dynamics. *Physical Review B* **92**, 094411 (2015). URL https://link.aps.org/doi/10.1103/PhysRevB.92.094411.

[291] Hansen, P., Clausen, C., Much, G., Rosenkranz, M. & Witter, K. Magnetic and magneto-optical properties of rare-earth transition-metal alloys containing Gd, Tb, Fe, Co. *Journal of Applied Physics* **66**, 756–767 (1989). URL http://aip.scitation.org/doi/10.1063/1.343551.

[292] Mimura, Y., Imamura, N., Kobayashi, T., Okada, A. & Kushiro, Y. Magnetic properties of amorphous alloy films of Fe with Gd, Tb, Dy, Ho, or Er. *Journal of Applied Physics* **49**, 1208–1215 (1978). URL http://aip.scitation.org/doi/10.1063/1.325008.

[293] Mosca, D. *et al.* Oscillatory interlayer coupling and giant magnetoresistance in Co/Cu multilayers. *Journal of Magnetism and Magnetic Materials* **94**, L1–L5 (1991). URL https://linkinghub.elsevier.com/retrieve/pii/030488539190102G.

[294] van Hees, Y. L. W., van de Meugheuvel, P., Koopmans, B. & Lavrijsen, R. Deterministic all-optical magnetization writing facilitated by non-local transfer of spin angular momentum. *Nature Communications* **11**, 3835 (2020). URL http://www.nature.com/articles/s41467-020-17676-6. 2001.09033.

[295] Bergeard, N. *et al.* Tailoring femtosecond hot-electron pulses for ultrafast spin manipulation. *Applied Physics Letters* **117**, 222408 (2020). URL http://aip.scitation.org/doi/10.1063/5.0018502. 2006.07005.

[296] Igarashi, J. *et al.* Engineering Single-Shot All-Optical Switching of Ferromagnetic Materials. *Nano Letters* **20**, 8654–8660 (2020). URL https://pubs.acs.org/doi/10.1021/acs.nanolett.0c03373.

[297] Remy, Q. *et al.* Energy Efficient Control of Ultrafast Spin Current to Induce Single Femtosecond Pulse Switching of a Ferromagnet. *Advanced Science* **7**, 2001996 (2020). URL https://onlinelibrary.wiley.com/doi/10.1002/advs.202001996.

[298] Liao, J. *et al.* Controlling All-Optical Helicity-Dependent Switching in Engineered Rare-Earth Free Synthetic Ferrimagnets. *Advanced Science* **6**, 1901876 (2019). URL https://onlinelibrary.wiley.com/doi/abs/10.1002/advs.201901876.

[299] Bass, J. & Pratt, W. P. Spin-diffusion lengths in metals and alloys, and spin-flipping at metal/metal interfaces: an experimentalist's critical review. *Journal of Physics: Condensed Matter* **19**, 183201 (2007). URL https://iopscience.iop.org/article/10.1088/0953-8984/19/18/183201.

[300] Schellekens, A. J., Kuiper, K. C., de Wit, R. & Koopmans, B. Ultrafast spin-transfer torque driven by femtosecond pulsed-laser excitation. *Nature Communications* **5**, 4333 (2014). URL http://www.nature.com/articles/ncomms5333.

[301] Roth, T. *et al.* Temperature Dependence of Laser-Induced Demagnetization in Ni: A Key for Identifying the Underlying Mechanism. *Physical Review X* **2**, 021006 (2012). URL https://link.aps.org/doi/10.1103/PhysRevX.2.021006.

[302] Kuiper, K. C. *et al.* Spin-orbit enhanced demagnetization rate in Co/Pt-multilayers. *Applied Physics Letters* **105**, 202402 (2014). URL http://aip.scitation.org/doi/10.1063/1.4902069.

[303] Ding, M. & Poon, S. J. Tunable perpendicular magnetic anisotropy in GdFeCo amorphous films. *Journal of Magnetism and Magnetic Materials* **339**, 51–55 (2013). URL http://dx.doi.org/10.1016/j.jmmm.2013.03.007.

Appendix A

Transition rates

In this appendix, we discuss the transition from equation (5.18) to equation (5.19). First, one uses the wave vector representation for the conduction electrons:

$$c_{is} = \frac{1}{\sqrt{N}} \sum_{\mathbf{q}} e^{i\mathbf{q}\cdot\mathbf{r}_i} c_{\mathbf{q}s} \tag{A.1}$$

Where one should not confuse the number of lattice site N appearing as factors with the letter N indexing many body states. We note that the spin magnetic number is still a good quantum number as the longitudinal part of the s-d Hamiltonian commutes with s_i^z. We also use the fact that localized and itinerant spin operators act in independent spaces:

$$\begin{aligned} W^{\nu}_{m+1,m} = \frac{J_\nu^2 \pi}{2N^2\hbar} \sum_{NN'} \sum_{ij} \sum_{\mathbf{pqp'q'}} & \left\langle m+1 \left| S_i^+ \right| m \right\rangle \left\langle m \left| S_j^- \right| m+1 \right\rangle \\ & \left\langle N \left| c^\dagger_{\mathbf{p}\downarrow} c_{\mathbf{q}\uparrow} \right| N' \right\rangle \left\langle N' \left| c^\dagger_{\mathbf{q}'\uparrow} c_{\mathbf{p}'\downarrow} \right| N \right\rangle e^{i\mathbf{r}_i\cdot(\mathbf{q}-\mathbf{p})} e^{i\mathbf{r}_j\cdot(\mathbf{p}'-\mathbf{q}')} \\ & \frac{\rho_{N'N'}}{\Xi} \delta(E_N - E'_N + \Delta_\nu) \end{aligned} \tag{A.2}$$

Where we only focus on the term that increases the localized spin value for simplification as each transverse term in the Hamiltonian gives rise to separate transition rates. Next, we consider the electronic factors. These terms will be non zero if the effect of $c^\dagger_{\mathbf{p}\downarrow} c_{\mathbf{q}\uparrow}$ on $|N'\rangle$ is to transform it into $|N\rangle$. This means that $|N\rangle$ and $|N'\rangle$ must be identical up to one electron that has an opposite spin and a different wave vector (in general) in $|N\rangle$ compared to $|N'\rangle$. It also directly follows that $\mathbf{p} = \mathbf{p}'$ and $\mathbf{q} = \mathbf{q}'$. When the electronic factors are not zero, $\left\langle N \left| c^\dagger_{\mathbf{p}\downarrow} c_{\mathbf{q}\uparrow} \right| N' \right\rangle \left\langle N' \left| c^\dagger_{\mathbf{q}'\uparrow} c_{\mathbf{p}'\downarrow} \right| N \right\rangle = 1$. For given wave vectors $\mathbf{q}$ and $\mathbf{p}$, one can always factor $\exp(-\beta(\varepsilon_{\mathbf{q}\uparrow} - \mu_\uparrow))$ out of the density matrix element and $[1 + \exp(-\beta(\varepsilon_{\mathbf{q}\uparrow} - \mu_\uparrow))][1 +$

$\exp(-\beta(\varepsilon_{\mathbf{p}\downarrow}-\mu_\downarrow))]$ out of the grand canonical partition function. Following standard manipulations[34], the sum over the many body states can be simplified and one then gets:

$$W^\nu_{m+1,m}=\frac{\pi}{2\hbar}\sum_{ij}\sum_{\mathbf{pq}}J^\nu_{i\mathbf{qp}}J^{\nu*}_{j\mathbf{qp}}\left\langle m+1\left|S_i^+\right|m\right\rangle\left\langle m\left|S_j^-\right|m+1\right\rangle \\ \frac{e^{-\beta(\varepsilon_{\mathbf{q}\uparrow}-\mu_\uparrow)}}{1+e^{-\beta(\varepsilon_{\mathbf{q}\uparrow}-\mu_\uparrow)}}\frac{1}{1+e^{-\beta(\varepsilon_{\mathbf{p}\downarrow}-\mu_\downarrow)}}\delta(\varepsilon_{\mathbf{p}\downarrow}-\varepsilon_{\mathbf{q}\uparrow}+\Delta_\nu) \tag{A.3}$$

Where we used $J^\nu_{i\mathbf{qp}}=J_\nu\exp(i(\mathbf{q}-\mathbf{p})\cdot\mathbf{r}_i)/N$. It is important to note that the localized spins depend on lattice sites here. Otherwise, their matrix elements could be taken out of the sum and the complex exponential factors in $J^\nu_{i\mathbf{qp}}$ would lead to $\mathbf{q}=\mathbf{p}$. In that case, no transfer of momentum to the localized spins is taken into account. Such transfer actually exists and in order to consider the spatial inhomogeneity of localized spins, one needs to consider magnons[70]. As explained in chapter 3, magnons are usually taken into account through a Holstein-Primakoff transformation whose expansion is only valid for small spin deviations or classical spins. Because we consider quantum spins and possibly large spin deviations (and because we also do not have magnons at all in this MFA), we need another approach. Here, we will assume that the localized spins matrix elements do not depend on lattice site (consistently with Gridnev's model assumptions[92]) but transfer of momentum to the localized spins will still be permitted by assuming that $J^\nu_{i\mathbf{qp}}$ depends on wave vectors in a (unknown) more complicated way. Recognizing Fermi-Dirac distributions $f_s(\varepsilon_{\mathbf{q}s})=1/(\exp(\beta(\varepsilon_{\mathbf{q}s}-\mu_s))+1)$ and replacing the sum over wave vectors by integrals over energy:

$$W^\nu_{m+1,m}=\frac{\pi}{2\hbar}S^{\nu+}_m\sum_{ij}\int J^\nu_i(\varepsilon)J^{\nu*}_j(\varepsilon)D_\uparrow(\varepsilon-\Delta_\nu)f_\uparrow(\varepsilon-\Delta_\nu)D_\downarrow(\varepsilon)\left[1-f_\downarrow(\varepsilon)\right]\mathrm{d}\varepsilon \tag{A.4}$$

Where the energy dependence of $J^\nu_i(\varepsilon)$ is unknown. Because scattering happens for energies close to the Fermi energy, the latter quantity may be averaged over the Fermi surface and taken out of the integral. We also average it over lattice site such that $\left\langle J^\nu_i(\varepsilon)J^{\nu*}_j(\varepsilon)\right\rangle=\lambda^2J^2_\nu/N^2$ and λ then parametrizes the effect of localized spins spatial inhomogeneity. Taking this into account and also considering the other transverse term of the Hamiltonian, we get:

$$W^\nu_{m\pm1,m}=\frac{\pi}{2\hbar}J^2_\nu\lambda^2S^{\nu\pm}_m\int D_{\uparrow(\downarrow)}(\varepsilon\mp\Delta_\nu)f_{\uparrow(\downarrow)}(\varepsilon\mp\Delta_\nu)D_{\downarrow(\uparrow)}(\varepsilon)\left[1-f_{\downarrow(\uparrow)}(\varepsilon)\right]\mathrm{d}\varepsilon \tag{A.5}$$

Calculating this standard integral, one obtains equation (5.19) with $C_\nu=(\pi/2\hbar)J^2_\nu\lambda^2D_\uparrow(\varepsilon_F)D_\downarrow(\varepsilon_F)$, where we assumed that the densities of states are constant close to the Fermi energy ε_F. Then the densities of states only need to be known at the Fermi energy as usual. As mentioned in chapter 5, one needs an additional parameter, λ, even though

the exchange of angular momentum has the same origin as conduction electrons and localized spins exchange splitting. In reference 92, the role of λ is replaced by the average of the Bloch function over the Fermi surface. However, we believe that this is not quite right because the Bloch functions do not directly contain information about the inhomogeneity of the localized spins system.

Appendix B

Sample side excitation results in GdFeCo/Cu(10)/[Co/Pt]

This appendix shows similar results as the ones presented in section 7.3 except that laser pulse irradiation is done directly from the sample side while MOKE microscopy is done through the substrate. As we observe qualitatively similar results, this allows us to rule out the role of SDSE in the magnetization reversal observed in these structures.

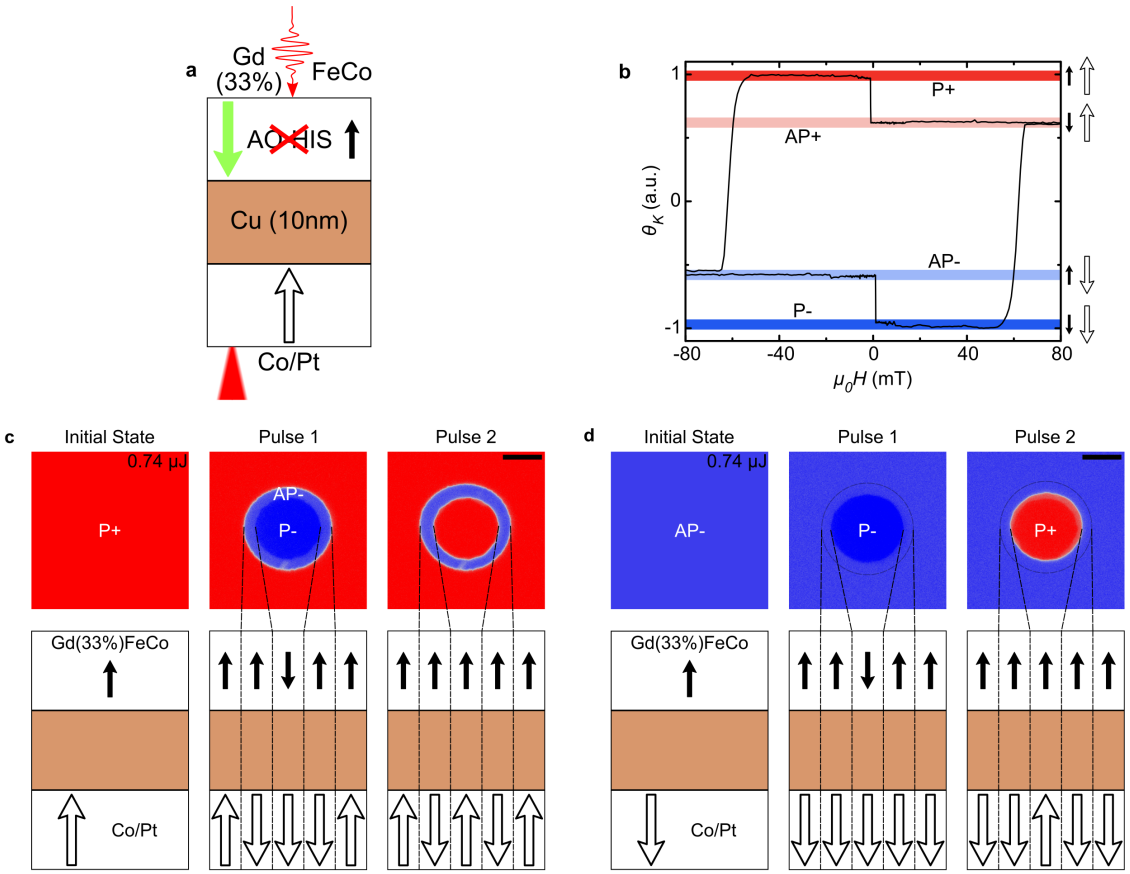

Figure B.1: (a) shows the simplified sample structure together with the experimental situation for MOKE microscopy. The red cone indicates on which side MOKE microscopy is performed and the wiggly arrow indicates on which side we send single laser pulses. (b) shows the hysteresis loops for $x = 33\%$, performed through the substrate side just as MOKE microscopy. The colored horizontal bars represent the color of the magnetic configuration in the MOKE microscopy images ((c) and (d)). (c) and (d) show the results of sending single laser pulses of high fluence on the $Gd_xFeCo/Cu/[Co/Pt]$ sample with $x = 33\%$ from P+ (c) and AP- (d) configurations. The pulse duration is 35 fs and the pulse energy is 0.74 µJ. The scale bars are 30 µm long.

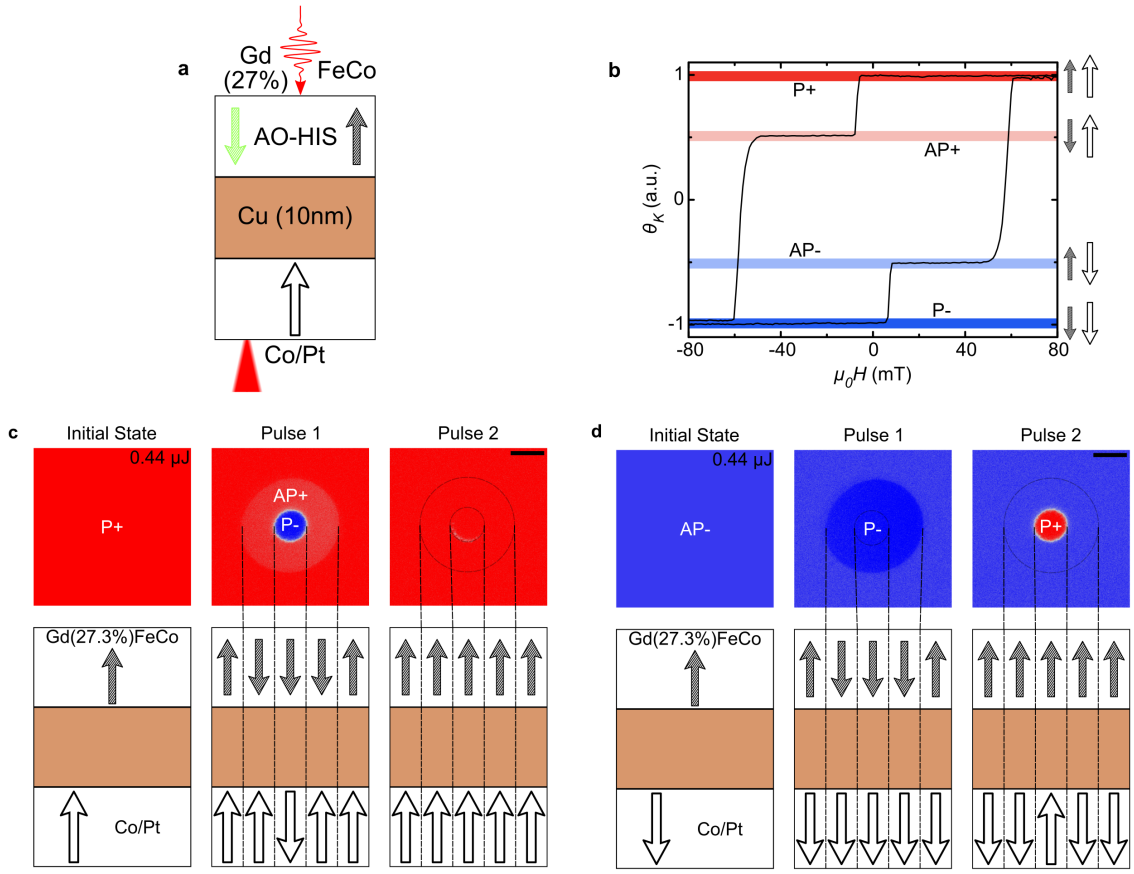

Figure B.2: (a) shows the simplified sample structure together with the experimental situation for MOKE microscopy. The red cone indicates on which side MOKE microscopy is performed and the wiggly arrow indicates on which side we send single laser pulses. (b) shows the hysteresis loops for $x = 27\%$, performed through the substrate side just as MOKE microscopy. The colored horizontal bars represent the color of the magnetic configuration in the MOKE microscopy images ((c) and (d)). (c) and (d) show the results of sending single laser pulses of high fluence on the Gd_xFeCo/Cu/[Co/Pt] sample with $x = 27\%$ from P+ (c) and AP- (d) configurations. The pulse duration is 35 fs and the pulse energy is 0.44 µJ. The scale bars are 30 µm long.

Résumé de la thèse

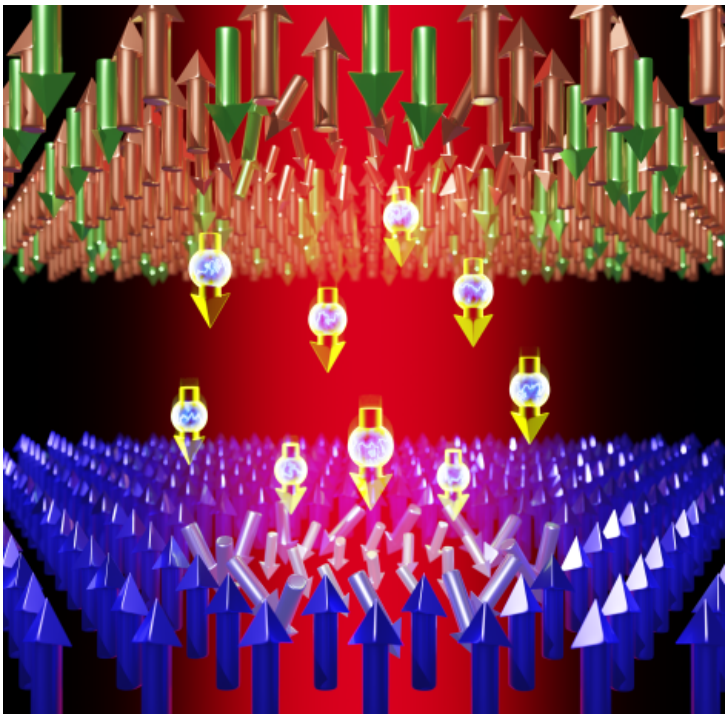

Représentation des systèmes considérés dans cette thèse.

Le spin est un objet physique particulier. Il est relié au moment cinétique d'une particule, c'est-à-dire une quantité conservée par rotation. Il est aussi associé au moment magnétique de l'électron qui contribue majoritairement au magnétisme des matériaux dits ferromagnétiques ou ferrimagnétiques. Les matériaux ferromagnétiques sont caractérisés par un seul réseau d'atomes magnétiques alors qu'un matériau ferrimagnétique possède deux sous réseaux magnétiques avec des aimantations pointant dans des directions opposées. Certains matériaux ferrimagnétiques possèdent une propriété particulière appelée le retournement tout optique indépendant de l'hélicité[189,238] (AO-HIS pour *All Optical Helicity Independent Switching* en anglais). Un matériau qui a de l'AO-HIS est un matériau qui retourne localement son aimantation si un

pulse laser, généralement d'une durée de quelques dizaines de femtosecondes, l'irradie. Ce mécanisme a surtout été observé dans l'alliage GdFeCo[189,238] mais aussi plus récemment dans MnRuGa[213]. Ce phénomène, tout comme la désaimantation ultra rapide[97], n'est pas autorisé par la thermodynamique standard et est le résultat d'un état hors équilibre transitoire. Quand le système n'est pas à l'équilibre, il n'est pas décrit par une seule température et un seul potentiel chimique (supposant que ces deux grandeurs suffisent à décrire la thermodynamique du système). La température peut dépendre de la position dans le système ou alors elle peut même être différente pour différentes particules ou quasi-particules. C'est aussi le cas pour le potentiel chimique qui peut généralement dépendre de la position et du spin. Cependant, on a aussi parfois un état hors équilibre caractérisé par le fait qu'aucune température ne peut être définie. Cette complexité par rapport aux phénomènes à l'équilibre rend l'étude de ces systèmes compliquée mais intéressante d'un point de vue fondamental. Dans le cas du GdFeCo, les phénomènes hors équilibres en jeux sont une différence de température entre les électrons de conduction (qui peuvent dépendre du spin), les phonons et les spins ainsi que d'une différence de potentiel chimique entre les électrons de spin up et de spin down. En particulier, les spins, formant l'aimantation du système, ne sont pas à l'équilibre entre eux ni avec les électrons. Comme ceux-ci sont cependant en interaction, l'état hors équilibre va forcer des transferts d'énergie et de moment cinétique pour rétablir l'équilibre. Au cours de ces transferts, le moment cinétique peut passer d'un sous réseau magnétique à un autre ce qui va permettre à l'aimantation totale du système de se retourner. Cependant, le moment cinétique ne passe pas directement d'un sous réseau à un autre. En effet, les électrons magnétiques du gadolinium sont fortements localisés et ils doivent donc intéragir tout d'abord avec des électrons de conduction sur un même site atomique. Le moment cinétique est donc transféré tout d'abord aux électrons de conduction puis seulement à l'autre sous réseau magnétique. Ainsi, durant ce processus, les électrons de conduction vont gagner du moment cinétique qui va créer, entre autre, une différence de potentiel chimique entre les électrons de spin up et de spin down. Comme les électrons de conduction sont très mobiles, ils peuvent généralement transporter le moment cinétique qu'ils portent ailleurs, par exemple à cause d'un gradient de température ou d'énergie. Ceci fut observé expérimentalement[170]. Lors de la désaimantation ultra rapide du GdFeCo (suivie d'un retournement ou non de l'aimantation), celui-ci va générer un courant de spin qui va pouvoir quitter le GdFeCo s'il est en contact avec une couche métallique, typiquement une couche de cuivre. Il a été récemment observé que l'effet de ce courant de spin, combiné à la désaimantation ultra rapide due à un seul pulse laser femtoseconde, permet de retourner l'aimantation d'un matériau ferromagnétique[249]. Ceci est très intéressant car autrement, le retournement de l'aimantation d'un matériau ferromagnétique

nécessite plusieurs pulses laser polarisés circulairement[190,191]. C'est dans ce contexte que se situe le travail présenté dans cette thèse. Nous souhaitons étudier la dynamique hors équilibre de l'aimantation, engendrée par des pulses laser femtoseconde, dans des matériaux métalliques où il peut y avoir du transport de spin.

Avant de présenter nos résultats, nous commençons par rappeler des concepts de physique de base tels que la conservation de l'énergie et du moment angulaire, le concept de spin, l'hamiltonien basse énergie du système ou nous discutons aussi la validité du concept d'aimantation de manière générale. Nous présentons ensuite les différentes approches et les différents résultats théoriques et expérimentaux qui ont déjà été faits dans le domaine générale de la dynamique hors équilibre de l'aimantation. Nous présentons ensuite nos propres méthodes expérimentales et théoriques.

Le principe physique étudié dans cette thèse est représenté schématiquement dans la figure ci-dessus. En haut, on peut voir le GdFeCo avec les flèches vertes qui représentent les moments magnétiques des atomes de gadolinium alors que les flèches rouges représentent les moments magnétiques des métaux de transition (le fer et le cobalt). Lorsque l'on excite le système avec un pulse laser femtoseconde (au centre en rouge) un courant de spin représenté par les petites flèches jaunes va sortir de la couche de GdFeCo. Celui-ci interagit ensuite avec l'aimantation d'un matériau ferromagnétique, comme des multicouches de Co/Pt, qui a été fortement réduite à cause de l'action du laser. Le courant de spin peut ensuite transférer son moment cinétique au matériau ferromagnétique qui va donc se retourner. De nombreuses questions sont toujours sans réponse dans ce genre de système et nous nous proposons de répondre à certaines d'entre elles dans cette thèse. D'abord, nous étudions un système légèrement différent composé de deux couches différentes de GdFeCo séparées par une couche de cuivre. Nous montrons que pour un alliage de GdFeCo contenant 30% de gadolinium, les électrons de conduction sont polarisés par le gadolinium alors que pour 20% la polarisation est donnée par les métaux de transition. Ceci est en accord avec l'observation expérimentale que nous faisons que le retournement de l'aimantation du GdFeCo avec 20% de gadolinium peut se faire avec un seul pulse laser si l'aimantation du gadolinium dans la couche avec 30% de gadolinium est dans la direction opposée de l'aimantation des métaux de transition dans la couche avec 20% de gadolinium. Dans le cas contraire, aucun retournement n'est observé et si la couche de GdFeCo avec 20% de gadolinium est isolée dans un échantillon différent, aucun retournement ne peut être observé non plus. Ceci montre que le courant de spin est en effet la cause du retournement de l'aimantation du GdFeCo avec 20% de gadolinium. De plus, nous montrons que la couche avec 30% de gadolinium ne doit pas nécessairement se retourner pour que l'on puisse observer le retournement de

l'aimantation de l'autre couche.

Le système précédent est très complexe à cause du fait que les matériaux en jeu sont ferrimagnétiques. Pour simplifier le problème, nous retournons ensuite dans la configuration présentée dans la figure ci-dessus où l'on a un matériau ferromagnétique au lieu de la couche de GdFeCo avec 20% de gadolinium. Dans ce cas là, nous nous intéressons séparement au rôle du chauffage de la couche ferromagnétique par les pulses laser et le rôle des courants de spin. Pour étudier le rôle du chauffage, nous considéront différents matériaux ferromagnétiques ayant des températures de Curie différentes. Nous observons que l'énergie nécessaire pour retourner l'aimantation de la couche ferromagnétique augmente lorsque sa température de Curie augmente, indiquant que le matériau ferromagnétique doit être suffisamment désaimanté pour que le retournement puisse se faire. Pour étudier le rôle du courant de spin, nous changeons la durée du pulse laser ou la concentration en gadolinium dans l'alliage de GdFeCo. En effet, lorsque cette concentration augmente, il a été montré que le moment cinétique relâché par la couche de GdFeCo dans une couche métallique voisine augmente également. Nous observons dans ce cas qu'augmenter la concentration de gadolinium réduit l'énergie nécessaire pour retourner l'aimantation de la multicouche ferromagnétique. Ceci montre que le courant de spin ne fait pas qu'autoriser le retournement de l'aimantation en lui donnant une direction privilégiée mais il y a bien un transfert de moment cinétique non négligeable qui s'effectue. Dans le cas où la durée du pulse est augmentée, cela ralentie la dynamique de l'aimantation du GdFeCo et diminue ainsi l'intensité du courant de spin qui est généré. Des résultats similaires au cas où la concentration en gadolinium est changée sont ainsi obtenus. Enfin, nous avons augmenté l'épaisseur de la couche de cuivre entre le GdFeCo et la couche ferromagnétique jusqu'à ce que la lumière du pulse laser ne puisse plus attendre la couche ferromagnétique. Cependant, nous observons qu'il est toujours possible de retourner l'aimantation de la couche ferromagnétique avec uniquement un seul pulse laser femtoseconde. Ceci montre que la lumière en elle même n'est pas nécessaire mais seulement un transfert rapide de chaleur et de moment cinétique.

Dans un dernier temps, nous avons cherché à savoir à quelle vitesse le retournement de l'aimantation du matériau ferromagnétique s'effectue. En utilisant une technique expérimentale qui mélange de la microscopie à effet Kerr avec les techniques pompe-sonde, nous avons pu obtenir la dynamique de l'aimantation de cette couche ferromagnétique en fonction de la position sur l'échantillon. Nous avons observé que le retournement s'effectue en environ 400 femtosecondes pour un pulse laser d'une durée de 100 femtosecondes, ce qui est le retournement d'aimantation le plus rapide jamais observé. Ces mesures nous permettent aussi d'élucider le rôle de l'aimantation de chaque espèce chimique de l'alliage de GdFeCo dans le retournement

de l'aimantation du matériau ferromagnétique. En particulier, nous voyons qu'à des échelles de temps extrêmement courtes (par rapport à la durée du pulse laser) d'environ 200 fs, le courant de spin issue de la désaimantation des métaux de transition peut aussi permettre un retournement de l'aimantation mais qui est cependant transitoire. Nous pouvons aussi obtenir de ses mesures qu'après le retournement de l'aimantation en environ 400 femtosecondes, l'aimantation de la couche ferromagnétique reste dans un état de non équilibre jusqu'à environ deux picosecondes. L'effet du courant de spin est si important que nous observons qu'il peut augmenter l'aimantation de la couche ferromagnétique de 30% par rapport à une situation sans courant de spin. Cet effet, que nous dénommons réfrigération de spin (*spin cooling* en anglais) est aussi lui même ultra rapide apparaissant en seulement quelques picosecondes.

Ces mesures expérimentales ont été supplémentées par des calculs théoriques. Ces calculs sont basés sur des équations de cinétique quantique pour le transport d'énergie et de moment angulaire. Des approximations standards sont faites pour simplifier la résolution de ces problèmes. En particulier, il est supposé que l'approximation de Markov est vérifiée, où l'on néglige les effets mémoire, et on suppose aussi que l'énergie est strictement conservée. Dans le contexte de l'équation de Von Neumann pour la matrice de densité, cela donne la règle d'or de Fermi qui nous permet de calculer des taux de transition. En combinant ces taux de transitions avec l'équation de Boltzmann pour les électrons, les phonons et les spins quantiques localisés avec les interactions correspondantes, on peut obtenir un ensemble d'équations couplées qui, une fois résolues, donnent la dynamique de la température et du moment cinétique dans le système. Pour déclencher l'état de non équilibre, il est cependant nécessaire de considérer l'interaction de la lumière avec la matière. Dans le cadre de ce modèle semi-classique, nous avons généralisé une approche standard de telle sorte à pouvoir modéliser les effets des pulses laser de manière plus réaliste. Nous discutons cependant les limitations de considérer l'interaction lumière matière dans ces approches semi-classiques. Néanmoins, nous trouvons, sans aucune procédure de fit, que les résultats donnés par ces calculs théoriques reproduisent qualitativement nos résultats expérimentaux. En particulier, les énergies nécessaires pour le renversement de l'aimantation du matériau ferromagnétique sont retrouvées avec seulement un facteur deux de différence et avec une tendance identique lorsque l'on varie des paramètres tels que la température de Curie. Dans le cadre des mesures de dynamique du renversement magnétique ultra rapide du matériau ferromagnétique, nous sommes capable de reproduire le renversement en moins d'une picoseconde grâce au courant de spin provenant du gadolinium ou grâce à celui provenant des métaux de transition. Nous pouvons aussi savoir si l'aimantation est à l'équilibre avec les électrons ou non et nous pouvons reproduire l'effet de spin cooling susmentionné.